Covalent-Triazine based Framework Photocatalysts for the Hydrogen Production from Water

Thesis submitted in accordance with the requirements of the University of Liverpool for the degree of Doctor in Philosophy by

Christian Meier

November 2018
Student ID Number 201096326

Department of Chemistry
University of Liverpool

Supervision: Professor Andrew I. Cooper, Dr R. Sebastian Sprick, Dr Anna G. Slater

First, I would like to acknowledge the funding from the Engineering and Physical Sciences Research Council which supported this PhD studentship.

I am grateful to my supervisor, Professor Andy Cooper, for his support, time, and advice over the last few years. It is a generous advantage to have a free choice of research, and it was a pleasure to discuss topics apart from science. Thank you Andy!

A big thank you to Dr Sebastian Sprick and Dr Michael Briggs for their detailed input and advice. Their support went above and beyond many aspects in chemistry, and I want to thank the whole supervisory team for their time. I am grateful to Dr Sebastian Sprick and Dr Rebecca Greenaway for their time to read and correct this thesis.

Many thanks also to Rob Clowes who did introductory training and custom-made solutions for all the equipment used. Without your support, it would have been less funny in the high-throughput environment.

And of course to all members of the Cooper group, the former CMD-staff and the MIF-staff for the discussions, their warm welcome and collaborations. Further special thanks to Dr Martijn A. Zwijnenburg and co-workers, and Dr Kim E. Jelfs and co-workers for the theoretical calculations about water splitting.

I would also like to thank my family for their steady source of support, as much can change in around four years.

1 Abstract

Photocatalytic hydrogen production from water is a research area of growing interest as hydrogen has been identified as a potential energy carrier of the future. This work presents polymeric photocatalysts based on covalent triazine-based frameworks (CTFs) for hydrogen and oxygen evolution under sacrificial conditions.

Covalent triazine-based frameworks consist of triazine units and linkers that covalently connect them. A systematic study of variable linker length ranging from phenylene to quarterphenylene was investigated in a small family of CTFs (CTF-1 to CTF-4). Polymers CTF-1 to CTF-4 were synthesised from nitriles *via* trifluoromethanesulfonic acid catalysis, and CTF-2 Suzuki to CTF-4 Suzuki were synthesised using the Suzuki-Miyaura polycondensation. The materials properties were fine-tuned by modifying the monomers. The optical properties of the CTFs were compared to the hydrogen evolution rates in the presence of platinum co-catalyst under sacrificial conditions. A decrease of the band-gap with a longer linker length was found in both reaction types – from 2.95 eV to 2.48 eV for CTF-1 to CTF-4 and from 2.93 eV to 2.85 eV for CTF-2 Suzuki to CTF-4 Suzuki. The acid-catalysed CTF-2 was found to produce the highest hydrogen rate of 265 µmol g^{-1} h^{-1} and further studies focused on the low hydrogen evolution rates of CTF-1.

In the second chapter, a library of 40 CTFs was synthesised using Suzuki-Miyaura polycondensations. The hydrogen evolution was tested under sacrificial conditions and using platinum as a co-catalyst. The target was to discover photocatalysts that demonstrated higher hydrogen evolution rates than found for CTF-2 with 265 µmol g^{-1} h^{-1}, and the best performing photocatalyst CTF-15 was found to enhance the evolution rate. In comparison to CTF-2, a ten-fold increase was achieved to around 3000 µmol g^{-1} h^{-1} under visible light irradiation. The linker units used for the polymer synthesis include phenyl derivatives with 1,3- and 1,4-substitution, fluorobenzenes, and heterocycles containing nitrogen, oxygen, sulfur and selenium. Subsets of structurally similar monomer linkers were compared by using optical data, fluorescence life-time spectroscopy, nitrogen accessible surface areas, transmission measurements in solution, and contact angle measurements. A correlation between the band-gap, fluorescence life-time, and average transmission from the scavenger mixture was found to describe the four best photocatalysts of the series. A high-throughput (HT) setup was used to test the library for hydrogen evolution and the results were compared to manual measurements. The two best performing catalysts were clearly identified with both methods. Additional investigations were carried out to study the hydrogen evolution dependency on the scavenger system, and the structurally related

photocatalysts CTF-15 and CTF-16, synthesised using cyanobenzene and *para*-dicyanobenzene linkers, respectively, are discussed.

The library of 40 CTFs was then investigated for oxygen evolution under sacrificial conditions using silver nitrate on the HT setup, and oxygen was detected when CTF-14 was tested. Unfortunately, this photocatalyst decomposed during photocatalysis. As the CTF library showed low oxygen evolution rates using silver nitrate, the CTFs were screened with the co-catalysts gold, RuO_2, and $Co(OH)_2$ and were found to show moderate oxygen evolution rates of up to 35 µmol g^{-1} h^{-1} for CTF-41 in combination with gold, while there is still limited evidence of water as the source of oxygen.

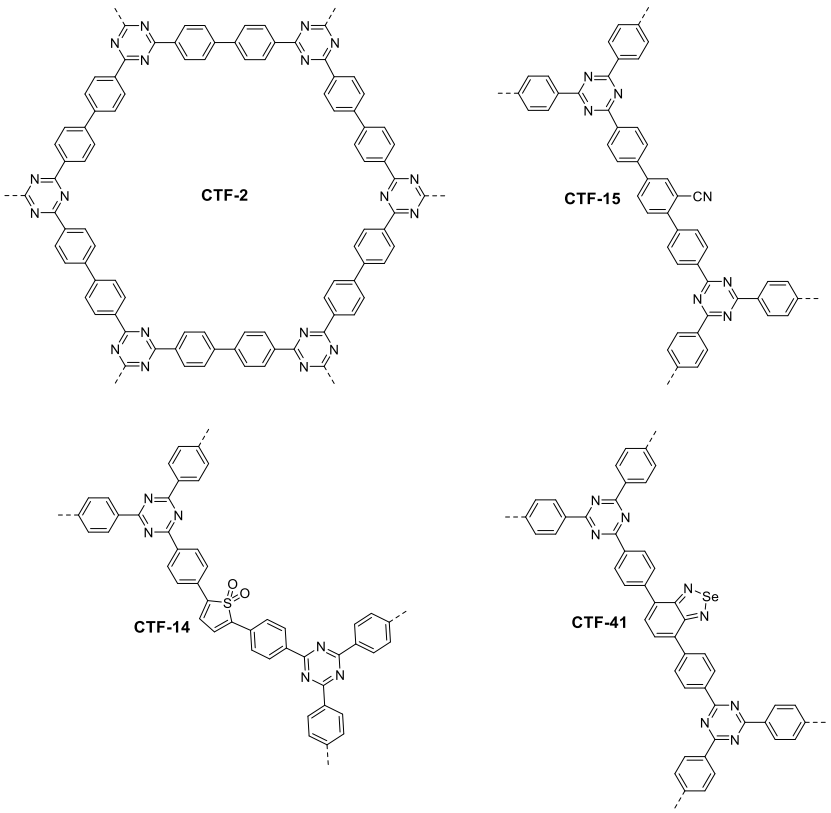

Figure A-1: CTF photocatalysts: CTF-2 and CTF-15 were found to be the best photocatalysts for hydrogen evolution from TEA/water/MeOH in presence of platinum co-catalyst. CTF-14 was found to be unstable during photocatalysis, and CTF-41 was found to be the best catalyst for oxygen evolution from silver nitrate with a gold co-catalyst.

2 Declaration of academic integrity

This research project is my original work and has not been presented for a degree or other awards in any university or institution of higher learning.

I confirm that I have read and understood the University's Academic Integrity Policy.

I confirm that I have acted honestly, ethically and professionally in conduct leading to assessment for the programme of study.

I confirm that I have not copied material from another source nor committed plagiarism nor fabricated, falsified or embellished data when completing the attached piece of work. I confirm that I have not copied material from another source, nor colluded with any other student in the preparation and production of this work. All figures in this work are drawn for this thesis and not copied from the references.

Part of the results were summarised in the following articles: (*supervision; ‖photocurrent measurement; †design of high-throughput workflow and technical support; ‡computational work)

Meier, C. B.; Sprick, R. S.*; Monti, A.‡; Guiglion, P.‡; Lee, J.-S. M.‖; Zwijnenburg, M. A.‡; Cooper, A. I.* *Polymer* **2017**, *126*, 283.

Meier, C. B.; Clowes, R.†; Berardo, E.‡; Sprick, R. S.*; Jelfs, K. E.‡; Zwijnenburg, M. A.‡; Cooper, A. I.* *manuscript in preparation*.

Signature…….. Date……..

Christian B. Meier

3 List of abbreviations

ANW	Poly(azomethine) networks
AQY	Apparent quantum yield
BET	Brunauer-Emmett-Teller
bpy	2,2'-Bipyridine
CB	Conduction band
CMP	Conjugated microporous polymer
COD	Cyclooctadien
COF	Covalent organic framework
CP	Co-polymer
CTF	Covalent triazine-based framework
CTP	Conjugated triazine-based polymers
DEA	Diethylamine
DMF	Dimethylformamide
DFT	Density functional theory
EA	Electron affinity
EDW	Electron donating group
EQE	External Quantum Efficiency
EWG	Electron withdrawing group
ESI	Electrospray ionisation
FT-IR	Fourier-transform infrared
FWHM	Full width at half maximum
GC	Gas chromatograph / gas chromatography
GPC	Gel permeation chromatography
g-C_3N_4	Graphitic carbon nitride
HER	Hydrogen evolution rate
HRMS	High resolution mass spectrometry

HT	High-throughput
ICP	Inductively coupled plasma
IP	Ionisation potential
MeOH	Methanol
MOF	Metal–organic framework
NHE	Normal hydrogen electrode
NMR	Nuclear magnetic resonance
OER	Oxygen evolution rate
OPP	Oligo(*p*-phenylene)
PIM	Polymer of intrinsic microporosity
PCP	Porous conjugated polymers
PPP	Poly(*para*-phenylene)
PL	Photoluminescence
PXRD	Powder X-ray diffraction
OER	Oxygen evolution rate
PPy	Poly(pyridine-2,5-diyl)
RT	Room temperature
SA	Surface area
SHE	Standard hydrogen electrode
SNP	Sulfur-and nitrogen-containing polymers
SP-CMP	Spirobifluorene CMP
TAS	Transient absorption spectroscopy
TBPT	Tris[4-(4,4,5,5-tetramethyl-1,3,2-dioxaborolan-2-yl)phenyl]-1,3,5-triazine
TCSPC	Time-correlated single photon counting
TD-DFT	Time-dependent density functional theory
TEA	Triethylamine
TEM	Transmission electron microscopy
TFPT	1,3,5-Tris-(4-formyl-phenyl)triazine
TEOA	Triethanolamine
TGA	Thermal gravimetric analysis

THF	Tetrahydrofuran
TPT	2,4,6-Triphenyl-1,3,5-triazine
Triflic acid	Trifluoromethanesulfonic acid
UV-Vis	Ultraviolet-visible
VB	Valence band
XPS	X-ray photoelectron spectroscopy

4 Introduction

4.1 Conjugated microporous polymers

Organic porous materials have been investigated since the late 1960s, when Davankov and co-workers reported hypercrosslinked polystyrene networks to be microporous[1] with pores widths below 2 nm.[2] Their synthesis, based on Friedel-Craft alkylations to achieve multiple structural bridges between neighbouring benzenes and further studies, focussed intensively on polymers made from polystyrene.[3] With the exception of poly(arylcarbinol) networks,[4,5] the preparation of microporous organic network polymers was unexplored. In 2004, polymers with intrinsic microporosity (PIMs)[6–9] were introduced, and hypercrosslinked poly(aniline)s were prepared for hydrogen storage.[10] Figure I-1 shows some examples of microporous organic polymers.

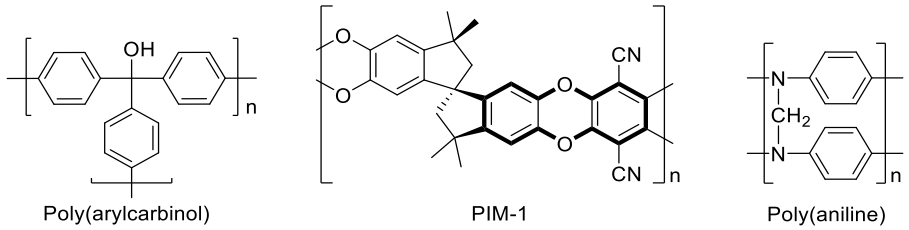

Figure I-1: Examples of microporous organic polymers.[5,7,10]

Zeolites,[11] metal-organic frameworks (MOFs),[12] and covalent-organic frameworks (COFs)[13] represent further porous materials and were reported to be crystalline. In 2007, a new class of polymers with permanent microporosity and π-conjugation was reported: conjugated microporous polymers (CMPs).[14] CMPs are conjugated and covalently linked,[15] and can be synthesised with high internal surface areas.[16] The diversity in CMPs is driven by the variety in size, shape, functionality, and connectivity of the building blocks used to form these amorphous networks. This enormous pool of monomers has been successfully used to tune the polymers' properties. For example, it is possible to vary the pore size to maximise the surface area for specific applications. Due to their structural variety and applications, inter alia in gas adsorption, heterogeneous catalysis, and light harvesting, , the number of reported CMPs is rapidly growing. Various π-units have been used as building blocks (Figure I-2) and synthetic approaches were employed on different reaction types, e.g. Suzuki-Miyaura cross-coupling,[17] Yamamoto coupling, [17,18] Sonogashira-Hagihara coupling,[14,19] Schiff-base condensation,[20] and cyclotrimerisation reaction.[21,22]

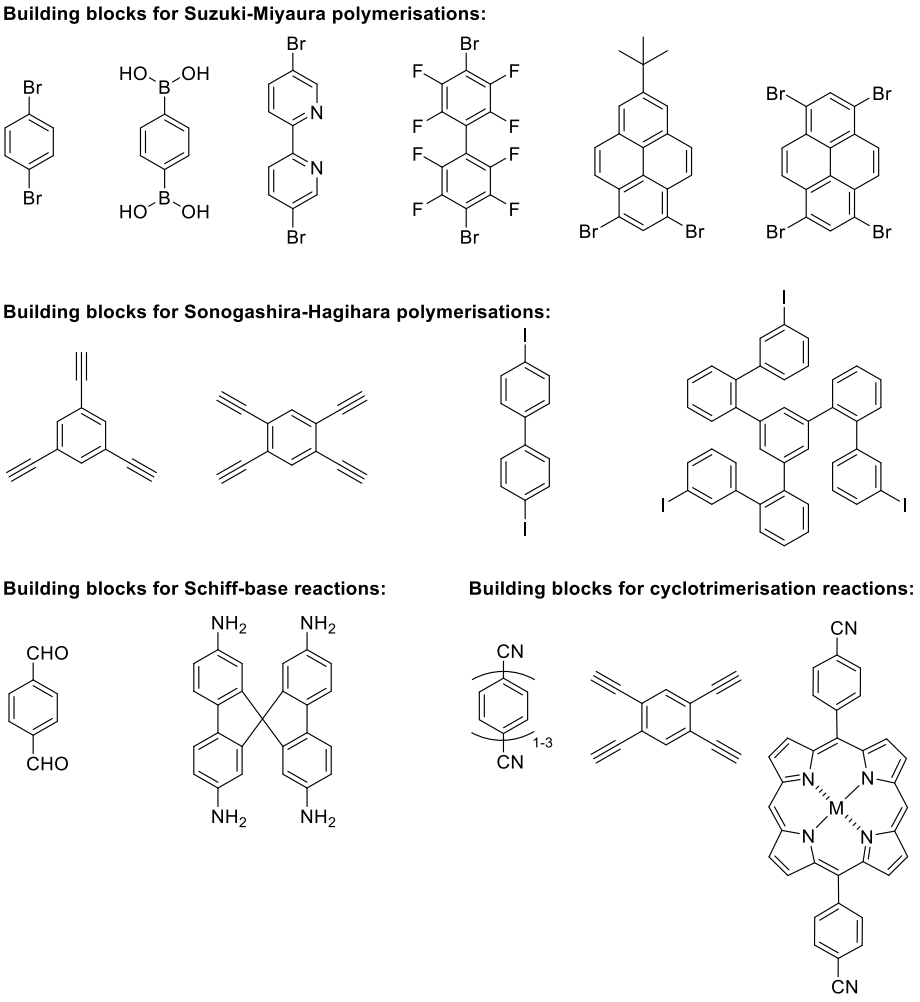

Figure I-2: Selected building blocks used in the formation of CMPs.[16]

The exceptional structural diversity of CMPs has led to their use in a number of applications. Often, their small pores or high surface area are responsible for their functional use. Examples are the adsorption and storage of gases, such as hydrogen[21,23] or methane,[24] and their use as molecular sponges to separate organic solvents from water.[25] In the field of heterogeneous catalysis, an iron(III) loaded metallaporphyrin (FeP-CMP)[26] demonstrated the loading of metals as the catalytic centres to oxidise sulfides to sulfoxides (Figure I-3). There are advantages in using CMP based heterogeneous catalysts: the porphyrin unit is used to build three-dimensional networks with pores that allow the transport of the reactants to the catalytic sites and the release of the product. After the reaction, the insoluble polymeric catalyst is recovered for reuse by centrifugation, while the product remains in solution. Mass transport limitations of the substrate or the product in the narrow channels might off-set the benefits of higher surface area, but can be overcome by varying the network structure.

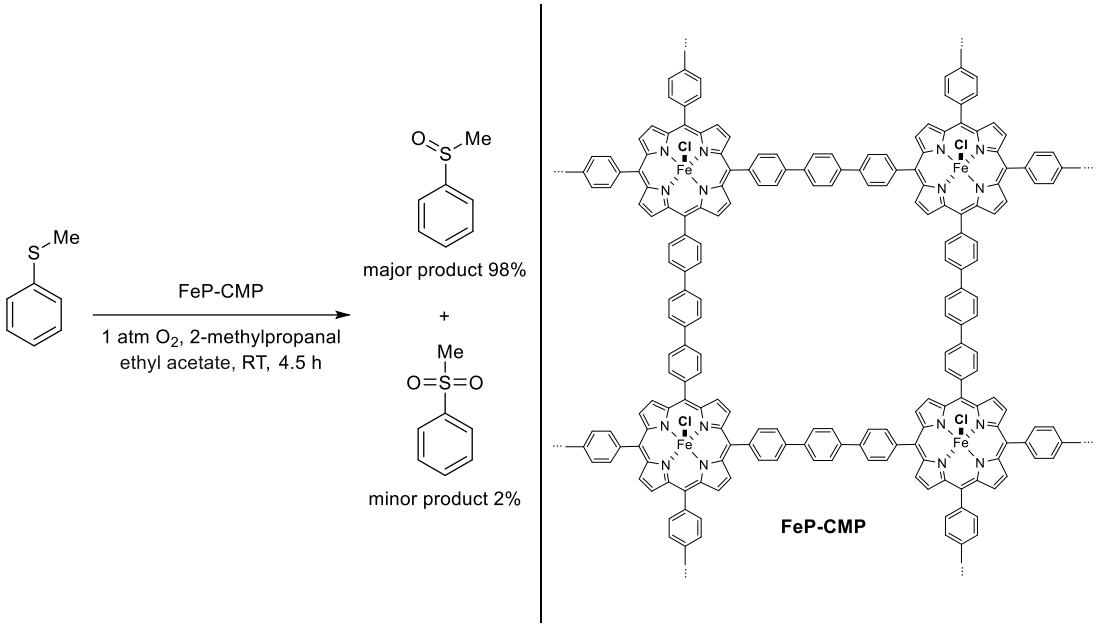

Figure I-3: CMP based heterogeneous catalyst with an iron centre to transform sulfides to sulfoxides[26] (idealised structure).

In addition to heterogeneous catalysis, CMPs have been used as light emitters,[27] as well as for energy storage.[28] Polyphenylene-based PP-CMP,[29] for example, work as light-harvesting antennae and support energy migration over the network (Figure I-4). The micropores were used to encapsulate Coumarin 6 as an energy-accepting guest.

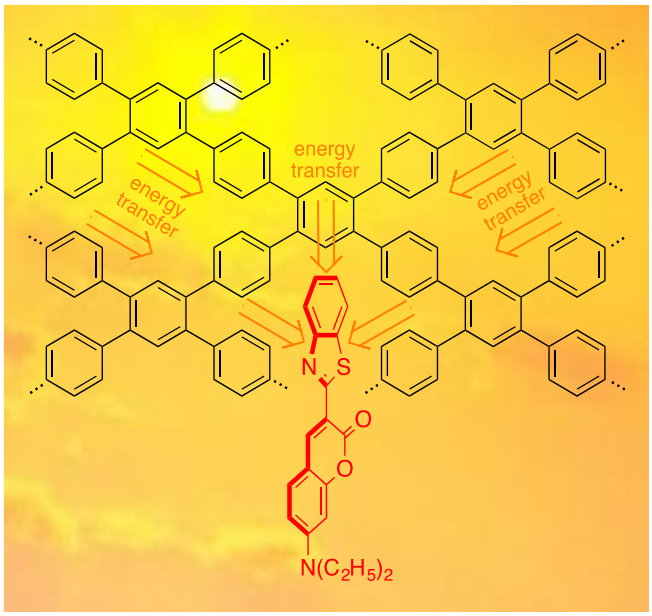

Figure I-4: Polyphenylene-based PP-CMPs harvest light and transfer the collected energy to Coumarin 6 acceptors (red).[29]

4.2 Hydrogen as a renewable energy fuel

Hydrogen could be the next generation fuel as it has a high energy capacity and does not form any environmental pollutants when oxidised with oxygen to form water.[30] A large amount of research has focused on finding scalable, green techniques to produce hydrogen. At present, hydrogen is mostly produced in energy-consumingprocesses that release the greenhouse gas carbon dioxide. [31,32] Among them, steam methane reforming of natural gas accounts for 48% of the global hydrogen production, followed by partial oxidation of oil (18%) and coal gasification (18%).[33] Only 4% of hydrogen is currently produced from electrolysis (Figure I-5).

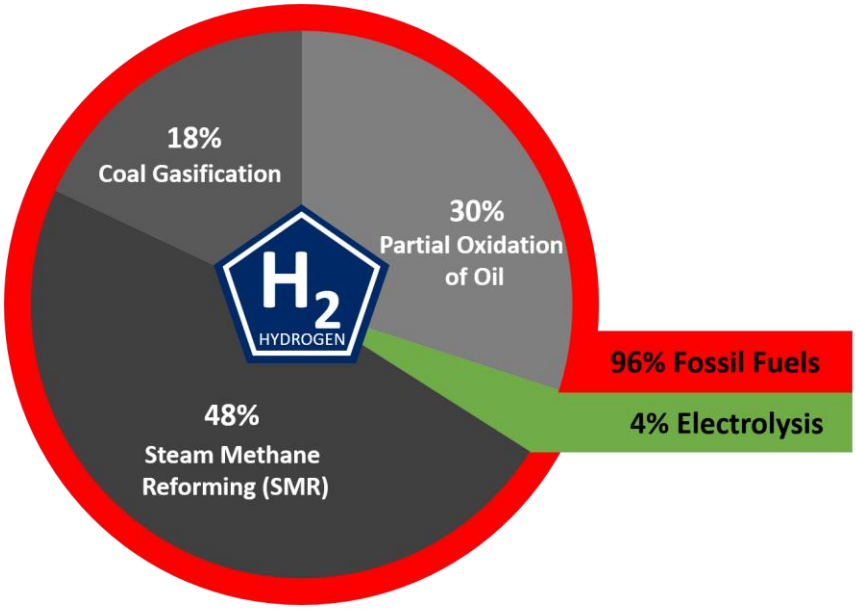

Figure I-5: Overview of the global hydrogen production in 1999.[33]

Currently, hydrogen is used predominately in industrial processes: ammonia production, applications in the food industry, metal/glass production, electronic industry, and chemical industry/refining (Figure I-6). In total, the global production exceeded 683000 tons in 2016,[33] and its use is believed to continue to increase due to applications in electric grid stabilisation (water electrolysis to hydrogen and oxygen from surplus solar energy), natural gas and hydrogen grid structures, and the future demand in transportation.[34]

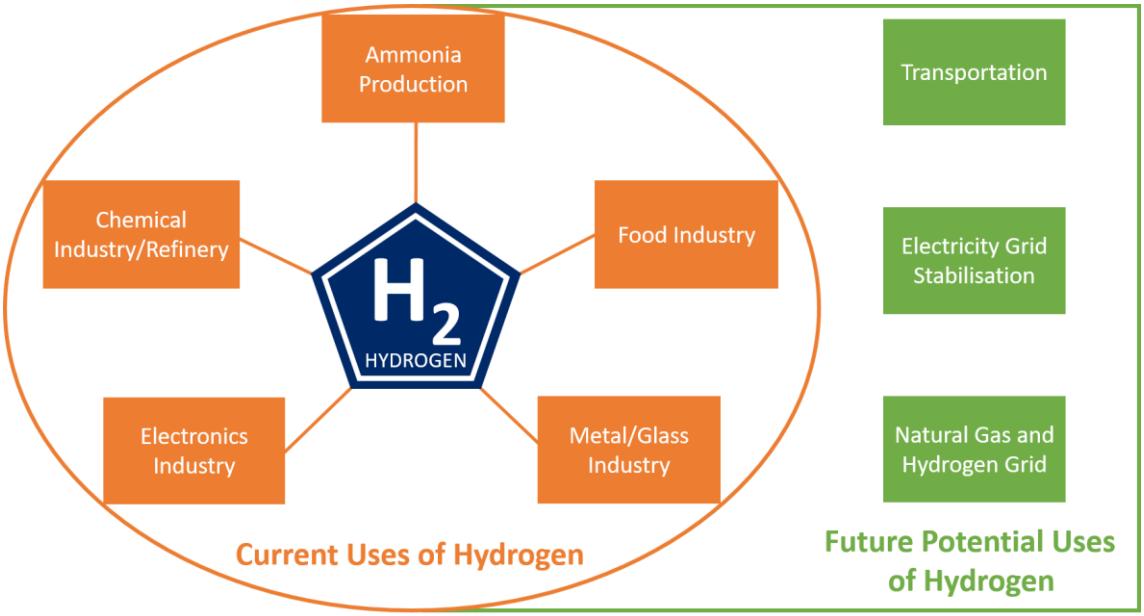

Figure I-6: Current and potential future uses of hydrogen.[34,35]

By considering energy and environmental issues, hydrogen has to be produced from water using a renewable energy source. In an ideal reaction, oxygen can be released from water and later on recombined in fuel cells to produce energy. This type of hydrogen production has the advantage of zero carbon dioxide emissions in its generation process but needs external energy supplies to produce hydrogen, e.g. solar light collected with photocatalysts for water-splitting. Solar energy and water may be considered an almost unlimited resource that could fulfil global energy requirements if successfully harnessed.[30]

After initial electrolysis experiments on titanium dioxide electrodes,[36] Fujishima and Honda[37] discovered in 1972 the electrochemical photolysis of water to hydrogen using TiO_2 (rutile) electrodes. This setup requires ultraviolet light (UV) to promote the water oxidation. Further developments and optimisation led to a huge number of inorganic semiconductors with the approach to shift the band edge to the visible region of the solar spectrum.[30,38,39] Prominent examples, apart from titanium dioxide, are cadmium sulfide and strontium titanate. After initial work of decomposing water vapour on solid NiO-$SrTiO_3$ surfaces with a low evolution rate of 0.27 µmol h^{-1},[40] the photocatalyst was found to decompose water into H_2 and O_2 with an increased activity of 100 µmol h^{-1} when the powder was dispersed in water.[41] This impressive boost in activity by 370 times was the successful start of powdered photocatalysts dispersed in the reaction mixture. Advantages of particulate photocatalysts are their low cost production and operational cost[42] that set a competitive price to hydrogen produced from fossil fuels, mainly steam reforming.[31] A study of the United States Department of Energy also

predicts photocatalysis to be more economical than photovoltaic-assisted electrolysis and photoelectrochemical cells for hydrogen production.[31]

4.3 Theoretical considerations of photocatalysis

Photocatalytic reactions have been studied intensively and can be divided into three processes: photon absorption, formation and separation of the electron-hole-pair, and catalytic surface reactions. One example is the artificial photosynthesis that splits water into H_2 and O_2 with a standard Gibbs free energy of $\Delta G^{\theta} = 237$ kJ mol^{-1}. [43] The positive ΔG^{θ} reflects an endergonic chemical reaction that requires an external energy source to undergo the reaction, e.g. photons provided by sunlight. While the band-gap energy (E_g) is given by the energy difference of the oxidation and reduction potential (or 1.23 V *vs.* the normal hydrogen electrode (NHE)), [43,44] spontaneous overall water splitting requires overpotential for both the oxidation and the reduction site to thermodynamically drive the reactions, *i.e.* the position of the conduction band (CB) and valance band (VB) give an indication if the reduction or oxidation could thermodynamically happen. In comparison to the normal hydrogen electrode, the band position of the conduction band E_{CB} has to be located at a more negative potential than the reduction potential E_{red} (H^+/H_2) = 0.00 V and the band position of the valence band E_{VB} has to be more positive than the oxidation potential E_{ox} (O_2/H_2O) = 1.23 V (Figure I-7).[45,46]

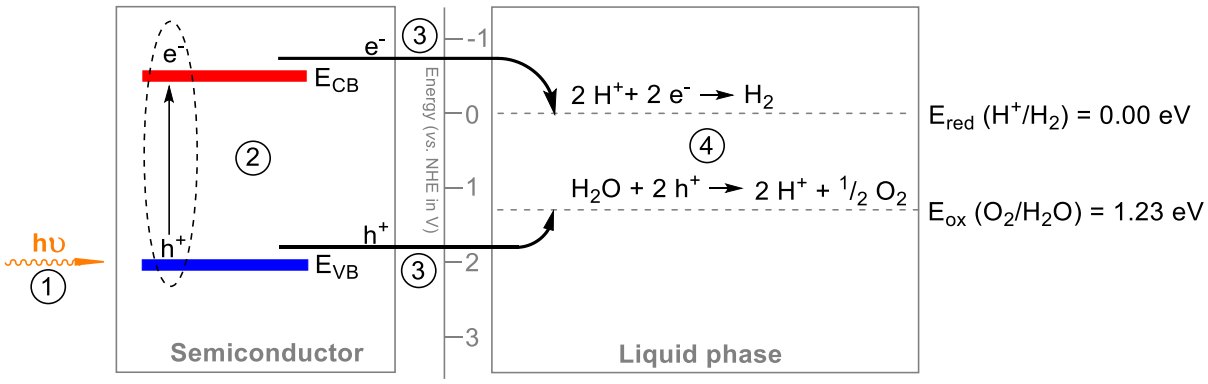

Figure I-7: Scheme for photocatalytic water splitting.

The challenges in developing effective photocatalysts for water splitting are summarised as follows: firstly, the photocatalyst has to be stable in the operating conditions. The reaction intermediates, side-products, and products (H_2 and O_2) are in close contact with the photocatalyst and could lead for example to redox-reactions that change the photocatalyst's properties and performance. Further, there is the requirement to absorb light ① (Figure I-7). If the photocatalyst is designed for visible light activity, the band-gap should be below 3.0 eV, corresponding to a wavelength of λ = 420 nm,[43] or above 1.23 eV, corresponding to a wavelength of 1008 nm. The total solar energy in the visible light

(λ = 400-800 nm) contributes to 53% of the total solar energy, while the higher photonic energy of the UV light (λ < 420 nm) only accounts for 4% of the total solar energy.[47] Electrons in the semiconductor are then photoexcited during absorption from the valence band (VB) to the conduction band (CB) ② - ideally, every absorbed photon would induce an electron excitation. The photocatalyst then separates the charges, and supports the migration of the electron and the hole to the interface ③. The promotion of surface chemical reactions to form hydrogen and oxygen is the final step ④.

Considering all of these previous requirements, most materials cannot fulfil the full variety of properties. Although many materials can be predicted and designed with band-gaps below 3.0 eV, the positions of the conduction and valence band often limit the water splitting to only one half-reaction.

Since the discovery of TiO_2 for the hydrogen reduction, many inorganic photocatalysts were presented and are summarised in reviews.[30,38,39] Among them, titanium dioxide, cadmium sulfide, and strontium titanate are widely studied, and activities over 20000 μmol g^{-1} h^{-1} for hydrogen and 10000 μmol g^{-1} h^{-1} were reported for Sr_3TiO_3:Na from pure water when $Rh_xCr_{2-x}O_3$ was used as co-catalyst for both half reactions.[48]

Co-catalysts can assist in electron-hole separation and offer active sites to lower the activation energy needed in water splitting applications.[49] For inorganic semiconductors, metals like ruthenium, rhodium or platinum can be loaded to the surface to promote the reduction; and catalysts such as RuO_2[49] or IrO_2[47] are used to promote the oxidation. Sacrificial donors or acceptors can be added to the aqueous solution to screen materials for either of the half-reactions, and to reveal mechanistic insights of photocatalysis, while the sacrificial conditions also suppress the charge-recombination, which is seen as the biggest challenge in the field with high recombination rates of the e^-/h^+-pairs.[50]

Nevertheless, this approach of a split study for hydrogen and oxygen photocatalysts was used to combine two photocatalysts for overall water splitting.[51] Examples are an assembly of cobalt-phosphate clusters/silicon/NiMoZn, known as the artificial leaf,[52] and $SrTiO_3$:La,Rh/Au/$BiVO_4$:Mo sheets.[53]

4.4 Organic photocatalysts

Despite early work on the use of polymers as organic photocatalysts, only a few oligo- and polymers have been investigated for hydrogen production (graphitic carbon nitride is discussed on page 19) In 1985, the UV-photoreduction of water to hydrogen by poly(*p*-phenylene)[54] (PPP) in the presence of sacrificial amines was reported in moderate rates. The polymer was synthesised using a Kumada coupling from the organomagnesium derivative of 1,4-dibromobenzene and polymerised with

$Ni(COD)_2$ catalyst.[55] The structure of the tridecamer is shown in Figure I-8, as it was reported with 13 monomer units and 4-bromophenyl end groups.

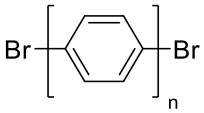

Poly(*p*-phenylene) with n ≈ 13

Figure I-8: Light harvesting polymers that act as photocatalysts for water.

Additional work also focussed on oligomers of PPP synthesised using Grignard reagents of the dibromoaryls and $NiCl_2$(bpy).[56] 4,4'-Dibromobiphenyl was used to obtain PPP-7 and the 1,4-dibromobenzene was polymerised to obtain PPP-11. The number represents the estimated average number of *p*-phenylene units in the polymers, which were calculated to be 6.5 and 11 based on gel permeation chromatography (GPC), respectively. Both polymers produced hydrogen when tested in methanolic aqueous triethylamine (TEA) solutions and $\lambda > 290$ nm irradiation, but PPP-11 massively outperformed PPP-7 (52 µmol g^{-1} h^{-1} *vs.* 3 µmol g^{-1} h^{-1}, respectively). PPP-11 was loaded with ruthenium, platinum, and rhodium, and it was found that the hydrogen evolution could be enhanced up to 40 times for Ru-loaded oligomers. The results show the influence of the chain length and the co-catalyst to the amount of hydrogen evolved. Furthermore, D_2O experiments for the Ru-loaded oligomers confirmed water as the source of hydrogen.

Similar experiments were carried out on regioirregular poly(pyridine-2,5-diyl)[57] (PPy). In the presence of Ru co-catalyst, the photocatalysis in a solution of water/TEA/MeOH under $\lambda > 400$ nm was enhanced by more than 14 times in comparison to PPy on its own, showing a hydrogen evolution rate of 220 µmol g^{-1} h^{-1}. Experiments with D_2O/TEA/CD_3OD/$RuCl_3$ confirmed water was the primary source of hydrogen with the ratio for D_2, HD and H_2 determined to be 73:23:4, respectively.

Mechanistic studies have also been reported on oligo(*p*-phenylenes) (OPPs) model compounds[58] with smaller chain lengths. The photoreduction was tested for OPP-6 (*p*-sexiphenylene) down to OPP-2 (*p*-biphenylene), and OPP-3 (*p*-terphenylene) in particular was investigated in detail. The authors demonstrated that a minimum length of three phenylenes was necessary for charge separation of photoinduced electrons and holes.

In addition to the oligomers, ruthenium as a co-catalyst was investigated in the oxidation state 0 and +III.[58] The experiments showed that $RuCl_3$ used for proton reduction needs to be reduced to Ru^0. The authors also investigated the influence of the oxidation product acetaldehyde that is formed in the process. By adding acetaldehyde to the OPP-3/TEA system, an enhanced formation of ethanol and a decreased hydrogen evolution were measured. The formation of a polymer radical anion could be

confirmed in the presence of TEA. Shorter life-times for the radical anion OPP-3$^{\bullet-}$ were measured by transient absorption spectroscopy in presence of water and acetaldehyde, indicating a fast electron transfer to acetaldehyde and the induced reduction to ethanol.

On the basis of these combined results,[56,58] the authors postulated a mechanism (Figure I-9) for the hydrogen reduction using polymeric photocatalysts. In the first step, the light-induced formation of an excited singlet ^{1}Polymer* takes place, before the quenching with TEA produces the radical anion Polymer$^{\bullet-}$ and the radical cation TEA$^{\bullet+}$ (equation I-1). The Polymer$^{\bullet-}$ than releases an electron that can be used for photocatalysis. A dehydrogenation of TEA forms the *N,N*-diethylamino-1-ethyl radical (equation I-2). This radical can act as a further electron source to quench the hole of the ^{1}Polymer* while being oxidised to the cation $Et_2NC^+HCH_3$. Hydrolysis of the cation gives diethylamine and acetaldehyde. Acetaldehyde is further reduced to ethanol by electrons and protons (equation I-5). Due to the expected electron transfer from Polymer$^{\bullet-}$, this step reduces the activity of the proton reduction. The photoreduction of water was ruthenium-catalysed to form hydrogen (equation I-4), while the reduction of Ru(III) to Ru(0) also requires electrons (equation I-3).

The use of triethylamine as sacrificial electron donor could drive the proton reduction without the use of polymeric photocatalysts, while control experiments in the absence of photocatalysts showed no hydrogen evolution.[59] Decomposition products of triethylamine could further drive the proton reduction, as diethylamine (equation I-2) was found to act as sacrificial electron donor for polymeric photocatalysts.[17] The triethylamine radical ($Et_2NC^{\bullet}HCH_3$, equation I-2) is formed through the reductive quenching of the excited ^{1}Polymer* in a 1:1 ratio according to the mechanism, and a selective synthesis or detection of this radical could clarify if increased proton reduction is driven by its formation rather than conduction band electrons from the polymer. Fluorescence life-time decays were used to determine Stern-Volmer quenching rate constants of TEA with PPP.[58] The quenching rate constants were found to be between 3 x 10^9 M^{-1} s^{-1} to 10 x 10^9 M^{-1} s^{-1} indicating a rapid electron transfer *via* reductive quenching of TEA to the excited polymer (^{1}Polymer*) to form the polymer radical anion Polymer$^{\bullet-}$ and the radical cation TEA$^{\bullet+}$.

First electron source:

(I-1) Polymer $\overset{h\nu}{\rightleftharpoons}$ ^{1}Polymer* $\xrightarrow{NEt_3}$ Polymer$^{\bullet-}$ 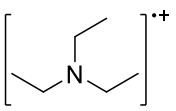 $\xrightarrow{-\ H_{15}C_6N^{+\bullet}}$ Polymer + e^-

Second electron source:

(I-2) 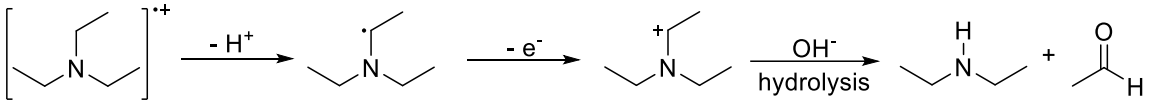

Ruthenium catalysed photoreduction of water:

(I-3) $RuCl_3 \xrightarrow{3\ e^-} Ru^0 + 3\ Cl^-$

(I-4) $H_2O \xrightarrow{Ru^0,\ e^-} 1/2\ H_2 + OH^-$

Reduction of acetaldehyde

(I-5) 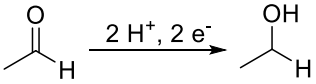

Figure I-9: Overall reactions for photocatalytic hydrogen production.

Renewed interest in polymers for hydrogen production from water focussed on nitrogen rich materials. Poly(triazine imide) polymers[60] doped with 4-amino-2,6-dihydroxypyrimidine, or a network of heptazine,[61] as well as graphitic carbon nitrides with low molecular weight,[62] were found to split water under sacrificial conditions. By far the most-studied and most-utilised nitrogen rich polymers are graphitic carbon nitrides (g-C_3N_4). Although precursors of g-C_3N_4 like melon can be found in works by Berzelius and Liebig around 1830,[63] heterogeneous catalysis on this polymer surface was not studied until 2006 with Friedel-Crafts reactions.[64,65] In 2009, Antonietti and coworkers introduced g-C_3N_4 as a visible-light photocatalyst (Figure I-10).[66] The material is synthesised by thermal condensation of organic starting materials and is stable up to 600 °C. By using variable precursors like cyanamide or melamine and adapting the reaction conditions, the band gap can be modified in a range of 2.65 - 2.89 eV. The position of the conduction band and valence band are -1.1 eV and +1.6 eV, respectively, *vs.* the normal hydrogen electrode (NHE), which theoretically enables overall water splitting. Further engineering to narrow the band-gap was demonstrated with elemental doping, for example boron doping lowered the band gap from 2.70 eV to 2.66 eV, and co-polymerisation of dicyanamide with different amounts of babituric acid allowed band-gaps between 2.67 and 1.58 eV to be obtained.[67] The red-shift of the band-edge is essential to produce better photocatalytic performance as the fraction of UV irradiation is only 4% of the incoming solar light, while 46% lies in the visible light.[30]

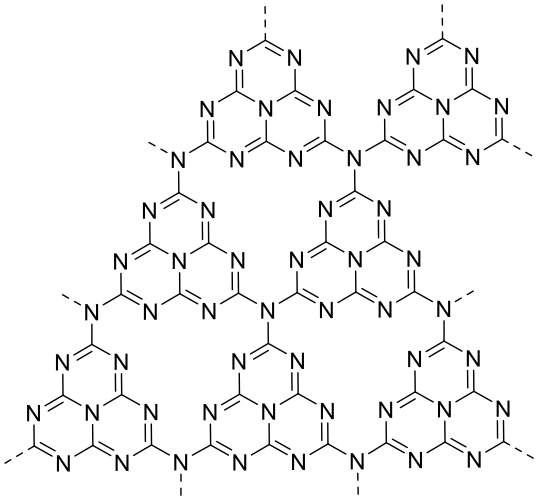

Figure I-10: Representation of a defectless melon-based g-C_3N_4 structure.

Further strategies for performance enhancement were also tested. The separation of polymeric multi-layered g-C_3N_4 was investigated to obtain higher surface areas for the photocatalysis. Exfoliation was tested by the Scotch-tape-assisted method,[68] using organic solvents,[69] acidic[70] or basic[71] media, also in combination with sonication and thermal approaches.[72] Besides the development of nanosheets, the design of g-C_3N_4 morphologies was investigated. Porous g-C_3N_4,[73] hollow spheres,[74] and nanorods[75] are examples of materials with large surface areas and porous structures to improve the interactions between the catalyst and the substrate. By far, the most work can be found on composite materials of g-C_3N_4 that support the separation of photoinduced charge carriers. The co-catalysts range from metals oxides like TiO_2,[76] WO_3,[77]or Ag_2O[78] and silver halogenides[79] for dye degradation to metal chalcogenides for proton reduction such as CdS as quantum dots [80] or $CuInS_2$ as device substrates[81] As metal-free co-catalysts, polypyrrole[82] and poly(3-hexylthiophene) were used.[83]

The latest developments also include graphitic carbon nitrides covered with layered $Co(OH)_2$ for improved oxygen evolution,[84] or the use carbon nanodots (C-dots) on g-C_3N_4 to obtain both hydrogen and oxygen as product gases simultaneously.[85] For the metal-free C-dots@g-C_3N_4, the formation of hydrogen peroxide *via* a two-electron pathway and the catalyst-induced decay of hydrogen peroxide was postulated. Further, carbon nitride synthesised from dicyandiamide was described for overall water splitting using platinum and cobalt co-catalysts.[86]

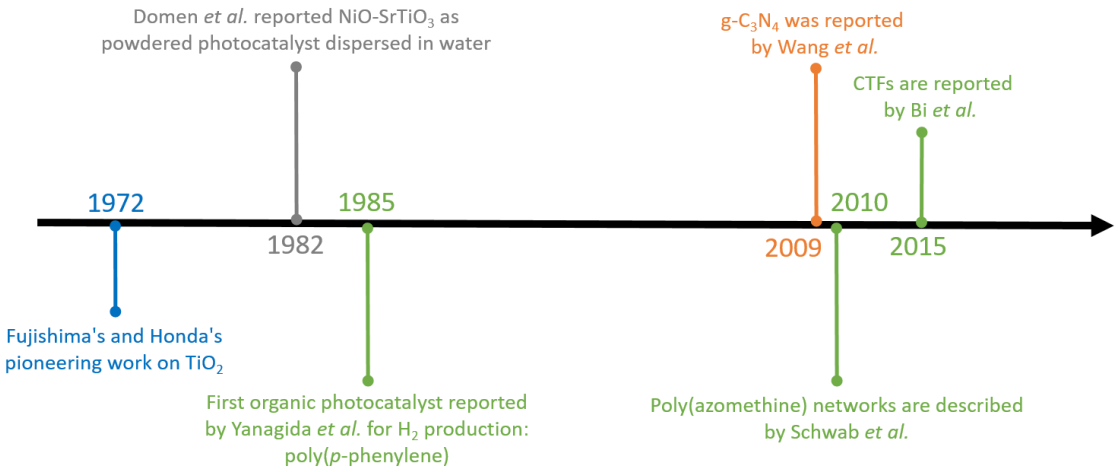

Figure I-11: Short overview of the polymeric evolution of photocatalysts. Additionally, early findings on inorganic TiO_2 and powdered NiO-$SrTiO_3$ photocatalysts dispersed in water are also shown.

Besides these developments on $g\text{-}C_3N_4$, recent work has focussed on polymers. In 2010, catalysts for solar hydrogen production from water were reported based on poly(azomethin) networks (ANW).[87] Moderate evolution rates of up to 70 µmol g^{-1} h^{-1} were measured for ANW 2 in a solution of water/TEOA synthesised from 1,3,5-tris(4-aminophenyl)benzene and naphthalene-2,6-dicarb-aldehyde. In 2015, a library of structurally related organic CMP photocatalysts that produce hydrogen from water/diethylamine was reported.[17] By using Suzuki-Miyaura polycondensations, band-gap engineering was achieved and the authors found that an increasing pyrene content decreases the band-gap. Fifteen CP-CMPs (co-polymer-conjugated microporous polymers) were tested, and the statistical co-polymer CP-CMP10 synthesised from 1,3,6,8-tetrabromopyrene and 1,4-benzene diboronic acid with a feed ratio of 1:2 was found to be the best photocatalyst in the series with a band-gap of 2.33 eV (Figure I-12). Remarkably, the presented catalysts used visible light to evolve H_2, whereas most reported polymers like PPP are only active in the ultraviolet range. A long-term test was carried out for the best performing polymer CP-CMP10 over 100 hours, with an average hydrogen evolution rate of 174 µmol g^{-1} h^{-1} observed, indicating that the catalyst has a good stability. Additional time-dependent density functional theory ((TD)-DFT) calculations supported these findings with large thermodynamic driving-forces for the proton reduction. Although no noble metal was used as a co-catalyst, residual palladium from the Suzuki-Miyaura polycondensation is present. Therefore, the role of palladium in the hydrogen evolution was investigated by treating the reaction solution with carbon monoxide. After treatment, no decrease of activity was observed. This either indicates that carbon monoxide does not bind to the palladium residues or that the palladium residues do not change the photocatalytic activity. Furthermore, the hydrogen evolution rate was not found to correlate to the microporosity of these statistical co-polymers, but with optical properties.

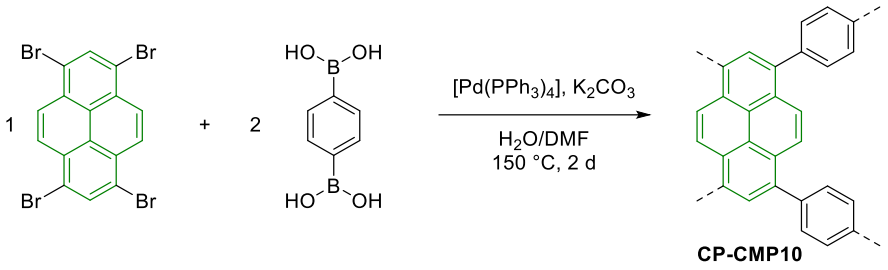

Figure I-12: Synthesis of CP-CMP10 by Suzuki-Miyaura polycondensation.[17]

In this fast developing field, further polymers were reported to be suitable for hydrogen evolution including CMPs,[88–91] linear polymers,[59,91–93] covalent organic frameworks (COF),[94–96] and triazine based materials.[97–104]

For CMPs, achievements for photocatalytic active polymers were presented by testing linkers regarding their length, geometry and degree of planarisation.[88] Hydrogen evolution rates up to 120 µmol g^{-1} h^{-1} (λ > 420 nm) were measured for the spirobifluorene-based CMP (SP-CMP, Figure I-13) from water/TEA/MeOH, while methanol was used as a co-solvent. No activity was found for 1,3,5-linkers under λ > 420 nm illumination due lower conjugation lengths for *meta*-linkages, while the 1,2,4,5-benzene worked better when elongating the linker from phenylene to biphenylene.

A screen of 16 linkers was reported for 4,8-di(thiophen-2-yl)benzo[1,2-*b*:4,5-*b'*]dithiophene based networks to investigate donor-acceptor systems.[89] In the case of phenylene linkers, donor-donor matches showed hydrogen evolution rates up to 842 µmol g^{-1} h^{-1} under 200-1050 nm irradiation, in the presence of the sacrificial donor TEA. A decrease in activity was detected when going from phenylene to terphenylene. When donor-acceptor polymers were investigated using 5,5'-bipyridyl, pyridines, and diazines, an increase in activity was measured in most cases. While *meta* and *ortho* substituted pyridine based CMPs showed rates of 833-2917 µmol g^{-1} h^{-1} due to a reduced conjugation, the *para*-pyridine CMP demonstrated a hydrogen evolution rate of 5000 µmol g^{-1} h^{-1} under 200-1050 nm irradiation. Pyrazine and pyrimidine linked CMPs were the two most active materials reported with an activity of 8633 and 8908 µmol g^{-1} h^{-1} under 200-1050 nm irradiation, respectively. A loading of 2 wt. % platinum co-catalyst nearly doubled the apparent quantum yield at λ = 400 nm to 1.93% for the best performing polymer PCP10 (Figure I-13) that further showed an activity of 2333 µmol g^{-1} h^{-1} under λ > 400 nm irradiation. An increased light absorption in the pyrazine containing polymer ($E_{g,opt}$ = 615 nm), combined with an increased wettability and semi-crystallinity are attributed to the high performance of PCP-10.

A two-dimensional aza-fused CMP (Figure I-13) was also reported formed by a metal-free condensation of 1,2,4,5-benzenetetramine tetrahydrochloride and hexaketocyclohexane,[90] with a

band-gap of 1.22 eV and tested for photocatalytic oxygen evolution from 0.01 M $AgNO_3$ solution with La_2O_3 as pH buffer. Under λ > 420 nm irradiation, the oxygen evolution rate (OER) was measured and found to be 37 μmol g^{-1} h^{-1}, and an activity of 16 μmol g^{-1} h^{-1} was found for irradiation in the NIR (λ > 800 nm). The stability of the CMP after 12 hours was confirmed by ^{13}C solid-state NMR and XPS measurements. Labelling experiments with H_2O^{18} confirmed water as the source of oxygen, as ^{18}O-^{18}O with a m/z value of 36 was detected. After exfoliation, an increased OER of 132 μmol g^{-1} h^{-1} was measured, and was further enhanced to 572 μmol g^{-1} h^{-1} by the deposition of $Co(OH)_2$ as a co-catalyst.

A series of CMPs based on benzothiadiazoles and substituted phenylene cores with 1,2,4/1,3,5/1,2,4,5-substitution have also been developed. Comparisons were made between six polymers formed with varying feed ratios of 1,3,5-phenyltriboronic acid tris(pinacol) ester and benzene-1,4-diboronic acid (B-BT). All polymers were active under visible-light (λ > 420 nm) with TEOA as electron scavenger and 3 wt. % platinum co-catalyst. The highest hydrogen evolution rate was measured in a benzothiadiazole-based CMP for the 1,3,5-substituted B-BT-1,3,5 with 400 μmol g^{-1} h^{-1} (Figure I-13). By gradually reducing the number of crosslinking units, the 3D character of the CMPs decreased and led to a linear, alternating co-polymer (B-BT-1,4) produced from benzothiadiazole and phenylene. Along the series, an increase of the band-gap correlated with the loss of activity when increasing the content of crosslinker. Consequently, the linear co-polymer B-BT-1,4 had the lowest band-gap with 2.17 eV, and exhibited the best hydrogen evolution rate of 2320 μmol g^{-1} h^{-1} under visible light.

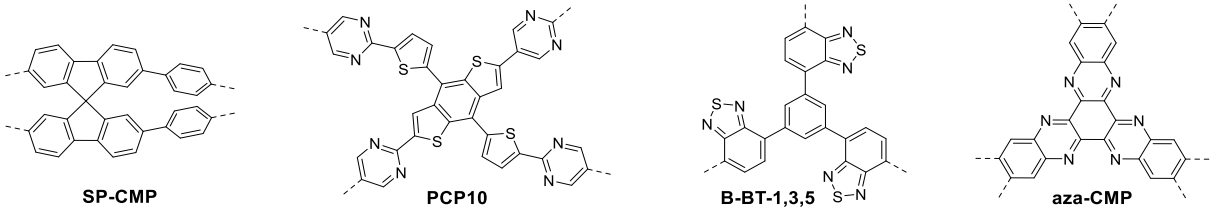

Figure I-13: Examples for CMPs from literature: SP-CMP,[88] PCP10,[89] and B-BT-1,3,5[91] as hydrogen evolution catalysts, and aza-CMP as oxygen catalyst.[90] Note that PCP10 is a regioirregular polymer due to the pyrazine monomer used.

Studies on linear systems have also been, ranging from biphenylene to quinquephenyl, and linear co-polymers of planarised systems of carbazole, fluorene, dibenzo[*b*,*d*]thiophene, dibenzo[*b*,*d*]thiophene sulfone, and phenylene. An increase of hydrogen evolution activity under λ > 295 nm was observed for increasing linker length from biphenylene to quinquephenylene when going along the series, with a correlated red-shift of the absorption on-set increased the light absorption. The fused analogues of poly(*p*-phenylene) were found to be semi-crystalline and beneficial for the hydrogen evolution rates due to both a decrease in phenylene-phenylene torsion angles and an increase in conjugation, which

potentially increased charge carrier mobilities. The authors describe the increase in hydrogen evolution activity through planarisation, while the band-gap comparison of oligomers and fused systems alone could not describe increased performances. The most active co-polymer P7 (Figure I-14) was synthesised from dibromo-dibenzo[*b*,*d*]thiophene sulfone and benzene-1,4-diboronic acid and showed hydrogen evolution rates from water/TEA/MeOH of 1492 µmol g^{-1} h^{-1} under λ > 420 nm irradiation. Its apparent quantum yield was determined to AQY_{420nm} = 7.2%.

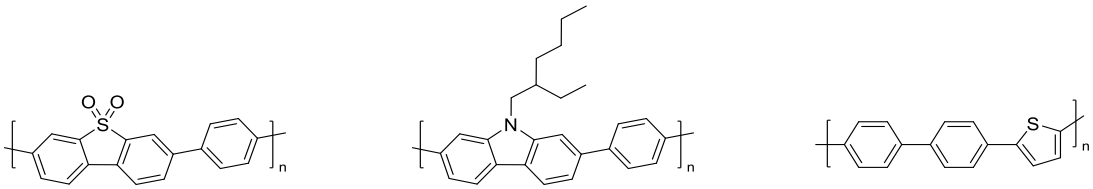

Figure I-14: Examples of linear co-polymers as hydrogen evolution catalysts: P7,[59] P8-s,[92] and P12.[93]

Organic soluble linear photocatalysts were reported on structural analogues of the previously presented co-polymer of 1,4-benzenediboronic acid and 2,7-dibromo-9*H*-carbazole,[59] with a hydrogen evolution rate of 552 µmol g^{-1} h^{-1} (water/TEA/MeOH, λ > 295 nm irradiation). The co-polymer of 1,4-benzenediboronic acid bis(pinacol) ester and 2,7-dibromo-9-(2-ethylhexyl)-9*H*-carbazole (P8), and the co-polymer of 1,4-benzenediboronic acid and 2,7-dibromo-9-(hexadecyl)-9*H*-carbazole (P9)[92] were both found to have a chloroform soluble (P8-s, P9-s), and insoluble (P8-i, P9-i) fraction. A molecular weight of M_w = 2100 g mol^{-1} was measured for P8-s (Figure I-14) by gel permeation chromatography, while the insoluble fraction could not be dissolved in any other common organic solvents and is expected to have a higher molecular weight. Glass slides were coated with P8-s and the UV-Vis absorption was compared to the powder and chloroform solution. While band-gaps of 2.79 eV and 2.81 eV were found for the film and the powder of P8-s, a blue-shift was observed in chloroform solution. When testing their activity from water/TEA/MeOH, the suspended powders of P8-i evolved 860 µmol g^{-1} h^{-1} under λ > 295 nm irradiation, and P8-s was found to show an activity of 544 µmol g^{-1} h^{-1}. Lower activities of 80 µmol g^{-1} h^{-1} and 128 µmol g^{-1} h^{-1} were detected for P9-s and P9-i, respectively. An explanation for the lower performance of P9-s in comparison to P8-s was found to be due to a higher hydrophobicity and lower crystallinity. Initial delamination of the P8-s films on glass slides under the reaction conditions were avoided by using rough SnO_2 glass slides and a hydrogen evolution rate of 450 µmol g^{-1} h^{-1} could be achieved. Transient absorption spectroscopy (TAS) was measured for P8-s films and revealed longer life-times of the excited states for water/TEA/MeOH mixtures than water or water/MeOH solutions. The authors concluded from long-lived absorption TAS results of P8-s in the presence of TEA ($t_{1/2}$ = 50 ps) an electron polaron state.

Further, methanol was not found to be beneficial for the life-time of the excited state, supporting its use as a wetting agent.

Linear co-polymers of *p*-phenylene and 2,5-thiophene were investigated and the band-gap was found to decrease with a higher content of thiophene.[93] (TD-)DFT calculations were carried out for all polymers and predicted a lower driving force for an increasing thiophene content. All co-polymers were found to perform better than the homopolymers PPP or polythiophene under λ > 420 nm irradiation from water/TEA/MeOH. The best performing polymer P12 (Figure I-14) consisted of 33% thiophene content, and had an evolution rate of 420 µmol g^{-1} h^{-1} under λ > 420 m irradiation. For 50% thiophene content, the hydrogen evolution dropped off, and the two polymers P13 and P14 (AABB and ABAB) were found to have different absorption on-sets, leading to hydrogen evolution rates of 250 and 175 µmol g^{-1} h^{-1}, respectively. Both these results show the dependency of the photocatalytic activity on the arrangement of the building blocks and the composition of the polymer. When structurally random co-polymers were synthesised and tested, lower activity was found in comparison to the ordered co-polymers and support the previous results. A further influence by the residual metal catalyst used for the polymerisation was reported – in the case of Stille coupled polymers, tin was found to decrease the hydrogen evolution performances.

COF structures have also been investigated by the group of Lotsch using reversible condensation reactions.[94–96] A 2D geometry was achieved when the COFs were built up from azines. Along the series from 1,3,5-tris(4-formylphenyl)benzene to 2,4,6-tris(4-formylphenyl)-1,3,5-triazine (Figure I-15), DFT-calculations regarding the planarity of the building block were carried out. The authors predicted that an increasing nitrogen content for the 1,3,5-substituted core leads to a continuous decrease of the dihedral angle up to 0°.

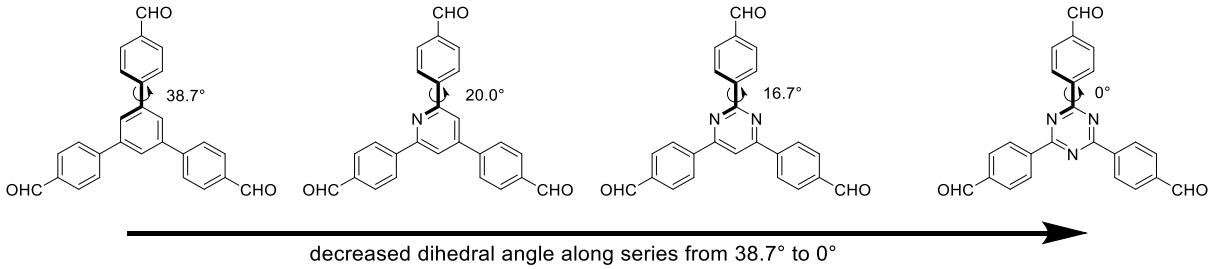

Figure I-15: Predicted decrease of the dihedral angle for COF precursors – only one dihedral angle is highlighted here in bold.

Surface areas up to 1537 m^2 g^{-1} and high crystallinity were measured for N_3-COF (Figure I-16) formed *via* condensation of 2,4,6-tris(4-formylphenyl)-1,3,5-triazine and hydrazine. A hydrogen evolution rate of 1703 µmol g^{-1} h^{-1} was measured from phosphate-buffered saline (pH 7)/TEOA/0.68 wt. % Pt at

λ > 420 nm. The stability of the COF after the hydrogen release experiment was confirmed using FT-IR and solid-state NMR before and after photocatalysis.

An isoelectronic COF was synthesised from 2,2',2''-(1,3,5-benzenetriyl)tris-5-bromopyridine and hydrazine to change the electronic structure of the resulting PTP-COF[95] (Figure I-16). DFT calculations revealed a dihedral angle of 17.0° in the phenyl tripyridine building block. The band-gap was determined to be 2.1 eV and was found not to correlate with the expected catalytic performance concluded from the series of COFs reported before.[94] As a possible explanation, the lower crystallinity observed was thought to be due to the disordered building block and its 512 possible conformers which could cause changes in stacking. Although higher quantum yields and longer photoluminescence life-times were measured for the PTP-COF in comparison to N_3-COF, the HER from TEOA/water with platinum co-catalyst was determined to be 84 µmol g^{-1} h^{-1}.

A hydrazone-based COF has also been synthesised from 2,4,6-tris(4-formylphenyl)-1,3,5-triazine and 2,5-diethyoxy-terephthalohydrazide (TFPT-COF, Figure I-16). The band-gap was estimated to be 2.79 eV and the BET surface area was determined to be 1190 m^2 g^{-1} based on argon sorption measurements. Photocatalytic tests were carried out with sodium ascorbate as the sacrificial electron donor and a platinum co-catalyst, giving a hydrogen evolution rate of 230 µmol g^{-1} h^{-1}. PXRD measurements after photocatalysis indicated the loss of long range order, and the BET surface area was reduced to 410 µmol g^{-1} h^{-1}, possibly due to the exfoliation of the COF in water. The COF's initial properties were recovered by re-applying the synthesis conditions after photocatalysis. A higher hydrogen production rate of 1970 µmol g^{-1} h^{-1} was found with 2.2 wt. % platinum co-catalyst and TEOA, while a reduction of the HER was observed after 5 h, indicating the instability of the COF under these conditions.

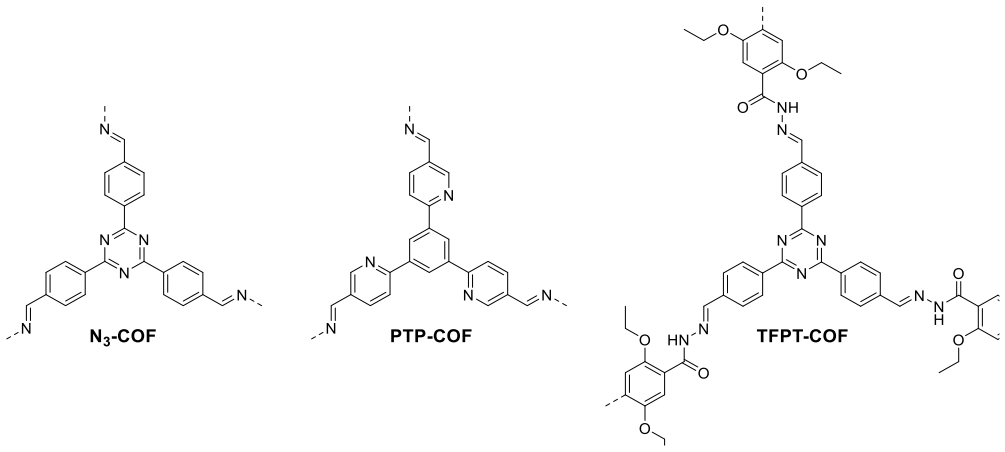

Figure I-16: Examples of COFs used as hydrogen evolution catalysts: N_3-COF,[94] PTP-COF[95] and TFPT-COF.[96]

As an overview, Table 1 summarises the hydrogen evolution of the discussed polymers in each category. Every polymer was tested in a scavenger system, in which the photocatalyst was found to be stable and showed stable hydrogen evolution rates, but often a co-catalyst was required to stabilise the hydrogen evolution. Bearing these differences in mind, the comparison of these values needs to be seen as an estimation at best.

Apart from the direct observation of evolution rates, the intensity and wavelength of the incident light needs to be taken into account as the gas evolution relies both on the experimental setup and conditions used.[105] By taking these additional factors into account, a comparison can be achieved by calculating the external quantum efficiencies (EQE),[105–107] as stated in equation (I-6) where $n_{Hydrogen}$ is the moles of hydrogen measured, N_A is the Avogadro constant, h is the Planck constant, and c is the speed of light. Further, $t_{irradiation}$ is the irradiation time, λ the wavelength used, I the intensity, and A the irradiated area.[106] The higher the value of the EQE, the better performing the material is.

(I-6) EQE = (number of reacted electrons) / (number of incident photons) x 100 %

= (2 x number of evolved hydrogen molecules) / (number of incident photons) x 100 %

$= (2 \times n_{Hydrogen} N_A h c) / (t_{irradiation} \lambda I A) \times 100\ \%$

Table 1 also gives an overview of the EQE calculated for each of the discussed materials. While some low performing polymers, such as SP-CMP were found to have an $EQE_{420\ nm}$ of 0.23%,[88] the linear polymer P7 was found to have an $EQE_{420\ nm}$ of 7.2%.[59] However, both of these polymers exceed PPP that was reported with an $EQE_{420\ nm}$ of 0.1%.[88]

Table 1: Overview of organic photocatalysts used for hydrogen evolution and discussed previously in each category.

Polymer	Category	H_2 Evolution Rate	EQE	Conditions[a]	Reference
CP-CMP10	CMP	174 µmol g^{-1} h^{-1}	-	λ > 420 nm cut-off filter DEA/water	[17]
SP-CMP	CMP	120 µmol g^{-1} h^{-1}	0.23% λ = 420 nm	λ > 420 nm cut-off filter water/TEA/MeOH	[88]
PCP10	CMP	2333 µmol g^{-1} h^{-1}	1.93% λ = 400 nm	λ > 400 nm cut-off filter water/TEA/2 wt. % Pt	[89]
B-BT-1,3,5	CMP	400 µmol g^{-1} h^{-1}	-	λ > 420 nm cut-off filter TEOA/3 wt. % Pt	[91]
B-BT-1,4	linear polymer	2320 µmol g^{-1} h^{-1}	4.01% λ = 420 nm	λ > 420 nm cut-off filter TEOA/3 wt. % Pt	[91]
P7	linear polymer	1492 µmol g^{-1} h^{-1}	7.2% λ = 420 nm	λ > 420 nm cut-off filter water/TEA/MeOH	[59]
P8-s	linear polymer	544 µmol g^{-1} h^{-1}	0.56% λ = 420 nm	λ > 295 nm cut-off filter water/TEA/MeOH	[92]
P12	linear polymer	420 µmol g^{-1} h^{-1}	1.4% λ = 420 nm	λ > 420 nm cut-off filter water/TEA/MeOH	[93]
N_3-COF	COF	1703 µmol g^{-1} h^{-1}	0.44% λ = 450 nm	λ > 420 nm cut-off filter phosphate-buffered saline (pH 7)/TEOA/0.68 wt. % Pt	[94]
PTP-COF	COF	84 µmol g^{-1} h^{-1}	-	λ > 420 nm cut-off filter TEOA/3 wt. % Pt	[95]
TFPT-COF	COF	1970 µmol g^{-1} h^{-1}	2.2% λ = 400 nm	λ > 420 nm cut-off filter TEOA/2.2 wt. % Pt	[96]

[a] The illumination was done in all cases with 300 W xenon light sources.

4.5 Covalent triazine-based frameworks as polymeric photocatalysts

Covalent triazine-based frameworks (CTFs) are a further class of polymers for the application of water splitting. While triazine precursors can be used to synthesise carbon nitrides[108] with an idealised C to N ratio of 3:4, CTFs have a lower C to N ratio (4:1 in the case of CTF-1 for an idealised repeating unit). In computational studies, both C_3N_4 and CTFs were stated as potential photocatalysts for oxygen evolution due to low ionisation potentials,[109] and were reported to evolve oxygen in the presence of the sacrificial electron acceptor silver nitrate.[97,98,110]

To date, photocatalytically active CTFs have been synthesised by a range of chemicals which can be divided in two categories. The first category uses pre-formed triazine building blocks and linker units – examples are CTFs with amide functionalities synthesised from melamine and pyromellitic dianhydride at 325 °C,[102] the use of trithio-cyanuric acid to synthesise a disulfide bridged CTF,[101] sulfur- and nitrogen-containing polymers (SNP) as donor-acceptor systems synthesised *via* Sonogashira-Hagihara cross-couplings at 100 °C,[103,111] and COF structures based on imine bonds.[94,96]

The second category forms the triazine units during the synthesis. Ionothermal approaches have been used with synthesis temperatures exceeding 350 °C,[99,100,112–114] causing partial carbonisation of the polymers. Lower temperature routes to form triazines involve the use of trifluoromethanesulfonic

acid (triflic acid) as a strong Brønsted catalyst for the trimerisation of nitriles,[97,104,110,115] microwave heating to form hydrazones from building blocks[96] or CTFs from dinitriles,[98] and the polycondensation of aldehydes and terephthalamidine dihydrochloride.[116] However, most of these synthetic routes involve harsh conditions that limit the access to large scale production and show a low functional group tolerance to acid-instable starting materials. Figure I-17 gives an overview of three synthetic routes that can be used to form the triazine unit.

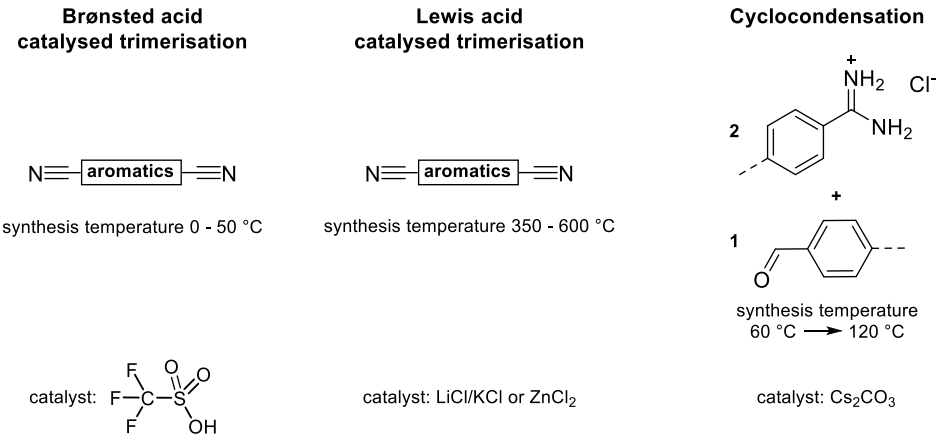

Figure I-17: Synthetic routes to CTFs by Brønsted catalysis, Lewis acid catalysis, and condensation under basic conditions.

The use of Brønsted acid catalysed trimerisation was studied by NMR,[117] and a stepwise mechanism using triflic acid was proposed (Figure I-18). The Brønsted acid first protonates the nitrile (I) to form a carbocation (II). A further nitrile (R-CN) then attacks the electrophile (II) to form another carbocation (III). In the next step, the triazine consisting of three nitriles is formed (IV) before the aromatic cycle is closed (V). A subsequent workup with base reveals the final product (VI).

The trimerisation of nitriles with metal salts at temperatures above 400 °C is also a known synthetic route to triazines since 1971,[118] and a similar mechanism as shown for triflic acid is expected.[119] The Lewis acid Zn^{2+} coordinates to the nitrile to form a carbocation that initiates the formation of triazines. In the case of cyclocondensations from aldehydes, a mechanism is postulated showing imine intermediates.[120] The final triazine unit is formed by ammonia release and aromatisation with caesium carbonate in solution.

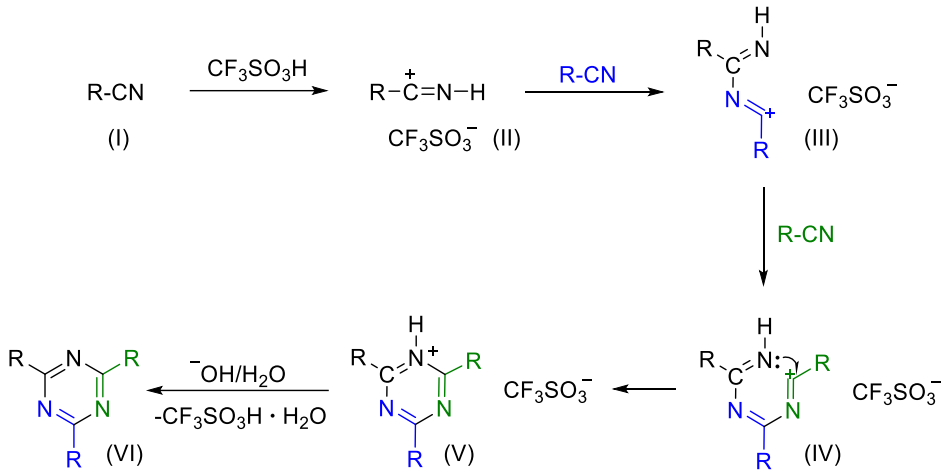

Figure I-18: Proposed mechanism for the formation of triazines from nitriles using triflic acid.[117]

Bi *et al.*[97] reported CTFs as photocatalysts using triflic acid catalysis to produce the polymers CTF-T1 from terephthalonitrile, and CTF-T2 from methylterephthalonitrile. The addition of triflic acid was carried out at 0° C before the reaction was stirred at 25°C for three days. CTF-T1 (Figure I-19) had its nitrogen uptake measured and showed a low Brunauer-Emmett-Teller surface area of 19 $m^2\ g^{-1}$, and the band-gap was determined to be 2.94 eV by UV-Vis spectroscopy, recorded in the solid-state. Hydrogen evolution was tested under visible light irradiation (300 W xenon light, $\lambda > 420$ nm cut-off filter) using triethanolamine as the scavenger and H_2PtCl_6 as the co-catalyst. The rate was calculated for CTF-T1 at 100 µmol $g^{-1}\ h^{-1}$, while CTF-T2 showed a hydrogen evolution of 25 µmol $g^{-1}\ h^{-1}$. For both polymers, the stability was tested in 20 hour length experiments with evacuation every 4 hours. Increasing evolution rates were found in the first two runs, stabilising after eight hours. FT-IR, TEM, and PXRD measurements were all recorded after photocatalysis for CTF-T1, and showed the stability of the polymer. Wavelength dependent analyses revealed the highest activity at 350 nm. Oxygen evolution was also tested for CTF-T1 after $RuCl_3$ was calcined on the material. The active material RuO_2@CTF-T1 was tested by ICP for its co-catalyst loading and was found to have 6.2 wt. % RuO_2 present. A steady and linear oxygen evolution of 8 µmol $g^{-1}\ h^{-1}$ in 0.01 M silver nitrate solution, and La_2O_3 as pH buffer agent, was measured.

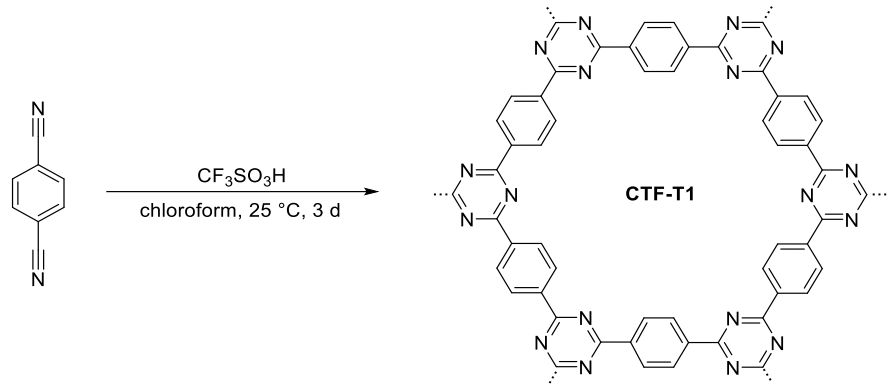

Figure I-19: Synthetic route to CTF-T1 by Brønsted catalysis with trifluoromethanesulfonic acid (triflic acid).[97]

A two-step synthetic approach was reported for CTF-1.[100] First, the polymer is formed *via* triflic acid catalysis. Second, zinc chloride is added and the reaction mixture is heated for up to 30 min at 400 °C in an open crucible to achieve a structural order. Colour changes were initially observed after as little as 2.5 minutes, possibly indicating further condensation, and darker CTFs were obtained with extended heating times, possibly showing increased carbonisation of the polymer. UV-Vis absorption spectroscopy confirmed a red-shift of the absorption with an increased heat exposure up to 30 min, while CTF-1_10 min was heated for 10 min at 400 °C to result in a polymer with a band-gap of 2.26 eV. When tested for its hydrogen evolution activity with platinum co-catalyst, the best result was measured for CTF-1_10 min showing 1072 µmol g^{-1} h^{-1} from 0.05 M phosphate buffer/acetonitrile/TEOA under λ > 420 nm irradiation.

A further CTF was synthesised *via* triflic acid catalysis at 25 °C from tetra(4-cyanophenyl)ethylene (Figure I-20) and was found to have a band-gap of 2.25 eV. Three applications for this CTF were investigated: 119 µmol g^{-1} h^{-1} hydrogen evolution from phosphate buffer solution (pH 7)/TEOA/MeOH/2.3 wt. % platinum/200-1050 nm irradiation, CO_2 adsorption (56 cm^3 g^{-1}), and sensing of nitroaromatics by fluorescence quenching.

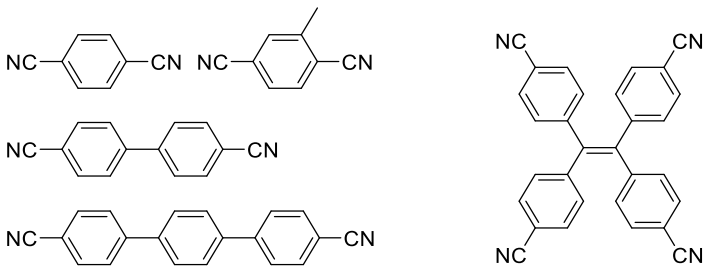

Figure I-20: Nitriles used for the synthesis of CTFs.

Oxygen evolution of acid-catalysed CTFs was tested on a series of three CTFs synthesised with different linker lengths from 1,4-benzenedicarbonitrile to [1,1':4',1''-terphenyl]-4,4''-dicarbonitrile (Figure I-20)

at 100 °C using triflic acid.[110] The photocatalytic activity was tested in 0.01 M silver nitrate solution with La_2O_3 as pH buffer under 300 W xenon-lamp top illumination (λ > 300 nm). The best performing polymer was found to have a biphenylene linker (CTP-2) with a moderate oxygen evolution rate of 20 μmol g^{-1} h^{-1}. A screen with transition metal co-catalysts showed an increase in the oxygen evolution rate to 100 μmol g^{-1} h^{-1} when CTP-2 was immersed in a 3 wt. % stock solution of $Co(NO_3)_2$ and steam distilled to get $Co(OH)_2$@CTP-2. The loading of cobalt in $Co(OH)_2$@CTP-2 was determined by elemental mapping analysis, XPS analysis, and UV-Vis spectroscopy. The electrochemical impedance of the CTFs was measured by preparing polymer coated indium tin oxide electrodes. The impedance for all polymers was lower under λ > 300 nm irradiation in comparison to measurements in the dark. A further decrease in the electrochemical impedance was found for $Co(OH)_2$@CTP-2 in comparison to CTP-2, which indicates a fast generation and separation of excitons that led to a high oxygen evolution rate with $Co(OH)_2$@CTF-2.

CTF-1 was also synthesised by a microwave-assisted route.[98] A series of four polymers were synthesised at 20 W, 50 W, 100 W, and 200 W microwave irradiation and analysed by Raman spectroscopy and PXRD. Along the series from 20 W to 100 W, the Raman spectra revealed a rise of the G^+ band at 1613 cm^{-1} that indicates a higher planarity and amount of sp^2-structures. Simultaneously, the distortion and carbon defects in each layer were found to decrease, as seen on the decline of the G^- band at 1519 cm^{-1} and D band at 1416 cm^{-1}, respectively. Overall, the ratio of the G^+ and D band increased from 20 W to 100 W, showing less defects in the CTF. However, no increase of the ratio was found when going from 100 W to 200 W. In the PXRD, a peak at 2θ = 7° was observed and assigned to a hexagonal unit cell. The peak intensity was found to increase with enhanced microwave power up to 100 W, with the highest crystallinity found for CTF-1-100 W. A decrease in crystallinity was observed when going from CTF-1-100 W to CTF-1-200 W, possibly due to distortions that break hexagonal unit cells due to strong vibrations at high microwave power. Overall, all polymers acted as oxygen evolution catalysts with a RuO_2 co-catalyst in 0.2 M silver nitrate solution under 300 W xenon-lamp illumination (λ > 420 nm). The best material was found to be 2.6 wt. % RuO_2/CTF-1-100 W with an oxygen evolution rate of 140 μmol g^{-1} h^{-1}. From 20 W to 100 W, an increase in the oxygen evolution was detected, while RuO_2/CTF-1-200W was found to produce less oxygen than RuO_2/CTF-1-100 W, possibly due to the carbonisation caused by the high microwave irradiation. When RuO_2/CTF-1-100 W was tested over three runs, the total amount of oxygen evolved was found to be more than six times the amount present in the photocatalyst, based on RuO_2. Potential air leakage in the sealed system was monitored by nitrogen as an internal standard. The stability of the RuO_2/CTF-1-100 W photocatalyst after the oxygen evolution reaction was confirmed by FT-IR, Raman and XPS spectroscopy. CTF-1-100 W was also loaded with 2 wt. % platinum and a hydrogen evolution rate of

5500 µmol g^{-1} h^{-1} was achieved from water/TEOA/MeOH. When tested for overall water splitting over 6 hours in pure water, both platinum and ruthenium(IV)oxide were used as co-catalysts. The gas evolutions were found not to represent the expected ratio of 2:1, with a moderate total hydrogen evolution of 7 µmol, and a total oxygen evolution of 5 µmol.

Table 2: Overview of CTFs for oxygen evolution.

Polymer	O_2 Evolution rate	Conditions	Reference
RuO_2@CTF-T1	8 µmol g^{-1} h^{-1}	300 W xenon light, λ > 420 nm cut-off filter, 0.01 M $AgNO_3$, La_2O_3	[97]
$Co(OH)_2$@CTP-2	100 µmol g^{-1} h^{-1}	300 W xenon light, λ > 300 nm cut-off filter, 0.01 M $AgNO_3$, La_2O_3	[110]
RuO_2/CTF-1-100W	140 µmol g^{-1} h^{-1}	300 W xenon light, λ > 420 nm cut-off filter, 0.2 M $AgNO_3$	[98]

5 Aims and goals

The goal of this work was to synthesise new polymeric photocatalysts for water-splitting that show high activity for hydrogen evolution. For these performance improvements, covalent triazine-based frameworks were selected as a subclass of CMPs. At the start of this work, there was only a single report by Bi *et al.*[97] on the use of CTFs produced by acid catalysis for water splitting, in which two polymers were synthesised from terephtalonitrile (CTF-T1) and methylterephthalonitrile (CTF-T2) (Figure I-20, left).

CTFs are an attractive class of polymers that were not tested for photocatalytic hydrogen evolution intensively. They can be established using various synthetic protocols including ionothermal, acid catalysed, sulfur-mediated, and Friedel-Crafts approaches.[121] This offers the possibility to compare CTFs synthesised by different routes to study the influence on the hydrogen reduction, as this was not reported previously. The synthetic route was e.g. found in linear polymers to lower the hydrogen evolution rates significantly when using tin-catalysis.[93]

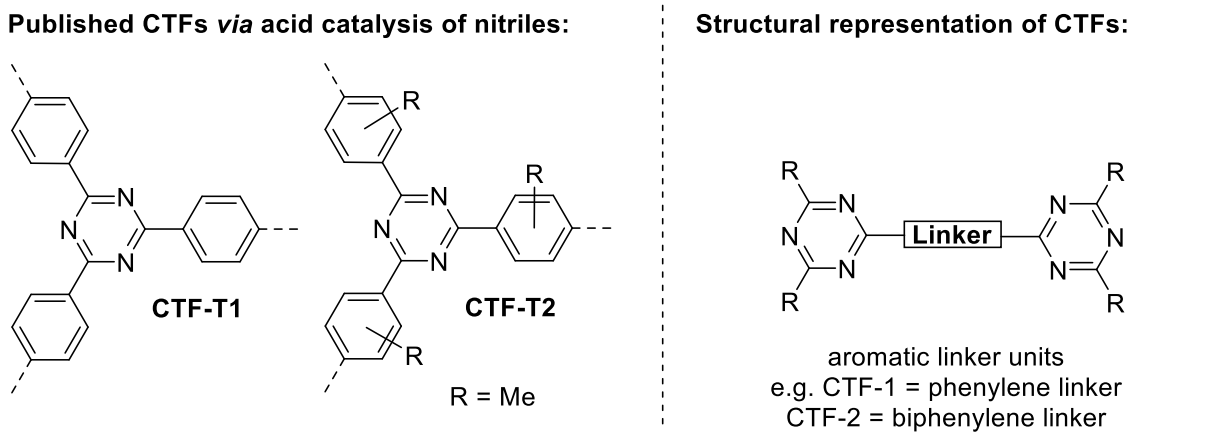

Figure I-21: Structures of the two published photocatalysts CTF-T1 and CTF-T2[97] (left). Note that the acid catalysis produces regioirregular CTF-T2. Structural representation of CTFs with variable linker length (right).

As shown in Figure I-21 (right), the extension of the aromatic linker units is a target to study to fine-tune the polymers properties and to see the influence of the linker unit on the hydrogen evolution rate.

Following this initial study, a larger library of CTFs with more than 20 polymers should be synthesised. Heteroaromatic systems are desired to be incorporated in the linker unit, such as pyridine, pyrazine, carbazole, and dibenzo[*b*,*d*]thiophene sulfone. A synthetic route needs to be chosen with a large functional group tolerance that also allows the incorporation of nitrile groups in the aromatic units. Based on high-throughput measurement capabilities, the optical properties of the polymers could be investigated, as well as their fluorescence life-time, sorption behaviour, wettability behaviour, and crystallinity.

Furthermore, the number of samples will allow the introduction of the advantages of a high-throughput screening protocol for the investigation of powdered photocatalysts under solar simulated light. The system could be used to investigate the photocatalysts regarding their hydrogen evolution under solar simulated light, and manual runs carried out in quartz flasks to highlight the importance of high-throughput screens. Further, test of the CTF library for oxygen evolution on the HT system was targeted.

Structures for new CTFs planned in this work:

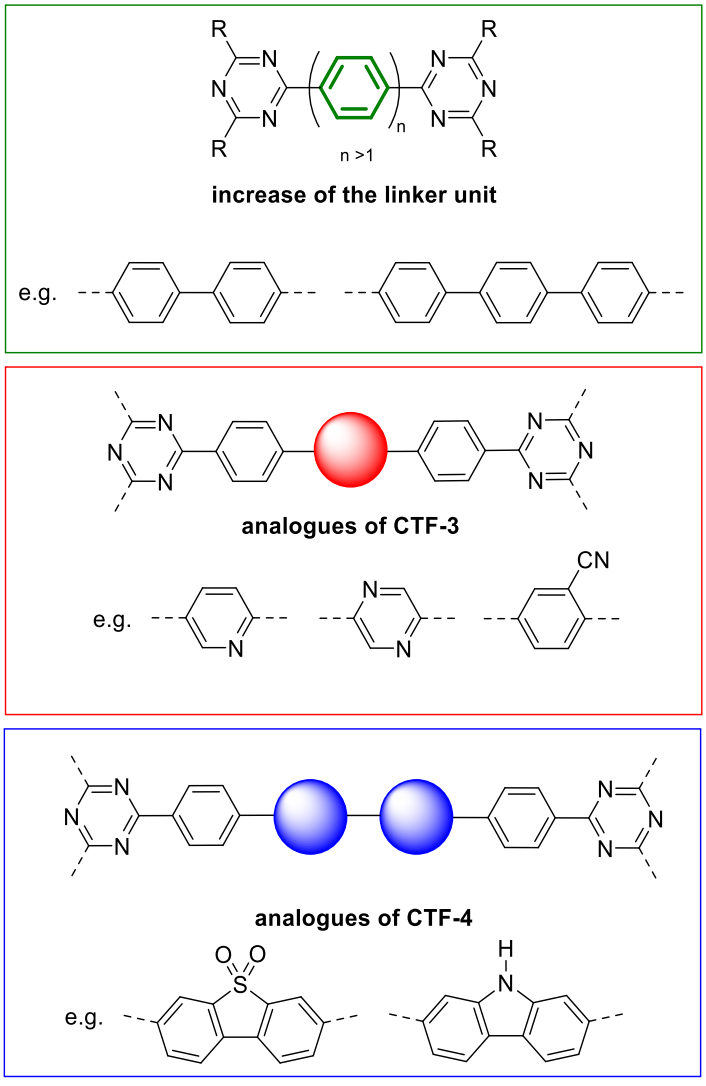

;

Figure I-22: Planned structures of new CTFs. The numerate CTF-x represents the number of phenylene linkers inbetween the triazines.

6 Aryl based CTFs

Covalent triazine-based frameworks for photocatalytic water splitting were first synthesised by the trimerisation of 1,4-benzenedicarbonitrile and 2-methyl-1,4-benzenedicarbonitrile using triflic acid.[97] Based on these results, a systematic increase of the linker unit from phenylene to quarterphenylene was investigated. Two synthetic routes were compared: CTF-1 to CTF-4 were synthesised *via* triflic acid cyclisations and CTF-2 Suzuki to CTF-4 Suzuki were synthesised *via* Suzuki-Miyaura polycondensations. The polymers with the same linker length were compared regarding: their properties, their hydrogen evolution performances from water under sacrificial conditions, their performance with a platinum co-catalyst, and the influence of residual palladium left in the materials from their synthesis.

6.1 Trimerisation of nitriles to form CTF-1 and CTF-2

Using trifluoromethanesulfonic acid (triflic acid), a trimerisation of the terminal nitriles can be performed to synthesise a material named CTF-1, where the numerate 1 is equivalent to phenyl (Figure 1). In the literature, CTF-1 was produced by the slow addition of triflic acid with a syringe to the monomer solution. However, this procedure was modified as triflic acid is one of the strongest monoprotonic organic acids and corrosive.[122] Therefore, the manual handling and transfer time was minimised by having triflic acid in the glass flask. The slow addition of the monomers dissolved in chloroform at a rate of 2 mL min^{-1} with a syringe pump was reported previously and carried out to produce CTF-1 in 63% yield.[123] The polymerisation was confirmed using TGA under air, with a decomposition on-set temperature of 220 °C for CTF-1 (Figure 78, appendix). In comparison, the monomer 1,4-benzenedicarbonitrile has a TGA decomposition on-set temperature of 138 °C (Figure 75, appendix). Further, the UV on-set is red-shifted from 378 nm for the monomer (Figure 76, appendix) to 421 nm for CTF-1.[124] The porosity to nitrogen was determined with a SA_{BET} = 9 $m^2 g^{-1}$. Both the porosity and the FT-IR spectra[124] of CTF-1 are similar to previous reports.[125] The synthesis is described in subsection 10.10, appendix.

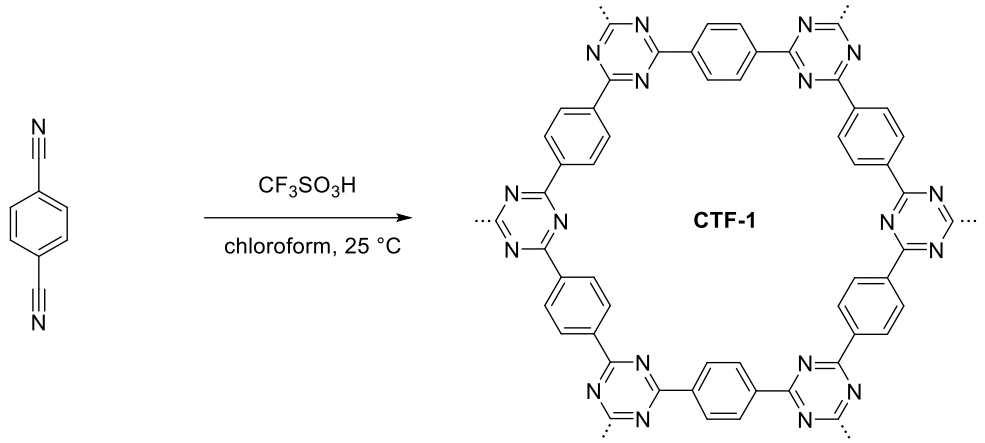

Figure 1: Trimerisation of 1,4-benzenedicarbonitrile with trifluoromethanesulfonic acid (triflic acid) to synthesise CTF-1. A representative polymeric structure is shown, although it is very likely that the polymer will have defects. For mechanistic insights, see Figure I-18, page 30.

Parallel to the synthesis of CTF-1, the polymerisation of 4,4'-biphenyldicarbonitrile was carried out using triflic acid to synthesise CTF-2 that consists of biphenylene linkers in between the triazine cores. The reaction produced CTF-2 in a yield of 73% after workup, and the polymerisation was confirmed by a TGA decomposition on-set temperature of 275 °C for CTF-2 (Figure 78, appendix) in comparison to 198 °C for 4,4'-biphenyldicarbonitrile, (Figure 75, appendix) and the red-shifted UV-Vis on-set to 453 nm[124] in comparison to the monomer UV on-set of 395 nm (Figure 76, appendix). The porosity to nitrogen was found to be SA_{BET} = 880 $m^2 g^{-1}$. Both the porosity and the FT-IR spectra[124] of CTF-2 are similar to previous reports.[125] The synthesis is described in subsection 10.10, appendix.

6.2 Synthesis of the monomers [1,1':4',1''-terphenyl]-4,4''-dicarbonitrile and [1,1':4',1'':4'',1'''-quarterphenyl]-4,4'''-dicarbonitrile

The monomer [1,1':4',1''-terphenyl]-4,4''-dicarbonitrile for CTF-3 was synthesised by a Suzuki-Miyaura coupling reaction of 4-bromobenzonitrile and 1,4-phenylenebisboronic acid (Figure 2, A). The product was analysed by ^{1}H NMR spectroscopy in chloroform-d (Figure 91 and Figure 92, appendix) showing signals in the aromatic region at 7.80 ppm and 7.72 ppm which agree with literature values[126] Further, HRMS showed a base peak $[M+H]^+$ for m/z 281.1073 (calculated 281.1080), and the elemental analysis confirmed the purity of the monomer. The synthesis is described in subsection 10.7, appendix.

In a further Suzuki-Miyaura coupling, [1,1':4',1'':4'',1'''-quarterphenyl]-4,4'''-dicarbonitrile was synthesised (Figure 2, B). As a starting material, 4,4'-dibromobiphenyl was cross-coupled with 4-cyanophenylboronic acid to give the monomer for the synthesis of CTF-4. The product was analysed by ^{1}H NMR spectroscopy (Figure 93 and Figure 94, appendix) in dimethyl sulfoxide showing signals in

the aromatic region at 7.96 ppm and 7.91 ppm which agree with literature values.[127] Further, HR-MS showed a base peak $[M+H]^+$ for m/z 357.1395 (calculated 357.1395), and the elemental analysis confirmed the purity of the monomer. The synthesis is described in subsection 10.8, appendix.

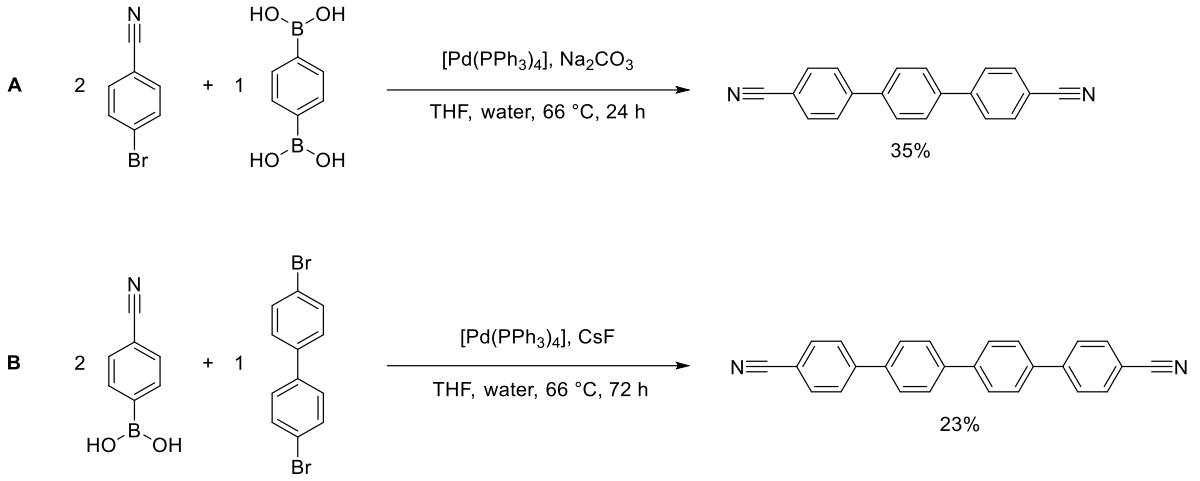

Figure 2: Synthetic routes to the monomers [1,1':4',1''-terphenyl]-4,4''-dicarbonitrile (A) and [1,1':4',1'':4'',1'''-quarterphenyl]-4,4'''-dicarbonitrile *via* Suzuki-Miyaura coupling (B).

The catalytic cycle of transition metal cross-coupling reactions to construct carbon-carbon bonds is based on three processes: oxidative addition, followed by transmetalation, followed by reductive elimination.[128] For the Suzuki-Miyaura coupling, organoboron reagents are activated with the help of base to facilitate the transmetalation step. The catalytic cycle is shown in Figure 3 on the cross-coupling of 4-bromobenzonitrile and phenyleneboronic acid (compareable to Figure 2, A).

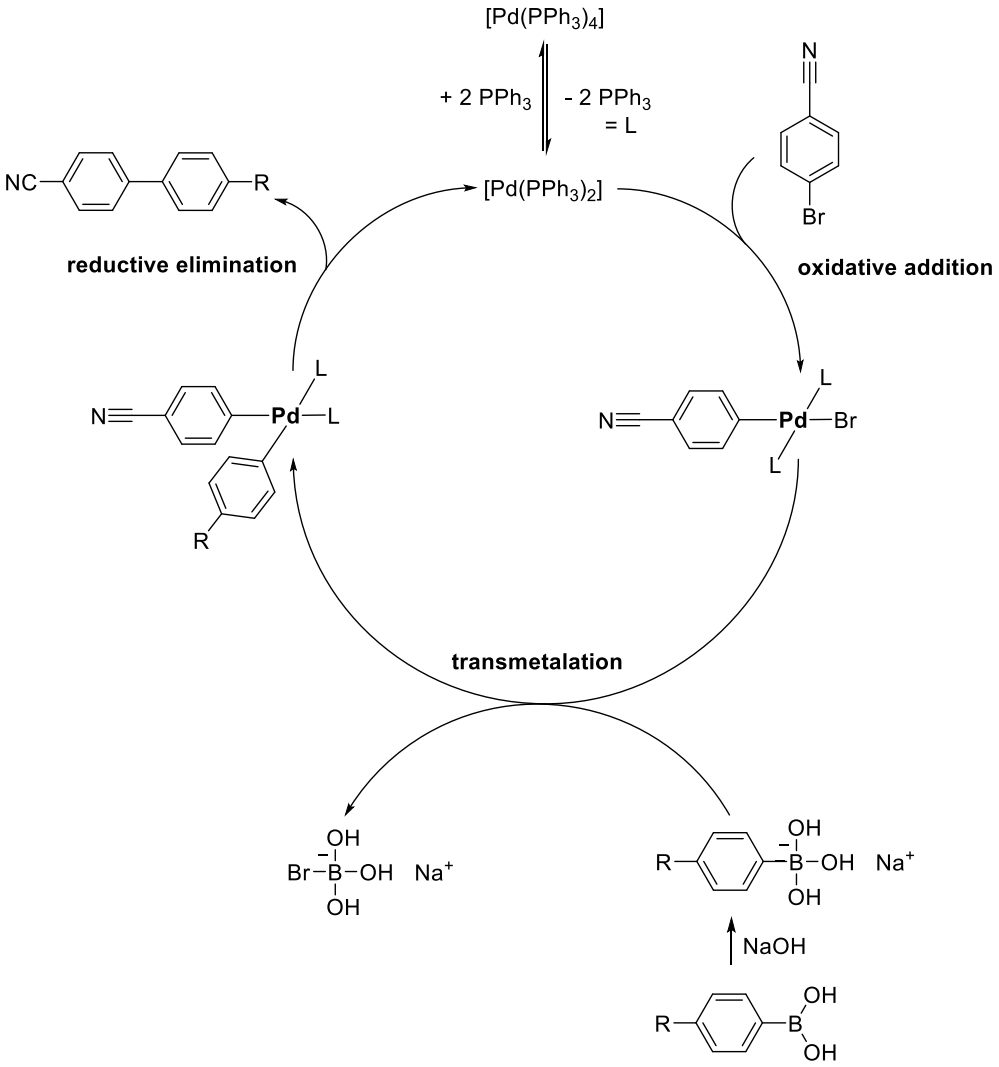

Figure 3: Catalytic cycle of the Suzuki-Miyaura cross-coupling including the base activation of the boronic acid.[128]

6.3 Synthesis of CTF-3 and CTF-4 by trimerisation, and analysis of CTF-1 to CTF-4

The dicarbonitriles of terphenylene (A) and quarterphenylene (B) were trimerised with triflic acid as described before in subsection 6.1 to give CTF-3 and CTF-4 and good yields of 70% and 80%, respectively (Figure 4). The polymerisation of CTF-3 was confirmed by a TGA decomposition on-set temperature of 294 °C (Figure 78, appendix) in comparison to 260 °C for [1,1':4',1''-terphenyl]-4,4''-dicarbonitrile (Figure 75, appendix), and the red-shifted UV-Vis on-set from 437 nm (Figure 76, appendix) to 473 nm[124]. For CTF-4, the TGA on-set was measured to be 360 °C (Figure 78, appendix) in comparison to 270 °C for [1,1':4',1'':4'',1'''-quarterphenyl]-4,4'''-dicarbonitrile (Figure 75, appendix), and the red-shifted UV-Vis on-set from 455 nm (Figure 76, appendix) to 500 nm[124] in comparison to the monomer.

Overall, all of the polymers were insoluble in common organic solvents such as acetone, methanol, *n*-hexane, dichloromethane, toluene, tetrahydrofuran, and *N,N*-dimethylformamide. For the polymers

CTF-1 to CTF-4, the FT-IR spectra[124] showed nitrile peaks in the region of around 2230-2220 cm^{-1} which might result from the endgroups or defects present in the final polymer. However, hydrolysis products of nitriles such as amides were not found[129] – analysing FT-IR spectra, no strong C=O stretches were found for amides[129] at around 1650 cm^{-1}, or carboxylic acids[129] at around 1700 cm^{-1}.[130]

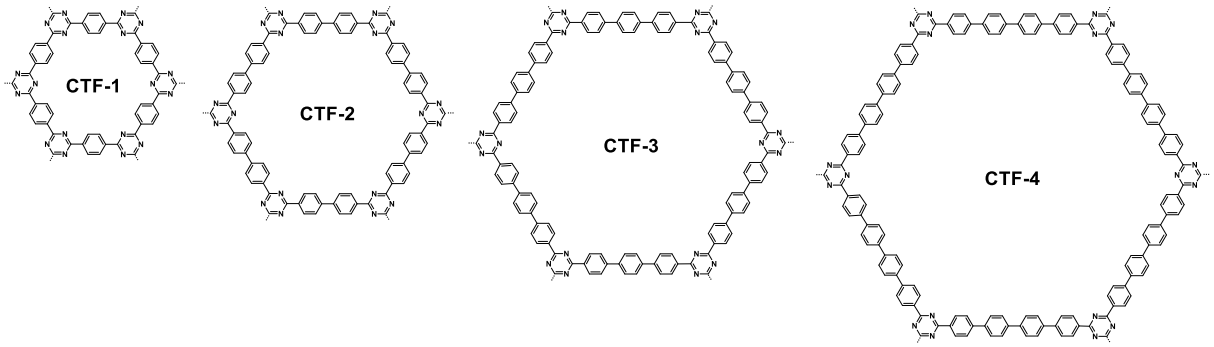

Figure 4: Overview of the polymers CTF-1 to CTF-4 synthesised by trimerisation of nitriles with triflic acid. Idealised structures are shown.

6.4 Suzuki-Miyaura polycondensation to synthesise CTFs

The Suzuki-Miyaura polycondensation has been applied in the synthesis of conjugated polymers.[131] In the case of poly-(*para*-phenylene)s (PPP) synthesised from 1,4-dibromo-2,5-dihexylbenzene, the reaction gave PPP chains with a degree of polymerisation of around 28 as determined by size-exclusion chromatography in 1,2-dichlorobenzene.[132,133] In the Cooper group, active polymeric photocatalysts were also found when synthesised *via* a Suzuki-Miyaura polycondensation.[17,59,88,92] while for example low hydrogen evolution rates were observed for polymers synthesised by a Stille coupling.[93]

Following the Suzuki-Miyaura approach, the building blocks to synthesise CTF-1 Suzuki to CTF-4 Suzuki were identified to couple aromatic units directly to one another. Starting form 2,4,6-tris(4-bromophenyl)-1,3,5-triazine, cyanuric chloride was chosen to synthesise CTF-1 Suzuki, 2,4,6-tris[4-(4, 4,5,5-tetramethyl-1,3,2-dioxaborolan-2-yl)phenyl]-1,3,5-triazine (TBPT) to achieve CTF-2 Suzuki, 1,4-phenylenediboronic acid or 1,4-benzenediboronic acid bis(pinacol) ester to produce CTF-3 Suzuki, and 4,4'-biphenyldiboronic acid or 4,4'-bis(4,4,5,5-tetramethyl-1,3,2-dioxaborolan-2-yl)biphenyl to gain access to CTF-4 Suzuki.

In all polymerisations, 2,4,6-tris(4-bromophenyl)-1,3,5-triazine is required and was therefore synthesised on a large scale (Figure 5). After an initial trimerisation with 1 g of 4-bromobenzonitrile in chloroform under triflic acid catalysis, a yield of 72% (720 mg) was achieved after double trituration (Figure 5). The ^{1}H NMR spectrum in chloroform-d showed two signals in the aromatic region at δ = 8.61 ppm (d, J = 8.5 Hz) and δ = 7.72 ppm (d, J = 8.5 Hz) with an integral ratio of 1:1. In the

$^{13}C\{^{1}H\}$ NMR spectrum, the benzene carbons were found to be present, while no carbon atom could be assigned to the triazine ring due to the weak signal intensity. Both spectra match the literature values.[134] Further, HRMS showed a base peak for $[M+H]^+$ of m/z 543.8654 (calculated 543.8660), and the elemental analysis confirmed the purity of 2,4,6-tris(4-bromophenyl)-1,3,5-triazine.

The reaction was also suitable for scaling-up – for example 20 g of 4-bromobenzonitrile were used to synthesise the product in a yield of 85% (17.0 g). The full characterisation is described in subsection 10.510.6, and the spectra can be found in Figure 83 - Figure 85, appendix.

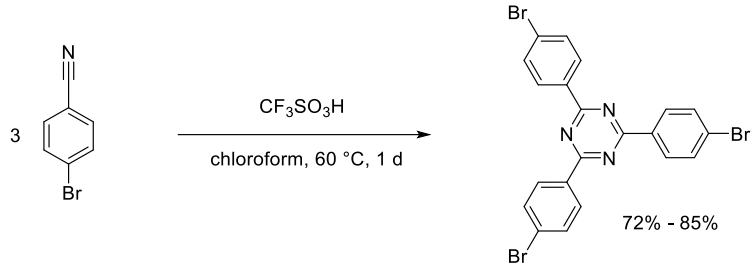

Figure 5: Synthesis of 2,4,6-tris(4-bromophenyl)-1,3,5-triazine.

For CTF-1 Suzuki and CTF-2 Suzuki, the synthesis of TBPT was carried out (Figure 6). The compound is not literature known, and the Suzuki-Miyaura borylation with bis(pinacolato)diboron[17,135] was used to avoid the triple lithiation of the starting material.[136–138] The synthesis was done on large scales using 10 g of 2,4,6-tris(4-bromophenyl)-1,3,5-triazine and gave the product in 85% (10.7 g) yield after the double trituration from methanol. The full characterisation is described in subsection 10.6.

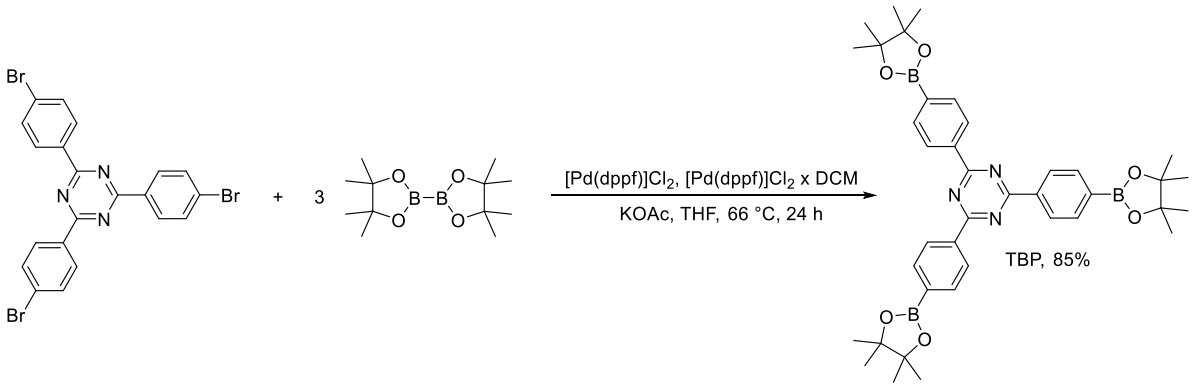

Figure 6: Suzuki-Miyaura borylation to form 2,4,6-tris[4-(4,4,5,5-tetramethyl-1,3,2-dioxaborolan-2-yl)phenyl]-1,3,5-triazine (TBPT).

In the ^{1}H NMR spectrum, two doublets of the reactant in chloroform-d can be seen at δ = 8.61 and 7.72 ppm, while the aromatic product signals appear at δ = 8.75 and 8.01 ppm (Figure 86 - Figure 88, appendix). The methyl group product signals of the pinacol ester are visible at δ = 1.40 ppm (Figure 7).

In the $^{13}C\{^1H\}$ NMR spectrum (Figure 89, appendix), two new signals at δ = 84.1 and 24.9 ppm were detected which belong to the quaternary carbon and the methyl groups of the pinacol ester, respectively. Further, HRMS showed a base peak for $[M+H]^+$ of m/z 687.3876 (calculated 687.3895), and the elemental analysis confirmed the purity of the monomer.

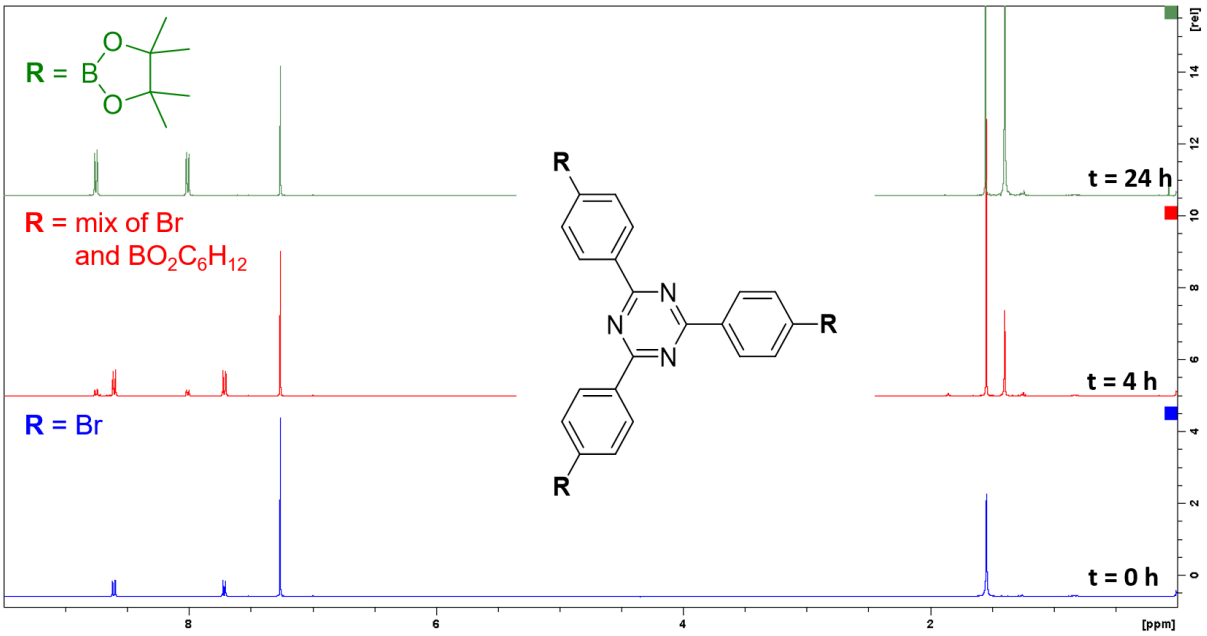

Figure 7: Stacked ^1H NMR spectra for the Suzuki-Miyaura borylation of 2,4,6-tris(4-bromophenyl)-1,3,5-triazine (bottom, blue) to form 2,4,6-tris[4-(4,4,5,5-tetramethyl-1,3,2-dioxaborolan-2-yl)phenyl]-1,3,5-triazine (TBPT, top, green), and the ^1H NMR in progress control after 4 h (middle, red). The aromatic reactant signals can be seen at δ = 8.61 and 7.72 ppm, while the aromatic product signals appear at δ = 8.75 and 8.01 ppm. The methyl group product signals of the pinacol ester is also visible at δ = 1.40 ppm.

6.5 Synthesis of CTF-1 Suzuki and CTF-2 Suzuki

For the synthesis of CTF-1 Suzuki, the cross-coupling of 2,4,6-trichloro-1,3,5-triazine (cyanuric chloride) and TBPT was attempted using the Suzuki-Miyaura protocol established in the literature.[17,59] However, after workup, no polymer was obtained. It could be possible that oligomers with a low degree of polymerisation were formed, but more likely, is the mismatch choice of the reaction conditions. Cyanuric chloride can be deactivated by three equivalents of water[139] – the products would be hydrochloric acid and 1,3,5-triazine-2,4,6-triol - a tautomer to 1,3,5-triazine-2,4,6(1*H*,3*H*,5*H*)-trione. Both forms would no longer be reactive for the cross-coupling and could therefore explain the absent polymerisation (Figure 8).

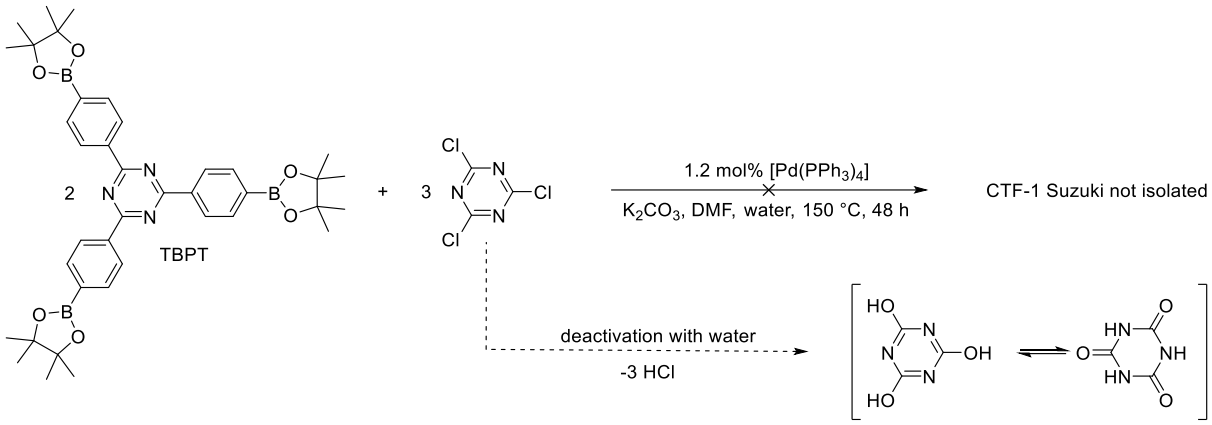

Figure 8: Attempt to synthesise CTF-1 Suzuki from cyanuric chloride under the given Suzuki-Miyaura polycondensation protocol and possible deactivation of cyanuric chloride in the presence of water (dashed arrow).

Parallel to CTF-1 Suzuki, the synthesis of CTF-2 Suzuki was carried out (Figure 9 and subsection 10.11). The polymerisation was confirmed by a red-shifted UV-Vis on-set to 423 nm,[124] in comparison to 2,4,6-tris(4-bromophenyl)-1,3,5-triazine at 371 nm (Figure 76, appendix).

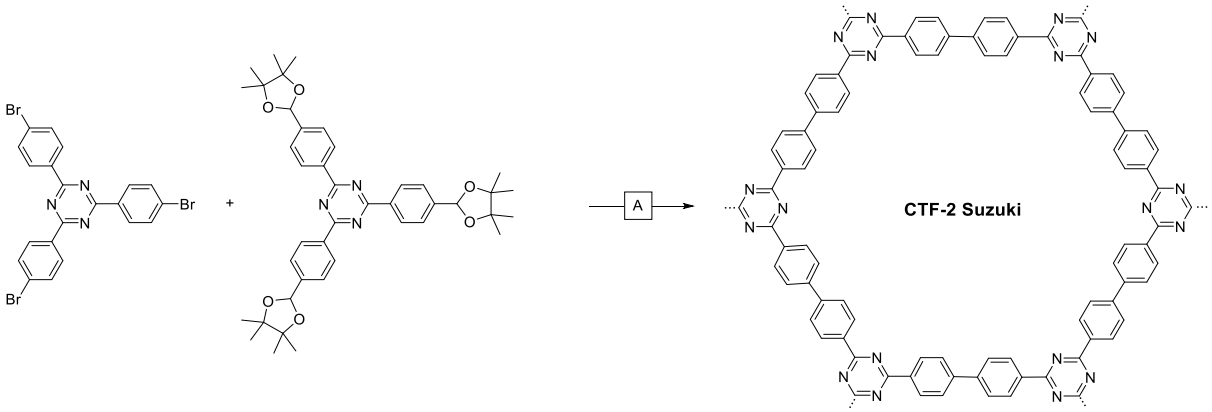

Figure 9: Synthesis of CTF-2 Suzuki *via* the Suzuki-Miyaura polycondensation. Conditions A: 1.2 mol% $[Pd(PPh_3)_4]$, K_2CO_3, DMF, water 150 °C, 48 h. A representative polymeric structure is shown, although it is very likely that the polymer will have defects.

6.6 Synthesis of CTF-3 Suzuki and CTF-4 Suzuki

CTF-3 Suzuki and CTF-4 Suzuki were also obtained with the Suzuki-Miyaura polycondensation (synthesis see subsection 10.11). 2,4,6-tris(4-bromophenyl)-1,3,5-triazine was cross-coupled with 1,4-phenylenediboronic acid, or 4,4'-bis(4,4,5,5-tetramethyl-1,3,2-dioxaborolan-2-yl)biphenyl to achieve CTF-3 Suzuki in 73% yield and CTF-4 Suzuki in 71% yield after Soxhlet extraction with cyclopentyl methyl ether (Figure 10). The polymerisation was confirmed for CTF-3 Suzuki and CTF-4 Suzuki by TGA

decomposition on-set temperatures of 292 °C and 369 °C,[124] respectively, while 1,4-phenylenediboronic acid and 4,4'-bis(4,4,5,5-tetramethyl-1,3,2-dioxaborolan-2-yl)biphenyl as monomer units showed TGA decomposition on-sets temperatures of 150 °C and 190 °C (Figure 75, appendix). Further, the UV-Vis on-set for CTF-3 Suzuki was found to be red-shifted to 431 nm[124] in comparison to the monomer at 315 nm (Figure 76, appendix), and CTF-4 Suzuki exhibited a red-shift to 435 nm[124] in comparison to its monomer at 309 nm (Figure 76, appendix). In comparison to CTF-3 and CTF-4 (subsection 6.3), the UV-Vis on-set of the polymers CTF-3 Suzuki and CTF-4 Suzuki are more blue-shifted, which could possibly be due the variety of endgroups present after Suzuki couplings.[140]

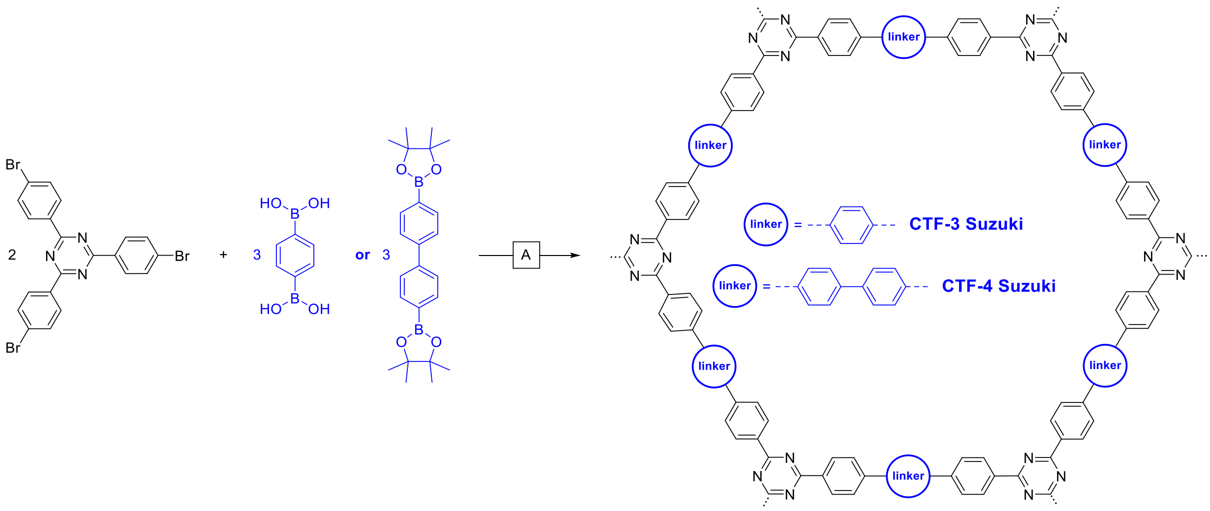

Figure 10: Synthesis of CTF-3 Suzuki and CTF-4 Suzuki *via* the Suzuki-Miyaura polycondensation. Conditions A: 1.2 mol% [Pd(PPh_3)$_4$], K_2CO_3, DMF, water 150 °C, 48 h. A representative polymeric structure is shown, although it is very likely that the polymer will have defects.

6.7 Palladium content of CTF-2 Suzuki to CTF-4 Suzuki

All CTFs were insoluble in common organic solvents tested (*i.e.*, acetone, methanol, *n*-hexane, dichloromethane, toluene, tetrahydrofuran, and *N,N*-dimethylformamide). For the inductively coupled plasma mass spectrometry (ICP), the polymers were microwave digested using *aqua regia*. The residual palladium was found to be 0.27 wt. % for CTF-2 Suzuki, 0.07 wt. % for CTF-3 Suzuki, and 0.65 wt. % for CTF-4 Suzuki (Table 3).

Table 3: Overview of the palladium content in Suzuki coupled CTFs.

Sample	Pd content by ICP-OES / wt. %
CTF-2 Suzuki	0.27
CTF-3 Suzuki	0.07
CTF-4 Suzuki	0.65

Conditions: 40 mg of samples were microwave digested using nitric acid and hydrochloric acid. The resulting solutions were run on the ICP-OES instrument calibrated with yttrium internal standard and palladium calibration standards at 340 nm. Analysis carried out by Exeter Analytical, Coventry.

6.8 SEM analysis of the polymers

After work-up, the polymers were obtained as macroscopic particles (CTF-1, CTF-2 Suzuki, CTF-3 Suzuki, CTF-4 and CTF-4 Suzuki) or as macroscopic flakes (CTF-2 and CTF 3). A ball mill was used to reduce the particle size, and SEM images were recorded to estimate the decrease in particle size (Figure 11). A contamination with metal impurities was from the stainless steel grinding jar and grinding balls was not found (energy-dispersive X-ray spectroscopy).[124] A reduction of particle size from around 100 µm to 10 µm was found for CTF-1, while a decrease from several millimetres to a few hundred micrometres was determined for CTF-2, CTF 3, CTF-2 Suzuki and CTF-3 Suzuki. No decrease in particle size was observed for CTF-4 and CTF-4 Suzuki after ball milling, possibly due to the softness and lower density of the networks.

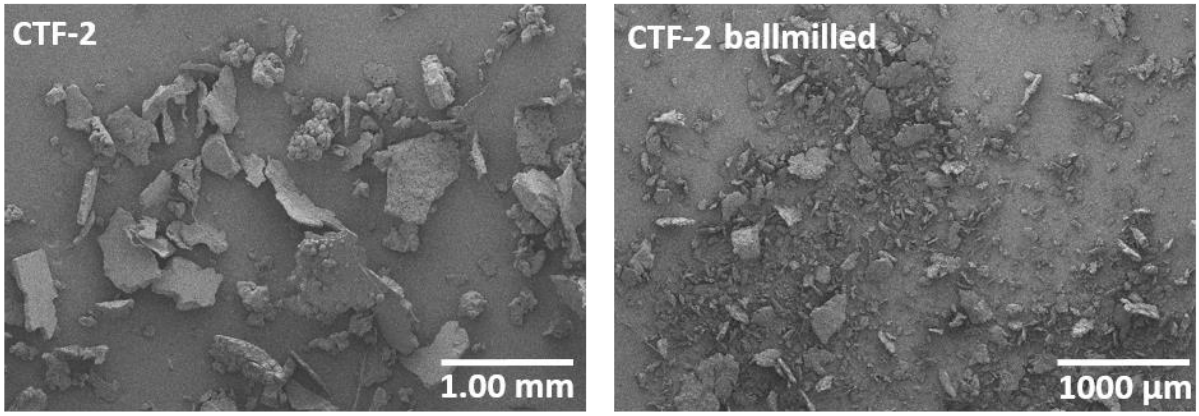

Figure 11: SEM-pictures of polymer CTF-2 – left: after workup – right: after ball milling. A reduction of particle size was determined after ball milling from around one millimetre to a few hundred micrometres.

6.9 PXRD spectra of the polymers

In order to compare the two synthetic routes to produce CTF-1 to CTF-4, and CTF-2 Suzuki to CTF-4 Suzuki, the crystallinity of the polymers were investigated. In this approach, the idea was to determine if crystalline materials can be achieved by the triflic acid trimerisation route, in comparison to the non-

crystalline materials formed from the Suzuki-Miyaura polymerisations to compare the influence of ordered structures on the hydrogen evolution rates of the polymers.

The recorded powder X-ray diffraction spectra (PXRD) of the ball milled polymers appeared featureless (Figure 12), while limited order of the as-synthesised polymers could have been affected by the ball mill. Comparing the polymers with the same linker length but formed using different protocols, both routes resulted in amorphous materials without any long range order. The absence of PXRD peaks below 2θ = 10° exclude 2D structures like covalent organic frameworks (COFs) as possible reaction products.[94,96,141] It is believed that only dynamic bond formation can lead to crystalline structures.[141,142] Further, the aromatisation of three nitriles to form a triazine core (compare subsection 4.5, Figure I-18) is not known to be reversible. By contrast, the trimerisation of nitriles at a synthesis temperature of 400 °C in molten zinc chloride[112,113] or a microwave assisted synthesis[98,125] were reported to give polymers of limited crystallinity. It is also known that the decomposition of 1,3,5-triazine to hydrogen cyanide happens at temperatures above 600 °C without a catalyst[143] – a temperature that could potentially be lowered under catalytic conditions. Nevertheless, both methods result in non-crystalline polymers and are found to be non-reversible routes to form CTFs.

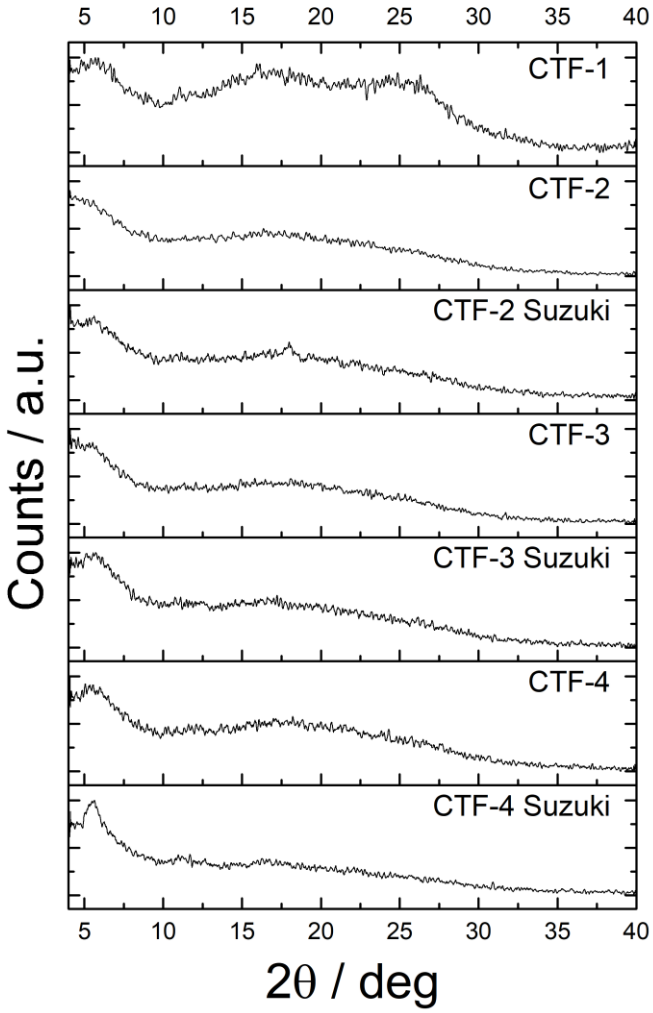

Figure 12: Normalised PXRD spectra of all ball milled polymers.

6.10 Properties of the CTFs produced *via* acid catalysis and Suzuki-Miyaura polycondensation

Although Figure 4 and Figure 10 indicate pores inside the material, porosity measurements of the ball milled polymers towards nitrogen at 77 K did not always showed sorption behaviour for the CTFs. It is noteworthy to say that the increase of the linker length, from phenylene to quarterphenylene, does not correlate directly with the sorption properties. For CTF-1, a moderate BET surface area of 9 $m^2 g^{-1}$ was determined, while CTF-2 has the highest surface area of all polymers tested at 560 $m^2 g^{-1}$. For CTF-3 and CTF-4, the SA_{BET} was determined to be 258 $m^2 g^{-1}$ and 0 $m^2 g^{-1}$, respectively. The results confirm that a simple increase of the linker length does not correlate with a higher BET surface area in CMPs, as reported previously.[144] The increased flexibility of longer linkers due to conformational freedom, and interpenetration of the chains, was previously reported to decrease the pore volume,[144] while more rigid systems like COFs had an increasing pore volume and higher sorption rates when

increasing the spacer length and growth of the layers.[145] For the polymers CTF-2 Suzuki, CTF-3 Suzuki, and CTF-4 Suzuki, the results show BET surface areas of 209 $m^2 g^{-1}$, 380 $m^2 g^{-1}$, and 100 $m^2 g^{-1}$ respectively (

Table 4).

Further, the polymers were also investigated for their absorption behaviour of hydrogen at 77 K, and CO_2, Kr, and Xe at 298 K. The absorbed quantities of all gases were moderate, while the best results were found for CTF-2 in all cases, with uptakes of 0.45 mmol g^{-1} for Kr, 1.25 mmol g^{-1} for CO_2, and 5.35 mmol g^{-1} for hydrogen.

The data in Table 4 shows no clear trend which synthesis protocol yields in higher surface areas, as e.g. CTF-2 has a higher SA_{BET} than CTF-2 Suzuki, while CTF-3 and CTF-4 have lower SA_{BET} than CTF-3 Suzuki and CTF-4 Suzuki. Similar, the CO_2 uptake was found to be better for CTF-2 than for CTF-2 Suzuki, while CTF-3 and CTF-4 have lower CO_2 uptakes than CTF-3 Suzuki and CTF-4 Suzuki. It can be seen that the synthetic conditions influences the surface area and uptake, as these measurements depend strongly on the synthetic condition.[14]

Table 4: Surface areas (SA_{BET}) and gas uptakes for hydrogen, carbon dioxide, krypton and xenon for ball milled CTF samples. The polymer CTF-2 has the highest uptake for all gases tested.

Polymer	SA_{BET} ($m^2 g^{-1}$)	Quantity absorbed (mmol g^{-1})			
		H_2 uptake, 1 bar, 77 K	Kr uptake 0.9 bar, 298 K	Xe uptake 1 bar, 298 K	CO_2 uptake 1 bar, 298 K
CTF-1[1]	9	0.28	0.10	0.13	0.17
CTF-2[2]	560	5.35	0.45	1.73	1.25
CTF-2 Suzuki	209	0.90	0.12	0.25	0.19
CTF-3	258	3.34	0.35	1.16	0.81
CTF-3 Suzuki	380	3.04	0.27	0.86	0.84
CTF-4	0	0.37	0.15	0.39	0.34
CTF-4 Suzuki	100	2.62	0.27	0.74	0.49

The surface area (SA_{BET}) was calculated from the isotherms of nitrogen adsorption-desorption plots with the Brunauer-Emmett-Teller (BET) model. [1]CTF-1 was tested as prepared and showed a SA_{BET} = 10 $m^2 g^{-1}$. [2]CTF-2 was tested as prepared and showed a SA_{BET} = 880 $m^2 g^{-1}$.

6.11 UV-Vis and photoluminescence measurements

The optical gap of the polymers was determined from the polymeric on-set of UV-Vis measurements in the solid-state (Figure 13). It is expected that the fitting of the absorption edge represents the lowest energy difference between the valence band and the conduction band.[146] Using step-growth

polymerisations,[147] the full characterisation of the resultant insoluble CTFs is challenging. Typical approaches such as gel permeation chromatography cannot be used to determine the molecular weight, and the polymerisation is expected to give a distribution of polymer lengths. Furthermore, defects, residual end groups, and catalyst residues, will result in an average value for the absorption on-set.

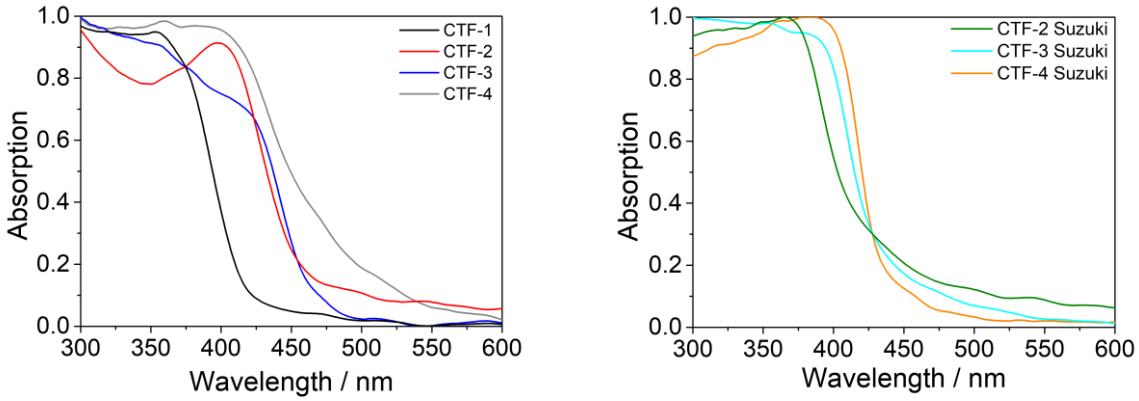

Figure 13: Normalised solid-state UV-Vis spectra for CTF-1 to CTF-4 (left), and CTF-2 Suzuki to CTF-4 Suzuki (right).

In both series of the polymers, the optical gap decreases when going to a longer linker unit (phenyl to quarterphenylene for CTF-1 to CTF-4 and biphenyl to quarterphenylene for CTF-2 Suzuki to CTF-4 Suzuki). For CTF-1 to CTF-4, the optical gap showed a decrease along the series from 2.95 eV to 2.48 eV, and the optical gap for CTF-2 Suzuki to CTF-4 Suzuki decreased from 2.93 eV to 2.85 eV (Table 5). While a difference in the optical gap of 0.47 eV was found for the acid catalysed polymers, the Suzuki-Miyaura catalysed polymers show a narrower optical gap difference of only 0.08 eV. As a reason, the polymerisation route must be considered: the cyclisation of nitriles to synthesise triazines for CTF-1 to CTF-4 is a multi-step catalysis. The polymer end groups will be nitriles or imines from incomplete trimerisations (compare subsection 4.5, Figure I-18). For the Suzuki coupled polymers, the polymeric structure is formed by adding either the bromine monomers or the borylated monomers to give a network with bromine or hydrogen end groups. Further, the decomposition on-set temperature in the TGA was lower for CTF-2 (290 °C) than for CTF-2 Suzuki (476 °C), indicating a higher degree of condensation and molecular weight for the latter polymer (Figure 78).

All polymers were tested upon excitation at $\lambda_{ex} = 280$ nm and showed weak fluorescence. One characteristic peak was measured between 448 and 476 nm (Table 5 and Figure 77, appendix). No trends within either series of polymers was found, and the small observed Stokes' shifts indicate the rigidity of the materials.

Table 5: Photophysical properties and TGA on-set temperature for the polymer photocatalysts.

Polymer	Optical gap[a] / eV	λ_{em}[b] / nm
CTF-1	2.95	469
CTF-2	2.73	448
CTF-3	2.62	468
CTF-4	2.48	476
CTF-2 Suzuki	2.93	466
CTF-3 Suzuki	2.88	452
CTF-4 Suzuki	2.85	467

[a] The optical gap was determined from the on-set of absorption in the solid-state UV-Vis spectrum; [b] λ_{em} was recorded at λ_{ex} = 280 nm (Figure 77, appendix).

6.12 Computational work

An additional contribution to the understanding of the hydrogen performance of the polymers was obtained from a collaboration with the group of Dr Martijn Zwijnenburg at University College London. In these thermodynamic calculations, the potentials associated with free charge carriers are calculated using an approach introduced by Zwijnenburg and co-workers[148,149] based on density functional theory calculations on a cluster model of the CTF. A dielectric screening model was used to describe the aqueous environment of the CTF.

The ionisation potential (IP) is the amount of energy required to remove an electron to the vacuum to give a positive ion and electron affinity (EA) is the amount of energy when an electron is added to a neutral molecule to give a negative ion.[149] The first oxidation is hereby related to the energy of the highest occupied molecular orbital.[150] The ionisation potential (IP) and electron affinity (EA) of the polymers follow equations (6) and (7), written as reductions. These standard reduction potentials are conclusions of the dissociation of the exciton, an electron-hole pair formed after the absorption of light.

$$\mathrm{CTF} + \mathrm{e}^- \rightleftarrows \mathrm{CTF}^- \text{ (EA)} \quad (6)$$

$$\mathrm{CTF}^+ + \mathrm{e}^- \rightleftarrows \mathrm{CTF} \text{ (IP)} \quad (7)$$

In equation (6) and equation (7), CTF describes the neutral CTF model in its electronic ground state, and CTF^- and CTF^+ are the CTF models with a free electron or a free hole, respectively. When the value of EA is more negative than -0.41 V at pH 7, the proton reduction is thermodynamically feasible. Similarly, when the IP is more positive than +0.82 V at pH 7, the oxidation of water is thermodynamically feasible. Figure 14 shows the results from this computational modelling. According to the calculations, the driving force for CTF-1 is the largest, and decreases with increasing

phenylene units, and all polymers are expected to be able to reduce protons as they all have significant overpotential.

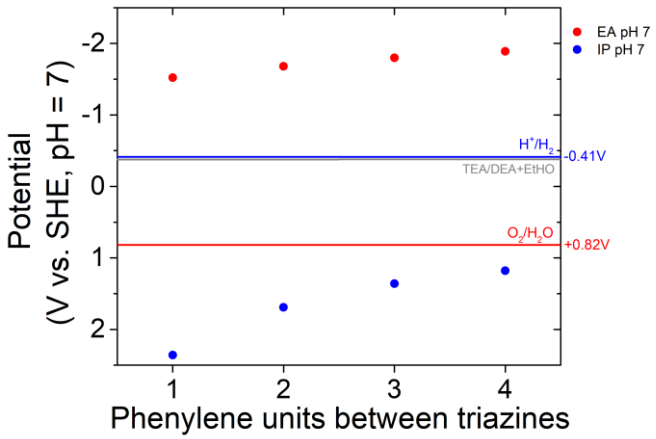

Figure 14: Predicted values of the ionisation potential (IP) and electron affinity (EA) standard reduction potentials of CTF-1 to CTF-4 with 1 to 4 phenylene units between the triazines. The standard reduction potentials for the proton reduction (blue line), water oxidation (red line), and triethylamine oxidation (grey line) to diethylamine and acetaldehyde (TEA/DEA+EtHO) are shown for clarity. All potentials are calculated for pH = 7 and a relative dielectric permittivity of 80.1 (water).

6.13 Hydrogen evolution experiments

All of the materials synthesised were then tested for hydrogen evolution from water. The seven polymers presented are able to absorb visible light, an advantage over inorganic materials like TiO_2[30] and to first reports of polymeric photocatalysts,[17] which are only active under UV-light. All polymers, with the exception of CTF-1, show broad absorption in the visible region, and the shift of absorption to visible light from CTF-1 to CTF-4 shows the tailorability of polymeric properties in comparison to g-C_3N_4.[66] A photocatalytic setup with a 300 W Xenon lamp and a $\lambda > 420$ nm cut-off filter was used to illuminate the dispersed photocatalyst in a quartz flask. Further, triethanolamine (TEOA) was used as scavenger in water, as previously employed for CTFs.[94,97,99] A co-catalyst loading of 3 wt. % platinum was realised by *in situ* photodeposition on the polymer,[87,97,151] while the polymer co-catalyst interface was not further analysed in this work. To determine the rate of the hydrogen evolution, a sample of the headspace was taken every hour for typically five hours, and analysed by gas chromatography - the slope resulting from the series of data points was calculated, alongside the standard deviation of the slope (Figure 15 and Table 6).

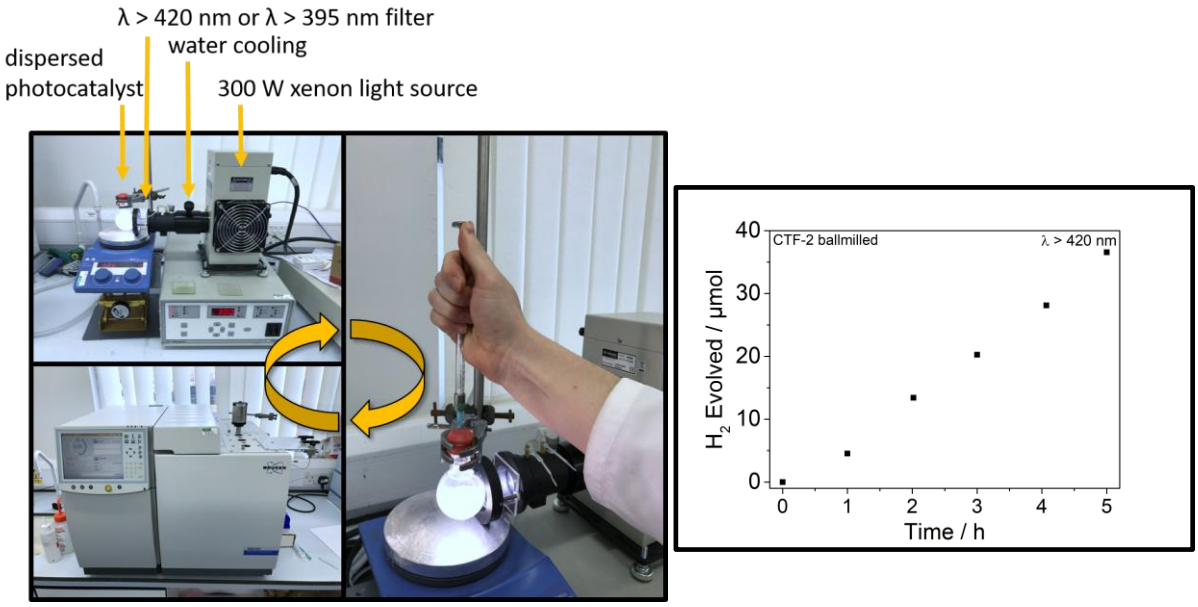

Figure 15: Setup of the manual hydrogen measurement *via* GC-analysis (left) to obtain hourly measurements for the analysis of the hydrogen evolution rate (right).

All materials with the exception of CTF-1, CTF-4 and CTF-4 Suzuki were found to produce hydrogen. Interestingly, CTF-1 did not show hydrogen evolution under these conditions, although the band-gap and TGA on-set of decomposition matched the reported values, and hydrogen evolution was reported previously.[97] A change in the synthesis temperature to 50 °C, after the addition of the monomer solution to triflic acid, resulted in a material that showed an activity of 35 ± 1 µmol g^{-1} h^{-1} for the hydrogen evolution from water. On comparison of the TGA profiles of the two polymers (Figure 79, appendix), it can be seen that CTF-1 formed at 25 °C has a lower thermal stability under air than CTF-1 formed at 50 °C (238 °C and 260 °C, respectively), that might indicate a lower degree of polymerisation.

The polymers were found to consist of large particles (subsection 6.8) that were barely dispersible in the water mixtures. For all as-synthesised polymers, a ball mill was used to reduce the particles and showed a minimum improvement by 1.8 times for CTF-1, and up to 3.1 times for CTF-4 Suzuki (Table 6). The obtained rates for hydrogen evolution were 35 µmol g^{-1} h^{-1} for CTF-1, 296 µmol g^{-1} h^{-1} for CTF-2, and 45 µmol g^{-1} h^{-1} for CTF-3 under λ > 420 nm irradiation. Slightly lower photocatalytic activity was found for the Suzuki-Miyaura synthesised polymers - the performances were determined to 265 ± 5 µmol g^{-1} h^{-1} for CTF-2 Suzuki, and 44 ± 2 µmol g^{-1} h^{-1} for CTF-3 Suzuki under λ > 420 nm irradiation. Overall, both routes resulted in polymers with similar photocatalytic activity despite some differences in the optical properties. Higher rates for polymeric photocatalysts were reported under λ > 420 nm illumination from water/TEA/MeOH for the linear homopolymer of dibenzo[*b,d*]thiophene

sulfone[152] with a HER of 3260 ± 164 µmol g^{-1} h^{-1} followed by the co-polymer poly(dibenzo[*b,d*]thiophene sulfone-*co*-phenylene) with a HER of 1492 ± 32 µmol g^{-1} h^{-1}.[59]

Table 6: Hydrogen evolution rates (HERs) for the polymer photocatalysts.

Sample	H_2 Evolved[a] / µmol g^{-1} h^{-1} for ball milled samples	H_2 Evolved[a] / µmol g^{-1} h^{-1} for as prepared samples
CTF-1 25 °C	0[b]	0[b]
CTF-1 50 °C	35 ± 1	19 ± 1
CTF-2[1]	296 ± 11	167 ± 3
CTF-3[1]	45 ± 1	20 ± 1
CTF-4[1]	0[b]	0[b]
CTF-2 Suzuki[1]	265 ± 5	90 ± 3
CTF-3 Suzuki[1]	44 ± 2	14 ± 1
CTF-4 Suzuki[1]	0[b]	0[b]

[a] The hydrogen evolution rate (HER) was measured using 25 mg of the ball milled samples in water, 20% triethanolamine and 3 wt. % platinum as a co-catalyst under λ > 420 nm illumination from a 300 W xenon lamp; [b] No hydrogen evolved during a typical 5 h run.

6.14 The low activity of CTF-1

All materials were probed for their hydrogen evolution to investigate if materials with longer linkers can evolve more hydrogen than CTF-1 synthesised at 50 °C, which has a rate of 35 µmol g^{-1} h^{-1} and was calculated to have the strongest driving force (subsection 6.12). When comparing the hydrogen evolution rates from water/TEOA/MeOH in presence of platinum co-catalyst (Figure 16), it can be seen that CTF-1 does not have the highest evolution rate in the series tested, although this could be expected when going from the 0 µmol g^{-1} h^{-1} for CTF-4 over 45 µmol g^{-1} h^{-1} for CTF-3 and 296 µmol g^{-1} h^{-1} for CTF-2.

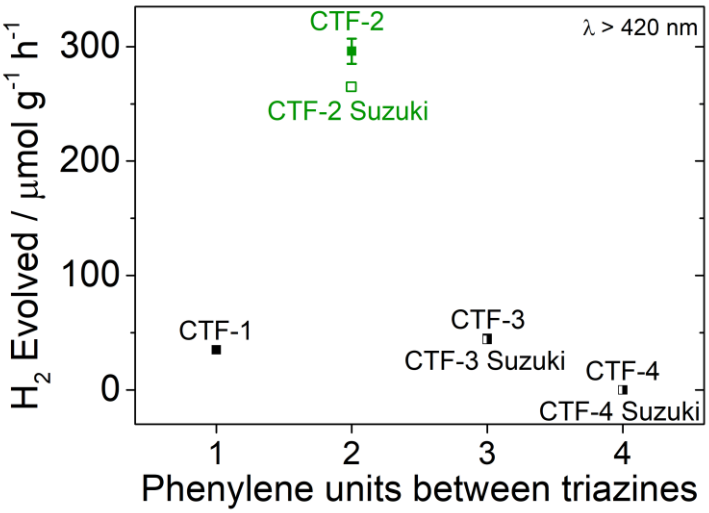

Figure 16: Photocatalytic hydrogen evolution rates (HER) correlated with the length of the phenylene spacers between the triazine units. Each measurement was performed with 25 mg ball milled photocatalyst from water/triethanolamine mixtures (90 vol. % / 10 vol. %) with 3 wt. % platinum co-catalyst under visible-light irradiation (λ > 420 nm). The error bars for CTF-1, CTF-3 and CTF-3 Suzuki are in the range of 3-4 µmol g^{-1} h^{-1}.

To further investigate the low activity of CTF-1, the polymers CTF-1 and CTF-2 were tested under irradiation with two filters: a λ > 295 nm filter was used to illuminate under UV-Vis irradiation, while a U-340 filter (light from 259 – 390 nm) was used to have UV-light exclusively (Figure 17). For the λ > 295 nm illumination, the hydrogen evolution of CTF-2 increased by 26% from 296 µmol g^{-1} h^{-1} (λ > 420 nm) to 374 µmol g^{-1} h^{-1}, and CTF-1 increased by 245% from 35 µmol g^{-1} h^{-1} (λ > 420 nm) to 86 µmol g^{-1} h^{-1}. When going to UV-only light with the U-340 filter (light from 259 – 390 nm), the performance of CTF-2 decreases to 111 µmol g^{-1} h^{-1}, while the hydrogen evolution of CTF-1 increases to 118 µmol g^{-1} h^{-1}, even outperforming CTF-2 under these conditions. These experiments show the hydrogen evolution characteristic of the polymers towards their illumination preference and indicate that CTF-1 is predominantly active under UV-light. These results help to explain the moderate evolution observed in the previous tests under λ > 420 nm illumination: as the on-set of the polymer was determined to be 421 nm and the λ > 420 nm filter is transmittant from λ > 390 nm (Figure 17, left), a small amount of photons are passed through the filter to contribute to the photocatalysis. Nevertheless, CTF-1 cannot outperform CTF-2 even under λ > 295 nm which can be related to the broader light absorption of CTF-2 reaching to the visible light of the solar spectrum.

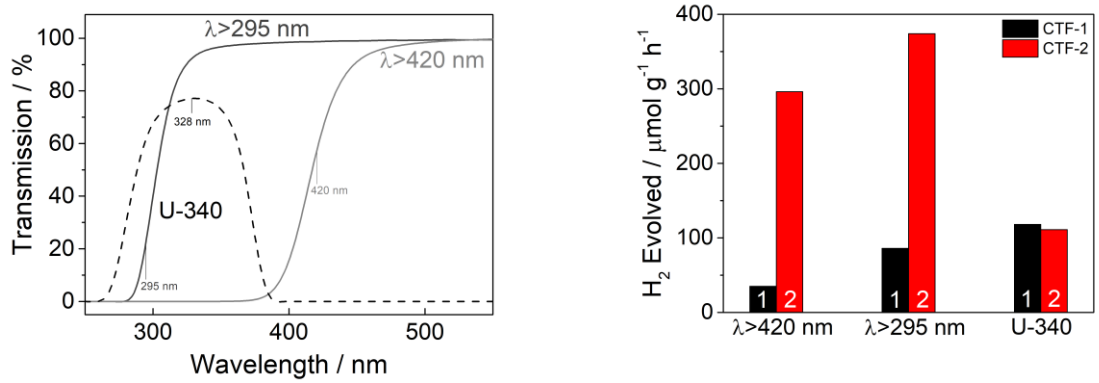

Figure 17: Transmission characteristics of the filters (left): two cut-off filters with a wavelength transmission above λ > 295 nm and λ > 420 nm, and one UV-only filter were used (U-340, max. 328 nm, FWHM ± 44 nm) – (right): hydrogen evolution of CTF-1 and CTF-2 under these three filters.

6.15 External quantum efficiency (EQE) and stability of CTF-2

In further studies, the best performing material CTF-2 was investigated. First, the wavelength dependency of the photocatalytic hydrogen evolution was investigated as described in the literature.[106] No photocatalytic activity was observed under λ = 600 nm, λ = 550 nm or λ = 500 nm illumination using band-pass filters, showing that there is a threshold energy necessary for CTF-2 to drive the photocatalysis. The illumination at λ = 420 nm yielded an EQE_{420nm} of 1.6% (± 10 nm, FWHM, Figure 18). This value is four times higher than poly(*p*-phenylene) ($EQE_{420\ nm}$ = 0.4%), but does not exceed poly(dibenzo[*b,d*]thiophene sulfone-*co*-phenylene) with an $EQE_{420\ nm}$ of 7.2%.[59]

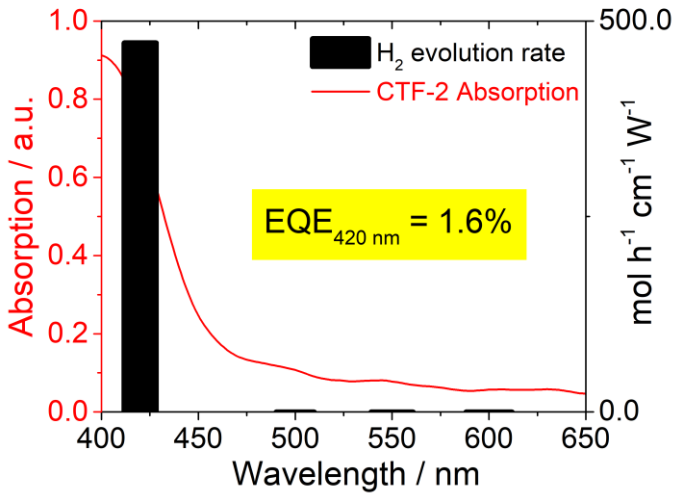

Figure 18: Wavelength dependency of the photocatalytic hydrogen evolution for CTF-2 ball milled using band-pass filters (420 nm, 500 nm, 550 nm and 600 nm ± 10 nm, FWHM). The suspension of the polymer in water with 20 vol. % triethanolamine and 3 wt. % Pt was measured in a quartz cuvette with an area of 7.8 cm^2 for an illumination of at least 5 hours.

Further, the photocatalytic stability of CTF-2 was tested under 1.0 Sun illumination for a total of 38 hours (Figure 19) – an ABA-certified solar-simulator was used as the light source. The initial performance of 931 ± 38 µmol g^{-1} h^{-1} slightly decreased after three hours to a constant evolution rate of 526 µmol g^{-1} h^{-1}. This stabilisation shows an ongoing photocatalytic process that represents a permanent and repeatable hydrogen evolution. The reaction solution was kept the same, and the quartz flask was equipped with a new rubber seal and degassed before testing in the next run. After 38 hours, the polymer evolved more hydrogen than present in the material (Figure 19, blue dotted line), ruling out decomposition of the polymer as the source of hydrogen.

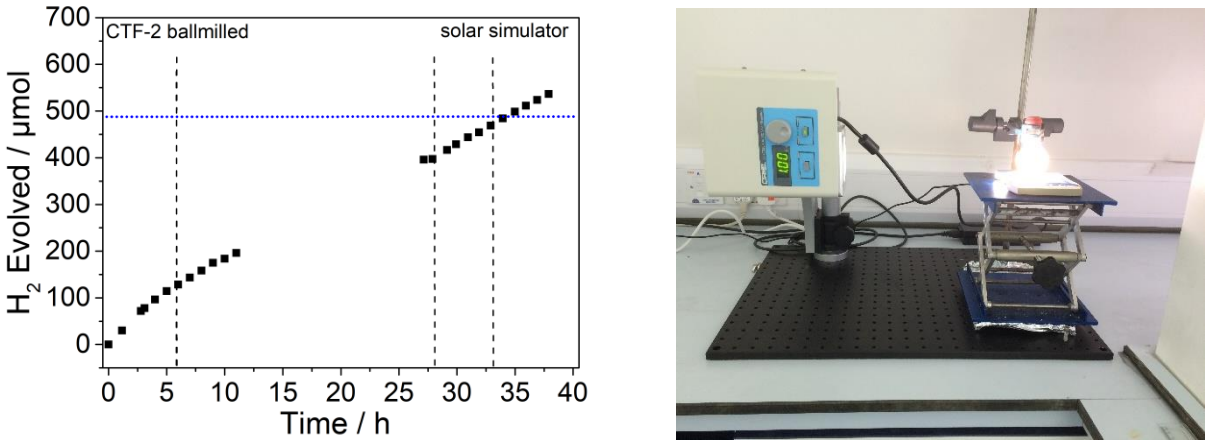

Figure 19: Cumulative amount of hydrogen evolved from 25 mg CTF-2 ball milled from water with 20 vol. % of triethanolamine and 3 wt. % Pt under ABA LED-based Solar Simulator irradiation (1.0 Sun). The dashed black vertical lines indicate when the reaction mixture was degassed; the short dotted blue line represents the maximal amount of 490 µmol hydrogen present in the polymeric photocatalyst (left). ABA LED-based Solar Simulator irradiation (1.0 Sun) (right).

Finally, spectroscopic analysis after photocatalysis was carried out (Figure 20). The FT-IR spectrum confirms the presence of a nitrile peak at 2228 cm^{-1} before, and at 2226 cm^{-1} after the reaction that can assigned to the terminal end-groups of CTF-2. Minor changes can be seen when comparing the spectra which could potentially be due to the platinum particle-polymer interaction, as palladium nanoparticles have been found to bind to conjugated polymers.[153,154] Further, the metal was also found to have an influence on the UV-Vis absorption of the polymer. While the band-gap of CTF-2 Suzuki is only slightly red-shifted after the photocatalysis from 423 to 428 nm, the band-gap of CTF-2 was strongly red-shifted from 453 nm to 644 nm. The results indicate either that there is an interaction between the photodeposited platinum and CTF-2, possibly due to the nitrile end-groups that can interact with the platinum co-catalyst in the case of CTF-2 but not in the case of CTF-2 Suzuki or a potential degradation of CTF-2 under sacrificial conditions. No test of the photocatalytic activity was done at $\lambda > 550$ nm after the reaction. Interactions between nitrile containing linear polymers and platinum were reported before with shifts of nitrile peaks around 10 cm^{-1}.[155]

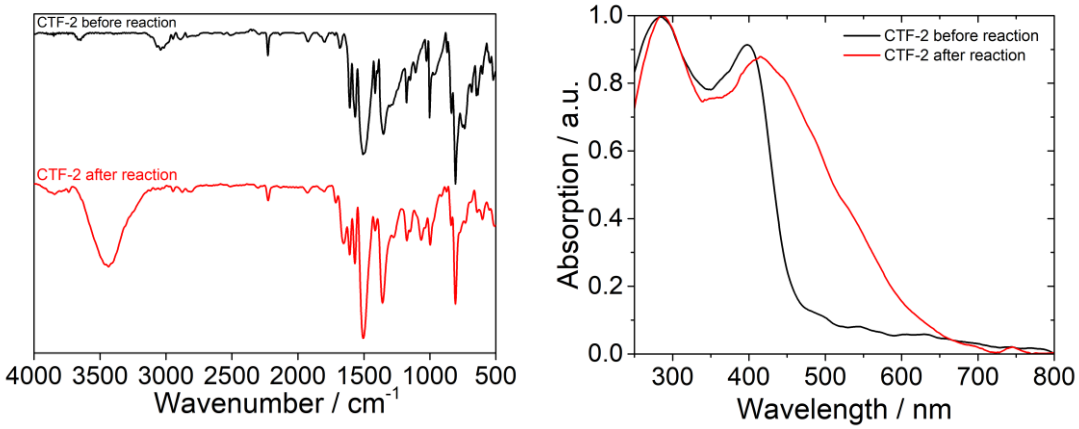

Figure 20: FT-IR spectra (left) and UV-Vis spectra (right) of CTF-2 before and after irradiation with visible light (λ > 420 nm) for 38 hours from water with 20 vol. % of triethanolamine and 3 wt. % Pt under 1.0 Sun with a ABA LED-based Solar Simulator. The band at 3450 cm^{-1} might indicate that some triethanolamine and/or water was still present in the pores of the material.

6.16 Photocatalytic activity from triethylamine and methanol

Based on the theoretical calculations in subsection 6.12 describing CTF-1 to CTF-4 as being feasible for hydrogen reduction and recent reports from the Cooper group,[17,59,88] CTF-1 to CTF-4 were also tested with a further sacrificial electron donor. The photocatalytic hydrogen evolution of the ball milled polymers from water, triethylamine (TEA), and methanol with 3 wt. % platinum co-catalyst was investigated (Figure 21). Methanol acts as a wetting agent because TEA and water are only miscible below 18 °C in all mixing ratios,[156,157] while the use of methanol as a scavenger yielded low evolution rates. It was found that the hydrogen evolution from water/TEA/MeOH improved for all acid-catalysed CTFs. For CTF-2, the hydrogen evolution rate increased from 296 ± 11 to 358 ± 21 µmol g^{-1} h^{-1}. For CTF-1 and CTF-3, the hydrogen evolution rates nearly doubled from 35 ± 1 to 66 ± 3 µmol g^{-1} h^{-1} and from 45 ± 1 to 79 ± 5 µmol g^{-1} h^{-1} in this reaction mixture. A moderate hydrogen evolution rate of 24 ± 1 µmol g^{-1} h^{-1} for CTF-4 showed the strong impact of the sacrificial electron donor for the performance. At a fixed pH value, there is no difference in the thermodynamic ease of TEA and TEOA as the oxidation potential is very similar. Nevertheless, the more alkaline solution of TEA (pKa = 10.72)[158] is easier to oxidize than TEOA (pKa = 7.76),[158] and lower hydrogen evolution of linear polymers from TEOA in comparison to TEA were reported previously.[59,92]

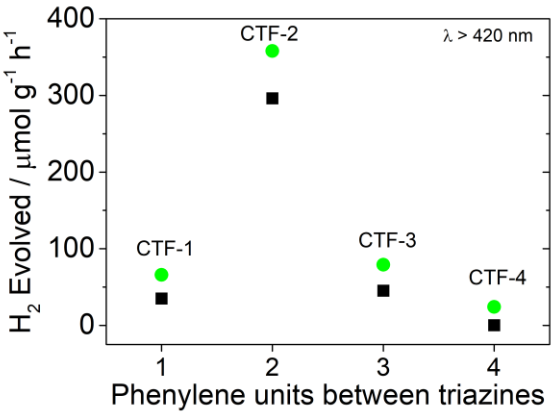

Figure 21: Comparison of scavengers for CTF-1 to CTF-4 – with triethylamine (TEA) as scavenger (green dots), all polymers exhibit an increase in performance, and even CTF-4 showed a moderate hydrogen evolution rate. The black squares represent the hydrogen evolution rates in the case of triethanolamine (TEOA) as scavenger. Conditions TEOA: 25 mg polymer ball milled, water, 20 vol. % triethanolamine, and 3 wt. % Pt. Conditions TEA: 25 mg polymer ball milled, water, 10 vol. % triethylamine, 10 vol. % methanol, and 3 wt. % Pt.

Further, the contact angle of CTF-2 could not be determined due to the polymer swelling when in contact with water (Figure 22). Although no water contact angle within the polymer's porous structure was assigned, an interaction of the polymer and water can be seen as CTF-2 absorbs water like a sponge, in contrast to CTF-1 with a contact angle of 59 ± 3°. The contact angle can give an indication about the interaction of the polymer with water, as the surface of the polymer can either be hydrophobic or hydrophilic. A hydrophilicity of the polymer is desired, as the interaction of the polymer and water is seen as necessary for water splitting.[67]

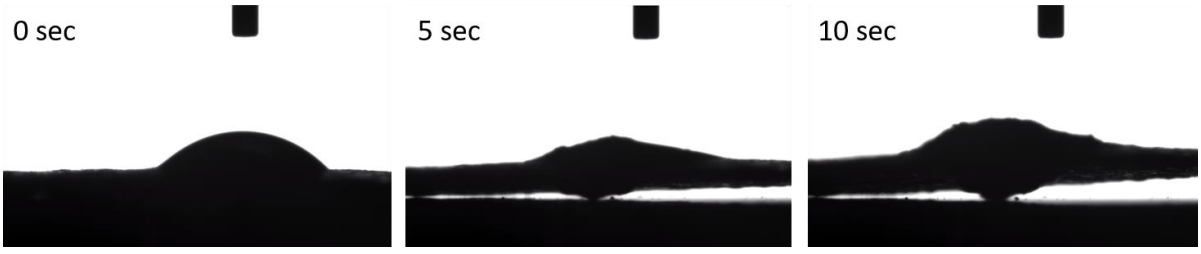

Figure 22: Swelling of CTF-2 when measuring the contact angle with water.

6.17 The role of palladium for the photocatalytic activity

CMPs have previously been investigated as metal-free photocatalysts.[17] When the Suzuki-Miyaura polycondensation is used, the polymers were found to have residual palladium content from the

synthesis.[153,159,160] For the CTFs presented here, there is the acid catalysed route that trimerises the nitrile transition metal free, while the Suzuki-Miyaura polycondensation uses palladium catalysts.

By comparing the results for the photocatalytic reaction from triethanolamine (Figure 16), the polymers CTF-2/CTF-2-Suzuki, CTF-3/CTF-3 Suzuki and CTF-4/CTF-4 Suzuki showed similar activity, although they did have some differences in the optical properties and residual end groups. Nevertheless, both subgroups of polymers have the same idealised repeat unit, and an investigation of the residual palladium is therefore possible.

When CTF-2 Suzuki was tested without platinum co-catalyst in an aqueous solution of 20 vol. % triethanolamine, the photocatalytic activity was determined to be 121 ± 4 μmol g^{-1} h^{-1} (Figure 23). In comparison, a HER of 296 ± 11 μmol g^{-1} h^{-1} was measured when adding 3 wt. % platinum. These results are in line with observations for the hydrogen evolution activity of g-C_3N_4 with loaded co-catalyst – platinum is the most active co-catalyst followed by palladium.[161] Further control experiments were done with CTF-2 that was synthesised without palladium chemistry. The hydrogen evolution rates are 0 μmol g^{-1} h^{-1} for CTF-2 in water, CTF-2 in water with 20 vol. % triethanolamine and CTF-2 in water with 3 wt. % platinum co-catalyst.

These experiments show that CTF-2 is not active for hydrogen evolution in the absence of triethanolamine and platinum. Further, CTF-2 Suzuki was found to evolve hydrogen, indicating that residual palladium acts as a co-catalyst. Similar to co-catalysts tested on g-C_3N_4, palladium is less active than platinum as co-catalyst.[161] These results highlight that covalent triazine-based frameworks act as photoabsorbers that cannot be used as stand-alone photocatalysts for the hydrogen evolution from water, and show an improvement in hydrogen release when noble metal co-catalysts are used. Further studies on soluble polymers also confirmed palladium as a co-catalyst for the hydrogen evolution from water/TEOA,[162,163] while purification of the polymer decreased the residual palladium concentration below 1 ppm/0.0001% and resulted in a loss of hydrogen evolution from TEOA/water. By adding palladium co-catalyst, a threshold concentration around 40 ppm/0.004% palladium was observed to co-catalyse the hydrogen evolution from water/TEOA.

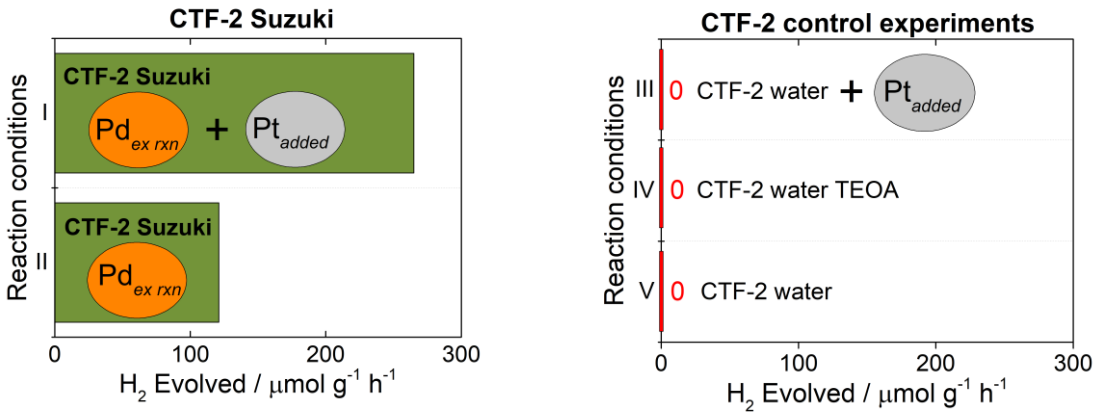

Figure 23: Palladium investigation for CTF-2 Suzuki – left: hydrogen evolution when using additional platinum co-catalyst – right: CTF-2 control experiments with three reaction conditions showing no hydrogen evolution.

In literature, the active co-catalyst formed by photodeposition of hydrochloroplatinic acid was previously investigated for TiO_2.[164,165] At basic pH, both $Pt(OH)_2$ and PtO_2 are first formed during the light induced reduction (equations 8-10) before being reduced to Pd(0) particles. Others reported recently a decomposition of a molecular palladium catalyst through ligand loss to metallic Pd(0) particles.[166]

(8) $[Pt(OH)_xCl_{6-x}]^{2-} + {}^{-}OH \rightleftharpoons [Pt(OH)_{x+1}Cl_{5-x}]^{2-} + Cl^{-}$ | x = 0-5

(9) $[Pt(OH)_4Cl_2]^{2-} + 4\ h^{+} \longrightarrow PtO_2 + O_2 + 4\ H^{+} + 2\ Cl^{-}$

(10) $[Pt(OH)_4Cl_2]^{2-} + 2\ e^{-} \longrightarrow Pt(OH)_2 + 4\ Cl^{-}$

The reaction solution was dried after *in situ* photodeposition on CTF-2 and subsequent 5 hours photocatalytic reaction to determine the size of the platinum particles. The particles were analysed with TEM – platinum particles with diameters in the range of 17-33 µm were determined, often aggregated in smaller clusters of up to 12 particles (Figure 24).

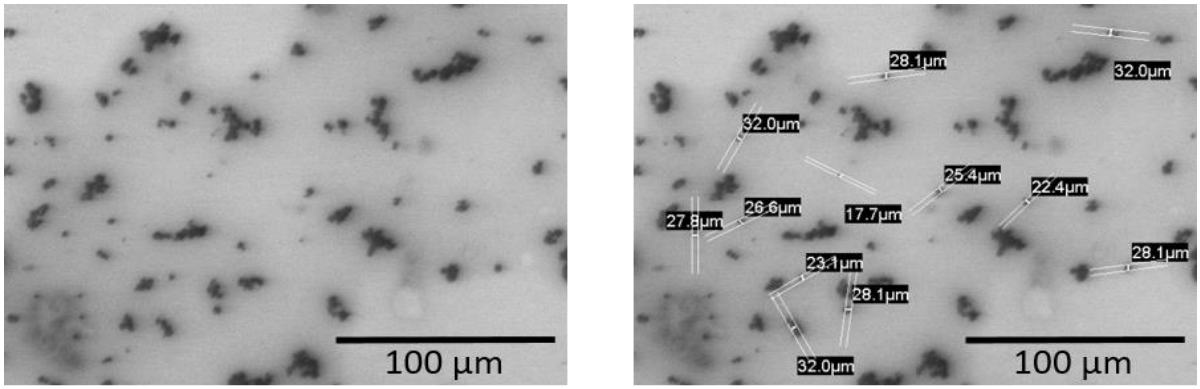

Figure 24: TEM pictures of photodeposited platinum particles with a diameter range of 17-33 µm on CTF-2.

6.18 Summary of aryl based CTFs

In this section on CTFs consisting of aryl linkers, it was shown that the route used to synthesise the polymers hardly influences the photocatalytic activity of the polymer when comparing materials with the same linker length synthesised by either acid catalysis or Suzuki-Miyaura polycondensation. Very likely, one polymer can be seen as a combination of multiple local catalytic active sites that transfer the energy simultaneously to the palladium co-catalyst. Eventually, oligomers of CTFs could also be used as photocatalysts, but a limited visible light absorption would be accompanied with these.

Further, the performance of the materials does not only relate to the band-gap, but also depends on the wavelength of the light used. The use of UV-Vis light did hereby moderately exceed the activity of CTF-2 for hydrogen evolution, while the less active CTF-1 benefited massively and led to an improved hydrogen evolution by a factor of two.

While a potential reduction of mass transport inside porous materials might suppress the photocatalysis, no result indicated this expectation. Indeed, the most porous material CTF-2 also showed the best photocatalytic performance. It can even be expected that chloroplatinic acid can diffuse into the pore, gets photodeposited, and contributes to the photocatalysis inside the pore.

Last but not least, the role of residual palladium was tested for its hydrogen evolution contribution. Due to the comparison of the polymers synthesised *via* the acid-catalysed route and the palladium catalysis, palladium was identified to act as a co-catalyst in CTFs. An improvement of the hydrogen evolution rate could nevertheless be achieved by photodeposited platinum on the polymer, showing that platinum is the best co-catalyst choice for CTFs.

7 A library of 40 CTFs

The Suzuki-Miyaura cross-coupling reaction is widely used in organic synthesis due to its high functional group tolerance.[167] Recently, it was further introduced in the synthesis of polymeric photocatalysts for water splitting.[17,59,88,92,93] As shown in chapter 6, covalent triazine-based frameworks can also be cross-coupled using the Suzuki-Miyaura polycondensation and CTF-2 Suzuki, CTF-3 Suzuki, and CTF-4 Suzuki were found to split water under sacrificial conditions using water/TEA/MeOH with 3 wt.% Pt.[124] The monomer 2,4,6-tris[4-(4,4,5,5-tetramethyl-1,3,2-dioxaborolan-2-yl)phenyl]-1,3,5-triazine (TBPT) used to synthesise CTF-2 Suzuki is an ideal building block as it allows the cross-coupling of a range of dibromo-linkers to the triazine containing monomer, and offers a wide synthesis scopeIn contrast, the synthesis of each boronic ester from each dibromo compound selected for a library would be a time-consuming approach. . This synthesis route offers the possibility to investigate a variety of CTFs that are not exclusively based on phenylene to quarterphenylene linkers in between the triazines.

In this chapter, the synthesis of a library consisting of 40 CTFs is described. With this uniquely large screen of polymeric photocatalysts, comparisons can be carried out regarding the functional groups incorporated, as well as the use of heterocycles as structural linkers can be investigated. The resulting polymers were tested for their optical properties, hydrogen evolution performances from water under sacrificial conditions, and investigated by computational studies. Figure 24 shows an overview of CTF-3 and CTF-4 analogues that can be targeted to create a structurally diverse set of CTFs.

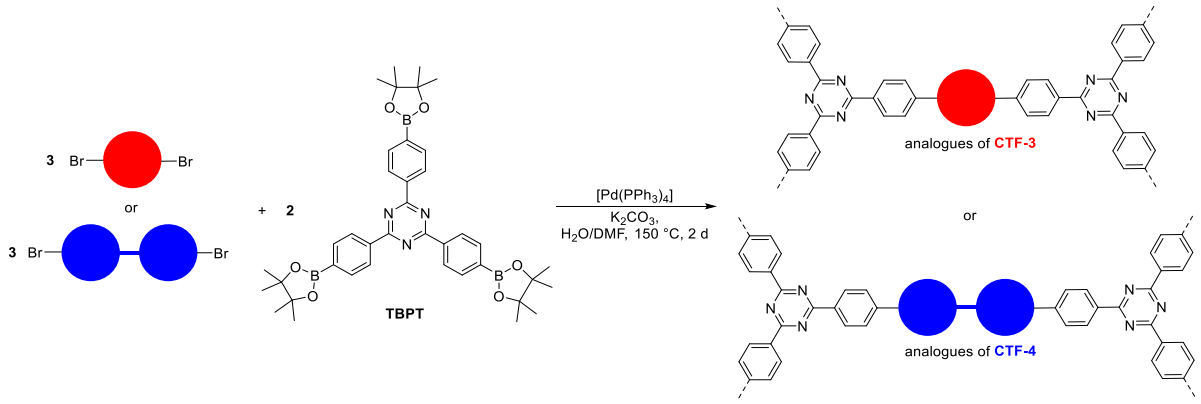

Figure 25: Synthesis of a library of 40 CTFs (abbreviation CTF-xx) with the Suzuki-Miyaura polycondensation protocol that represent structural analogues of CTF-3 and CTF-4.

Parallel syntheses with five polymerisations were carried out a total of eight times to achieve 40 CTFs in reaction stations that offer five heating positions for round bottom flasks (Radleys carousels). The

polymers are named CTF-5 to CTF-44 and are synthesised from the monomers M5 to M44, as shown in Figure 26. The dibromo-monomer used in the synthesis is given behind each abbreviation (i.e. CTF-5 was synthesised from M5) to allow the easy identification of the polymeric structures. Structurally similar linkers are grouped in to subsets: a benzene subset, a 5-membered ring heterocycle subset, a substituted benzene subset, a bipyridyl subset, a *N*-heterocycle subset, a planar fluorene-like subset, and an azoles and quinoxaline subset. The Suzuki-Miyaura polycondensation to synthesise all materials used the catalytic system $[Pd(PPh_3)_4]/K_2CO_3$/water/DMF at 150 °C. No optimisation of the reaction conditions was performed for any of the monomers, and because of this, the yields vary. Overall, based on the linker used, 22 polymers were obtained in good yield exceeding 90%, and 16 polymers were obtained in reasonable yields in the range of 37–87%. The lowest yielding reactions were CTF-23 (2,5-dibromo-1,4-benzoquinone) with a yield of 21%, and CTF-24 (2,5-dibromobenzene-1,4-diol) with a low yield of 11% (Table 15, appendix p. 143) – however, enough material was still obtained for characterisation and subsequent screens of their hydrogen evolution performance.

Previous examples of CTFs:

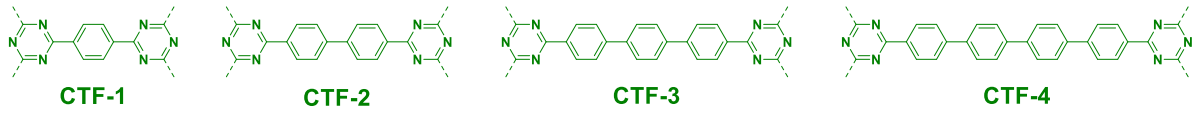

benzenes:

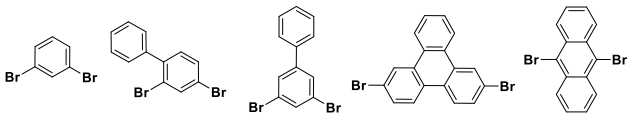

(M5) (M6) (M7) (M8) (M9)

5 membered ring heterocycles:

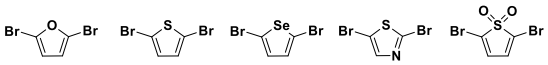

(M10) (M11) (M12) (M13) (M14)

substituted benzenes:

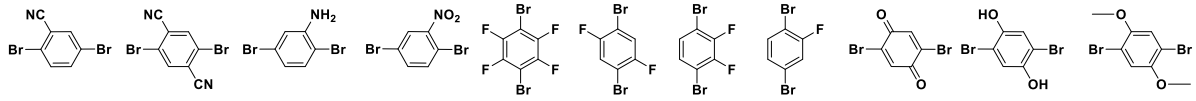

(M15) (M16) (M17) (M18) (M19) (M20) (M21) (M22) (M23) (M24) (M25)

bipyridyls:

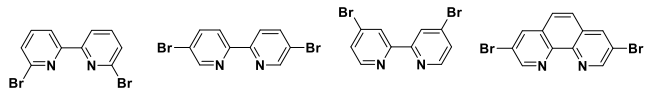

(M26) (M27) (M28) (M29)

***N*-heterocycles:**

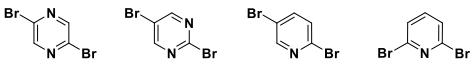

(M30) (M31) (M32) (M33)

planar systems:

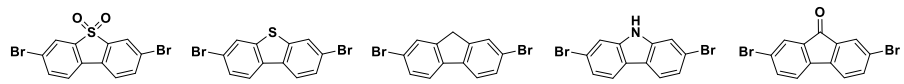

(M34) (M35) (M36) (M37) (M38)

azoles and quinoxaline:

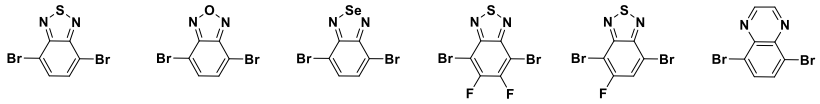

(M39) (M40) (M41) (M42) (M43) (M44)

Figure 26: Overview of the dibromo monomers M5-M44 used to synthesise the polymers CTF-5 to CTF-44. The dibromo compounds are categorised in subsets according to their structural similarity.

7.1 Characterisation of functionalised CTFs

The library of polymers was then characterised so a dataset analysis could be performed regarding underlying trends or factors relating to the hydrogen evolution performance of the CTFs (Table 15, p. 143 to Table 17, p. 146 appendix). The analysis included Fourier-transform infrared spectroscopy (FT-IR), powder X-Ray diffraction (PXRD), thermogravimetric analysis (TGA), UV-Vis spectroscopy, fluorescence spectroscopy, fluorescence life-time, water contact angle measurements, transmission

in water, transmission in a solution of water/TEA/MeOH, and nitrogen adsorption/desorption to probe their porosity.

7.2 FT-IR, PXRD and TGA analysis of the polymers

Initially, the polymers were characterised by FT-IR spectroscopy to ensure the incorporation of the linkers had occurred during synthesis. In the FT-IR spectra, strong vibrations were found for all polymers around 1510 and 1360 cm^{-1}, which are characteristic for aromatic C=C bending modes. For the carbonyl bridge head in CTF-38 (2,7-dibromo-9-fluorenone), the strong vibration at 1710 cm^{-1} could be assigned. CTF-15 (2,5-dibromobenzonitrile) and CTF-16 (2,5-dibromo-1,4-benzenedicarbonitrile) show two characteristic bands at 2226 cm^{-1} and 2228 cm^{-1}, respectively, that can be assigned to the aromatic nitriles. The phenol linker in CTF-24 (2,5-dibromobenzene-1,4-diol) shows a broad peak around 3430 cm^{-1}. Figure 27 shows the FT-IR spectra of the polymers mentioned and confirms the co-polymerisation of TBPT with the dibromo-monomers.

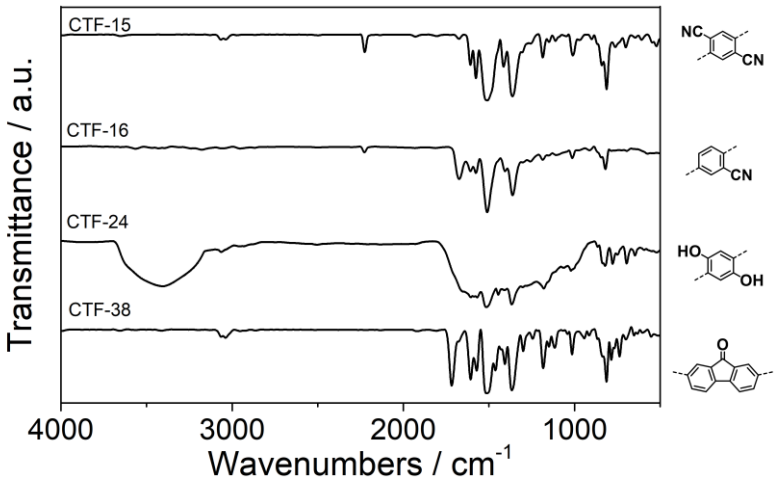

Figure 27: FT-IR spectra of four CTFs that show modes of their linkers.

PXRD analysis was then carried out to probe the crystallinity of the samples – the recorded PXRD spectra appear featureless and revealed the formation of amorphous polymers. A broader shoulder can be found in the spectra of the polymers CTF-8 (2,7-dibromotriphenylene), CTF-14 (2,5-dibromothiophene dioxide), CTF-30 (2,5-dibromopyrazine), CTF-31 (2,5-dibromopyrimidine), CTF-34 (3,7-dibromo-dibenzothiophene-*S,S*-dioxide), CTF-35 (3,7-dibromo-dibenzothiophene), CTF-40 (4,7-dibromobenzo[*c*][1,2,5]oxadiazole), and CTF-42 (4,7-dibromo-5,6-difluorobenzo[*c*][1,2,5]thiadiazole. These findings rule out the formation of covalent organic frameworks with characteristic long-range order peaks below $2\theta = 10°$ and suggest that the material forms a more complex network. An explanation is the non-reversibility of the palladium catalysed synthesis route (subsection 6.9) that is

not known to form crystalline materials.[141,142,168] Figure 28 shows three examples of PXRD-spectra – CTF-14 (2,5-dibromothiophene dioxide), CTF-15 (2,5-dibromobenzonitrile), and CTF-34 (3,7-dibromo-dibenzothiophene-*S,S*-dioxide).

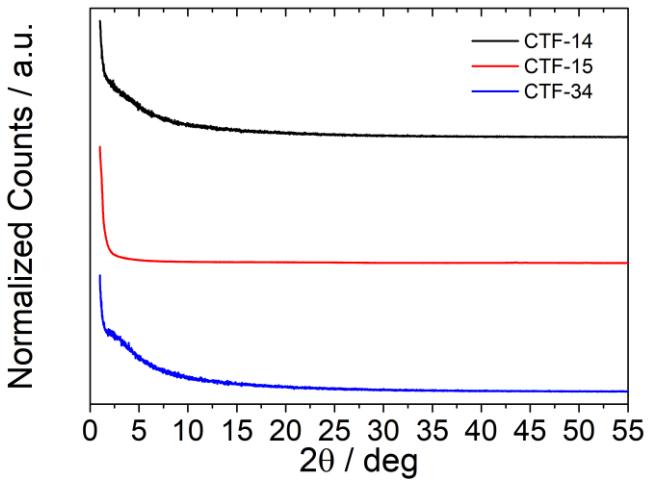

Figure 28: Normalised PXRD-spectra of three CTFs in the library.

TGA analysis was then carried out under air and confirmed the formation of polymers in comparison with the on-set temperatures of the monomers, with all also showing good thermal stability (compare Table 15, p. 143 appendix). Generally, most of the polymers were stable up to 400 °C, e.g. CTF-15 (2,5-dibromobenzonitrile) was thermally stable up to 412 °C. In comparison, common building block 2,4,6-tris[4-(4,4,5,5-tetramethyl-1,3,2-dioxaborolan-2-yl)phenyl]-1,3,5-triazine (TBPT) was measured with a decomposition temperature of 333 °C, 2,4,6-triphenyl-1,3,5-triazine (TPT) with 218 °C, and all dibromo-monomers below 249 °C. (Table 15, p. 143 and Table 18, p. 147, appendix).

However, three of the polymers rapidly degraded under heating in air. Polymer CTF-25 (1,4-dibromo-2,5-dimethoxybenzene) was found to have a weight loss of 29% in the temperature range of 381 - 394 °C, possibly caused by the weight loss of the methyl or methoxy group. For CTF-23 (2,5-dibromo-1,4-benzoquinone) and CTF-24 (2,5-dibromobenzene-1,4-diol), the loss was determined to be 40% and 37% at 300 °C, respectively. Both results indicate a low degree of polymerisation and are potentially related to the non-optimised catalysis conditions for these two systems – potentially caused by a slow oxidative addition to the palladium catalyst, while slow transmetalation is also seen as a reason for low yields of catalysis.[128] In contrast, dibromodimethoxybenzene does give polymer CTF-25 in 98% yield, but shows a strong weight loss of 35 % at 370 °C, potentially through the loss of a methyl or methoxy-group (compare Figure 29). It is worth noting that others have carried out Suzuki-Miyaura cross-couplings on tetrabromo-*p*-benzoquinones[169] with different catalytic systems that

improved the yields, but this was outside the scope of this study. If the polymers CTF-23 and CTF-24 were particularly good at hydrogen evolution, the synthetic route could be revisited and optimised at a later date.

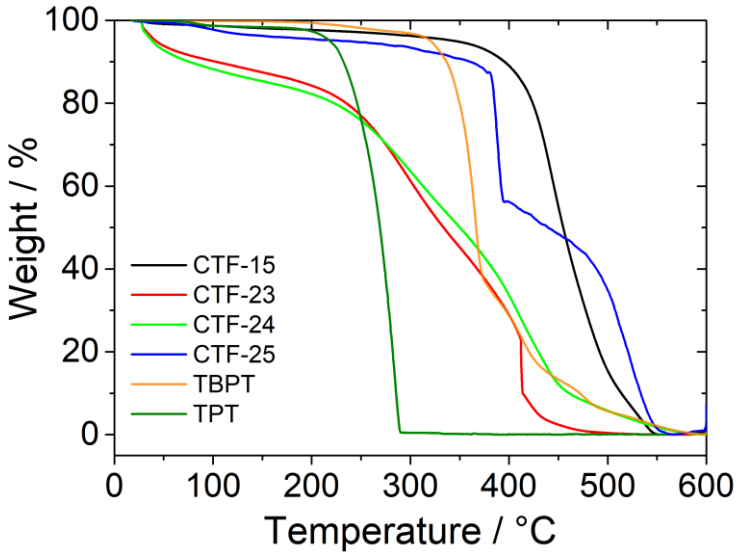

Figure 29: Thermogravimetric analysis curves for CTF-15 (2,5-dibromobenzonitrile), CTF-23 (2,5-dibromo-1,4-benzoquinone), CTF-24 (2,5-dibromobenzene-1,4-diol), CTF-25 (1,4-dibromo-2,5-dimethoxybenzene), and the monomer 2,4,6-tris[4-(4,4,5,5-tetramethyl-1,3,2-dioxaborolan-2-yl)phenyl]-1,3,5-triazine (TBPT) in air with a heating rate of 10 °C min^{-1}. For comparison, 2,4,6-triphenyl-1,3,5-triazine (TPT) is also shown and has a lower thermal stability than its borylated version.

7.3 Spectroscopic results, hydrophobicity and surface areas

UV-Vis absorption spectroscopy was then measured in the solid-state and the on-set was used to determine the band-gaps of the CTFs (linear extrapolation of the tangent line along the maximum change of absorption to determine the intersection with the wavelength). Interestingly, CTF-28 (4,4'-dibromo-2,2'-bipyridine) exhibited two on-sets that were calculated to be 2.96 eV and 1.61 eV, respectively. The lowest band-gap was determined for CTF-37 (2,7-dibromo-9*H*-carbazole) at 1.52 eV, while CTF-26 (6,6'-dibromo-2,2'-bipyridine) showed the widest band-gap of 3.08 eV. Overall, 30 polymers of the library (75%) had band-gaps in the region of 1.95 - 2.70 eV (Table 15, appendix, p. 143). Compared to the monomer on-sets measured by UV-Vis spectroscopy, most polymers showed a red-shift in their absorption (Table 15, p. 143 and Table 18, p. 147, appendix) and therefore further confirm the polymerisation had successfully occurred.

All polymers were weakly fluorescent and photoluminescence measurements were measured for 30 polymers with an excitation wavelength of λ_{ex} = 280 nm, with the peak maximum being detected between 400-501 nm. The remaining ten polymers were excited with an excitation wavelength of λ_{ex}=360 nm, and the maximum were measured between 530-581 nm (Table 15, p. 143 appendix).

Fluorescence life-time measurements were carried also out using time-correlated single photon counting in the solid-state (Table 15, p. 143, appendix). The data was fitted with an exponential decay of three life-times and the average life-times were found to be short (below 5.0 ns) for all polymers measured, with the exception of CTF-2 which had an average weighted life-time of 7.7 ns. For comparison, graphitic carbon nitride was also measured (commercially available Nicanite) and was found to have a short life-time of 0.7 ns, while synthesised bulk g-C_3N_4 was reported to have a slightly longer life-time with 2.7 ns.[170] The longest average life-times in this library were observed for CTF-33 (2,6-dibromopyridine) with 4.4 ns, CTF-16 (2,5-dibromo-1,4-benzenedicarbonitrile) and CTF-23 (2,5-dibromo-1,4-benzoquinone) with 3.0 ns, and CTF-6 (2,4-dibromo-1,1'-biphenyl) with 2.9 ns. Figure 30 shows an example of the measurement.

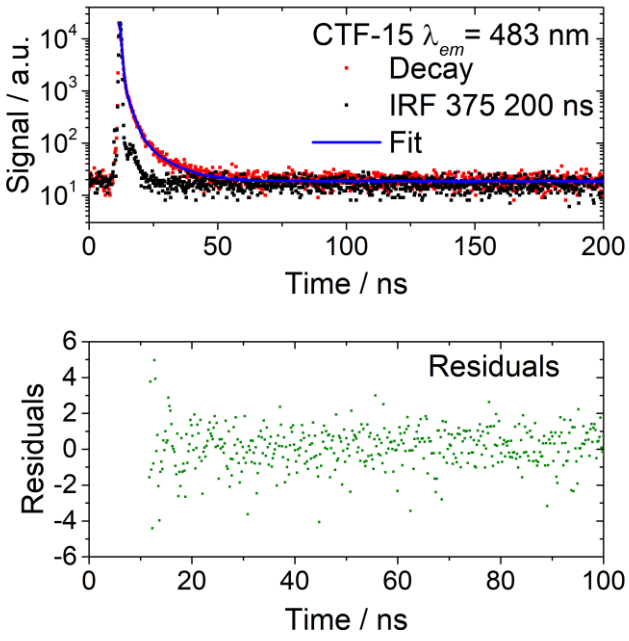

Figure 30: Time-correlated single-photon counting measurement of CTF-15 (2,5-dibromobenzonitrile) in the solid-state with λ_{ex} = 371 nm and λ_{em} = 483 nm.

Contact angle measurements were then performed with water and pressed pellets of the CTFs. Contact angles were measured in the range of 55° for CTF-14 (2,5-dibromothiophene dioxide) up to 106° for CTF-39 (4,7-dibromo-2,1,3-benzothiadiazole). For 12 of the polymers, swelling was found to occur in contact with water (Figure 31), indicating a strong interaction between the solvent and the polymer, *i.e.* the water droplet was absorbed by the porous polymer after it was dispensed. In these cases, no contact angle could be assigned (Table 15, p. 143 appendix). As the polymer is expanding during contact with water, it is likely that isotropic swelling is occurring that could increase the pore volume.[171,172] This could possibly lead to an improved permeability of water and scavengers, although capillary forces could retain solvent molecules in the pores and therefore decrease the diffusion of

solvents.[171] A comparison between CTF-3 Suzuki, CTF-15 (2,5-dibromobenzonitrile), and CTF-16 (2,5-dibromo-1,4-benzenedicarbonitrile) is shown in Figure 31. In short, a contact angle of 56 ± 3° was measured for CTF-3 Suzuki, while no contact angle was measured due to swelling when nitrile groups were introduced to the linkers (CTF-15 – mononitrile, and CTF-16 – dinitrile).

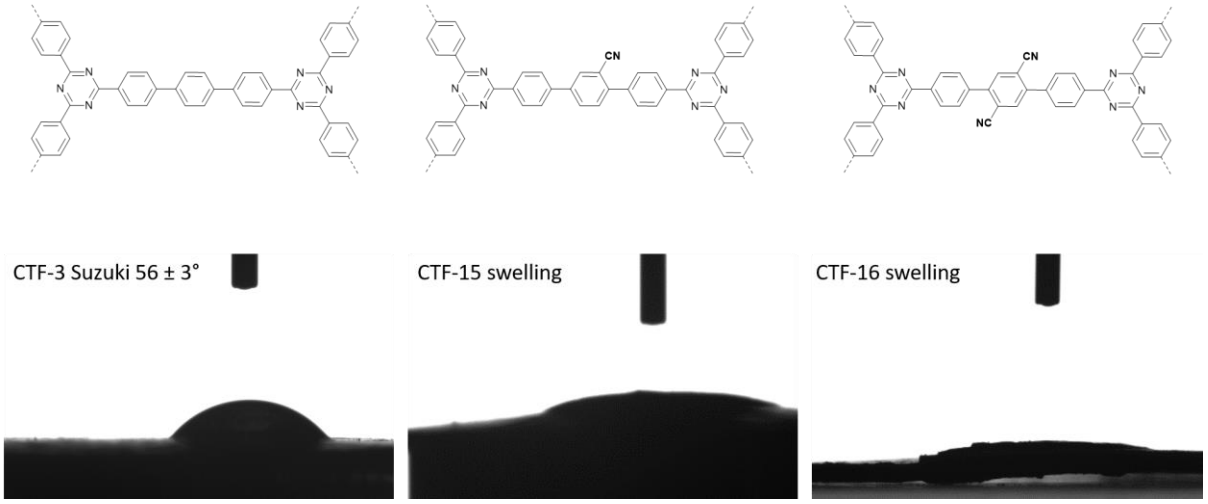

Figure 31: Contact angle measurements on three polymeric examples: While CTF-3 Suzuki showed a contact angle with 56 ± 3°, CTF-15 (2,5-dibromobenzonitrile), and CTF-16 (2,5-dibromo-1,4-benzenedicarbonitrile) swelled in contact with water.

Furthermore, the average transmission of the materials were analysed in water and in a water/TEA/MeOH mixture using an 880 nm light source (Turbiscan Formulaction). The polymer were dispersed in the solution using an ultrasonic bath before the measurement, and an average transmission in the height from 4-30 mm was determined to exclude floating and settled polymer particles (solvent height in vial: 1-35 mm). The average transmission was measured between 3.1-85.2% in water and 0.8-59.4% in a solution of water/TEA/MeOH (Table 15, p. 143 appendix).

Finally, all CTFs were tested for nitrogen adsorption/desorption to probe their porosity at 77 K. The apparent Brunauer-Emmett-Teller surface area (SA_{BET}) can divided into six categories: < 100 $m^2 g^{-1}$ (14 polymers); 100-200 $m^2 g^{-1}$ (10 polymers); 200-300 $m^2 g^{-1}$ (4 polymers); 300-400 $m^2 g^{-1}$ (4 polymers), 400-500 $m^2 g^{-1}$ (5 polymers); and > 500 $m^2 g^{-1}$ (5 polymers). The highest SA_{BET} of 708 $m^2 g^{-1}$ was found for CTF-9 (9,10-dibromoanthracene), and a complete overview can be found in Table 15, p. 143 appendix.

7.4 Hydrogen evolution analysis

With a library of 40 polymers in hand, the CTFs were tested for photocatalytic hydrogen evolution from water in the presence of triethylamine as sacrificial hole-scavenger and loaded *in situ* with 3 wt. % platinum as co-catalyst. Initially, all polymers were tested with a 300 W xenon lamp equipped

with a λ > 420 nm cut-off filter, and all materials, with the exception of CTF-24 (2,5-dibromobenzene-1,4-diol) and CTF-41 (4,7-dibromo-2,1,3-benzoselenadiazole), were found to produce hydrogen under these conditions with hydrogen evolution rates from 0 to nearly 3000 µmol g^{-1} h^{-1}. The best three materials were CTF-15 (2,5-dibromobenzonitrile) with a HER of 2943 ± 381 µmol g^{-1} h^{-1}, CTF-34 (3,7-dibromo-dibenzothiophene-*S,S*-dioxide) with 2373 ± 25 µmol g^{-1} h^{-1}, and CTF-30 (2,5-dibromopyrazine) with 1561 ± 150 µmol g^{-1} h^{-1}. Figure 32 and Table 16, p. 145 in the appendix summarise the data. A summary of the properties for the best photocatalyst are given in subsection 7.12, p. 94.

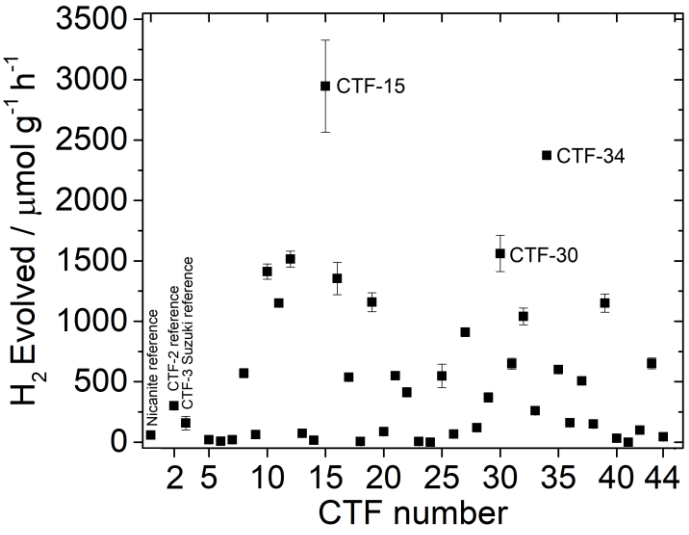

Figure 32: Overview of the hydrogen evolution rates for the CTF library. The analysis was measured with 25 mg photocatalyst in water/TEA/MeOH (1:1:1) and 3 wt. % platinum co-catalyst under λ > 420 nm irradiation. CTF-15 (2,5-dibromobenzonitrile), CTF-34 (3,7-dibromo-dibenzothiophene-*S,S*-dioxide), and CTF-30 (2,5-dibromopyrazine) are assigned as the three best photocatalysts.

The analysis of hydrogen evolution rates is rather time consuming if carried out on for a large number of samples, such as the 40 polymers in this CTF library. Including preparation steps, more than six hours were required to measure a single sample manually. Therefore, a high-throughput measurement capability was used to test the library – Figure 33 shows the overall workflow alongside some of the equipment used in the lab.

Briefly, water or aqueous solutions containing the desired sacrificial reagent were added to the reaction vials containing the pre-weighed solid photocatalysts (5 ± 0.5 mg). The solutions were added using a Chemspeed liquid handling robotic platform that is purged with nitrogen for six hours prior to the experiment to ensure an inert atmosphere. The vials are then capped inside the platform under nitrogen, and sonicated for 10 min before photolysis. A solar simulator (spectral match A, spatial

uniformity of irradiance A, temporal stability A, AM 1.5G filter) allows simultaneous illumination of 48 vials (46 samples and 2 blanks). The powdered catalysts are kept dispersed throughout the illumination by a continuous agitation using a roller/rocker device. Following illumination for 2 hours, the vials were loaded into a GC with an autosampler, and single headspace measurements for the analysis of the hydrogen evolution were carried out. Calibration gas measurements were carried out to enable conversion of the measured peak area output of the GC to the HER in µmol g^{-1} h^{-1} (**Error! Reference source not found.**, appendix).

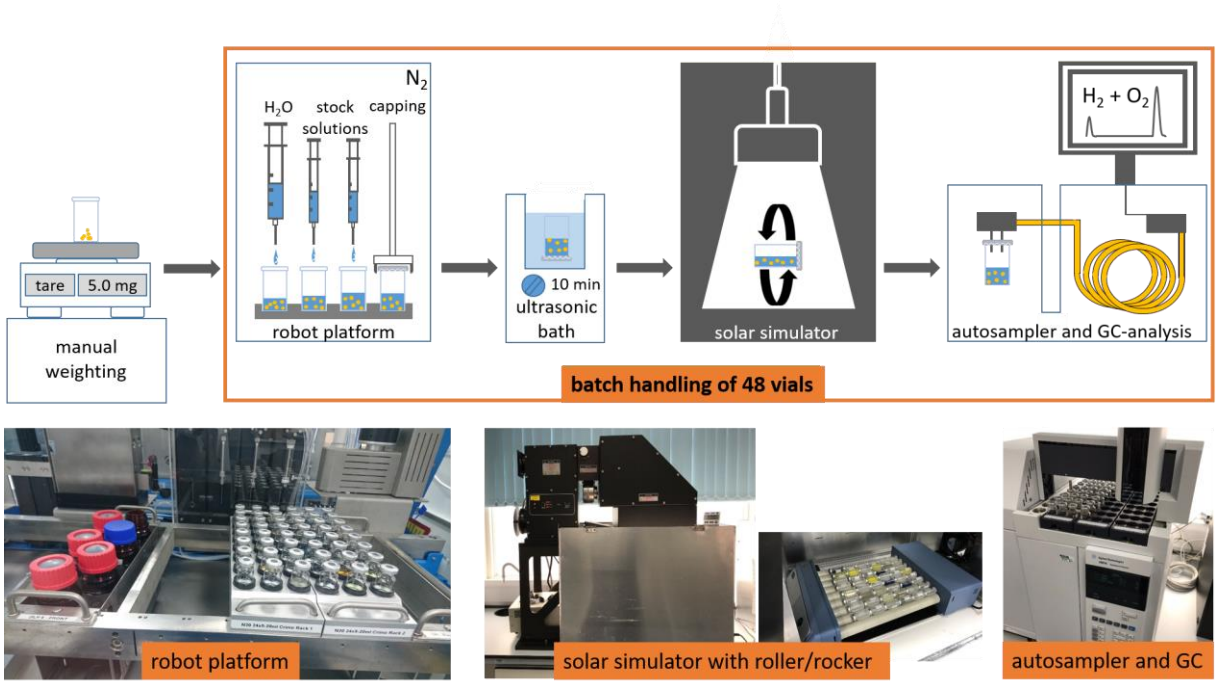

Figure 33: High-throughput workflow to test hydrogen production for powdered photocatalysts under nitrogen atmosphere. As currently configured, this setup can be used to characterize 46 samples and 2 blanks per run.

The illumination was carried out for no more than two hours to avoid saturation of the helium ionisation detector of the GC, while the system is used by multiple users in parallel (no change of the injection volume and no use of a split system possible). Overall, it was found that there is a good correlation between: The two highest-performing polymers, CTF-15 (2,5-dibromobenzonitrile) and CTF-34 (3,7-dibromo-dibenzothiophene-*S,S*-dioxide), are clearly identified by both the high-throughput technique and the manual HER measurements (Figure 34).

The illumination of the solar simulator starts from λ > 328 nm and allows UV-light to contribute to the photocatalysis experiments. In contrast, manual measurements were carried out on all 40 polymers to benchmark the HT-method with a λ > 420 nm cut-off filter (**Error! Reference source not found.**, appendix). It was found that polymers that are predominantly active under λ = 328-420 nm showed a much higher hydrogen evolution rate under the solar simulator, as might be expected. Examples are

CTF-5 and CTF-6 with a 26 fold increase in hydrogen evolution under solar simulated light, while CTF-15 and CTF-34, for example, showed 59 and 65% reduction respectively in the hydrogen evolution rates in comparison to the manual measurement under $\lambda > 420$ nm irradiation (Figure 34). An explanation can be found in the output of the xenon lamp with more than 1.0 sun, and the activity of the polymer in the visible region of the spectrum.

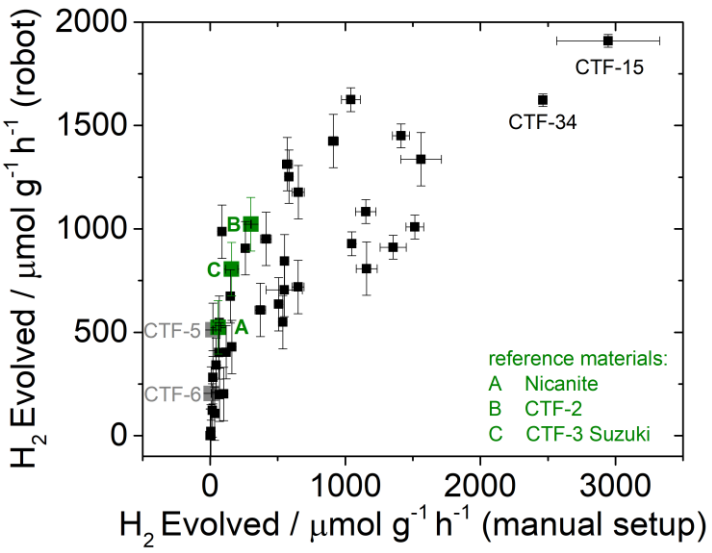

Figure 34: Analysis of hydrogen evolution rates for the CTF library: comparison of a manual measurements for five hours (x-axis) with high-throughput robotic measurements for two hours (y-axis). Commercially-sourced carbon nitride (Nicanite), CTF-2 as benchmark CTF, and CTF-3 Suzuki are also shown (manual run: 25 mg photocatalyst, 5 h measurement – robot run: 5 mg photocatalyst, 2 h measurement). Conditions: water/TEA/MeOH (1:1:1) with 3 wt. % Pt co-catalyst. The photocatalysts CTF-15 and CTF-34 are labelled and could be identified by both methods as the best two photocatalysts, while for example CTF-5 and CTF-6 show lower hydrogen evolution rates measured on the manual setup than on the high-throughput robotic measurements.

7.5 Advantages and limitations of the high-throughput setup

The advantage in using the high throughput methodology is the large time saving: the measurement is around 18 times faster than the sequential, manual measurements for the library of 40 polymers (time for manual runs: [1 h preparation + 5 h illumination] x 40 samples = 240 h without down-time between sequential measurements; time for robot run: 1 h preparation, 6 h degas of the HT-setup, 4 h robot dispensing, 2 h illumination = 13 h for 40 samples ≈ 20 min/sample). As this HT work-flow can measure a large amount of samples, the synthesis of the polymers are limiting the amount of samples that can be tested. This limitation can be avoided if the synthesis is either optimised changed, e.g. by producing the polymers also in the robotic platform by thermal or microwave synthesis.

For the requirement of repeated measurements to ensure reproducibility, this time would increase to 40 min per polymer. It could be argued that a quick screen can be done with only a single point

measurement on the manual setup as well, which would still require 1 h of preparation and 1 hour of measurement, adding up to a total of 80 hours, and still exceed the time required in the HT screen.

Apart from the advantages of rapid screening, the detection limit of the HT-setup excludes highly active materials from kinetic measurements. To overcome this limitation, the more active photocatalysts can be re-measured over shorter time scales to avoid saturation of the detector. Further, the HER determined by the HT measurement does not match the result of the hydrogen evolution rate measured using the manual setup. As an example, CTF-36 (2,7-dibromofluorene) was found to have a hydrogen evolution rate of 160 ± 13 µmol g^{-1} h^{-1} from water/TEA/MeOH (1:1:1) with 3 wt.% co-catalyst when tested on the manual setup (Figure 35). After a slow increase for 4 h, a linear HER was observed from 4 h to 7 h. In contrast, the kinetic run on the HT-setup (Figure 35) reveals a linear increase up to three hours with a HER of 554 ± 139 µmol g^{-1} h^{-1}, followed by a saturation up to 5 h.

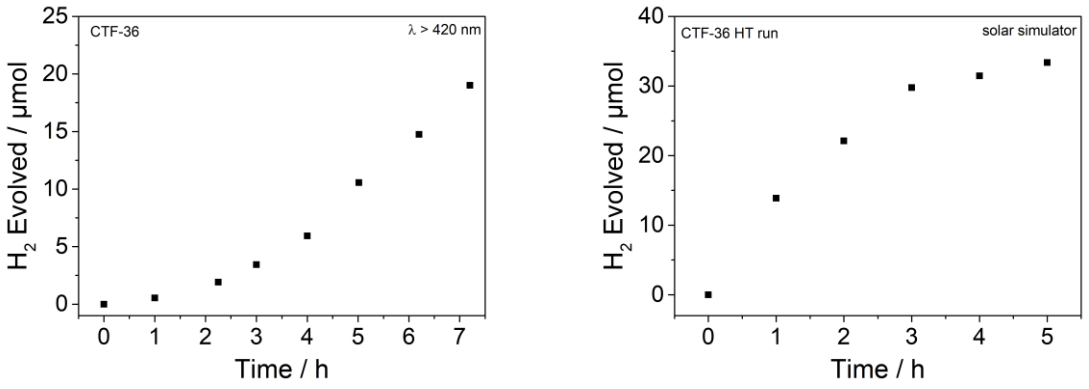

Figure 35: Comparison of hydrogen evolution rates for CTF-36 on the manual setup and the HT setup. The measurements were carried out in water/TEA/MeOH with 3 wt. % platinum. For the manual run, 25 mg CTF-36 was used, and for the HT run, 5 mg of CTF-36 was used. The data shown in the HT run has been normalised to a quantity of 25 mg to enable direct comparison.

There are a number of reasons why there might not be a linear correlation between the two measurement techniques. First, the two light sources are different; specifically, the certified solar simulator with a normalised intensity output of 1.00 sun, the spectral match over six spectral ranges in the region between λ = 400-1000 nm, and the temporal (AAA solar simulator). By setting the positioning the vials to the required working distance of 300 mm, the uniformity of the illumination was found to be 1.00 ± 0.02 sun in the 12x12 inch illuminated area. By contrast, the xenon lamps have a non-normalised output , even when using a λ > 420 nm filter is used and are expected to give a higher light intensity than the solar simulator (**Error! Reference source not found.**, appendix and **Error! Reference source not found.**, appendix). Second, the headspace volumes in the reactors are different; 6.9 mL in the high-throughput vials (2.35 times the solvent volume) *vs.* 46 mL in the manual

measurements (1.84 times the solvent volume). Third, the agitation methods are different in the two experiments (rolling/rocking *vs.* magnetic stir bar), which may affect sample dispersal and the interaction of the catalyst particles with the incident light.

7.6 HT scavenger screening of the best photocatalyst CTF-15

The low quantity of photocatalyst required to test hydrogen evolution in the HT setup offered the possibility to study various scavenger systems in combination with the platinum co-catalyst and the best performing photocatalyst CTF-15 (2,5-dibromobenzonitrile). The results show that CTF-15 achieves the highest performance with a HER of 1909 µmol g^{-1} h^{-1} in the scavenger system water/TEA/MeOH, followed by 5 vol. % TEA in water with a performance of 1830 µmol g^{-1} h^{-1} (Figure 36). Further, ascorbic acid and sodium sulfide showed moderate hydrogen evolution rates of 116 µmol g^{-1} h^{-1} and 139 µmol g^{-1} h^{-1}, respectively. Performances of 101 µmol g^{-1} h^{-1}, 82 µmol g^{-1} h^{-1}, and 77 µmol g^{-1} h^{-1} were detected for EDTA, L-cysteine and thiophenol, while iron(II) chloride, methanol, phenol and hydroquinone did not act as hole scavengers.

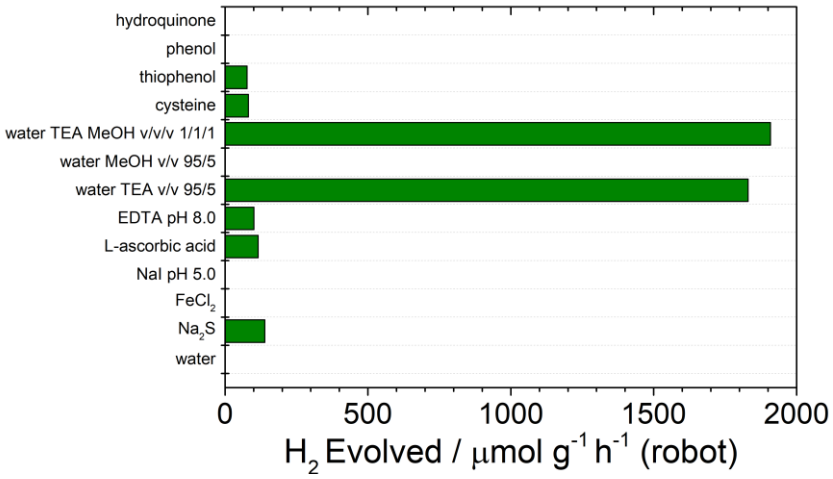

Figure 36: Scavenger screening for CTF-15 tested on the HT-setup. Conditions: 5.1 mL solvent and 5 ± 0.5 mg CTF-15. The concentration of the scavenger solution was 0.2 M unless stated otherwise.

7.7 Scavenger influence on the photocatalytic activity

The hydrogen evolution rates in water/MeOH/TEA with platinum co-catalyst of CTF-15 (2,5-dibromobenzonitrile) and CTF-34 (3,7-dibromo-dibenzothiophene-*S,S*-dioxide) are around 2900 and 2300 µmol g^{-1} h^{-1}, while CTF-16 (2,5-dibromo-1,4-benzenedicarbonitrile) shows a rate of around 1400 µmol g^{-1} h^{-1}. The most active material CTF-15 (2,5-dibromobenzonitrile) is an analogue of CTF-3 Suzuki which allows comparisons to this reference material (Figure 37). The additional cyano-group in the linker unit of CTF-15 (2,5-dibromobenzonitrile) was found to improve the hydrogen evolution rate

19 fold. One could assume the increase of cyano-groups at the linker unit could lead to a better performance in water/TEA/MeOH scavenger solution with platinum co-catalyst, but the results for CTF-16 using *para*-dicyanobenzene shows a decrease in performance by over 50%.

The dependance of the HER could be scavenger related, as the scavenger solutions are expected to wet the polymers differently. Water/TEA/MeOH, sodium sulfide, and ascorbic acid were compared using the HT-setup and transmission measurements were carried out (Figure 38). The standard reduction potentials *vs.* the standard hydrogen electrode SHE at pH 7.0 of the parent sacrificial donor are: -0.38 eV for TEA,[59] -0.46 eV for ascorbic acid,[173] and -0.45 eV for sodium sulfide.[174] For ascorbic acid and sodium sulfide, the pH values were measured to be 2.5 and 12.9, respectively.

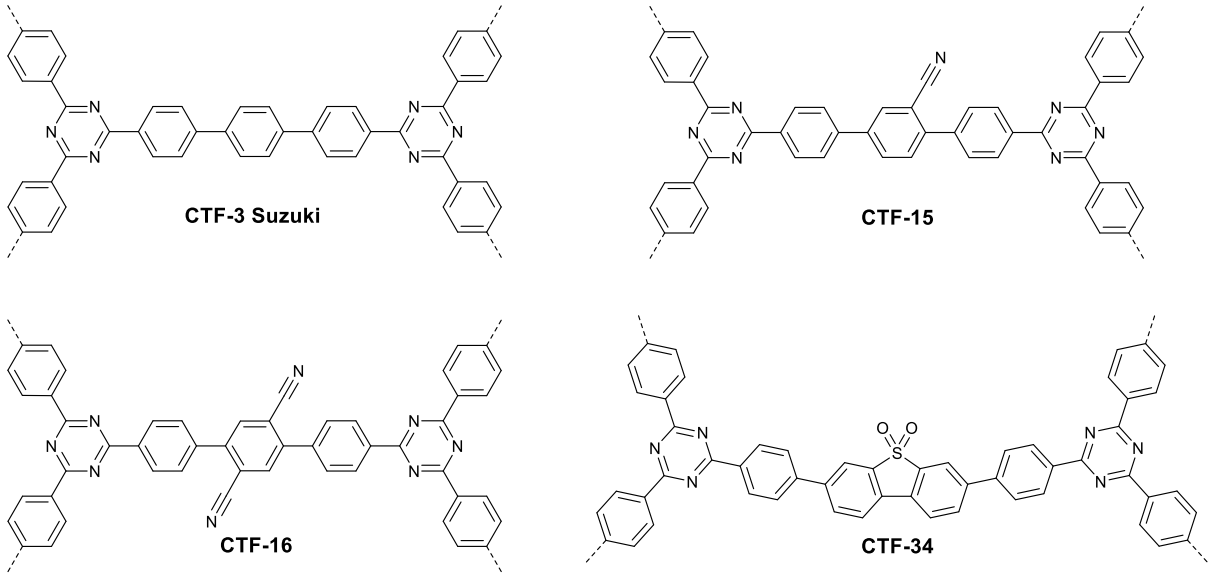

Figure 37: Overview of the four CTFs tested in the scavenger screen. CTF-3 Suzuki was used as reference material.

For water/TEA/MeOH, the parallel HT-study confirmed the decreasing series that was also observed in the manual study carried out in quartz flasks (Figure 38): CTF-15 (1979 µmol g^{-1} h^{-1}) > CTF-34 (1910 µmol g^{-1} h^{-1}) > CTF-16 (1039 µmol g^{-1} h^{-1}) > CTF-3 Suzuki (939 µmol g^{-1} h^{-1}). On switching to sodium sulfide, the hydrogen evolution rates were lower for all four CTFs tested, but CTF-34 was the best performing polymer with an evolution rate double that of the evolution rate of CTF-15 (650 and 325 µmol g^{-1} h^{-1}, respectively), which could be caused by wettability effects. Further, CTF-16 only shows 3% of the activity of CTF-15 in sodium sulfide and CTF-3 Suzuki did not act as photocatalyst in this scavenger solution. When using L-ascorbic acid as a scavenger, again CTF-15 outperformed CTF-34 with HER of 352 and 192 µmol g^{-1} h^{-1}, respectively. Lower HERs of 12 µmol g^{-1} h^{-1} were observed for CTF-16, and 0 µmol g^{-1} h^{-1} for CTF-3 Suzuki.

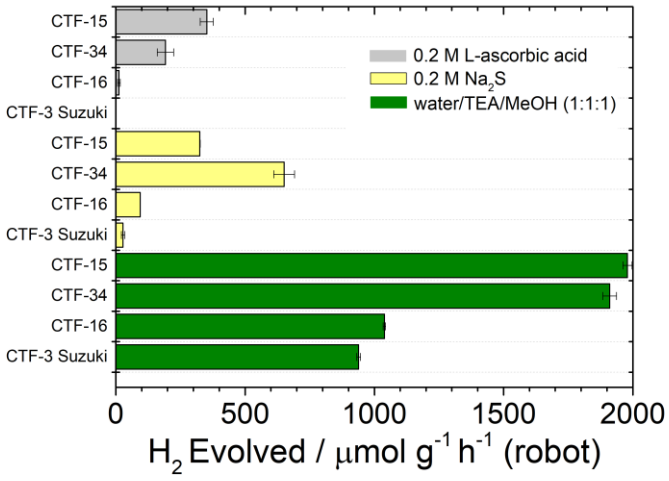

Figure 38: Scavenger screen for four polymers on the HT-setup. Conditions: 5.1 mL solvent and 5 ± 0.5 mg photocatalyst with 3 wt. % Pt in duplicated runs.

The transmission of the polymers were analysed in the scavenger systems with the average transmission measurement as described previously (subsection 7.3). The average transmission was measured in water/TEA/MeOH to be 0.8, 5.6, 0.8, and 26.8%, for CTF-15, CTF-16, CTF-34, and CTF-3 Suzuki, respectively. Higher average transmissions were detected when 0.2 M L-ascorbic acid was used with values of 29.4, 14.3, 57.2, and 49.1% for CTF-15, CTF-16, CTF-34, and CTF-3 Suzuki. In sodium sulfide, average transmissions of 23.1, 15.7, 24.9, and 25.7%, were observed for CTF-15, CTF-16, CTF-34, and CTF-3 Suzuki. For a summary of the measurements carried out on the four systems see Table 7, page 78.

From the screen, it can be seen that the reaction solution water/TEA/MeOH disperses the four CTFs more efficiently than either L-ascorbic acid or sodium sulfide, up to a 72 fold increase in the case of CTF-34 in L-ascorbic acid. The lowest average transmissions were found for the best performing polymers CTF-15 and CTF-34 with T = 0.8% (Table 7). CTF-15 is also much better dispersed in L-ascorbic acid than CTF-34 (T = 29.4% *vs.* T = 57.2% - Table 7), which could explain the improved hydrogen evolution rate of 352 µmol g^{-1} h^{-1} *vs.* 12 µmol g^{-1} h^{-1}, respectively. A strong correlation between the polymers dispersibility and the average transmission could not be found, as for example CTF-16 works better in sodium sulfide than CTF-15 (651 µmol g^{-1} h^{-1} *vs.* 325 µmol g^{-1} h^{-1}) with average transmission values of 15.7% and 23.1%, while the difference in the average transmission of CTF-16 and CTF-14 remains rather small at 24.9% and 25.7%, respectively. In L-ascorbic acid even, the better dispersed polymer CTF-16 shows a lower hydrogen evolution rate than CTF-15 (Table 7). Although the proton concentration is higher in ascorbic acid, a drastic decrease of the hydrogen evolution rates was detected. The pH dependency of the hydrogen evolution rates and higher performance under basic

conditions has been reported previously,[94,175] but no measurements of the dispersibility were investigated in these studies. The variety of hole scavengers such as alcohols, amines, and sufide/sulfite salts[59,106] used, show the search for optimal scavengers to find the most promising photocatalysts.

Table 7: Overview of CTFs in different scavenger systems regarding their average transmission and hydrogen evolution rates.

Polymer	Linker	Average Transmission / %			H_2 Evolved / µmol g^{-1} h^{-1}		
		water/TEA/ MeOH	0.2 M L-ascorbic acid	0.2 M sodium sulfide	water/TEA/ MeOH	0.2 M L-ascorbic acid	0.2 M sodium sulfide
CTF-15		0.8	29.4	23.1	1979	352	325
CTF-16	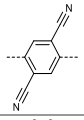	5.6	14.3	15.7	1039	192	651
CTF-34	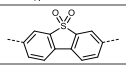	0.8	57.2	24.9	1910	12	94
CTF-3 Suzuki		26.8	49.1	25.7	158	0	28

7.8 Detailed analysis of CTF-15 as the best photocatalyst

The origin of high polymer performances for the hydrogen evolution could not be determined to be due to a single property of the polymers,[59,176] but it could be caused by a high level of palladium that acts as co-catalyst in photocatalysis.[124] The residual level of palladium from the polymer synthesis was tested by ICP analysis (Figure 39) for some selected CTFs: CTF-5 (1,3-dibromobenzene), CTF-14 (2,5-dibromothiophene dioxide), CTF-15 (2,5-dibromo-benzonitrile), CTF-16 (2,5-dibromo-1,4-benzenedicarbonitrile), CTF-34 (3,7-dibromo-dibenzo-thiophene-*S,S*-dioxide), CTF-37 (2,7-dibromo-9*H*-carbazole), CTF-40 (4,7-dibromobenzo-[*c*][1,2,5]oxadiazole), and CTF-41 (4,7-dibromo-2,1,3-benzoselenadiazole). The highest palladium content of 1.35 wt. % was found in CTF-5 (1,3-dibromobenzene) that demonstrated a moderate hydrogen evolution performance of 20 ± 2 µmol g^{-1} h^{-1}, followed by CTF-40 (4,7-dibromobenzo[*c*][1,2,5]oxadiazole) with 1.29 wt. %, and CTF-41 (4,7-dibromo-2,1,3-benzoselenadiazole) with 1.09 wt. %. CTF-15 (2,5-dibromobenzonitrile) which was found to be the best photocatalyst for hydrogen evolution was found to contain 0.76 wt. % palladium, while CTF-14 (2,5-dibromothiophene dioxide) had 0.80 wt. % palladium and evolved 184 times less hydrogen per hour, suggesting that the palladium content does not have a direct correlation with the hydrogen evolution performance in the case of these polymers. A further indication that the palladium content does not improve the hydrogen evolution performance is seen for CTF-34 (3,7-dibromo-dibenzothiophene-*S,S*-dioxide) as the second best photocatalyst which only contained 0.44 wt. % palladium, while CTF-16 (2,5-dibromo-1,4-benzenedicarbonitrile) showed a

0.54 wt. % palladium content with a lower evolution rate of hydrogen. Therefore, it can be concluded that while the tested polymers have residual palladium content, no correlation between the content of residual palladium and the hydrogen evolution rate was found. Other recent work[162,163] suggests that all of these polymers might be above the 'saturation limit' in terms of palladium content, which was stated at around 200 ppm/0.02 wt. %. The authors also tested an increased palladium content of 50000 ppm/5 wt. %, but found no significant increase in comparison to 200 ppm/0.02 wt. %. Although platinum was found to be a better co-catalyst than palladium for g-C_3N_4[161] and polymeric photocatalysts,[124] there is no spectroscopic analysis regarding these findings.

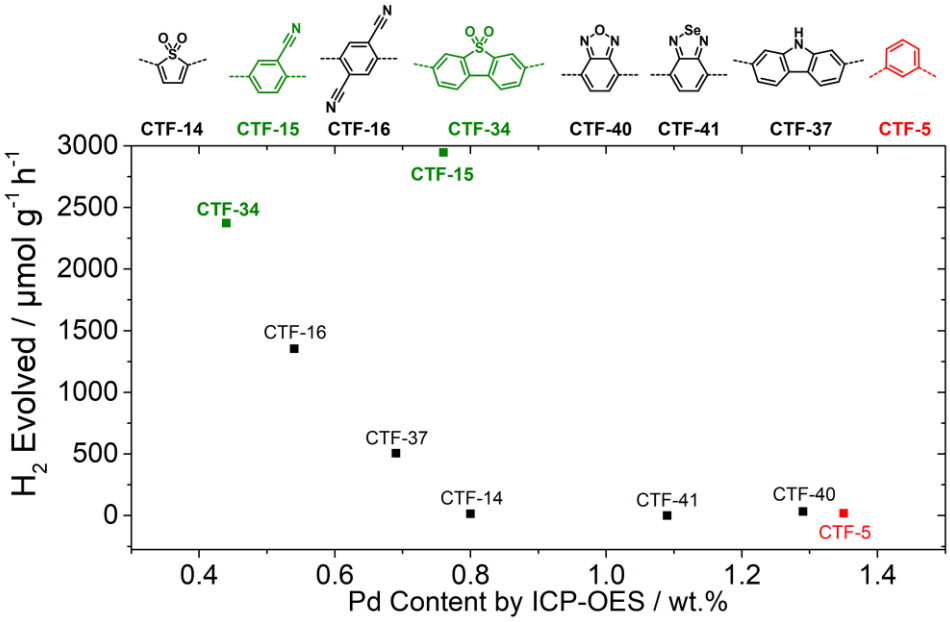

Figure 39: Palladium content as determined by ICP-OES of the polymer against the hydrogen evolution rate under visible light (λ > 420 nm) for manual runs. *Conditions:* 40 mg of each sample were microwave digested using nitric acid and hydrochloric acid. The resulting solutions were run on the ICP-OES instrument calibrated with yttrium internal standard and palladium calibration standards at 340 nm. Analysis carried out by Exeter Analytical, Coventry.

As shown in subsection 6.17, residual palladium from the synthesis acts a co-catalyst for the hydrogen evolution under sacrificial conditions. When CTF-15 (2,5-dibromobenzonitrile) was tested without platinum co-catalyst under λ > 420 nm irradiation, the hydrogen evolution rate decreased from 2946 ± 381 µmol g^{-1} h^{-1} to 1242 ± 208 µmol g^{-1} h^{-1} (58% decrease) in water/TEA/MeOH. A similar decrease in activity was also observed for CTF-2 (subsection 6.17). Even in absence of methanol as a wetting agent, a hydrogen evolution rate of 1690 ± 467 µmol g^{-1} h^{-1} was obtained from water/5% TEA/3 wt. % platinum. As this is a low reduction in comparison to the scavenger system water/TEA/MeOH, it was determined that the hydrogen evolution experiments could be done without methanol in the future to avoid additional hydrogen sources in the solution.

The photostability of CTF-15 (2,5-dibromobenzonitrile) was also tested over a cumulative time of 100 hours (Figure 40). First, CTF-15 was illuminated for 50 hours (10 x 5 hours) under λ > 420 nm irradiation (Figure 40, left). Each run was found to give a similar hydrogen evolution rate, and after recovery of the polymer powder, the experiment was continued with the scavenger solution replaced. A total quantity of 450 µmol hydrogen is expected to be present in CTF-15 – as this amount was exceeded after 6 hours, it can be concluded that the polymer itself is not the source of hydrogen. Next, the same polymer was also continued to for another 50 hours (10 x 5 hours) under solar simulated light (Figure 40, right) and showed reproducible results as well.

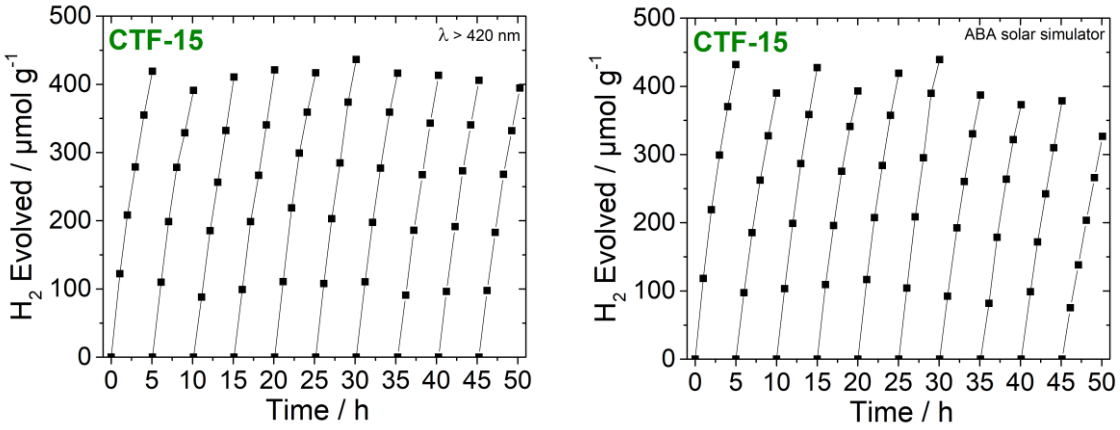

Figure 40: Hydrogen evolution of CTF-15 tested in water/TEA/MeOH and 3 wt. % platinum co-catalyst under visible light (λ > 420 nm, 50 h, left), and ABA solar simulated light (50 h, right).

After a total of 100 hours of photocatalysis, the polymer powder was then recovered, washed with THF and dried. On analysis, no significant changes in the FT-IR spectrum were observed (Figure 41A), and the nitrile band at 2226 cm^{-1} is still present. This suggests that a partial hydrolysis of the nitrile groups had not occurred, as the decomposition products formed would be amides and amines,[129] showing a band around 1600 cm^{-1}. It was found however that the surface area after photocatalysis was slightly decreased to SA_{BET} = 289 $m^2 g^{-1}$ (before photocatalysis SA_{BET} = 383 $m^2 g^{-1}$) which could be caused by platinum particles being present inside the pore (Figure 41B). Another fact that supports this hypothesis is the decrease of the pore volume from 0.33 $cm^2 g^{-1}$ before photocatalysis to 0.25 $cm^2 g^{-1}$ after photocatalysis. Finally, the optical measurements also indicate the stability of CTF-15 (Figure 41 C)-D)): the band gap remained at 2.58 eV as measured by UV-Vis spectroscopy, and the fluorescence spectrum further showed one peak at 469 nm under λ_{ex} = 280 nm (compare subsection 7.3).

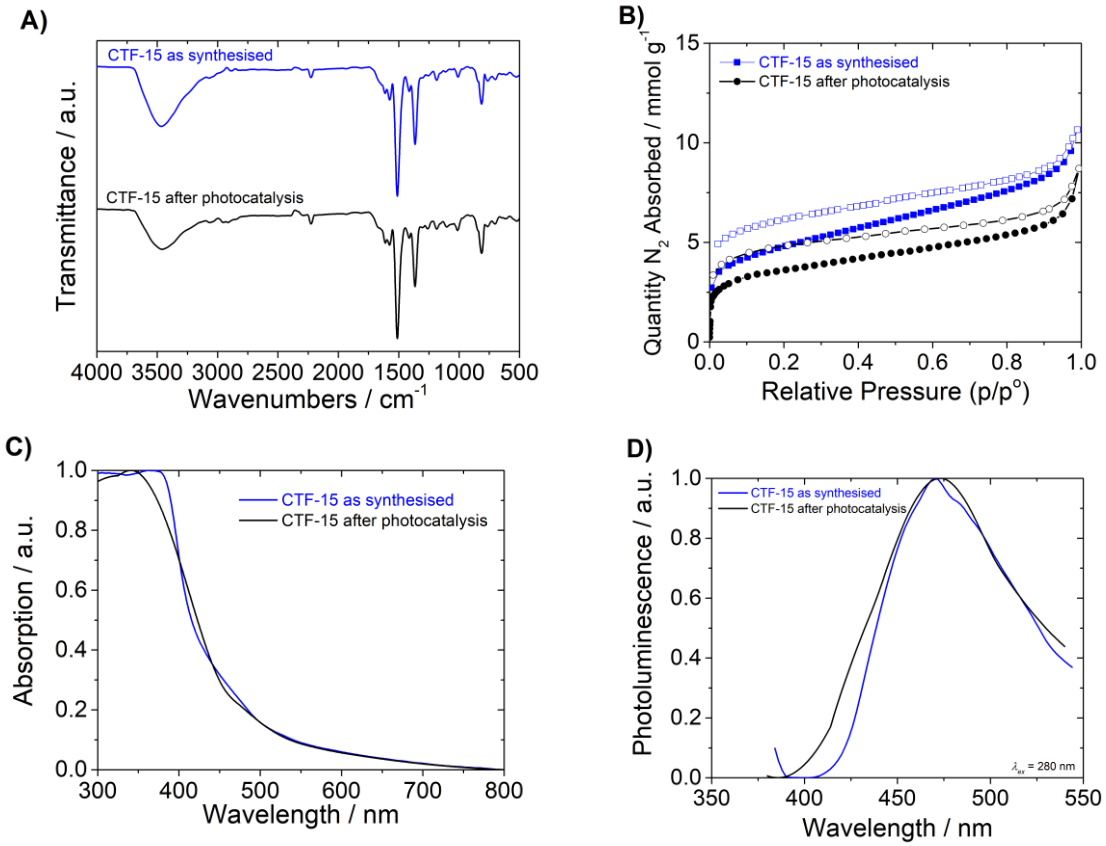

Figure 41: Analysis after 100 h of photocatalysis in water/TEA/MeOH with 3 wt. % platinum. A) FT-IR – B) Nitrogen sorption isotherms, measured at 77.3 K and up to 1 bar (desorption curves shown as open symbols) – C) UV-Vis in solid-state – D) Fluorescence in solid-state (λ_{ex} = 280 nm).

Alongside these measurements, the wavelength dependency of the hydrogen evolution from water/TEA/MeOH and 3 wt.% co-catalyst was measured (Figure 42). An external quantum efficiency (EQE)[106] was calculated for CTF-15 and found to be $EQE_{420\ nm}$ = 15.9% at λ = 420 nm (±10 nm, FWHM). This represents an increase by around ten times in comparison to the best performing material reported in the first chapter – CTF-2 in TEOA/water/3 wt. % Pt with an $EQE_{420\ nm}$ = 1.6% (subsection 6.15).[124] These EQE can be put into perspective to reported g-C_3N_4 nanosheets with an $EQE_{420\ nm}$ = 14% from TEOA/water/3 wt. % Pt, [177] and cadmium sulfide nanorods loaded with nickel phosphide as co-catalyst with a calculated $EQE_{450\ nm}$ = 41% from sodium sulfite/sodium sulfite.[178]

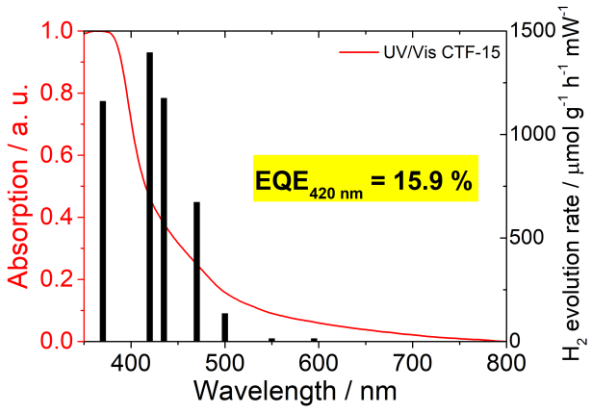

Figure 42: Wavelength dependency of the photocatalytic hydrogen evolution for CTF-15 using band-pass filters (370 nm, 435 nm, 470 nm, 500 nm ± 10 nm, FWHM) and a LED (420 nm ± 10 nm, FWHM). CTF-15 was dispersed in water/TEA/MeOH with 3 wt. % Pt in a quartz cuvette with an area of 7.8 cm^2 for an illumination of at least 5 hours.

7.9 Computational screening

For the 40 CTFs investigated, contribution to the understanding of the performance was obtained using computational modelling from a collaboration with the group of Dr Martijn Zwijnenburg at University College London and Dr Kim E. Jelfs, Imperial College London (see subsection 6.12 for details of the computation). All calculations presented were carried out by their research groups, while the analysis was done for this thesis independently. Overall, it was found that most of the polymers were calculated to straddle the oxidation and reduction potential of water (Figure 43), making overall water-splitting thermodynamically possible. The potentials of the EA are calculated to be between -1.95 V and -0.54 V, and the potentials of the IP are predicted between 0.74 V and 2.06 V.

Seven CTFs were found to have IP potentials between 0.74 V and 0.91 V and show low HERs, indicating a threshold of overpotential to the oxidation potential of TEA with 0.38 V, while the remaining 37 CTFs had calculated IP potential of up to 2.36 V in the case of CTF-1 and no correlation between the HER and the IP was found.

CTF-23 was calculated to have the lowest EA potential of -0.54 V in the CTF library and therefore has a small overpotential for the proton reduction, which coincides with a very low observed hydrogen evolution rate of 5 ± 1 µmol g^{-1} h^{-1}. Similar observations were also found for CTF-14 with an EA potential of -0.96 V and a HER of 16 ± 2 µmol g^{-1} h^{-1}. CTF-10 to CTF-13 (2,5-dibromofuran, 2,5-dibromothiophene, and 2,5-dibromo-selenophene) are structurally related and their EA potentials are predicted to lie between -1.70 to -1.57 V, and their IP potentials are predicted between 0.93 to 1.03 V, while showing HERs between in the range of 1151 ± 29 µmol g^{-1} h^{-1} to 1515 ± 66 µmol g^{-1} h^{-1}

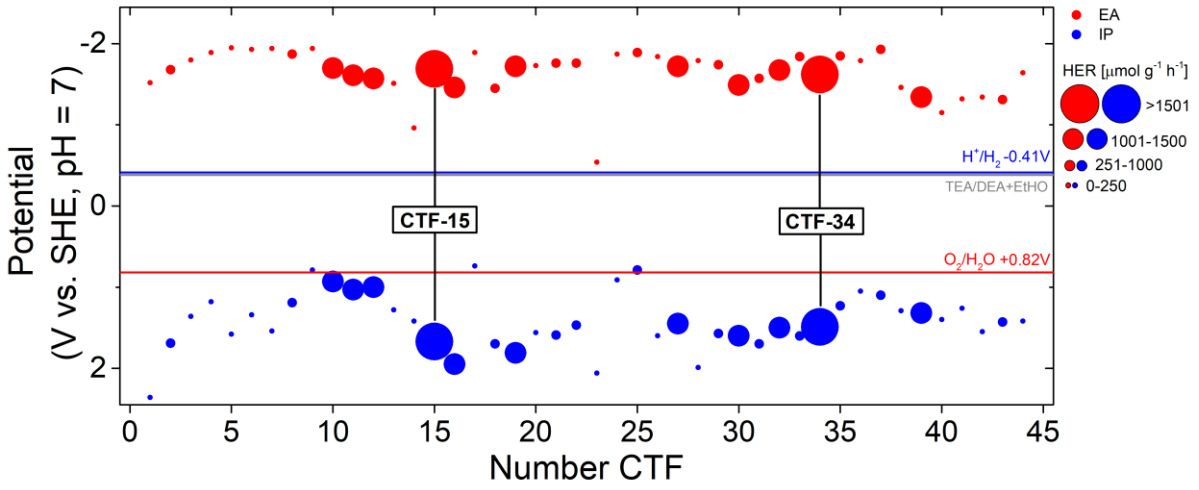

Figure 43: Predicted values of the ionisation potential (IP, blue) and electron affinity (EA, red) standard reduction potentials of CTF-5 to CTF-44. The size of the points correlates to the hydrogen evolution rate measured from water/TEA/MeOH with 3 wt. % Pt on the manual setup under λ > 420 nm irradiation. The standard reduction potentials for the proton reduction (blue line), water oxidation (red line), and triethylamine oxidation (grey line) are shown for clarity. All potentials are calculated for pH = 7 and a relative dielectric permittivity of 80.1 (water). The two best performing polymers CTF-15 and CTF-34 are highlighted.

An analysis of the EA and IP difference (fundamental band-gap) compared to the measured HERs did not result in a clear trend. CTF-14 has the lowest fundamental band-gap in the series of 2.38 eV (HER 16 ± 2 µmol g^{-1} h^{-1}), while CTF-23 has a fundamental band-gap of 2.60 eV (HER 5 ± 1 µmol g^{-1} h^{-1}), which is similar to CTF-12 that shows a higher HER of 1515 ± 66 µmol g^{-1} h^{-1}. The two best performing catalysts CTF-15 and CTF-34 have an IP that differs by 0.18 V (1.67 V and 1.49 V, respectively), and close EA potentials of -1.69 V and -1.62 V. In contrast, CTF-44 has an EA potential in between these values of -1.64 V and only shows a low hydrogen evolution rate of 44 ± 1 µmol g^{-1} h^{-1}.

However, the computational screen combined with the HERs did reveal the following trend for the library of CTFs (Figure 44 and **Error! Reference source not found.**, appendix): for a predicted EA potential between -1.94 V and -1.73 V, 19 CTFs showed HERs below 750 µmol g^{-1} h^{-1}. Similarly, the predicted EA potential between -1.31 V and -0.54 V for CTF-40, CTF-15, and CTF-23, correlated with low HERs below 33 µmol g^{-1} h^{-1}. On the other hand, for a calculated EA potential between -1.72 V and -1.34 V, 10 polymers exceeded HERs of 1000 µmol g^{-1} h^{-1}, while in the same range, eight polymers showed a HER below 1000 µmol g^{-1} h^{-1}. No correlation between the predicted IP potentials and the HER was found, with photocatalysts showing HERs above 1000 µmol g^{-1} h^{-1} and IP potentials in the wide range of 0.93 V to 1.95 V.

Therefore, the calculated EA potentials of the materials could theoretically be used to predict CTFs that show low HERs. For this library, the theoretical calculations defined 22 CTFs that could have been

ruled out as inactive photocatalysts, with the 18 CTFs that remained to be tested having an EA potential between -1.72 V and -1.34 V.

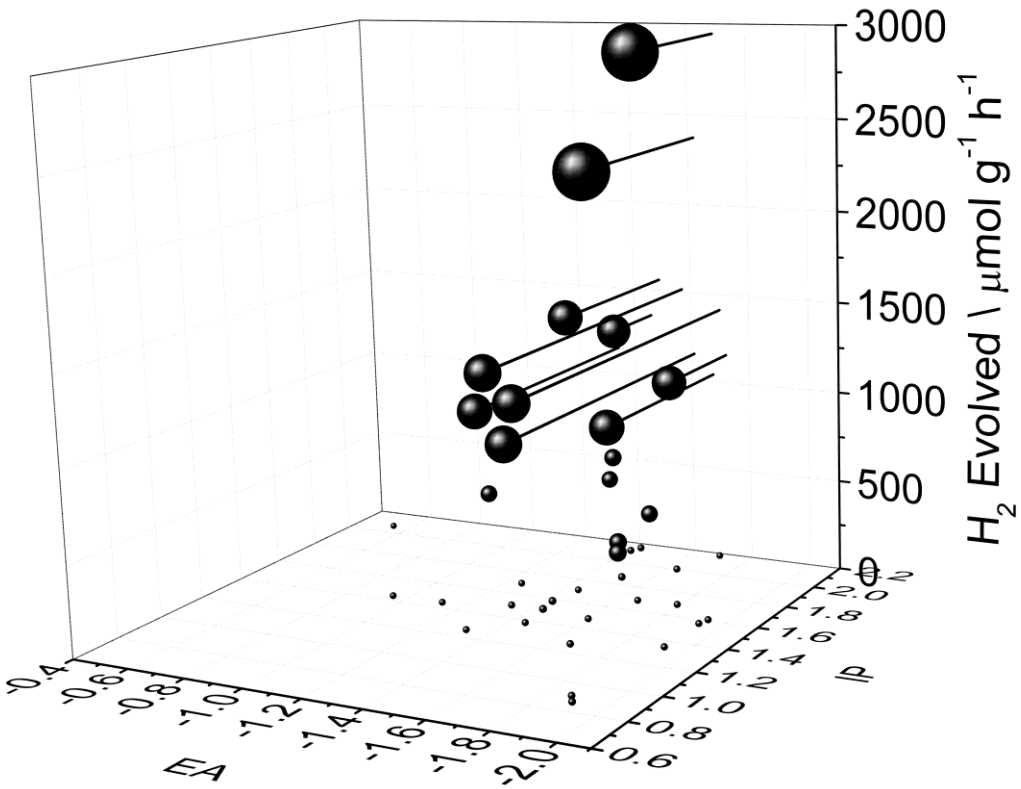

Figure 44: Predicted EA and IP potentials of CTF-5 to CTF-44 compared to the manual hydrogen evolution rate from water/TEA/MeOH with 3 wt. % Pt under λ > 420 nm.

7.10 Overall analysis of the HT-library

The presented screen of 40 different potential photocatalysts in this library raises the question if the dataset holds any information relating to general design rules for photocatalysts based on covalent triazine-based frameworks, or even for other photocatalysts in general. The dataset is summarised in Table 15 to Table 17 in the appendix, and the measurements that were carried out are visualised in Figure 45. A discussion of the FT-IR, PXRD, and TGA was included in subsection 7.2, which leaves eight other sets of measurement data, and the hydrogen evolution performance to investigate. During this analysis, two or three results were compared with the hydrogen evolution under sacrificial conditions.

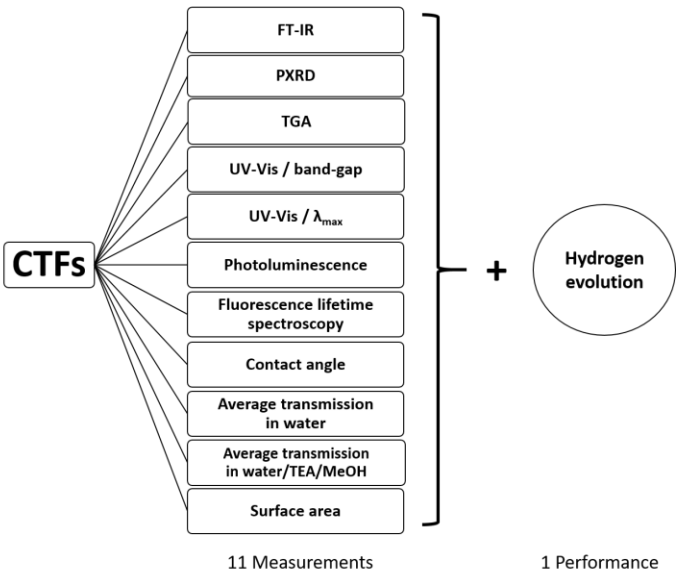

Figure 45: Overview of all measurements carried out for the CTF library.

The analysis was carried out by plotting data sets against each other in a relation to the hydrogen evolution rate in the Spotfire software and OriginPro 2015. This comparison was also used to test if the techniques are suitable to analyse CTFs, while e.g. the analysis of the photoluminescence or the PXRD did not reveal insights in the hydrogen evolution activity of the CTFs. The judgment of analysis techniques is hereby limited by their insolubility, while soluble linear co-polymers were tested regarding their molecular weight and influence on the HER.[92] When the band-gap was compared to the hydrogen evolution rates from the manual runs (Figure 46, left), CTF-15 and CTF-34 were found to be clear outlier when comparted of the majority of the CTFs. The result indicates that there is an optimal band-gap of around 2.6 eV. The analysis also revealed that the band-gap cannot be the only indicator for good performance, as many CTFs have a similar band-gap in this region (Figure 46, left). Therefore, the band-gaps were compared to the average transmissions of the CTFs in water/TEA/MeOH (Figure 46, right) – the best photocatalysts have an average transmission below 11.1%, and a band-gap between 460-480 nm. This indicates that the extinction coefficient could be targeted to improve the hydrogen evolution activity of the polymer.

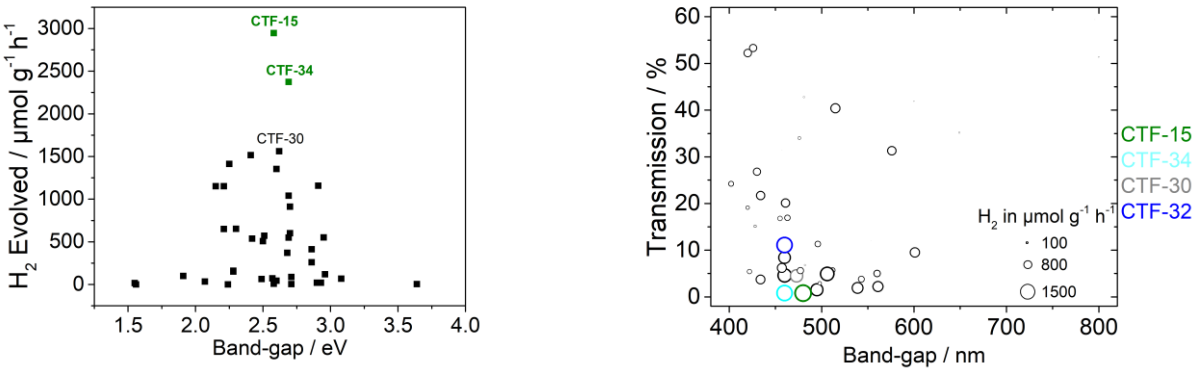

Figure 46: Analysis of band-gap *vs.* hydrogen evolution rate (left) from water/TEA/MeOH with 3 wt. % Pt, and correlation of band-gap and average transmission in water/TEA/MeOH to the hydrogen evolution rate in this scavenger solution (right).

An additional investigation to discover underlying trends was done using a heat map. For this purpose, the observed data of 41 CTFs (CTF-3 and CTF-5 to CTF-44) was normalised between 0-100% and divided into four categories: 0-25%, 26-50%, 51-75%, and 76-100% (Table 8). The highest hydrogen evolution rates, the most red-shifted band-gap, the longest fluorescence life-time, and the highest surface area were assigned with 100%, while 0% average transmission in water/TEA/MeOH and water are desired properties of the polymer. The most red-shifted band-gap was assumed to be beneficial for the performance of the polymers, as more light is absorbed. The heat map summarises the similar behaviour of CTF-15 and CTF-34 which were found to be the best two photocatalysts for hydrogen evolution: a similar band-gap around 2.6 eV, low transmission in water/TEA/MeOH, and a low fluorescence life-time characterise these porous polymers. A stronger deviation can already be seen for CTF-30 and CTF-12 as the third and fourth best materials, respectively. The transmission in water/TEA/MeOH is very low for CTF-30, while CTF-12 exhibits a high transmission (T = 4.5% and T = 40.4%, respectively). The average fluorescence life-time for CTF-30 was calculated to be 1.37 ns, while CTF-12 has an average life-time of 0.31 ns and evolves nearly the same amount of hydrogen. This analysis further supports the idea that there is no underlying pattern in the properties measured for the CTF library.

Table 8: Heat map analysis of normalised experimental data. The two best performing polymers CTF-15 and CTF-34 are framed. The observed data of 41 CTFs (CTF-3 and CTF-5 to CTF-44) was normalised between 0-100% and analysed.

Number Triazine	Hydrogen [%]	Band-gap[a] [%]	Transmission water/TEA/MeOH [%]	Transmission water [%]	Fluorescence life-time [%]	Surface area [%]
5	1	34	8	39	53	23
6	0	51	72	69	67	0
7	1	35	24	55	31	16
8	13	46	1	4	31	51
9	2	55	4	32	61	100
10	48	67	7	25	26	84
11	39	71	52	37	12	25
12	51	59	68	58	5	18
13	2	51	10	26	6	3
14	1	100	86	75	36	0
15	100	51	0	100	27	81
16	46	50	8	22	68	39
17	18	58	8	85	10	46
18	0	44	52	45	12	18
19	39	35	90	67	12	65
20	3	44	9	39	31	34
21	19	33	88	59	10	68
22	14	37	5	63	20	47
23	0	0	42	76	68	1
24	0	100	100	91	5	0
25	19	45	33	48	38	69
26	2	27	40	59	31	34
27	31	45	7	7	36	23
28	4	33	31	30	22	10
29	19	54	27	38	10	2
30	53	49	6	1	30	3
31	22	68	7	1	16	4
32	35	45	18	7	5	22
33	9	37	36	31	100	13
34	81	45	0	97	12	56
35	20	45	13	31	14	63
36	5	65	5	0	35	24
37	17	55	18	71	0	6
38	5	65	5	12	45	12
39	39	68	2	21	14	75
40	1	75	70	12	29	58
41	0	67	19	25	5	14
42	3	83	59	85	18	1
43	22	64	2	0	15	39
44	1	50	57	66	36	8
CTF-3 Suzuki	5	36	44	66	18	53

Legend:	0-25%	26-50%	51-75%	76-100%
lowest to highest values in the series from CTF-5 to CTF-44 and CTF-3 Suzuki				

[a] the most red-shifted band-gap = 100%, the most blue-shifted band-gap = 0%

7.11 Analysis of subsets

After the combined analysis of the CTF library, analysis of the individual subsets was carried out. It was hoped that structurally similar CTFs would make the overview easier, as a smaller dataset is investigated and findings for individual subsets can be compared.

All CTFs in the benzene subset give HERs that are significantly lower than CTF-3 (Figure 47). One exception is CTF-8 with a hydrogen evolution rate of 371 ± 39 µmol g^{-1} h^{-1} – this is 2.35 times higher than the HER of CTF-3 Suzuki. The three least effective polymers in this subset are CTF-5, CTF-6, and CTF-7, which contain *meta*-substituted linkers, whereas CTF-8, CTF-9, and CTF-3 have *para*-substituted linkers. Furthermore, the BET surface areas were found to be lower for the *meta*-linked polymers CTF-5 to CTF-7, measured between 10 to 168 m^2 g^{-1}, in comparison to CTF-3 Suzuki with a BET surface area of 380 m^2 g^{-1}. The *para*-substituted CTF-8 and CTF-9 also show high BET surface areas of 365 m^2 g^{-1} and 708 m^2 g^{-1}, respectively, which may contribute to their photocatalytic activity, and CTF-9 exhibits the lowest transmission in water/TEA/MeOH at 1.5%. To conclude, the use of the fused, planar triphenylene linker (M9) resulted in a photocatalyst that showed improved hydrogen evolution than found previously for CTF-1 to CTF-4.

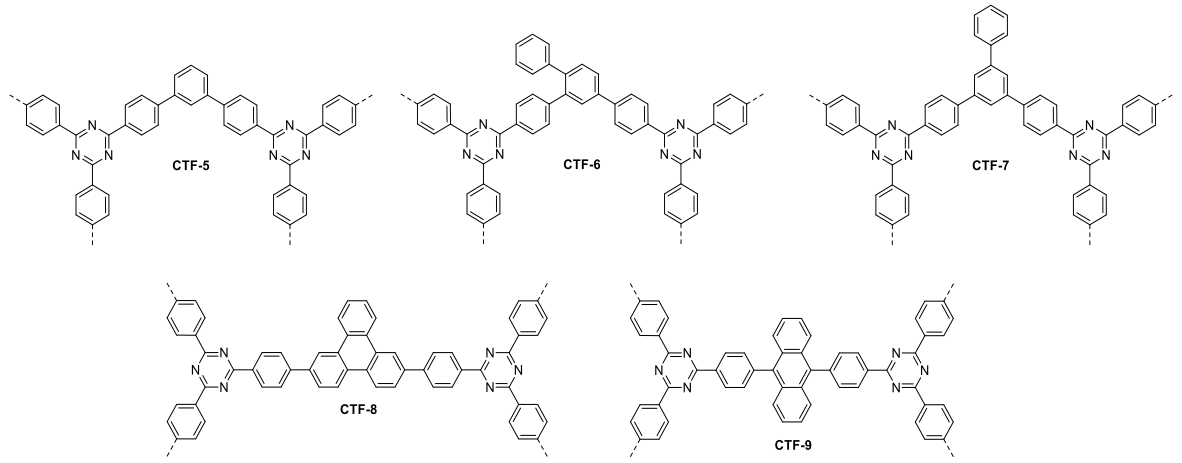

Figure 47: Overview of the benzene subset CTF-5 to CTF-9.

In the subset of 5-membered ring heterocycles (Figure 48), three of the CTFs showed improved hydrogen evolution performance than CTF-3 Suzuki, while the choice of chalcogen in the heterocycle linker for CTF-10 to CTF-12 determines the activity of the polymer. The best performing polymer CTF-12 (selenophene) significantly improved the HER – it showed almost ten times the activity of CTF-3 Suzuki with 1515 ± 66 µmol g^{-1} h^{-1}, followed by CTF-10 (furan) and CTF-11 (thiophene). Low activity was measured for CTF-13 and CTF-14 (the oxidised linker unit of CTF-11) with moderate

hydrogen evolution rates of 72 ± 3 µmol g^{-1} h^{-1} and 16 ± 2 µmol g^{-1} h^{-1}, respectively. CTF-14 was found to be a low band-gap polymer with a calculated band-gap of 1.55 eV, and showed high average transmissions T = 51.4% in water/TEA/MeOH and T = 64.4% in water (see also subsection 7.3), which may possibly explain its poor performance under these conditions. Fluorescence life-time measurements also show short average life-times below, with max. 1.62 ns for CTF-14.

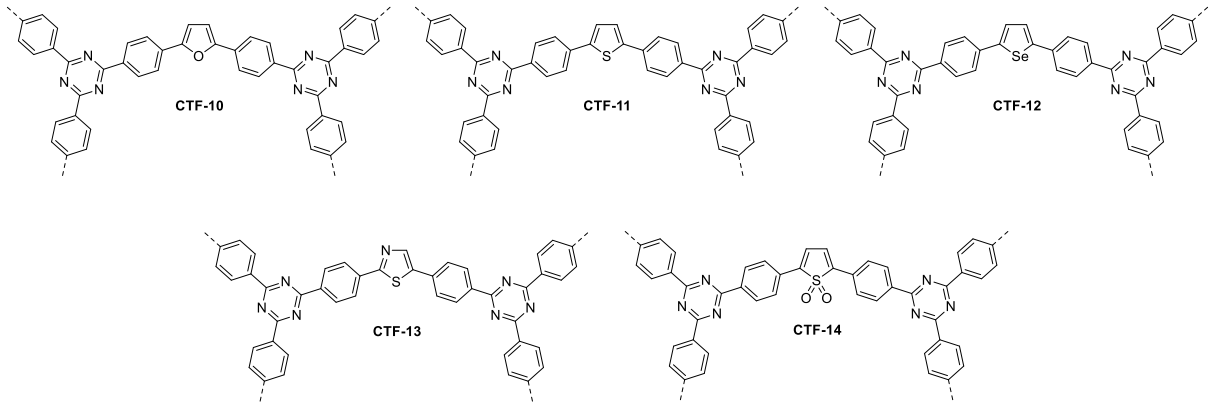

Figure 48: Overview of the 5-membered heterocycle subset CTF-10 to CTF-14.

The subset of substituted benzenes allows the influence of the type of substitution and the substitution pattern on the central phenylene ring of CTF-3 Suzuki to be investigated (Figure 49). It contains polymers that are far more effective for hydrogen evolution than CTF-3 Suzuki, as well as polymers that do not show any HER. The two most active materials in this subset are nitrile substituted benzene linkers, namely mono-nitrile substituted CTF-15, and dinitrile substituted CTF-16, with HERs of 2946 ± 381 µmol g^{-1} h^{-1} and 1354 ± 133 µmol g^{-1} h^{-1}, respectively. Both polymers have similar band-gaps of 2.58 eV for CTF-15 and 2.60 eV for CTF-16, which are very close to that measured for CTF-3 Suzuki with 2.62 eV.[124] Furthermore, both of these polymers swelled in contact with water, and the average life-times were calculated to be 1.23 ns for CTF-15, and 2.99 ns for CTF-16.

CTF-17 and CTF-18 contain an electron donating group (EDG) and an electron withdrawing group (EWG), respectively. The EDG in CTF-17 increases the HER significantly with respect to CTF-3 Suzuki (537 ± 30 µmol g^{-1} h^{-1}). In contrast, the EWG in CTF-18 causes a 97% decrease in the HER in comparison to CTF-3 Suzuki. Although both absorption on-sets are red-shifted in comparison to CTF-3 Suzuki (2.42 eV, 2.71 eV, and 2.88 eV, respectively), only the EDG in CTF-17 led to a 3.4 fold increase in performance.

The fluorobenzenes CTF-19 to CTF-22 can be grouped on their own within this subset: the best performing polymer is CTF-19 with a tetrafluorobenzene linker, followed by the monofluorobenzene

substituted CTF-22. The substitution pattern on the linker plays an important role on the hydrogen evolution: the 2,3-difluorobenzene containing CTF-21 has a HER that is 3.5 times higher than CTF-3 Suzuki (550 ± 28 μmol g^{-1} h^{-1}), while the 2,3-difluorobenzene containing CTF-20 gives a HER that is around half of CTF-3 Suzuki (87 ± 2 μmol g^{-1} h^{-1}). Reports on fluorinated PPPs were reported previously, and the authors generally found that fluorination increased the HER.[179]

The oxygen-substituted polymers CTF-23 and CTF-24 showed low activity when tested for their hydrogen evolution, while the methyl ether polymer CTF-25 showed a HER that was 3.5 times higher (548 ± 97 μmol g^{-1} h^{-1}) than that of CTF-3 Suzuki.

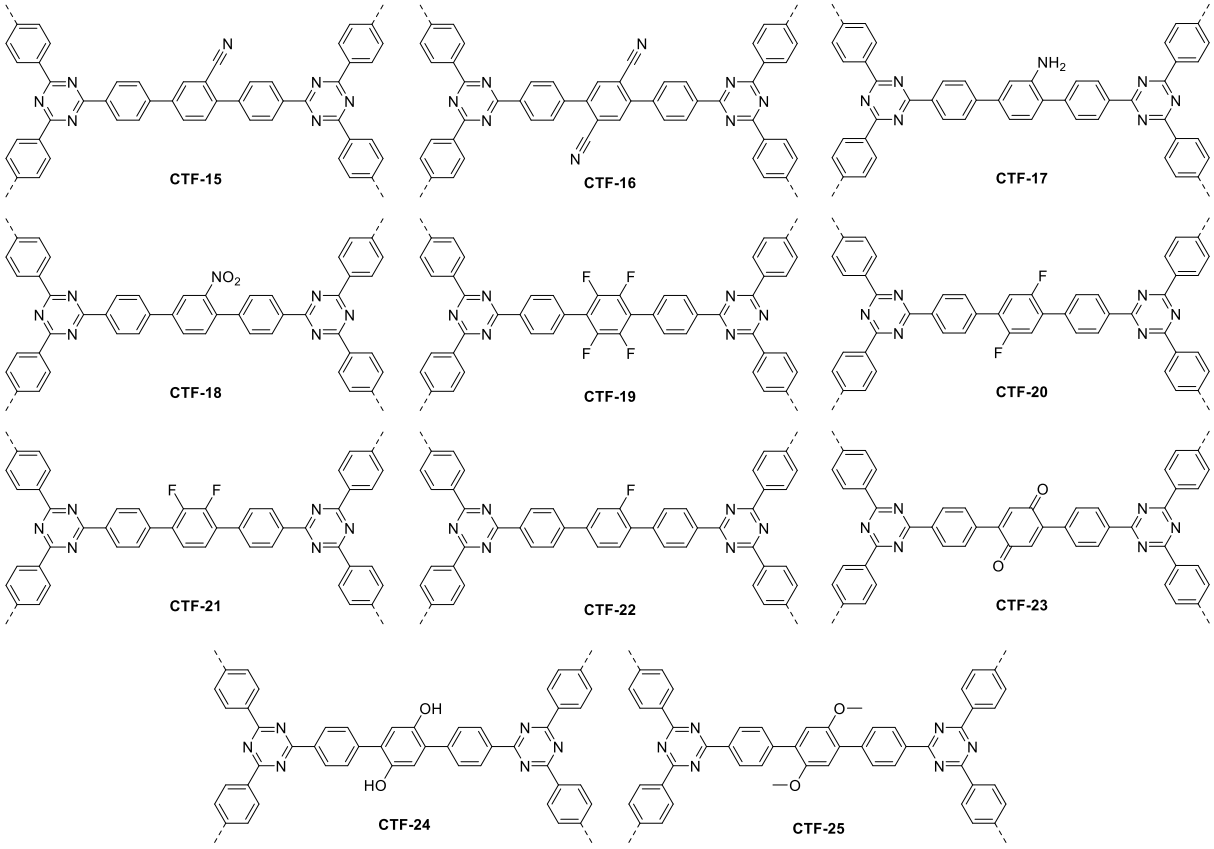

Figure 49: Overview of the substituted benzene subset CTF-15 to CTF-25.

Next, the subset containing four bipyridyl linkers was reviewed: CTF-27 and CTF-29 are synthesised from linear linkers – in contrast, CTF-26 and CTF-28 are synthesised from non-linear linker units (Figure 50). A linear co-polymer of *para*-phenylene and 5,5'-linked-2,2'-bipyridine was studied recently and showed a HER of 296 ± 28 μmol g^{-1} h^{-1} from water/TEA/MeOH. CMPs based on 5,5'-linked-2,2'-bipyridine (M27) and 3,8-linked-1,10-phenanthroline (M29) has also reported as photocatalysts from water/TEA under 200-1050 nm irradiation.[151] In the literature, the bipyridine linked CMP was discovered to have a higher HER and lower band-gap than the phenanthroline polymer. These observations were also found for CTF-27 with a HER of 911 ± 37 μmol g^{-1} h^{-1} and a band-gap of 2.70 eV,

in comparison to CTF-29 with a HER of 571 ± 37 µmol g^{-1} h^{-1} and a band-gap of 2.51 eV. In general, the substitution pattern of the bipyridyl linker plays an important role for the photocatalytic activity. The linker units in CTF-27 and CTF-29 led to an increase in the hydrogen evolution performance. In comparison to CTF-3 Suzuki, an enhanced activity of 5.8 times to 911 ± 37 µmol g^{-1} h^{-1} for CTF-27, and 3.6 times to 571 ± 37 µmol g^{-1} h^{-1} for CTF-29, was found. A reduction in the HERs was observed for the polymers CTF-26 and CTF-28 that contained non-linear linker units. An ongoing increase of the average transmission in the scavenger solution water/TEA/MeOH from T = 4.6% for CTF-27, to T = 16.9% for CTF-26, correlates with an increase in the hydrogen evolution, while no trend was found for the surface areas that have values ranging from 76 m^2 g^{-1} for CTF-28 to 242 m^2 g^{-1} for CTF-26.

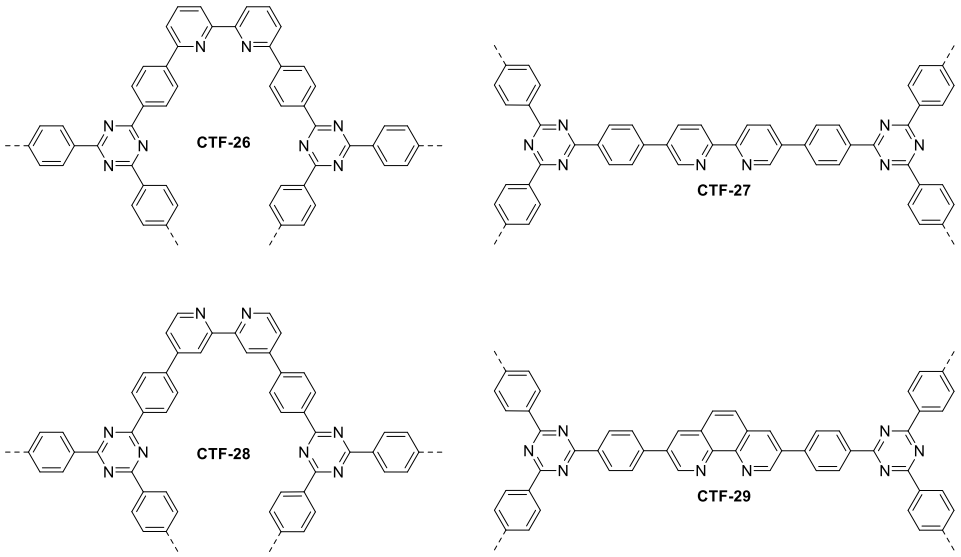

Figure 50: Overview of the bipyridyl subset CTF-26 to CTF-29.

Four further CTFs were prepared using *N*-heterocyclic linkers to obtain CTF-30 to CTF-33 that all gave higher HERs than CTF-3 Suzuki (Figure 51). A decreasing order was found for pyrazine (CTF-30) > pyrimidine (CTF-31) > pyridines (CTF-32, CTF-33). Like reported before, CMPs[89] and phenylene co-polymers[180] based on pyrazines showed higher activity than polymers based on pyrimidine, and polymers with 1,4-substituted pyridines showed higher HER than 1,3-substituted pyridines.

The band-gaps of CTF-30 and CTF-31 were measured to be 2.62 eV and 2.69 eV, respectively. Similar to the bipyridyl subset (Figure 50), *para*-substitution in CTF-32 favours higher HER than its *meta*-linked analogue CTF-33. A further analogy to the bipyridyl subset can be seen in the dispersibility with water/TEA/MeOH: with increasing transmission, a lower photocatalytic activity was measured.

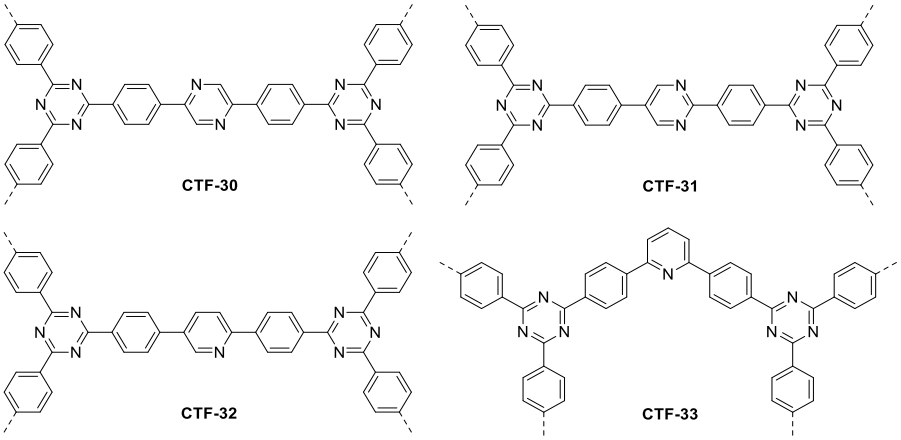

Figure 51: Overview of the *N*-heterocycle subset CTF-30 to CTF-33.

In the subset of planar systems (Figure 52), the second best photocatalyst of the entire library is present. Dibenzosulfone linkers and carbazole linkers have been reported as photoactive materials previously.[59,92,181] Here, a HER of 2373 ± 25 µmol g^{-1} h^{-1} was measured for CTF-34 – its reduced analogue, CTF-35, was found to be the second best photocatalyst within this subset (600 ± 37 µmol g^{-1} h^{-1}). Both materials exhibit nearly the same band-gap of 2.69 eV for CTF-34 and 2.72 eV for CTF-35 and represent the most porous CTFs in this subset. CTF-35 has a SA_{BET} = 446 m^2 g^{-1} and CTF-34 shows a SA_{BET} = 397 m^2 g^{-1}. Further, CTF-34 swells in contact with water, while a contact angle of 91° was determined for CTF-35. Improved interactions of the polymers with the scavenger system water/TEA/MeOH is shown in the transmission of T = 0.8% for CTF-34, and T = 8.4% for CTF-35. To summarise, no measurement was found to explain the hydrogen evolution rates from 150 ± 15 µmol g^{-1} h^{-1} for CTF-38 to 2373 ± 25 µmol g^{-1} h^{-1} for CTF-34. An explanation could be the diversity of the bridge functionalities that are not closely related.

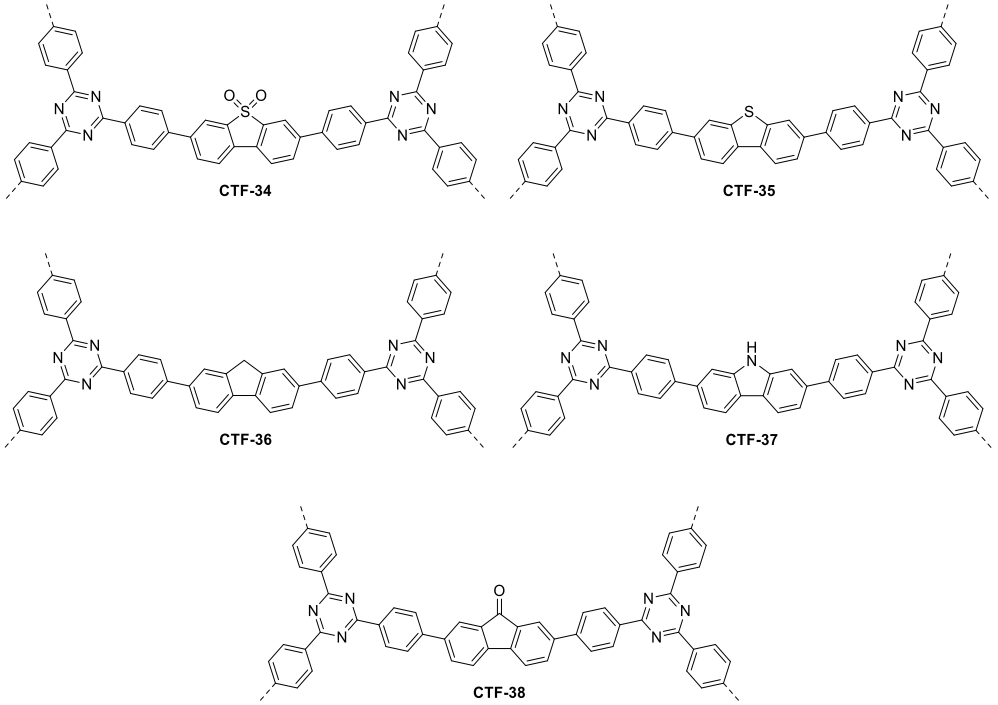

Figure 52: Overview planar systems to synthesise CTF-34 to CTF-38.

The last subset consists of five azoles and a quinoxaline as strong electron withdrawing linker units (Figure 53). Photocatalysts synthesised *via* Sonogashira-Hagihara couplings on 4,7-dibromo-2,1,3-benzothiadiazole and 2,4,6-tris(4-ethynylphenyl)-1,3,5-triazine were reported previously with low HER from water/acetonitrile and 3 wt. % co-catalyst. In this work, three benzothiadiazoles represent the best photocatalysts in this subset: CTF-39 (unsubstituted) > CTF-43 (monofluorinated) > CTF-42 (difluorinated). A decrease in the HER was found from 1151 ± 75 µmol g^{-1} h^{-1} for CTF-39 to 100 ± 2 µmol g^{-1} h^{-1} for CTF-42. As observed in previous subsets, the best performing photocatalyst CTF-39 exhibits the highest surface area in the subset with SA_{BET} = 536 m^2 g^{-1}. Further properties that were identified before for the lead photocatalyst were not found. In fact, even the opposite trend was observed: the band-gap of CTF-39 is red-shifted to 2.21 eV, the polymer does not swell in contact with water, and the average life-time of 0.7 ns is the lowest in this subset. Further comparisons of the best three photocatalysts showed average life-times of 0.70 ns, 0.72 ns, and 0.87 ns that are inverse to their HER. Following the chalcogens in group 16 of the chemical table, CTF-40 was compared to CTF-39 and CTF-41 with HERs of 33 ± 3 µmol g^{-1} h^{-1}, 1151 ± 75 µmol g^{-1} h^{-1}, and 0 µmol g^{-1} h^{-1}, respectively. Interestingly, benzothiadiazole (CTF-39) was found to be the best performing linker and not benzoselenazole (CTF-41) like expected from the previous investigated subset of 5-membered ring heterocycles (Figure 48). An outsider in this subset is represented by the quinoxaline based polymer CTF-44 which has the biggest band-gap of 2.60 eV and a moderate HER of 44 ± 1 µmol g^{-1} h^{-1}.

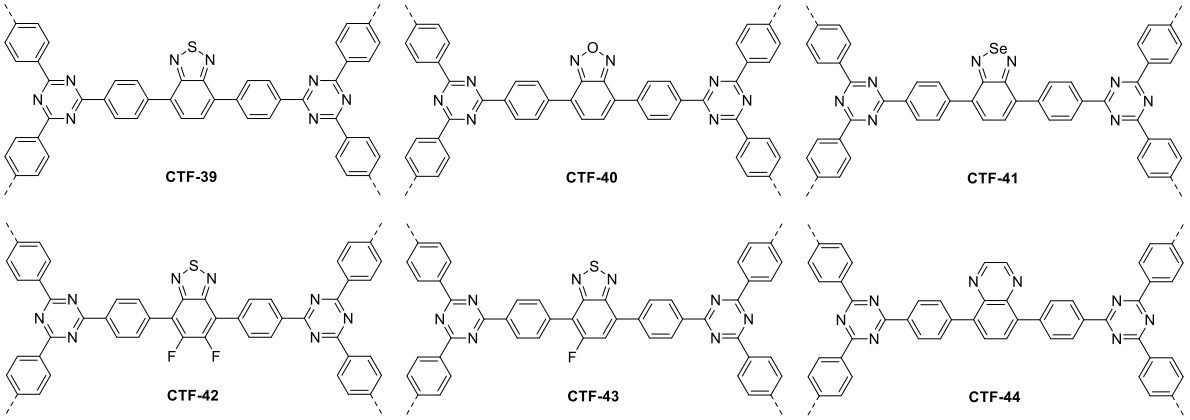

Figure 53: Overview of the azole and a quinoxaline subset CTF-39 to CTF-44.

7.12 Summary of the library of 40 CTFs

The synthesis and detailed analysis of 40 CTFs was carried out to investigate the properties of the CTFs, and to find design rules for new photocatalysts. Fluorescence life-time measurements for all materials revealed very short life-times, and did not correlate to their performance. It was further shown that a small band-gap, such as that found in CTF-14 only resulted in a moderate performing photocatalyst, although the light absorption is high. By simply shifting the absorption on-set in the red, no high performing photocatalyst could be obtained. Moreover, the best performing photocatalyst CTF-15 with around 3000 µmol g^{-1} h^{-1} hydrogen release absorbed less light than CTF-14, but showed a 185 time increase in the hydrogen evolution rate compared to CTF-14. Characteristics for CTF-15 are also a good dispersibility in water/TEA/MeOH, a surface area of 383 m^2 g^{-1}, a band-gap of 2.58 eV, and weak fluorescence. It further swells in contact with water – a property that was found for the best three performing catalysts, while CTF-12 as forth best photocatalyst has a contact angle of 66°. This suggests that the interaction with water is favoured, leading to a better wetting of the photocatalyst to improve the interface between the heterogeneous photocatalyst and water.

Another result of the analysis is that findings in one subset cannot be transferred to another subset: in the subset of five-membered ring heterocycles, the photocatalytic activity decreases from sulfur, oxygen to selenium heteroatoms, while in the azole subset, the photocatalytic activity decreases from selenium, oxygen to sulfur. This highlights that no conclusion from the findings of aromatic compounds can be transferred to design principles of new aromatic systems. Polymer CTF-39 is an example of this, as it is the best performing photocatalyst of its subset. While it showed the highest surface area in its subset, it behaviour was opposite to findings in other subsets: e.g. it did not swell, and its band-gap was red-shifted.

Calculations showed that an analysis regarding the EA and IP produces results that lay in a narrow range due to the structural similarity of the CTFs – unlike comparing categories of photocatalysts, the changes in the library are rather small and do not produce strong outliers. Nevertheless, it was found to predict materials that show low hydrogen evolution rates, e.g. CTF-14 and CTF-23.

With the use of the CTF library on the HT system, the benefit of fast and reliable testing was demonstrated. The system can handle around 100 samples a day to find high-performing photocatalysts for further analysis. Combinations of solvent systems for the catalyst and scavenger screenings can be carried out quickly to find optimal conditions for the photocatalyst, while using only a minimal amount of sample. This HT system should also be applicable to a range of other systems, such as inorganic photocatalysts, Z-schemes, or soluble organometallic photocatalysts.

8 Photocatalytic oxygen evolution

In the field of photocatalytic water splitting, more literature can be found on hydrogen production under sacrificial conditions. There are relatively few reports relating to the oxygen generation from polymeric materials under sacrificial condition,[90,182,183] and apart from g-C_3N_4, CTFs were also predicted[109] and found[97,98,110] to release oxygen under sacrificial conditions. Therefore, the CTF library was also investigated for oxygen evolution under sacrificial conditions.

8.1 Validation of the HT-robotic platform for the oxygen evolution

Unlike hydrogen, oxygen is an abundant gas in the earth's atmosphere at ground level making up around 21%.[184] All setups used to test for oxygen evolution face the same problem: how to reliably test potentially low performing photocatalysts when the background level of oxygen is high? A completely oxygen free environment is rather challenging, while the reduction of the oxygen background level is feasible. Often, the apparatus is evacuated before being inertised with noble gas or nitrogen. When the apparatus is flushed with noble gas, a residual level of nitrogen can moreover be used as an internal standard, while an increase during the measurement indicates a poorly sealed reactor and is used to detect leaks.[98]

The validation of the HT-robot platform was carried out using WO_3 (Sigma, ≥ 99%), which is known to be a good photocatalyst for the oxygen evolution reaction (OER).[185,186] An advantage of the HT setup is the flushing with nitrogen to minimize the amount of oxygen as background, while no vacuum is applied. When tested, it was found that a significant decrease of the oxygen level occurs within three hours, and a typical degas was scheduled for 6 h in order to be in the degas plateau region with an oxygen background level of 0.09 µmol in the entire sample (Figure 54). Whenever the background was subtracted, it is stated in the diagrams.

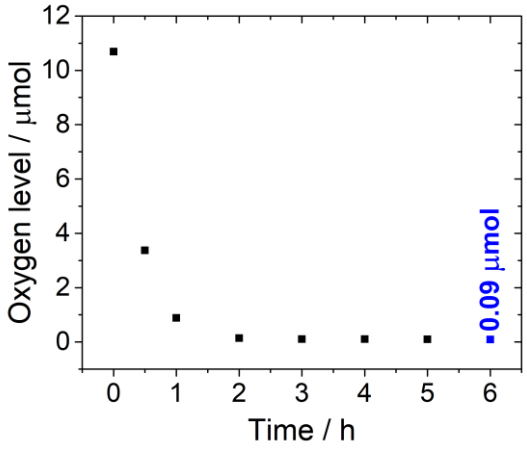

Figure 54: Oxygen level decrease for the Chemspeed Accelerator Swing platform. Empty vials were capped after 0-6 h after the nitrogen supply was opened to reduce the background level to 0.09 µmol in the entire sample. All measurement were done with six parallel vials. The error bars are too small to be visible in this graph.

In a second step, the dependency of the scavenger concentration was tested. Silver nitrate is widely used as an electron acceptor, forming colloidal silver, and was also found to work when tested with CTFs.[97] Concentrations vary in reported experiments, with values for the scavenger between 0.01 M[97] to 0.2 M for $AgNO_3$.[98] The reduction of Ag(I) is shown in equation (11).

(11) $AgNO_3 + 4\ e^- + 4\ H^+ \rightarrow 4\ Ag + 4\ HNO_3$

(12) $2\ H_2O + 4\ h^+ \rightarrow O_2 + 4\ H^+$

Therefore, concentrations of 0.001 M, 0.01 M, and 0.1 M were investigated, and 2 mg, 5 mg, and 10 mg of WO_3 as photocatalyst were used (Figure 55). While a $AgNO_3$ concentration of 0.001 M showed no increase in the OER when more photocatalyst was added, a higher amount of the photocatalyst WO_3 increased the oxygen evolution in both 0.01 M and 0.1 M $AgNO_3$ solutions. It is noteworthy to say that no linear increase in performance was seen when going from 2 mg to 5 mg, or even 10 mg, as for example in 0.01 M $AgNO_3$ the oxygen value after two hours was found to be 0.96 µmol for 2 mg WO_3, 1.33 µmol for 5 mg WO_3, and 1.65 µmol for 10 mg WO_3. For further experiments, the silver nitrate solutions were kept at 0.01 M or 0.1 M, due to the low concentration of 0.001 M being rate limiting for oxygen evolution. It was also found that the oxygen evolution decreased after two to four hours, an observation others reported as well and concluded a silver deposition on the photocatalyst blocking light, and therefore preventing irradiation to interact with the photocatalyst.[84]

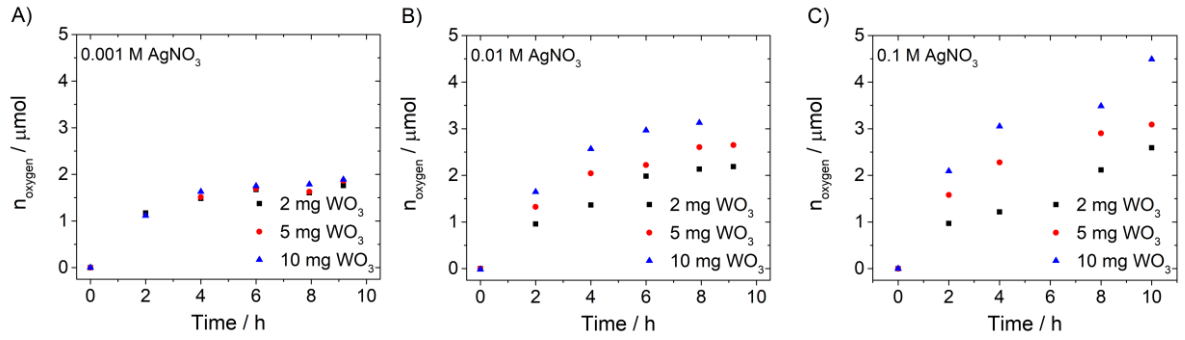

Figure 55: Concentration test of silver nitrate: A) 0.001 M, B) 0.01 M, and C) 0.1 M solutions, with WO_3 as photocatalyst (masses of 2 mg, 5 mg, and 10 mg). Single runs were carried out.

Parallel runs were then carried out to test the reproducibility of the robotic system (Figure 56). Four parallel samples were averaged for each data point, and every two hours, four vials were removed from the workflow to study the kinetics of the inverstigated system. An automated powder dispensing station (Quantos, Mettler Toledo) was used to weigh out 5 ± 0.2 mg of WO_3 in the HT-vials. In all cases, the background oxygen level was removed by subtracting oxygen levels measured for blanks in each run and the oxygen values converted to µmol g^{-1}. A total oxygen evolution of 473 ± 28 µmol g^{-1} and 531 ± 23 µmol g^{-1} were achieved in 2 h, for 10 mg of WO_3 in 0.01 M $AgNO_3$ and in 0.1 M $AgNO_3$, respectively. Similar to the experiment before, a rapid drop-off in the oxygen evolution was found after 4 h. In addition to GC analysis, the vials were opened after photocatalysis and the pH determined. A strong decrease in the pH value was found within the first two hours of photocatalysis: in the case of 0.01 M $AgNO_3$, from pH 5 to pH 3, and in the case of 0.1 M $AgNO_3$ from pH 4 to pH 3 (Figure 56). The decrease in pH correlated with a reduction in activity, indicating that the pH could additionally influence the activity of the photocatalyst, alongside potential silver depositions.

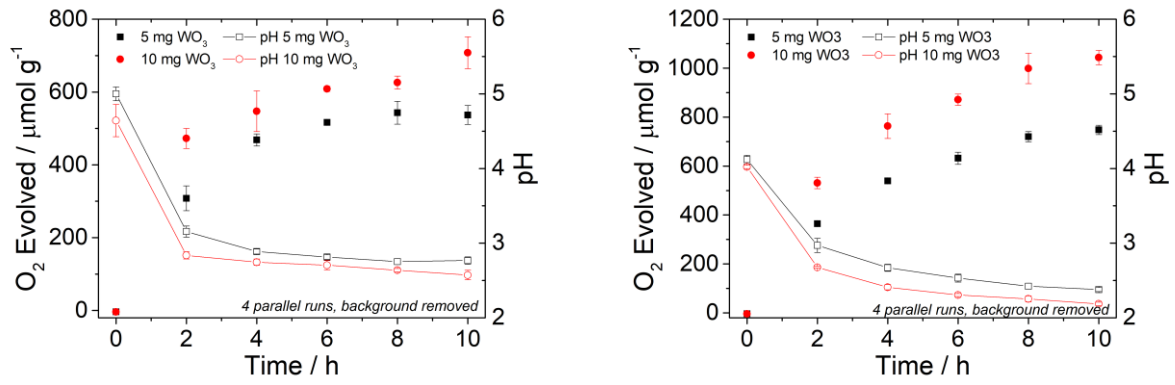

Figure 56: Parallel runs for 5 and 10 mg WO_3 in 0.01 M $AgNO_3$ (left) and 0.1 M $AgNO_3$ (right). Four vials were run for each data point, and the error bars were determined from the standard deviation. The pH values were measured after photocatalysis.

For comparison, Table 9 summarises previously reported oxygen evolution measurements using WO_3. While most tests were performed with Ag_2SO_4 as the scavenger (entries 1-4),[185] an OER of 34 µmol g^{-1} h^{-1} was found under λ > 410 nm with a 400 W xenon lamp from 0.05 M $AgNO_3$ (entry 5). This result is in the same magnitude as the investigation carried out on the HT setup (entry 6), while the higher OER measured can be explained by additional photons in the UV-region of the solar simulator spectrum.

Table 9: Overview of OER using WO_3.

Entry	Photocatalyst	Scavenger	O_2 Evolved	O_2 Evolved (converted)	Reference
1	WO_3B – 50 mg	Ag_2SO_4 – 250 µmol 5 mL glass vials	23 µmol in 20 min[a]	1380 µmol g^{-1} h^{-1}	[185]
2	WO_3 – 50 mg 99.99%	Ag_2SO_4 – 250 µmol 5 mL glass vials	11 µmol in 20 min[a]	660 µmol g^{-1} h^{-1}	[185]
3	WO_3 – 50 mg 99.9%	Ag_2SO_4 – 250 µmol 5 mL glass vials	9.8 µmol in 20 min[a]	588 µmol g^{-1} h^{-1}	[185]
4	WO_3 – 50 mg 99.5%	Ag_2SO_4 – 250 µmol 5 mL glass vials	6.5 µmol in 20 min[a]	390 µmol g^{-1} h^{-1}	[185]
5	WO_3 – 8 g/L 99.998%	$AgNO_3$ 0.05 M – 25 mL solution – Pyrex glass vials	485 µl in 3 h[b]	34 µmol g^{-1} h^{-1}	[186]
6	WO_3 – 10 mg ≥ 99%; size ≤ 20 µm	$AgNO_3$ 0.1 M – 12 mL HT vial	262 ± 24 µmol in 1 h[c]	262 ± 24 µmol g^{-1} h^{-1}	This work

[a] 400 W Hg arc λ > 300 nm – [b] 450 W Xe λ > 410 nm – [c] 20 min kinetic run

8.2 Investigation of the lower oxygen evolution rate after two hours

Due to the extended timescale between the first three measurement points at 0 h, 2 h, and 4 h, a detailed investigation was carried out with measurements conducted every 20 min for the first 3 hours, followed by measurements every 30 min up to 4 hours (Figure 57). The data was collected in parallel with four separate vials for each datapoint, and in the case of 0.01 M $AgNO_3$, a decrease in the OER was seen after 20 min. In the literature, the rate for the oxygen evolution of WO_3 from 0.1 M Ag_2SO_4 was also described to already decrease after 20 min,[185] possibly due to adsorbed silver on the photocatalyst. After 80 min, 373 ± 23 µmol g^{-1} and 335 ± 36 µmol g^{-1} oxygen was released from 0.01 M $AgNO_3$ and 0.1 M $AgNO_3$ in this work, respectively. Both values lie within the error range of each other, and the measurement in 0.1 M $AgNO_3$ shows a stable, linear response up to 80 min, while the decrease in pH also remained nearly linear with -0.74 h^{-1} over 80 min.

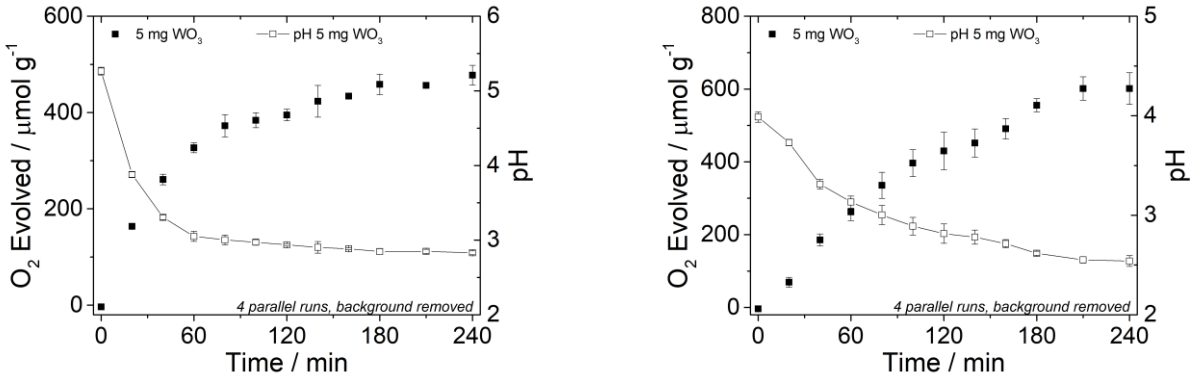

Figure 57: Parallel runs for 5 mg WO_3 in 0.01 M $AgNO_3$ (left) and 0.1 M $AgNO_3$ (right). Four vials were installed in a parallel run for each data point, and the error bars were determined from the standard deviation. The pH values were measured after photocatalysis.

It is possible that the lower activity after 80 min could be caused by a side effect of the photocatalysis reaction: the pH value lowers over time due to the production of four equivalents of protons per equivalent of oxygen produced, as seen in equation (11). According to the literature, the major reason why the OER decreases is speculated to be the silver deposition on the photocatalytic surface. While La_2O_3 is used widely as a buffer system, no report focuses on the recovery of the photocatalytic activity under sacrificial conditions. For this reason, the effect of the increasing of the pH value after the first run was investigated, by adjustment with sodium hydroxide solution.

In order to do this, the vials were opened after photocatalysis, and 25 µL (0-140 min), 50 µL (160-180 min), and 75 µL (210 min) of 0.1 M NaOH solution were added into two vials for each data point before the vials were tested again without any new $AgNO_3$ added. When the samples were tested, the cumulated irradiation time was calculated. From 0-40 min for the second run, the cumulated irradiation time is 0 min, 40 min, and 80 min, and was compared to 0 min, 40 min, and 80 min from the first run. In both series, a linear OER was found up to 80 min (Figure 58), while all data points were found to overlay up to t = 80 min.

From t ≥ 60 min in the second pH-adjusted run, the cumulated irradiation time increases drastically – i.e. 2x80 min or 2x200 min. Again, the oxygen evolved for t = 80 min in the second run overlays with the oxygen evolved in the first run (first run: 336 ± 36 µmol g^{-1}, and second run 327 ± 12 µmol g^{-1}), which indicates that the lower OER could be caused by the sacrificial conditions. For the second run, the cumulated irradiation time of t = 160 min (2 x 80min) shows a total oxygen evolution of 663 µmol g^{-1}, which is higher than that measured in the first run for t = 160 min (491 ± 28 µmol g^{-1}).

However, a slight decrease in activity was found for the second run from t ≥ 100 min, although the combined activity was still higher than in the first run (732 µmol g^{-1} for 2 x 100 min *vs.* 601 µmol g^{-1} for

210 min). These results show that the activity of the photocatalyst decreased due to the lower pH value of the solution with ongoing reaction time, but the accumulated silver deposition on the polymer does seem to decrease the OER over time.

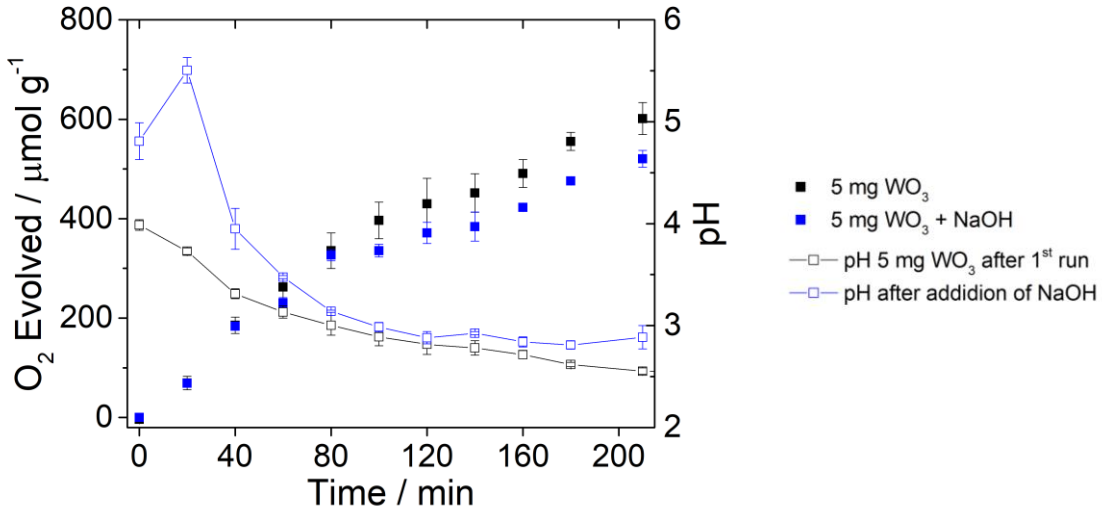

Figure 58: Oxygen evolution run for 5 mg WO_3 in 0.1 M $AgNO_3$ (black scatter) and corresponding pH values after the photocatalysis (black line). In the second run (blue scatter) vials *ex* photocatalysis were re-used, and the pH value was modified by the addition of NaOH (pH values after addition = blue line), before being tested again for photocatalysis. Values for the first run were averaged over three vials, and the second run over two vials.

8.3 Use of buffer systems for WO_3

The results of the previous section highlight the influence of the pH-value on the photocatalytic oxygen evolution rates. Three buffer systems were therefore tested: sodium acetate, H_2SO_4 buffer (pH 5 ± 0.2), and lanthanum (III) oxide. La_2O_3 is described in the literature as a buffer agent in water oxidation,[84,97] and reacts in contact with water to form lanthanum (III) hydroxide[187] (equation 12). While both lanthanum oxide and lanthanum hydroxide are insoluble in water, the formed $La(OH)_3$ acts as hydroxyl reservoir that balances the protons released from the oxygen evolution reaction (equation 13).[44,188]

(12) $La_2O_3 + 3\ H_2O \rightarrow 2\ La(OH)_3$

(13) $La(OH)_3 + 3\ HNO_3 \rightarrow La(NO_3)_3 + 3\ H_2O$

(14) $6\ AgNO_3 + 2\ La(OH)_3 \rightarrow 3\ Ag_2O + 2\ La(NO_3)_3 + 3\ H_2O$

The results of this investigation are shown in Figure 59. In comparison to the unbuffered solution with an OER of 262 ± 24 µmol g^{-1} h^{-1} after 1 h, the acetate buffer led to a significantly lower OER of 164 ± 10 mol g^{-1} h^{-1} (Table 10). When H_2SO_4 buffer is used, a small increase to 276 ± 2 µmol g^{-1} h^{-1} was

measured, and a further increase was observed for La_2O_3 at 301 µmol g^{-1} h^{-1} (15% improvement in comparison to the unbuffered solution). Furthermore, the acetate buffer was found not to be photostable - after 10 h, an increased level of 1500 ppm CO_2 was detected, while only 500 ppm was detected as the background level and in the H_2SO_4 buffer.

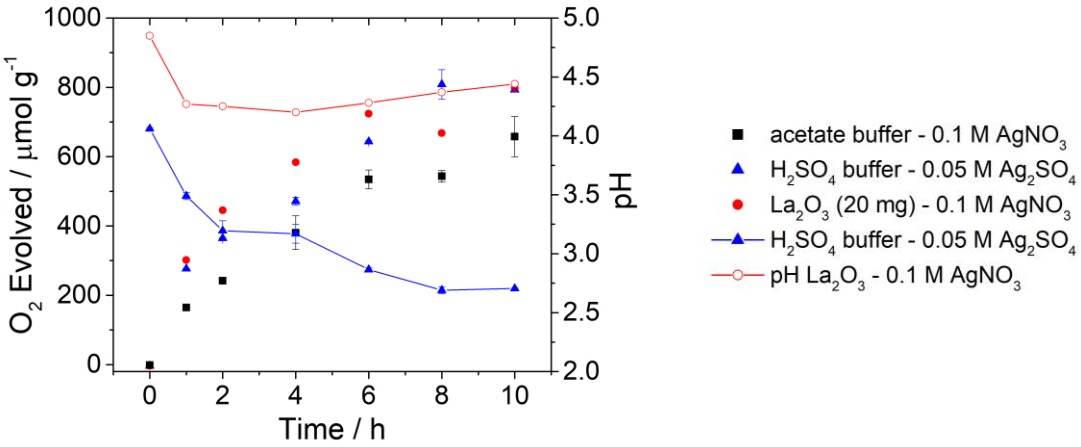

Figure 59: Oxygen evolution measurements for 5 mg WO_3 in buffer systems - 0.1 M $AgNO_3$ in combination with acetate buffer or La_2O_3, and 0.05 M Ag_2SO_4 in combination with sulfuric acid (pH 5.0 ± 0.2). The runs were carried out in duplicate, while La_2O_3 was tested in a single run. The pH values after photocatalysis are shown for H_2SO_4 buffer and La_2O_3.

In comparison to previous reports on $Sm_2Ti_2S_2O_5$, no suppression of the oxygen evolution was found in the absence of La_2O_3.[188] In all silver nitrate solutions, a decrease of the OER was found over two hours (Table 10). The unbuffered solution showed a total oxygen evolution of 430 ± 51 µmol g^{-1} after 120 min, while the La_2O_3 buffered solution was found to give a similar a total oxygen evolution of 445 µmol g^{-1} after 120 min.

Table 10: Overview of OERs for 5 mg WO_3 in $AgNO_3$ or Ag_2SO_4 for different buffer systems

Buffer	**Scavenger**	**O_2 Evolved / µmol g^{-1} (60 min)**	**O_2 Evolved / µmol g^{-1} (120 min)**
None [a]	0.1 M $AgNO_3$	262 ± 24	430 ± 51
Acetate buffer (0.1 M)	0.1 M $AgNO_3$	164 ± 10	241 ± 8
H_2SO_4 buffer (pH 5.0 ± 0.2)	0.05 M Ag_2SO_4	276 ± 2	364 ± 2
La_2O_3 (20 mg)	0.1 M $AgNO_3$	301	445

[a] Values extracted from Figure 58.

The results for WO_3 indicate that an increase of the OER can be enhanced by a higher scavenger concentration rather than the use of a specific buffer system. While WO_3 tolerates a pH range between 4.85 and 2.69 to act as an oxygen evolution photocatalyst, La_2O_3 stabilised the pH value around 4.32 ± 0.12. A recent investigation of the selectivity of WO_3 compares a protonation and

deprotonation pathway with hydrogen peroxide and oxygen as products, respectively.[189] The improvement for WO_3 as photocatalyst was found to be very low after 10 hours: in 0.1 M $AgNO_3$ with no buffer, the total amount of oxygen released was 747 ± 18 µmol g^{-1}, while the La_2O_3 buffered system was found to evolve 797 µmol g^{-1} oxygen. This results shows that silver deposition is the primary process that decreases the oxygen evolution rates of photocatalysts when silver(I) is used a scavenger.

8.4 Test of the CTF library for oxygen evolution

Next, the library of CTFs, previously studied for hydrogen evolution, were also investigated for oxygen evolution. For the screen, a 0.01 M $AgNO_3$ solution was used and the irradiation was carried out for 3 h. In the initial study, the CTF library from CTF-2 to CTF-44, and graphitic carbon nitride (commercially available Nicanite), were compared to silver nitrate blanks with an oxygen value of 0.35 µmol. However, only CTF-14 showed an increased oxygen value above the threshold with an OER of 11 µmol g^{-1} h^{-1}. While there could have been incorrectly sealed blank vials, repeated measurements still showed higher activity for CTF-14 (subsection 8.5). Another possibility for the low OERs is the potential for the absorption of oxygen by the porous polymers. However, CTF-6 (2,4-dibromo-1,1'-biphenyl) as a non-porous polymer, which for example has a SA_{BET} of 10 m^2 g^{-1}, showed a lower oxygen value than the blank. Overall, most of the vials were measured with an oxygen value of 0.15 µmol, but the four best materials were still further investigated (CTF-14, CTF-40, CTF-41, and CTF-42 - Figure 60, right).

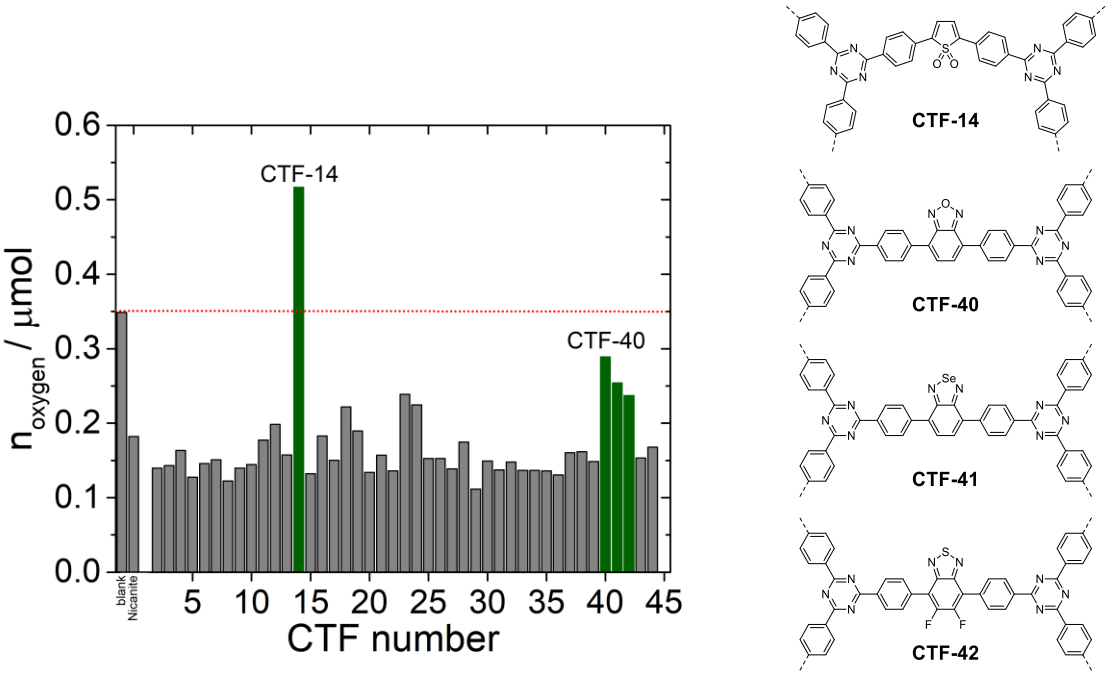

Figure 60: Oxygen evolution measurements for 5 mg CTF photocatalysts on the HT setup (left) – oxygen level detected after 3 h irradiation in 0.01 M $AgNO_3$. For comparison, Nicanite, CTF-2 and CTF-3 Suzuki were tested as well. The blank with 0.01 M $AgNO_3$ is averaged from two vials and is used as a threshold level of 0.35 µmol oxygen (red dotted line). CTF-16 and CTF-25 were tested in a separate run with a lower oxygen background level of 0.14 µmol and corrected for comparison in this graph. Structures of the four best photocatalysts shown (right).

8.5 Repeated runs for the best four photocatalysts

The four best photocatalysts from the HT-screen were retested in a separate run, with two repeats to double-check the initial results. Further, CTF-2 Suzuki, and CTF-3 Suzuki were included in this study as Wang and co-workers[110] reported these structures as oxygen evolution catalysts when synthesised from nitriles at 130 °C using triflic acid catalysis.

While the blank filled with 5.1 mL 0.01 M $AgNO_3$ solution showed an oxygen level of 0.149 ± 0.002 µmol mL^{-1}, surprisingly CTF-2 Suzuki and CTF-3 Suzuki were found to have a lower oxygen level of 0.07 µmol mL^{-1} and 0.08 µmol mL^{-1}, respectively (Figure 61). As described before, these porous polymers could potentially absorb oxygen formed during the reaction or could capture oxygen from the headspace. Unlike previous reports on CTFs,[98,110] no oxygen evolution was measured. Further, the oxygen levels were 0.971 ± 0.004 µmol for CTF-14, 0.419 ± 0.036 µmol for CTF-40, 0.284 ± 0.035 µmol for CTF-41, and 0.308 ± 0.016 µmol for CTF-42. These results confirmed that CTF-14 is indeed the best-performing oxygen evolution photocatalyst with a six-fold increase in comparison to the background level. The calculated OER for CTF-14 is 54.8 ± 0.1 µmol g^{-1} h^{-1}, while the material is not porous and has a SA_{BET} of 10 m^2 g^{-1}. CTF-40, CTF-41, and CTF-42 have OERs of 18.0 ± 2.5 µmol g^{-1} h^{-1}, 9.0 ± 2.4 µmol g^{-1} h^{-1}, and 10.6 ± 1.1 µmol g^{-1} h^{-1}. In general, these measurements can be seen as

indications for water oxidation, and additional isotopic labelling is required to confirm water as the source of oxygen.

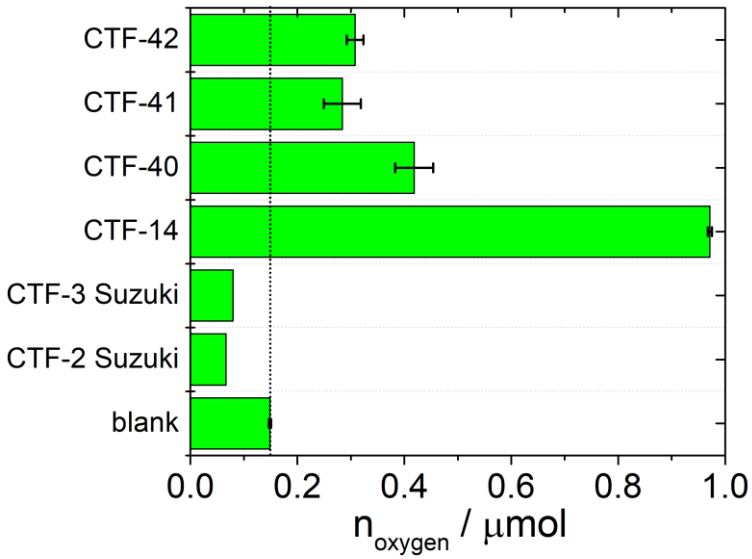

Figure 61: Oxygen evolution measurements for 5 mg CTF photocatalyst in 0.01 M $AgNO_3$ for three hours. Measurements were done with two repeats, except for CTF-2 Suzuki and CTF-3 Suzuki. The blank with 0.01 M $AgNO_3$ is averaged from two vials and is used as the threshold level of 0.15 µmol oxygen (black dotted line).

A second batch of CTF-14 was then used to further investigate the OER. The analysis showed the same result with a the band-gap of 1.55 eV for both the first and the second batch, while the photoluminescence peak was red-shifted for the second batch from 463 nm to 468 nm when excited with λ_{ex} = 280 nm. The TGA on-set temperature of 447 °C for the second batch was slightly higher than the TGA on-set temperature of 431 °C for the first batch, which indicates that a higher polymerisation was achieved in the second batch. Batch-to-batch changes in properties were reported by others on CMPs previously,[14] and in the case of CTF-14 it resulted in a higher oxygen evolution rate of 186 ± 2 µmol g^{-1} h^{-1} for the second batch, in comparison to 54.8 ± 0.1 µmol g^{-1} h^{-1} for the first batch.

Further kinetic oxygen evolution experiments were then carried out. The overall reaction time was 90 min, and every 10 min, two vials were measured for the oxygen evolution (Figure 62). After 10 min, the oxygen released was calculated to be 66 ± 15 µmol g^{-1}. However, already after 20 min, a slight decrease in the rate was observed as the total oxygen evolution was 122 ± 9 µmol g^{-1}. This short timescale matches the decrease in activity observed for WO_3 in previous reports,[186] and when tested before (subsection 8.2). Overall, the activity of the oxygen evolution continuously decreased in between 20 to 90 min, and after 90 min, a total amount of 224 ± 1 µmol g^{-1} oxygen has been evolved.

As the highest drop in activity was found after 10 minutes, which coincided with a pH drop from pH 3.95 to 3.05, the activity of the photocatalyst seems to be pH dependent. When the pH remains rather

constant around 2.82 ± 0.08 between 20 to 70 min, a stabilisation to a linear OER of around 1.4 µmol g^{-1} min^{-1} was measured.

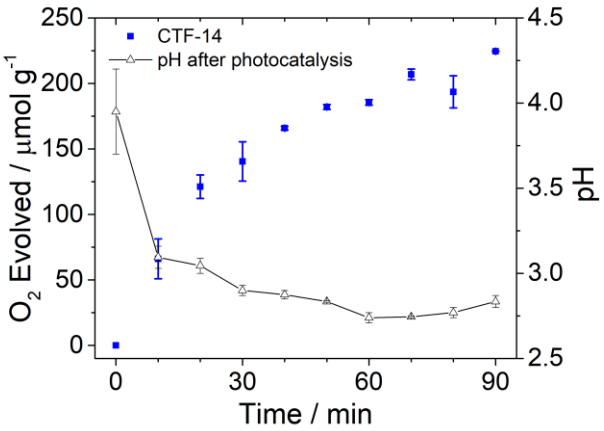

Figure 62: Oxygen evolution run for 5 mg CTF-14 in 0.01 M $AgNO_3$ for 90 min. Measurements were performed with two repeat runs, and the pH values were measured after photocatalysis.

8.6 Dispersibility improvements for CTF-14 with co-solvents

Due to the low dispersibility, CTF-14 was found to float on top of the scavenger solution. This might lead to a lower performance when irradiation is not introduced onto the top of the sample (top illumination in HT experiments, see subsection 7.4, Figure 33), as it is for the manual measurement where side illumination is used with the quartz flasks. Therefore, a co-solvent screen was carried out in 0.01 M $AgNO_3$ solution to determine which solvents decompose and release oxygen under photocatalytic conditions, with the aim of finding a co-solvent that could increase the average transmission of CTF-14. In the co-solvent test study, 10 solvents were added (10 vol. %) and tested for 10 h irradiation (Figure 63). Ethyl acetate, THF, and trifluorotoluene showed higher oxygen values than the blank at 0.35 µmol. Bis[2-(2-chlorethoxy)-ethyl]ether turned black, tetramethyl orthosilicate gelated and was not measured, and trimethyl orthoformate showed a high hydrogen release and the formation of a silver mirror. To conclude, seven co-solvents were not investigated further due to their interaction under irradiation in the scavenger solution.

The remaining four co-solvents showed an unexpected behaviour – acetone, acetonitrile, 1,4-dioxane, and *tert*-butyl methyl ether were found to decrease the oxygen content measured in comparison to the blank with an oxygen value of 0.31 µmol. In the case of acetone, the strongest decrease was found at 82 % to 0.04 µmol, followed by 1,4-dioxane with a oxygen value of 0.08 µmol. Acetonitrile and *tert*-butyl methyl ether showed a moderate decrease to 0.28 µmol and 0.25 µmol, respectively. The

decrease in the oxygen value was thought to potentially be due to a lower solubility of oxygen in these aqueous mixtures.

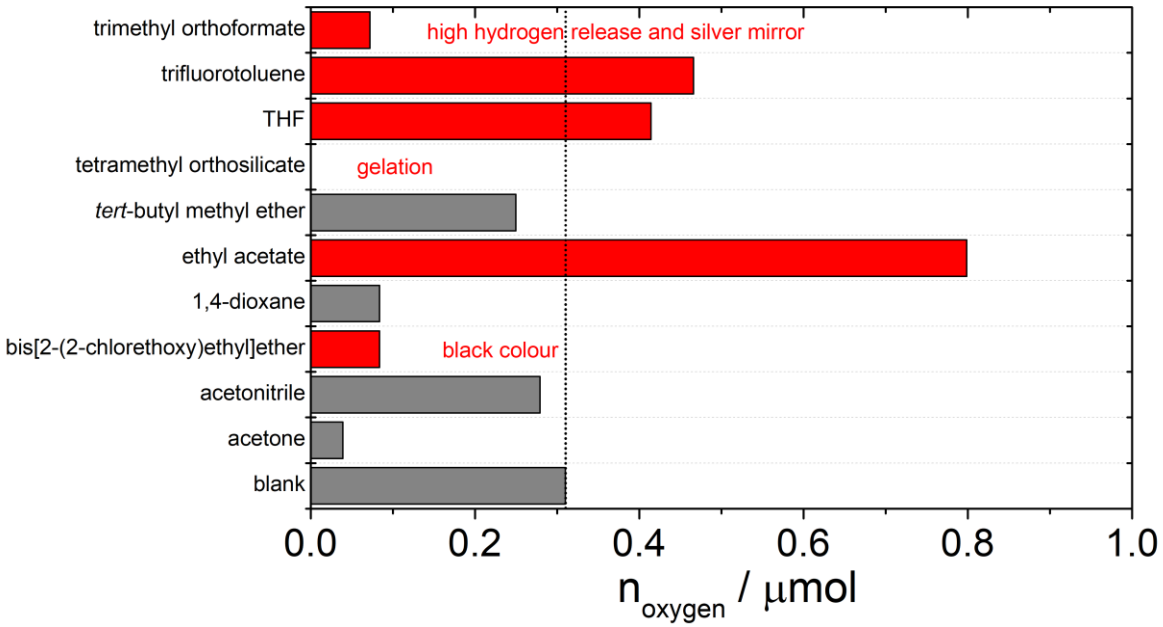

Figure 63: Co-solvent screening - oxygen determination with 0.01 M $AgNO_3$ and 10 vol. % co-solvent used. The blank with 0.01 M $AgNO_3$ is used as a threshold level of 0.31 µmol oxygen (black dotted line).

In an additional experiment, the four co-solvents (acetone, acetonitrile, 1,4-dioxane, and *tert*-butyl methyl ether) were tested for their oxygen release from 0.01 M $AgNO_3$ in presence of 20 mg La_2O_3 (Figure 64). While the oxygen amount of the blank was calculated to be 0.10 µmol in 0.01 M $AgNO_3$, an increase in the quantity of oxygen was detected for 1,4-dioxane and *tert*-butyl methyl ether, at 0.14 µmol and 0.17 µmol, respectively. Acetone and acetonitrile were again found to have a lower oxygen value of 0.03 µmol and 0.09 µmol, respectively, in comparison to the oxygen amount of 0.10 µmol of the blank (0.01 M $AgNO_3$), which indicates no interference with the scavenger under illumination for acetonitrile.

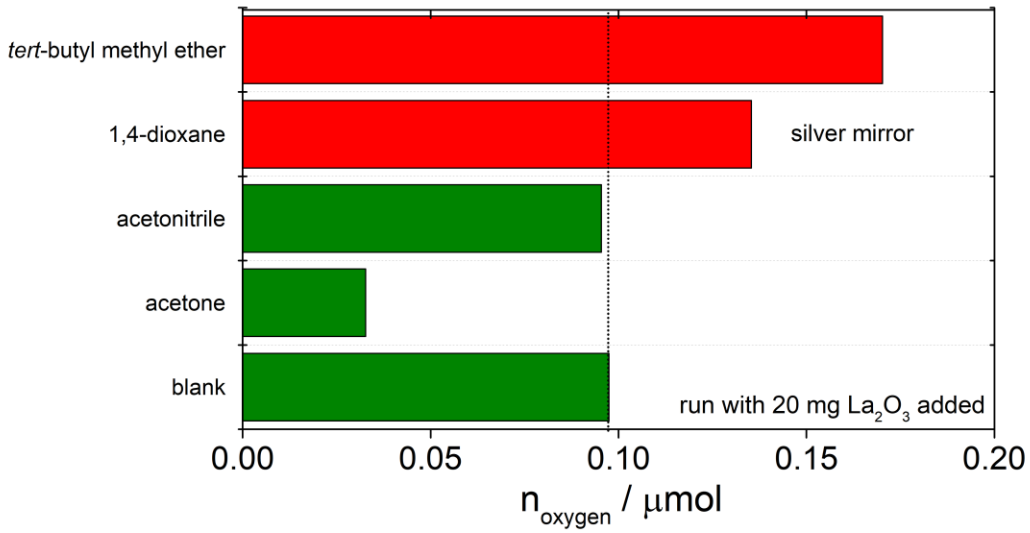

Figure 64: Co-solvent study when 20 mg La_2O_3 was added - oxygen determination in 0.01 M $AgNO_3$**.** The blank with 0.01 M $AgNO_3$ is used as a threshold level of 0.10 µmol oxygen (black dotted line).

Finally, the transmission of CTF-14 was investigated in 0.01 M $AgNO_3$ solution, and the co-solvent systems: acetone and 0.01 M $AgNO_3$ solution, and acetonitrile and 0.01 M $AgNO_3$ solution (Table 11, compare subsection 7.3). A lower average transmission of 14.0% for acetone and 15.3% for acetonitrile was found, indicating a better dispersibility of the polymer in the co-solvent solutions. In comparison, CTF-14 was found to have a high transmission of 64.4% in a neat 0.01 M $AgNO_3$ solution.

Table 11: Overview of the average transmission for CTF-14 in 0.01 M $AgNO_3$ solution and mixtures with co-solvents (10 vol. %).

Solution	Transmission / %
0.01 M $AgNO_3$	64.4
0.01 M $AgNO_3$ / 10 vol. % acetone	14.0
0.01 M $AgNO_3$ / 10 vol. % acetonitrile	15.3

8.7 Oxygen Evolution for CTF-14 with co-solvents

With improved average transmissions of the polymer achieved, a further run on the HT-setup was carried out using 0.01 M $AgNO_3$ and 20 mg La_2O_3 as pH buffer, for an illumination time of three hours to test the influence of the presence of co-solvents on the OER – Figure 65 shows the results of this screen. In short, neither acetone nor acetonitrile were found to improve the oxygen evolution of CTF-14 under these conditions. Contrary to what was expected, the lower average transmission found for photocatalysts in $AgNO_3$/co-solvents showed slightly lower oxygen evolution than in neat $AgNO_3$/La_2O_3 (OER of 171 µmol g^{-1} h^{-1}), although this result is probably within the error of the

measurement. A decrease in the oxygen evolution by 19% to 136 µmol g^{-1} h^{-1} was found for acetone, and by 7% to 158 µmol g^{-1} h^{-1} for acetonitrile.

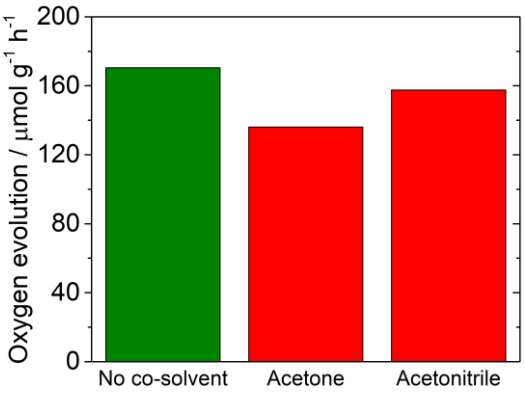

Figure 65: Co-solvent study for CTF-14 (5 mg) on the HT setup with 3 h irradiation – oxygen evolution in 0.01 M $AgNO_3$, 20 mg La_2O_3, and 10 vol. % co-solvent. No improvements in the oxygen evolution were found in comparison to the neat 0.01 M $AgNO_3$ and La_2O_3 (green bar).

One potential reason for why the co-solvents did not increase the OER might be the displacement of water molecules away from the polymers. Acetone and acetonitrile are organic solvents that will be in close contact with the organic polymer, reducing the water contact with the polymers surface. This is supported by a contact angle of 55 ± 7° for CTF-14 in water, and a transmission of 64.4% in water, compared to a lower transmission when 10 vol. % co-solvent is added (Table 11).

In two-dimensional materials such as graphitic nitride, an exfoliation was shown to break down the multi-layered structure of the polymer, while increasing the surface area to maximize the water contact, finally yielding in higher hydrogen evolution rates.[190] Unlike these polymers, the three-dimensional structure of CTFs cannot be exfoliated, while the increase in dispersibility did not correlate to an increase in the oxygen evolution rate. It also was shown that the co-solvents interfere with the polymer's ability to oxidize water.

8.8 Reproducibility of CTF-14

The reproducibility in both the synthesis, and oxygen evolution, of CTF-14 was then investigated. In total, 20 batches of CTF-14 were synthesised over four separate runs in parallel runs in a 5-position Radleys synthesis carousel. Overall, the synthetic reproducibility of CTF-14 was found to be poor. Table 11 shows a selection of batches that were analysed, with batch A and B included from the first HT screen and detailed analysis of CTF-14 for reference. For the other batches, C and D were produced from two different batches of the monomer TBPT, E had the palladium coupling catalyst and THF

replaced with a new batch, and F was synthesised with a fresh 2 M K_2CO_3 solution and a new batch of 2,5-dibromothiophenedioxide.

In all of these syntheses, the band-gap was measured between 1.55 eV and 1.57 eV, while the emission peak in the photoluminescence spectra was found between 463 nm for batch 1 and 472 nm for batch 6. Batch 2 exhibited the highest thermal stability at 447 °C determined by TGA in air, while all other batches had a lower thermal stability, ranging from 250 °C to 431 °C. This lower thermal stability indicates a lower degree of polymerisation, especially for batches 3-6. The surface areas were all found to be low, with SA_{BET} = 3 $m^2 g^{-1}$ for batch 4 up to SA_{BET} = 24 $m^2 g^{-1}$ for batch 2. Elemental analysis also confirmed batch-to-batch differences, which has been reported for CMPs previously.[14] Strong differences were found in the carbon content analysed, ranging from 56.22% (batch 3) up to 67.91% (batch 1), and the nitrogen content from 5.98% (batch 5) to 9.39% (batch 4). For batches 3-6, the evolved oxygen was also found to drop with OERs of 0-15 µmol g^{-1} h^{-1} measured.

Overall, the polymer CTF-14 was found not to be reproducible under these synthetic conditions. Even when changes of the monomer batches, catalyst, base, and solvent were tested, the OER did not reach the activity of batch 2 at 186 µmol g^{-1} h^{-1}.

Table 12: Overview of the measurements for CTF-14 batches.

CTF-14 Batch	Band-gap / eV [a]	PL max / nm [b]	TGA on-set / °C [c]	SA_{BET} / $m^2 g^{-1}$	Elemental Analysis [d]			O_2 Evolved / µmol g^{-1} h^{-1} [e]
					C / %	H / %	N / %	
A	1.55	463	431	10	67.91	3.87	6.40	55
B	1.56	468	447	24	63.66	4.03	6.71	186
C	1.57	470	348	10	56.22	3.53	6.11	0
D	1.57	468	324	3	66.45	4.44	9.39	15
E	1.56	467	309	7	58.50	4.92	5.98	12
F	1.55	472	250	16	64.74	4.36	8.47	0

[a] The optical gap was determined from the on-set of absorption in the solid-state UV-Vis spectrum; [b] λ_{em} was recorded at λ_{ex} = 280 nm; [c] TGA heating rate of 10 °C min^{-1} in air; [d] Calc. for $(C_{18}H_{10}N_2S)_n$: C, 75.50; H, 3.52; N, 9.78%; [e] tested from 0.01 M $AgNO_3$ solution on the HT-setup.

8.9 Photostability of CTF-14

The photostability of CTF-14 (batch 2) was also investigated after a 3 h run under solar simulated light. The UV-Vis spectra showed the same band-gap after photocatalysis, and the absorption is similar to the spectrum before photocatalysis (Figure 66A). The maximum of the photoluminescence spectrum is red-shifted past photocatalysis by 4 nm to 473 nm when excited with a wavelength of λ_{ex} = 280 nm

(Figure 66B). In the FT-IR spectrum (Figure 66C), some changes can be seen, and the number of FT-IR peaks decreases. Before photocatalysis, there are three peaks in the aromatic region at 1660 cm^{-1}, 1614 cm^{-1}, and 1567 cm^{-1}, while there is only one peak visible at 1613 cm^{-1} after photocatalysis. Further peaks at 1443 cm^{-1}, 1133 cm^{-1}, and 987 cm^{-1} are also missing after photocatalysis. A comparison to the spectrum of CTF-11 (2,5-dibromothiophene) showed no overlap, indicating that the reduced form of CTF-14 (2,5-dibromothiophene dioxide) is not present after photocatalysis.

The peaks around 1614 cm^{-1} and 1567 cm^{-1} were observed in CTF-5 to CTF-44, and assigned to 2,4,6-triphenyl-1,3,5-triazine co-polymer units. The absence of the peak at 1613 cm^{-1} after photocatalysis indicated a change inside the 2,4,6-triphenyl-1,3,5-triazine co-polymer unit of CTF-14. Further, the FT-IR spectrum after photocatalysis (Figure 66C) showed a hydroxyl group present in the polymer at 3453 cm^{-1} (broad peak). Combining both results, the presence of a phenol was tentatively considered by quenching an arenium ion with water.

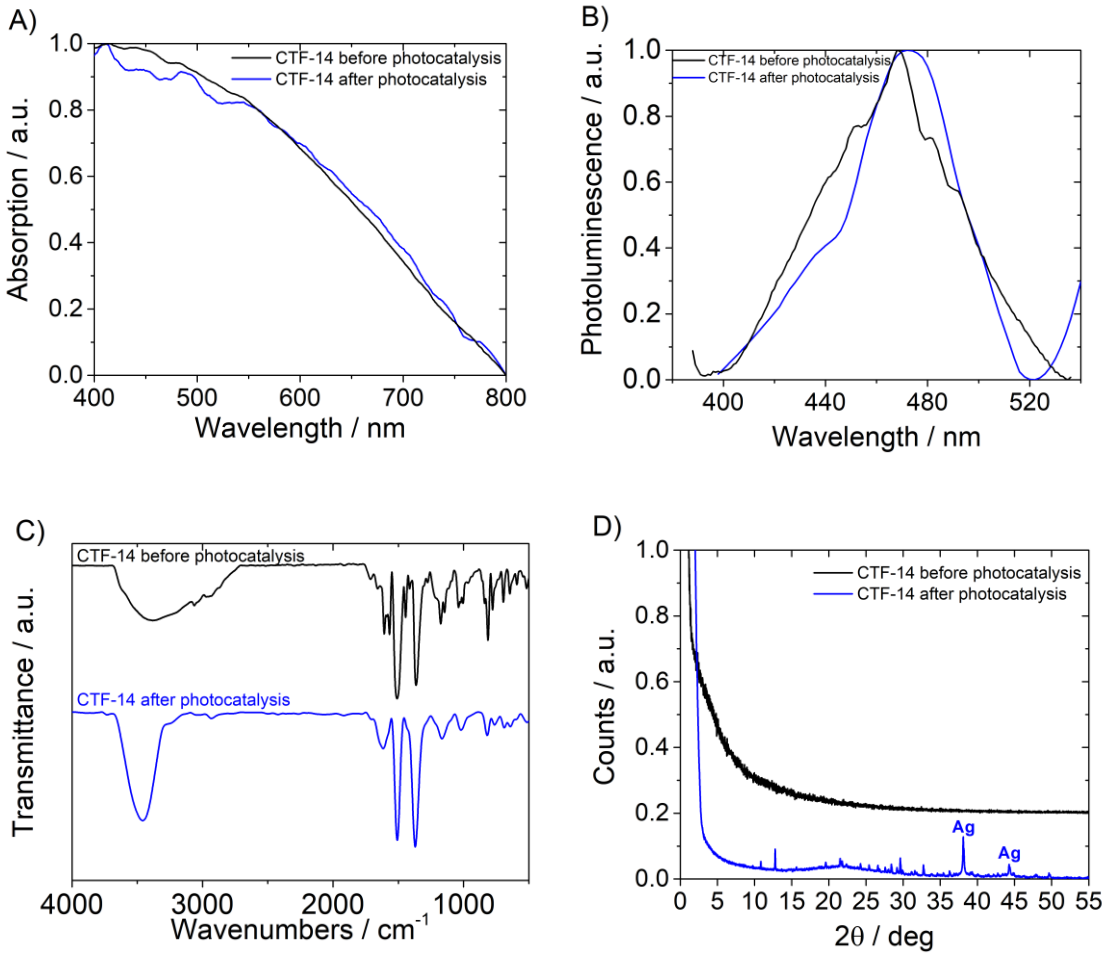

Figure 66: Photostability investigated of CTF-14 – A) UV-Vis spectra – B) Photoluminescence spectra under λ_{ex} = 280 nm – C) FT-IR spectra – D) PXRD spectra – before photocatalysis measured with the HT-sample holder and shifted by +0.2 a.u. for clarity, and after photocatalysis measured in a capillary.

In the PXRD spectra after photocatalysis (Figure 66D), many additional peaks were found between 10-55°. As described in the literature[191] and a previous report,[110] silver metal from the reduction of Ag^+ can be detected at $2\theta = 38°$ and 44° after photocatalysis. Other than that, this spectrum shows crystalline material after photocatalysis in the PXRD. In an attempt to determine what some of the crystalline components are, a PXRD comparison to the monomers 2,5-dibromothiophene dioxide and TBPT, as well as to related structures 2,4,6-tris(4-bromophenyl)-1,3,5-triazine and 2,4,6-triphenyl-1,3,5-triazine (TPT) was carried out (Figure 67). No overlay of the signal was found below $2\theta = 15°$. The comparison of the peaks between $2\theta = 15°$-33° showed that none of these four materials were present in the PXRD after photocatalysis. Further, a ^{1}H NMR spectrum in chloroform and mass spectrometry (ESI) were attempted, but both measurements were found to be not conclusive.

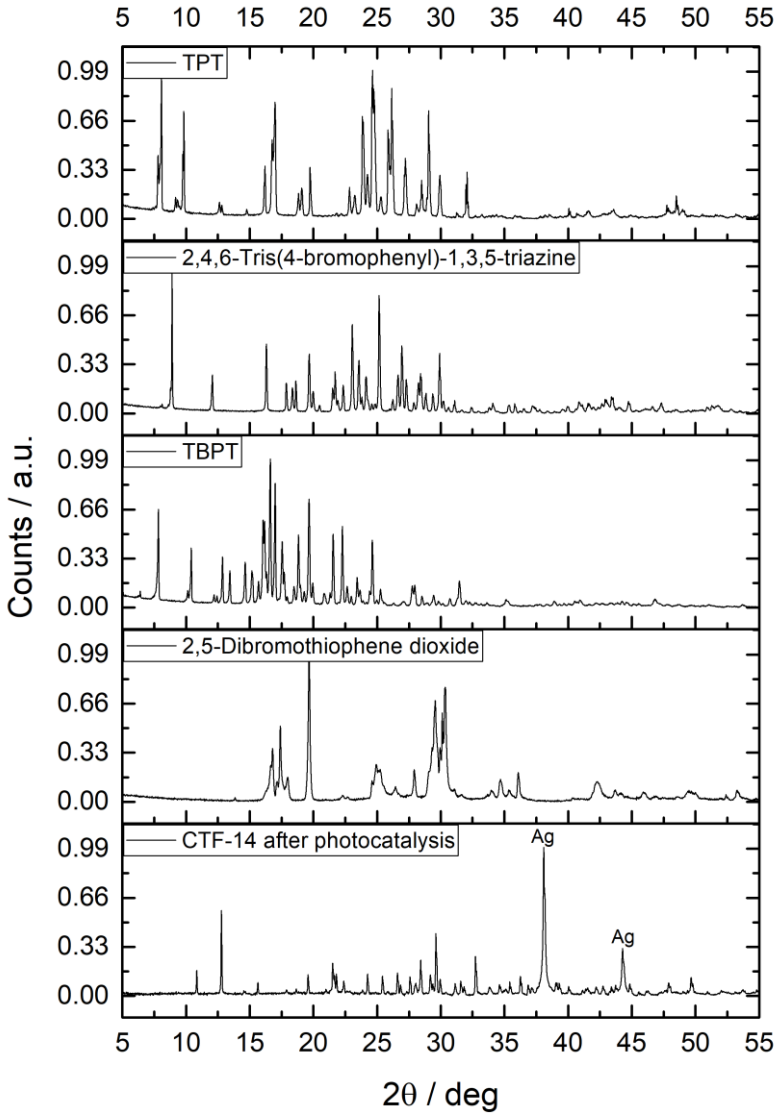

Figure 67: PXRD spectra of CTF-14 after photocatalysis compared to 2,5-dibromothiophene dioxide, TBPT, 2,4,6-tris(4-bromophenyl)-1,3,5-triazine and 2,4,6-triphenyl-1,3,5-triazine (TPT). For CTF-14 after photocatalysis, the background was removed.

8.10 Co-catalyst screening for the oxygen evolution reaction

Finally, in an attempt to improve oxygen evolution using CTFs, the use of co-catalysts was investigated. Co-catalysts are widely used in photocatalytic water-splitting, as many photocatalysts show no or low performance when tested without co-catalysts. Examples for the reduction of protons are the stable hydrogen evolution for g-C_3N_4 with platinum co-catalysts,[66] the search for optimal noble co-catalysts for g-C_3N_4 (HER for the loaded co-catalysts: Ir < Rh < Ru < Au < Pd < Pt),[161] and the study of CTFs with platinum co-catalysts.[97,124] For the oxygen evolution reaction, common co-catalysts are $Co(OH)_x$[84,110]

and RuO_2.[97,186,192] Examples of further noble metals for the oxidation of water include photodeposited gold from $AuCl_3$,[192] copper that is formed by the reduction of CuCl or $CuCl_2$ with hydrogen above 700 °C,[192] MnO_2,[193,194] Rh-nanoparticles,[195] NiO,[196] and IrO_2,[197] while the activity is pH dependent.

Therefore, using the CTF-library, 5 ± 0.5 mg photocatalyst were analysed in 0.1 M $AgNO_3$ solution with the co-catalysts RuO_2, gold, and $Co(OH)_2$ using the HT-setup. CTF-13, CTF-14, CTF-23, CTF-24, and CTF-29 were not investigated in these runs, as no polymer remained from the initial batches for testing.

All HT tests were carried out to search for hits, while the characterisation and optimisation of the CTF-co-catalyst interface was beyond the scope of this work.

The first co-catalyst tested was RuO_2 – the polymers were mixed with a stock solution of 0.7 wt. % $RuCl_3$, dried for 24 h and calcined for 16 h at 250 °C, before being illuminated under solar simulated light on the HT-setup for three hours (Figure 68). No additional wash was carried out to remove Cl^-. A threshold level of around 0.5 µmol oxygen was found for the control vials tested without photocatalyst (A) and without photocatalyst/with $RuCl_3$ (B). Overall, 23 combinations were measured with a lower oxygen level than 0.5 µmol, among them CTF-2 and CTF-3 Suzuki, while 14 polymers were found to exceed this threshold level. The three best performing materials with RuO_2 were CTF-42 (4,7-dibromo-5,6-difluorobenzo[*c*][1,2,5]thiadiazole) with an OER of 32 µmol g^{-1} h^{-1}, CTF-37 (2,7-dibromo-9*H*-carbazole) with an OER of 24 µmol g^{-1} h^{-1}, and CTF-19 (1,4-dibromotetrafluorobenzene) with an OER of 21 µmol g^{-1} h^{-1}.

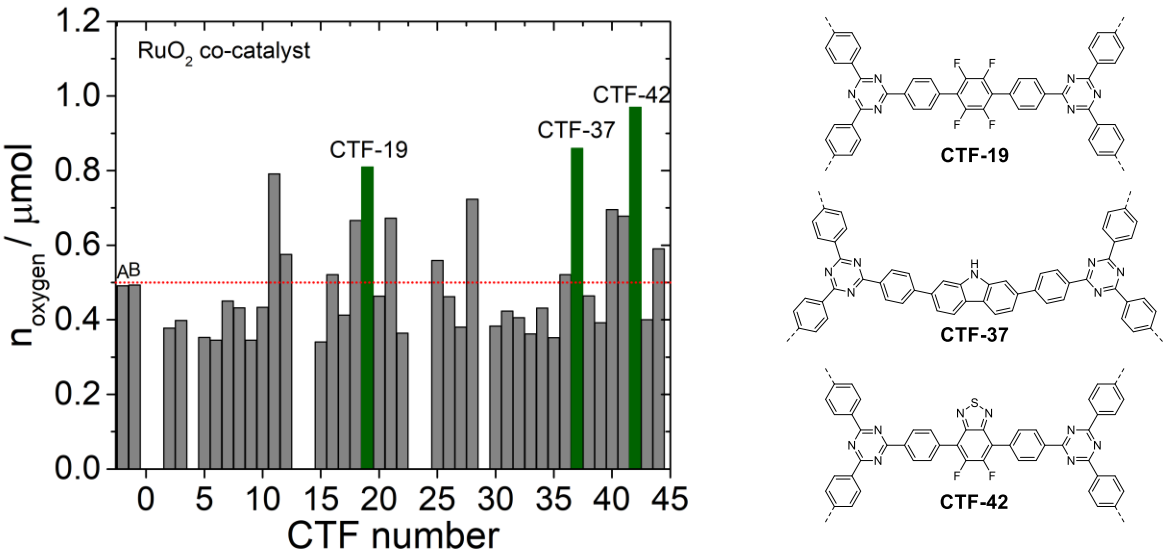

Figure 68: Ruthenium co-catalyst run for parts of the CTF library on the HT setup (left) – oxygen level detected after 3 h irradiation in 0.1 M $AgNO_3$. For comparison, CTF-2 and CTF-3 Suzuki were tested as well. A – blank test with 0.1 M $AgNO_3$; B – blank test with 0.1 M $AgNO_3$ and ruthenium chloride added giving a threshold level of 0.5 µmol oxygen (red dotted line).

CTF-13, CTF-14, CTF-23, CTF-24, and CTF-29 were not tested in this run. Structures of the three best photocatalysts shown (right).

The next co-catalyst investigated was gold. The polymers were mixed with a stock solution of $AuCl_3$, dried for 24 h at 120 °C before being tested for three hours under solar simulated light on the HT-setup (Figure 69). A threshold level of 0.58 µmol oxygen was found for the control vials tested without photocatalyst (A) and without photocatalyst/with $AuCl_3$ (B). Overall, 34 samples were measured with a lower oxygen level than 0.58 µmol, again among them were CTF-2 and CTF-3 Suzuki. With gold, the two best materials were found to be CTF-41 (4,7-dibromo-2,1,3-benzoselenadiazole) with an OER of 35 µmol g^{-1} h^{-1}, and CTF-43 (4,7-dibromo-5-fluoro-2,1,3-benzothiadiazole) with an OER of 22 µmol g^{-1} h^{-1}. Both materials could potentially form coordination bonds to gold with their selenium and sulfur heteroatoms to facilitate the oxygen evolution reaction – while further benzothiadiazoles (CTF-39 - 4,7-dibromo-2,1,3-benzothiadiazole and CTF-42 - 4,7-dibromo-5,6-difluorobenzo[c][1,2,5]-thiadiazole) were found not to have an increased OER when gold as a co-catalyst was used.

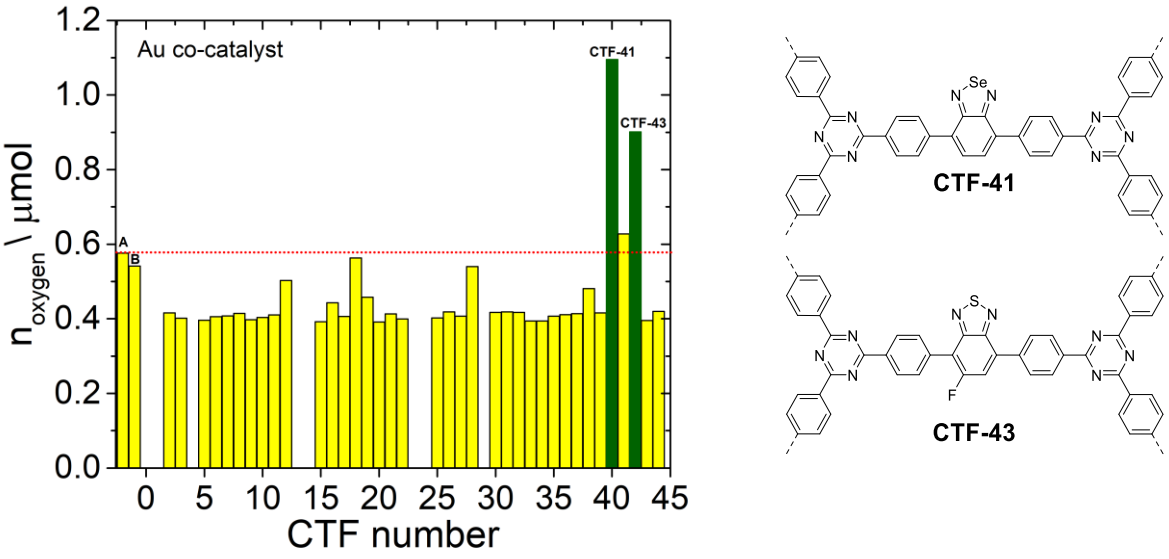

Figure 69: Gold co-catalyst run for parts of the CTF library on the HT setup (left) – oxygen level detected after 3 h irradiation in 0.1 M $AgNO_3$. For comparison, CTF-2 and CTF-3 Suzuki were tested as well. A – blank test with 0.1 M $AgNO_3$ is used as threshold level of 0.58 µmol oxygen (red dotted line); B – blank test with 0.1 M $AgNO_3$ and gold chloride added. CTF-13, CTF-14, CTF-23, CTF-24, and CTF-29 were not tested in this run. Structures of the two best photocatalysts shown (right).

Finally, a third co-catalyst, $Co(OH)_2$ was used. The polymers were mixed with a stock solution of $Co(NO_3)_2$ x $6H_2O$ for 30 min before ammonium hydroxide solution was added and the dispersion stirred for 2 hours. The polymers were then dried at room temperature and additionally for 24 h at 120 °C, before being tested for three hours under solar simulated light on the HT-setup (Figure 70). A threshold level of 0.37 µmol oxygen was found for the combination 0.1 M $AgNO_3$/$Co(OH)_2$ (B). In short,

none of the 37 polymers showed a higher oxygen level than the blank, when $Co(OH)_2$ as employed as co-catalyst.

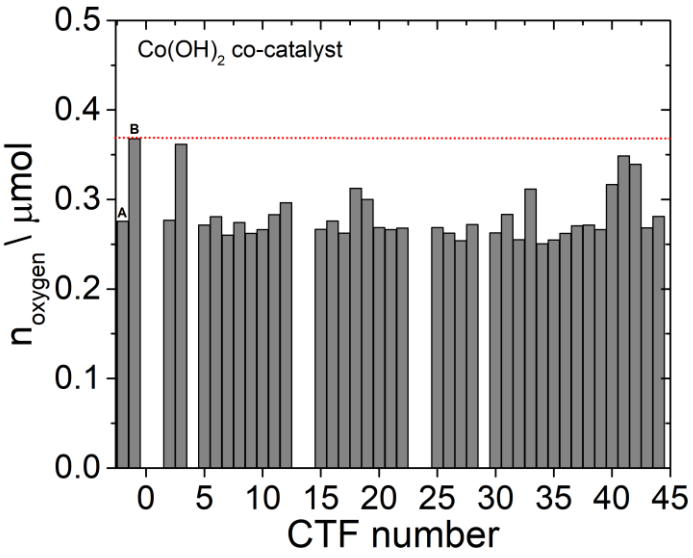

Figure 70: Cobalt hydroxide co-catalyst run for parts of the CTF library on the HT setup – oxygen level detected after 3 h irradiation in 0.1 M $AgNO_3$. For comparison, CTF-2 and CTF-3 Suzuki were tested as well. A – blank test with 0.1 M $AgNO_3$; B – blank test with 0.1 M $AgNO_3$ and cobalt hydroxide used as threshold level of 0.37 µmol oxygen (red dotted line). CTF-13, CTF-14, CTF-23, CTF-24, and CTF-29 were not tested in this run.

To conclude, the results of the CTF screen for oxygen evolution are summarised in Table 13. In total, five photocatalysts were found to evolve oxygen under sacrificial conditions using RuO_2 or gold co-catalyst, while no CTF photocatalyst was found to evolve oxygen when loaded with cobalt hydroxide as the co-catalyst. CTF-19 and CTF-37 only showed oxygen evolution when tested with the RuO_2 co-catalyst, and CTF-43 evolved oxygen when gold was used as the co-catalyst. RuO_2 was identified as the best co-catalyst for CTFs with oxygen evolution measured for three polymers (CTF-19, CTF-37, and CTF-42). For CTFs evolving no oxygen without a co-catalyst, RuO_2 was found to increase the oxygen evolution rate up to 32 µmol g^{-1} h^{-1} for RuO_2@CTF-42, which marks the second best material found in the study. In the case of the gold co-catalyst, Au@CTF-41 was found to show an OER of 35 µmol g^{-1} h^{-1} and is therefore the best performing photocatalyst for oxygen evolution tested in the screen. Unlike other polymers tested such as CTF-14 (thiophene dioxide), the two leading photocatalysts RuO_2@CTF-42 and Au@CTF-41 do not contain any oxygen in their polymeric structure, ruling out the polymer as the source of oxygen.

Table 13: Summary of CTFs for oxygen evolution.

Photocatalyst	Oxygen evolved / µmol g^{-1} h^{-1}			
	no co-catalyst [a]	RuO_2 co-catalyst [b]	Au co-catalyst [b]	$Co(OH)_2$ co-catalyst [b]
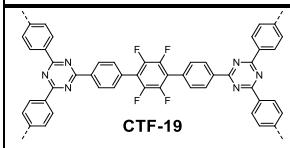 CTF-19	0	21	0	0
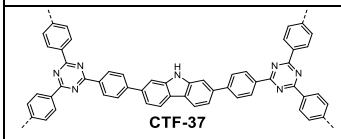 CTF-37	0	**24**	0	0
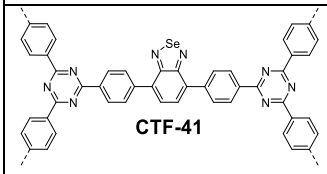 CTF-41	9	12	**35**	0
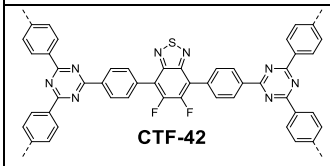 CTF-42	11	**32**	4	0
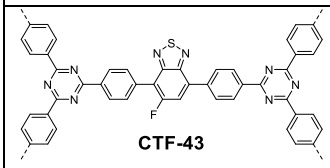 CTF-43	- [c]	0	22	0

[a] 0.01 M $AgNO_3$ – [b] 0.1 M $AgNO_3$ – [c] oxygen level below background level

8.11 Summary of photocatalytic oxygen evolution

In this chapter, the introduction of the HT-setup for the measurement of oxygen evolution was presented. The system showed repeatable results for tungsten(IV)oxide as an oxygen evolution benchmark photocatalyst. Threshold experiments for the scavenger concentration were carried out, showing that a concentration of 0.001 M $AgNO_3$ is limiting the photocatalytic activity, while 0.01 M and 0.1 M $AgNO_3$ were shown to result in higher OERs for WO_3 when a higher mass of photocatalyst was used.

Further, pH buffer systems for WO_3 were analysed to balance protons released during water oxidation. La_2O_3 was found to keep the reaction solution at a rather constant pH level over 10 hours, while the organic buffer sodium acetate was shown not to be photostable (CO_2 measured as decomposition product).

The analysis of 47 different CTF photocatalysts was presented regarding their oxygen evolution from 0.01 M silver nitrate. CTF-14 was found to be the best photocatalyst in the screen, and kinetic experiments on the HT system revealed a drop in activity after 20 min. Measurements of the pH-values after photocatalysis correlated with the drop in activity, but even under buffered conditions, the activity of the photocatalyst decreased over time. These results indicate that the photodeposition of silver on the photocatalyst is responsible for the decrease of the OER.

The activity dependency was investigated regarding the dispersibility of CTF-14 in the 0.01 M silver nitrate solution. A screen of 10 co-solvents was carried out from 0.01 M $AgNO_3$ under light irradiation, and eight co-solvents evolved oxygen on their own or in contact with La_2O_3 as buffer agent. The remaining co-solvents acetone and acetonitrile, were investigated for the oxygen evolution of CTF-14 from 0.1 M $AgNO_3$/La_2O_3, and no improvement in the oxygen evolution rate was found. This result indicates a close contact of the polymer with the organic solvent instead of water and therefore explains the lower oxygen evolution in comparison to the silver nitrate solution. After photocatalysis, it was found that the photocatalyst was not stable. New crystalline peaks were observed on the amorphous polymer background. Attempts to analyse *via* NMR spectroscopy and mass spectroscopy were not conclusive. To conclude, CTF-14 very likely decomposed during photocatalysis, and showed high OER through the release of oxygen from its co-polymer unit thiophene dioxide.

Finally, co-catalyst screens were carried out using the CTF-library and $Co(OH)_2$, RuO_2, and gold. Unlike previous reports for graphitic carbon nitride, cobalt was not found to act as co-catalyst. Gold worked in combination with CTF-41 (4,7-dibromo-2,1,3-benzoselenadiazole) and showed an OER of 35 µmol g^{-1} h^{-1}. However, RuO_2 was identified as the most promising photocatalyst for CTFs, and the best material of the screen was found to be RuO_2@CTF-42 with an OER of 32 µmol g^{-1} h^{-1}. The exact loading of the co-catalyst needs to be further analysed to conclude if a higher loading caused higher OER.

9 Conclusion and outlook

In this work, the synthesis, characterisation, and performance of 47 polymers for both the hydrogen and oxygen evolution from water was presented. All structures were constructed from covalent triazine- based frameworks. Seven polymers were produced from phenylene linkers in the range of phenylene to quarterphenylene to compare the influence of the synthetic route on the photocatalytic activity. A trade-off was found between the maximal driving force and the light absorption necessary to drive the hydrogen reduction. From the first report of photocatalytically active CTFs in 2015, the performance could be improved tenfold, with the best photocatalyst, named CTF-2, showing HER of around 300 µmol g^{-1} h^{-1} (Figure 71). The photocatalytic activity was found to be very similar for polymers synthesised by triflic acid catalysis and Suzuki-Miyaura polycondensation, with some minor variation in the optical properties. In both sets of the CTFs, UV-Vis spectra revealed a decrease in the optical gap with an increase of the phenylene spacers. Further, the role of palladium was investigated for CTFs – while no activity was found for palladium free CTFs, the polymers were found to evolve hydrogen with additional platinum as co-catalyst. Palladium residues from the synthesis step were found to act as a co-catalyst for the hydrogen evolution reaction, while a doubling of the hydrogen evolution rates was achieved with platinum co-catalyst.

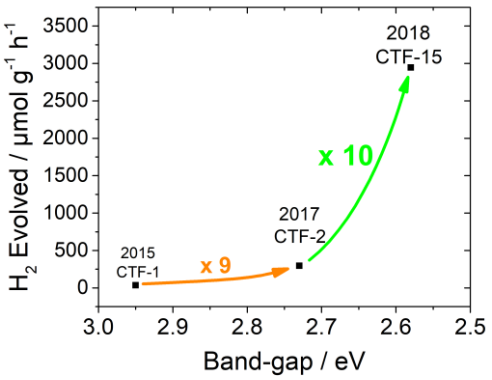

Figure 71: Improvements of hydrogen evolution rates for CTFs under λ > 420 nm: CTF-1 (water/TEOA/3 wt.% Pt), CTF-2 (water/TEOA/3 wt. % Pt), and CTF-15 (water/TEA/MeOH/3 wt. % Pt)

The majority of polymers were produced for a structurally diverse library of CTFs, and were synthesised by the Suzuki-Miyaura polycondensation. Forty different polymers were made and showed evolution rates ranging from 0-3000 µmol g^{-1} h^{-1}, with the best polymer having additional cyano groups present (CTF-15). Compared to CTF-1 in 2015, a 90-fold increase was found (Figure 71).

A large part of this research was focussed on developing the necessary high-throughput screens. For hydrogen evolution, the results were compared to manual kinetic measurements and the time saving aspect highlighted. Both measurement approaches were able to identify the best performing photocatalysts for the hydrogen reduction. Further, the photocatalysts were tested with different scavengers for the hydrogen reduction, and a smaller amount of catalyst was necessary in comparison to manual runs. While theoretical calculations are not able to predict structures of high performing hydrogen photocatalysts so far, the ability to measure a huge library of photocatalyst has been realised.

Further, the CTF photocatalysts were tested on the HT setup for oxygen evolution from water. Again, the time saving aspect of the HT-setup is key in this development and initial results were presented. The HT-system was validated with tungsten(IV) oxide photocatalyst, and buffer systems were found to stabilise the pH-value. Nevertheless, the buffers were not found to prevent the decrease in oxygen evolution, indicating a photodeposition of silver on the photocatalyst. The HT-system was shown to be sensitive for the oxygen detection of polymeric photocatalysts. The most active photocatalyst CTF-14 was tested extensively, while the results of the oxygen evolution rate were comparable to tungsten(IV) oxide. The analysis of CTF-14 after photocatalysis showed decomposition products, indicating the limited stability of the polymer and probable oxygen release from the thiophene dioxide linker present in the polymer.

Co-catalyst screens for the CTF-library were also carried out with ruthenium (III) chloride, gold chloride, and cobalt nitrate. After alkaline workup of cobalt nitrate, the formed cobalt hydroxide was not found to act as a co-catalyst for CTFs. In contrast, oxygen was detected from photodeposited Au@CTF in four combinations with CTF polymers, and RuO_2@CTF in five combinations. Oxygen evolution rates up to 35 µmol g^{-1} h^{-1} were measured for Au@CTF-41 (4,7-dibromo-2,1,3-benzoselenadiazole). To confirm water as the source of oxygen, the use of mass spectrometry and ^{18}O-labelled water needs to be carried out – a m/z distribution with 32 ($^{16}O^{16}O$), 34 ($^{18}O^{16}O$), and 36 ($^{18}O^{18}O$) would be visible. So far, this experiment could not be carried out as the oxygen evolution rates are too low.

The screen of the CTF-library identified azoles as the most promising subset for the oxygen evolution reaction (Figure 72). Among them, two CTFs contain thiadiazole units as linkers (CTF-42 and CTF-43), while one CTF contained a selenadiazole linker (CTF-41), and another contained an oxadiazole linker (CTF-40). As a suggestion for the continuing work on this project, two ideas are proposed. First, the use of microwave synthesis to speed up the synthesis steps for the Suzuki-Miyaura

polycondensation[198] can be introduced. Instead of reaction times of hours, the synthesis time could be reduced to 20 min.

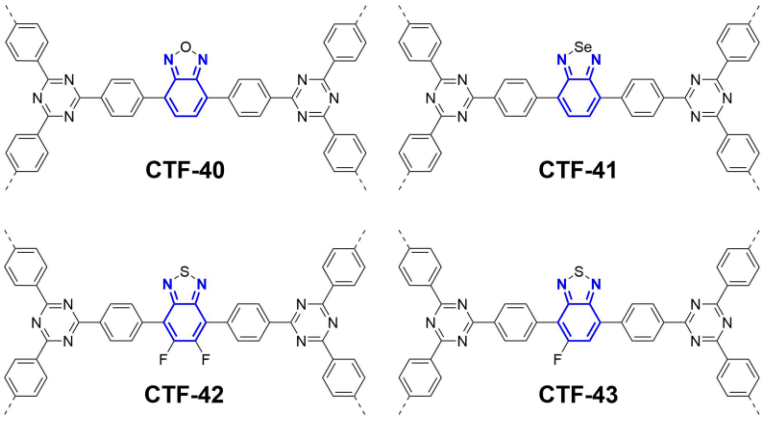

Figure 72: Active CTF photocatalysts containing azole linkers for the oxygen evolution from 0.1 M $AgNO_3$ and co-catalysts.

Further, the use of modified benzothiadiazole or benzoselenadiazole monomers could be investigated. There are variations of thiadiazoles in 5 and 6 positions (Figure 73) that could be used in further screens. Among them, there are incorporated pyridine units (M45-M47, commercially available), and a system based on 4,8-dibromobenzo[1,2-*c*;4,5-*c*']bis[1,2,5]thiadiazole (M48, commercially available). As the use of 5-fluoro-2,1,3-benzothiadiazole in CTF-43, and 5,6-difluorobenzo[*c*]-[1,2,5]thiadiazole in CTF-42 indicated, the electronegative substituents seems to increase the OER. Further EWG could also be introduced such as cyanides (M49+M50),[199,200] or nitrogroups (M51+M52, both commercially available).

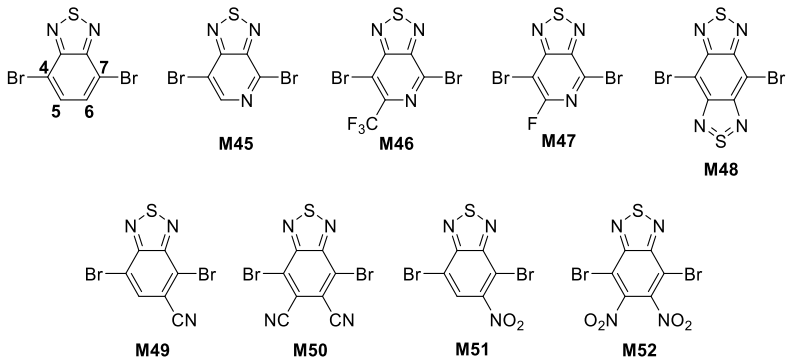

Figure 73: Proposed azole linkers for oxygen evolution experiments.

Moreover, the influence of sulfur and selenium could be investigated. Thiadiazoles and selenadiazoles can be synthesised from 4,5-difluoro-1,2-benzenediamine (Figure 74) in two steps to get 5,6-difluoro-4,7-diiodo-2,1,3-benzothiadiazole (M53), and 5,6-difluoro-4,7-diiodo-2,1,3-benzoselenadiazole (M54).[201] Building on (M53) and (M54), further variations at the 5- and 6-position are proposed. 4,7-

diiodo-2,1,3-benzothiadiazole-5,6-dicarbonitrile (M55) and 4,7-diiodo-2,1,3-benzoselenadiazole-5,6-dicarbonitrile (M56) can be synthesised using KCN.[202] Oxy- and thio- substitution in the 5-and 6-positions can lead to the monomers M57-M60, while the ether or thioethers can also be varied.[203] For solubility improvements, alkyl or polyethylene glycol chains could, for example, be added to make the polymer solution processable.[92] For the synthesis of monofluorinated azoles, 4-fluoro-1,2-benzenediamine is proposed to be tested to produce analogues of M55-M60. As shown in the literature, polymers can also be functionalised after polymerisation.[203] The library of CTFs already holds two benzothiadiazoles that can be used for test reactions: CTF-42 and CTF-43, synthesised from 4,7-dibromo-5,6-difluorobenzo[*c*][1,2,5]thiadiazole and 4,7-dibromo-5-fluoro-2,1,3-benzothiadiazole, respectively.

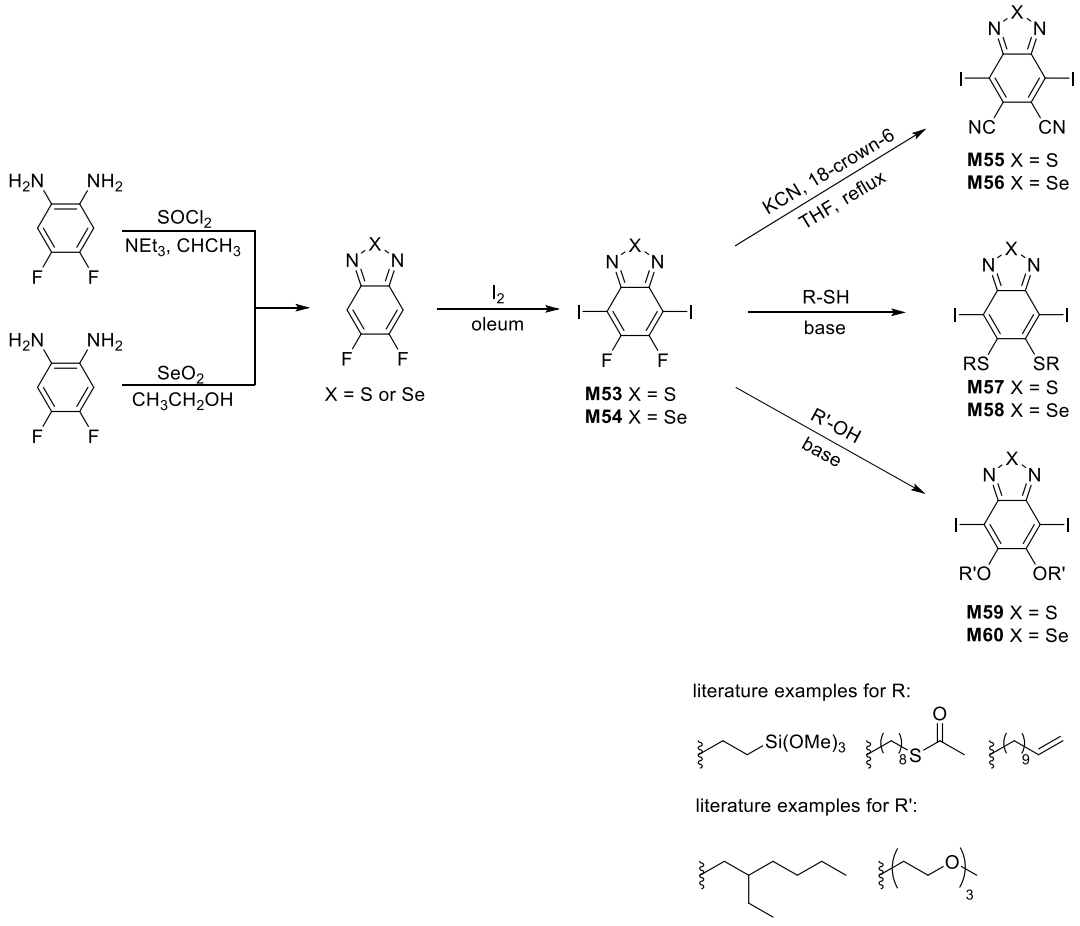

Figure 74: Synthesis of azole linkers from 4,5-difluoro-1,2-benzenediamine to synthesize M53 and M54.[201] Further steps can lead to a variation of the 5- and 6-position in benzothiadiazole and benzoselenadiazole: the use of KCN to obtain M55 and M56,[202] the use of thioalcohols to obtain M57 and M58 analogues,[203] and the use of alcohols to access M59 and M60 analogues.[203]

Once a successful oxygen evolution catalyst is found, the test for overall water-splitting can be carried out: for example, by connecting two light absorbers *via* a Z-scheme with a redox shuttle.[51] A stepwise investigation is highly advised, as materials not evolving hydrogen or oxygen are not likely to start to

work as photocatalysts when brought together for simultaneous gas evolutions. Still, the combination of hydrogen evolution catalyst, oxygen evolution catalyst, co-catalysts, redox-couples, and pH value leads to a large number of experiments and the detection of hydrogen and oxygen remains challenging. This large amount of variations could be carried out at with the introduced HT-workflow.

In summary, it was demonstrated that CTFs play in important role as hydrogen and oxygen evolution photocatalysts. The field of photocatalysis will develop away from hydrogen and oxygen evolution, as photocatalysts are explored for CO_2 reduction,[204] and chemical conversions.[205] Initial studies within the Cooper group have already been carried out with CTFs and show promising results.

For all of these experiments, the new high-throughput system developed here plays an important role. It has possible future applications in the screening and composition of photocatalysts, the testing of photocatalyst mixtures or composite materials – all such ideas can be tested in a short timescale to investigate directions of photocatalysis. For the less explored oxygen evolution reactions, the HT system is a fast measurement option that might help to accelerate the discovery of oxygen evolution catalysts. In the future, combinatorial materials science will produces large libraries that need high-throughput screening techniques to deal with the amount of samples synthesised. Overall, the increase of polymeric photocatalysts, and the understanding of the materials properties, can lead to a breakthrough discovery in the field of photocatalysis.

10 Experimental section

10.1 Analytical methods

^{1}H NMR spectra were recorded on a Bruker Avance 400 MHz spectrometer in $CDCl_3$ or dmso-d_6 at 25 °C. $^{13}C\{^{1}H\}$ NMR spectra were recorded at 101 MHz in $CDCl_3$ at 25 °C. All spectra are reported in ppm and are referenced to TMS at 0 ppm. Mass spectrometry was performed using an Agilent QTOF 7200 Spectrometer. Transmission FT-IR spectra were recorded on a Bruker Tensor 27 at room temperature; samples were prepared as KBr pellets. CHN Analysis was performed on a Thermo EA1112 Flash CHNS-O Analyzer using standard microanalytical procedures. Thermogravimetric analysis was performed on a TA instruments Q5000IR analyzer by heating samples at 10 °C min^{-1} under air in open aluminium pans from room temperature to 600 °C, and holding at 600 °C for 30 minutes. UV-Vis spectra and fluorescence spectra of the polymer powders were measured in the solid-state using a Shimadzu UV-Vis spectrometer and Shimadzu RF-5301PC fluorescence spectrometer at room temperature, respectively. Imaging of the polymer morphology was achieved on a Hitachi S4800 Cold Field Emission SEM, with secondary electron, backscatter, and transmission detectors. PXRD measurements were performed on a PANalytical X'Pert PRO MPD, with a Cu X-ray source, used in high-throughput transmission mode with Kα focusing mirror and PIXCEL 1D detector. TCSPC experiments were recorded on an Edinburgh Instruments LS980-D2S2-STM spectrometer with picosecond pulsed LED excitation sources and a R928 detector with a stop count rate below 5%. The instrument response was measured with colloidal silica (LUDOX® HS-40, Sigma-Aldrich) and the decays fitted in Fluoracle (Edinburgh Instruments). Nitrogen sorption isotherms were measured using a Micromeritics 2420 volumetric adsorption analyser. Average transmissions were recorded on a Turbiscan AGS from Formulaction. The pH-values of the reaction solutions were determined with a Mettler Toledo SevenMulti pH meter which was calibrated before the measurement.

10.2 Manual hydrogen evolution experiments

The reaction mixtures were prepared in a quartz flask and side-illuminated with a 300 W Newport Xe light-source (Model: 6258, Ozone free) for the time specified. For the illumination under simulated sun light, an Oriel LSH-7320 ABA LED-based Solar Simulator with an output of 1.00 sun was used (classification ICE 60904-9 2007: spectral match A, uniformity classification B, temporal stability A). The laser adjustment of the instrument was used to adjust the distance of the reaction flask. Gas samples were taken using a gas-tight syringe, and run on a Bruker 450-GC gas chromatograph equipped with a Molecular Sieve 13X 60-80 mesh 1.5 m × ⅛" × 2 mm *ss* column at 50 °C with an argon

flow of 40.0 mL min^{-1}. Hydrogen was detected with a thermal conductivity detector referencing against standard gas with a known concentration of hydrogen. Hydrogen dissolved in the reaction mixture was not measured and the pressure increase generated by the evolved hydrogen was neglected in the calculations. The rates were determined from a linear regression fit and the error is given as the standard deviation of the amount of hydrogen evolved. No hydrogen evolution was observed for mixtures of water/triethanolamine/H_2PtCl_6 or water/TEA/H_2PtCl_6 under $\lambda > 420$ nm, U-340 cut-off filter and $\lambda > 295$ nm illumination in the absence of a photocatalyst. The pH-values of the reaction solutions were determined after the photocatalysis experiments with a Mettler Toledo SevenMulti pH meter which was calibrated before the measurement.

10.3 Robotic hydrogen and oxygen evolution experiments

Vials (Agilent Technologies, crimp top, headspace, clear with graduation marks and write-on spot, flat bottom, 10 mL, 23 x 46 mm) were charged with 5.0 ± 0.1 mg of polymer powders (unless otherwise stated), and transferred to the Chemspeed Accelerator - SWING for liquid transfer. In the case of WO_3, 2 ± 0.5 mg, 5 ± 0.5 mg, and 10 ± 0.5 mg of WO_3 were weighed into the vials using an automated powder dispensing station (Quantos, Mettler Toledo). Degassed stock solutions were loaded into the robotic platform, and water from an ELGA water purification system was degassed with nitrogen and connected to the setup before the system was flushed with nitrogen from the house supply for the number of hours stated. The automatic setup reads out a CSV file with the amounts of liquids specified, dispenses the liquids and seals the vials with Agilent Technologies caps (crimp, headspace, with septum, 20 mm, silver aluminium cap with safety feature, molded PTFE/butyl septum). In the oxygen evolution runs, the total volume of the reaction mixture was set to 5.1 mL, containing water (1.6 mL), triethylamine (1.7 mL), methanol (1.7 mL) and H_2PtCl_6 solution (0.1 mL, 0.24 wt. % in H_2O). After the run is finished, the vials are manually shaken for 5 seconds and transferred to an ultrasonic bath to disperse the polymers in the reaction mixture. An Oriel solar simulator 94123A with an output of 1.0 Sun was used to illuminate the vials on a Stuart roller bar SRT9 for the time specified (classification IEC 60904-9 2007 spectral match A, uniformity classification A, temporal stability A, 1600 W Xenon lamp, 12 x 12 inch output beam, Air Mass 1.5G filter, 350-1000 nm). After photocatalysis, the samples are measured on an Agilent Technologies GC 7890B connected to an Agilent Technologies headspace sampler 7697A. No hydrogen evolution was observed for mixtures of water/triethylamine/methanol or water/triethylamine/methanol/H_2PtCl_6 under solar illumination in the absence of a photocatalyst. For the scavenger screenings of Na_2S, $FeCl_2$, NaI pH 5.0, ascorbic acid, EDTA pH 8.0, water/MeOH, cysteine, thiophenol, phenol and hydroquinone, no hydrogen was detected from the blanks. In the case of other compositions of scavengers, the concentrations used are stated.

10.4 Co-catalyst screen for oxygen evolution

Vials (Agilent Technologies, crimp top, headspace, clear with graduation marks and write-on spot, flat bottom, 10 mL, 23 x 46 mm) were charged with 5.0 ± 0.5 mg of polymer powders for each run. For the ruthenium loaded polymers (0.7 wt. %), 50 µL $RuCl_3$ stock solution in water (0.035 wt. %) was mixed with the polymers.[97] After drying, the mixture was calcined in air at 250 °C for 12 hours to achieve RuO_2@CTF. The cobalt hydroxide loaded polymers[84] (3 wt. %) were synthesised by adding 100 µL $Co(NO_3)_2$ x 6 H_2O stock solution in water (3 wt. %) to the polymers. After mixing for 30 min, 1 mL ammonium hydroxide solution (28 - 30%) was added, and the dispersion was mixed for another 60 min. The samples were dried at 120 °C to achieve $Co(OH)_2$@CTF. In both cases, the vials were filled with water and silver nitrate stock solution before being capped under a nitrogen atmosphere. For the gold loaded polymers (0.1 wt. %),[192] 100 µL $AuCl_3$ stock solution in water (5 wt. %), water and silver nitrate stock solution in water were transferred by the Chemspeed Accelerator – SWING to the vials containing the polymer powders, before the vials were capped under a nitrogen atmosphere. In these three runs, a silver nitrate concentration of 0.1 M was used.

10.5 Synthesis of 2,4,6-tris(4-bromophenyl)-1,3,5-triazine

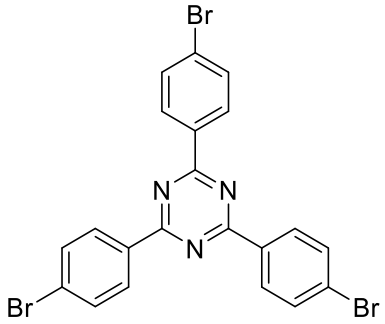

Trifluoromethanesulfonic acid (8.40 mL, 95.2 mmol) and 15 mL $CHCl_3$ were added to a 500 mL round-bottom flask under nitrogen and a solution of 4-bromobenzonitrile (5.25 g, 28.8 mmol) in 60 mL chloroform was added *via* a syringe pump at a rate of 2 mL min^{-1}. After the addition, the reaction was heated to 50 °C for 48 hours, cooled to room temperature, and added to 100 mL of aqueous ammonia solution (28.0-30.0% NH_3 basis) to neutralise the acid. The suspension was left stirring for 10 min after the addition of the ammonia solution. The resulting solid was collected by filtration and washed with 40 mL methanol twice, before the product was purified by trituration from 120 mL THF and dried under vacuum at 60 °C overnight to afford the product as a pale white solid (4.32 g, 81%). ^{1}H NMR (400 MHz, $CDCl_3$): δ 8.61 (d, *J* = 8.5 Hz, 6H), 7.72 (d, *J* = 8.5 Hz, 6H); $^{13}C\{^1H\}$ NMR (100 MHz, $CDCl_3$): δ 134.8, 132.0, 130.5, 127.9 (a carbon atom in the triazine ring could not be assigned due to the weak

signal intensity); HRMS (CI, CH_4): m/z calc. for $C_{21}H_{13}Br_3N_3$: 543.8660 $[M+H]^+$ found 543.8654; CHN analysis calc. for $C_{21}H_{12}N_3$: C, 46.19; H, 2.22; N, 7.70%, found C, 46.06; H, 2.27; N 7.63%.

10.6 Synthesis of 2,4,6-tris[4-(4,4,5,5-tetramethyl-1,3,2-dioxaborolan-2-yl)phenyl]-1,3,5-triazine

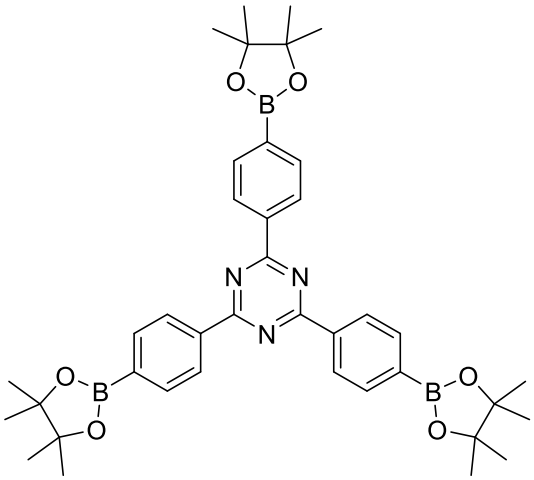

A mixture of 2,4,6-tris(4-bromophenyl)-1,3,5-triazine (1.0 g, 1.83 mmol), bis(pinacolato)diboron (2.421 g, 9.53 mmol), potassium acetate (831 mg, 6.01 mmol), $[Pd(dppf)]Cl_2$ (54.0 mg, 0.07 mmol), and $[Pd(dppf)]Cl_2$ x DCM (62.5 mg, 0.08 mmol) was added to a round-bottom flask and evacuated for 2 min under vacuum. The flask was flushed with nitrogen before THF (12 mL, anhydrous) was added and the solution was stirred at 66 °C for 20 h under a nitrogen atmosphere. The reaction mixture was cooled to room temperature, poured into 200 mL of water and the solid collected by filtration. A pale yellow solid was obtained by trituration from MeOH in 78% yield (988 mg). ^{1}H NMR (400 MHz, $CDCl_3$): δ 8.75 (d, *J* = 8.0 Hz, 6H), 8.01 (d, *J* = 8.0 Hz, 6H), 1.40 (s, 36H); $^{13}C\{^1H\}$ NMR (100 MHz, $CDCl_3$): δ 171.8 138.6, 135.0, 128.1, 84.1, 24.9 (a carbon atom in the triazine ring could not be assigned due to the weak signal intensity); MP: 296 °C; HRMS (CI, NH_3): m/z calc. for $[M+H]^+$ 687.3895; found 687.3876 (100%), $[C_{33}H_{38}B_2N_3O_4]^+$ 562.3004 (96), $[C_{27}H_{27}BN_3O_2]^+$ 436.2163 (28); IR (ν_{max}/cm^{-1}) 2980 (m), 1512 (s), 1350 (s), 1142 (m), 1084 (m), 1018 (m), 959 (m), 857 (w), 810 (m), 740 (m), 655 (m); CHN analysis calc. for $C_{39}H_{48}B_3N_3O_6$: C, 68.16; H, 7.04; N, 6.11%, found C, 67.07; H, 6.90; N 6.11%.

The reaction was monitored by ^{1}H NMR spectroscopy. To monitor the progress of the reaction, a 0.5 mL aliquot of the reaction solution was taken, mixed with 5 mL of water in a vial, filtered, and the solid was dried at the rotary evaporator. The chemical shift of the reactant in chloroform-d can be seen at δ = 8.61 and 7.72 ppm, while the product signals appear at δ = 8.75 and 8.01 ppm. A further product signal of the pinacol ester is visible at δ = 1.40 ppm. Complete borylation was usually detected

after 24 hours, and in the cases where the NMR spectrum revealed unfinished catalysis, additional 0.1 equivalent of bis(pinacolato)diboron were added before refluxing for another 24 hours.

10.7 Synthesis of [1,1':4',1''-terphenyl]-4,4''-dicarbonitrile

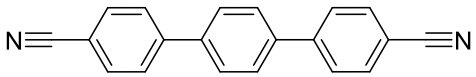

Under an argon atmosphere, benzene-1,4-diboronic acid (500 mg, 3.02 mmol, 1 eq), 4-cyanobenzeneboronic acid pinacol ester (1.37 g, 7.54 mmol, 2.5 eq), and $[Pd(PPh_3)_4]$ (85 mg, 57.3 µmol, 2 mol% Pd) were dissolved in THF (40 mL). A solution of 2 M aqueous Na_2CO_3 (3 mL) was added and the reaction mixture was refluxed for 24 h. After cooling to room temperature, the reaction mixture was diluted with hexane and water, and the solid collected by filtration. Column chromatography with DCM/hexane (v/v 3.5:1.2) gave the product in 35% yield (300 mg). ^{1}H NMR (400 MHz, $CDCl_3$): δ 7.80 (d, J = 4.4 Hz, 8H), 7.72 (one signal, 4H); $^{13}C\{^1H\}$ NMR (100 MHz, $CDCl_3$): δ 144.7, 139.4, 132.8, 128.0, 127.7, 118.8, 111.4; HRMS (CI, CH_4): m/z calc. for $[M+H]^+$ 281.1080, found 281.1073 (100%), $[C_{20}H_{13}N_3]^+$ 281.1073 (100); CHN analysis calc. for $C_{20}H_{12}N_2$: C, 85.69; H, 4.31; N, 9.99%, found C, 85.31; H, 4.27; N 9.67%. The NMR data is in accordance with literature values.[126]

10.8 Synthesis of [1,1':4',1'':4'',1'''-quaterphenyl]-4,4'''-dicarbonitrile CM 61

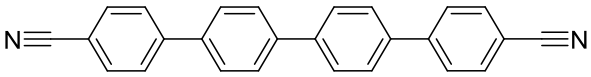

Under an argon atmosphere, 4,4'-dibromobiphenyl (904 mg, 2.9 mmol) and 4-cyanophenylboronic acid (894 mg, 6.08 mmol), CsF (1.76 g, 5.8 mmol), and $[Pd(PPh_3)_4]$ (168 mg, 5 mol% Pd) were dissolved in anhydrous THF (100 mL) and refluxed for 72 h. After cooling to room temperature, the reaction mixture was diluted with hexane and water and the solid was collected by filtration. Column chromatography with DCM/hexane (v/v 1:0.5) gave the product in 23% yield (240 mg). ^{1}H NMR (400 MHz, dmso-d_6): δ 7.96 (8 H, m), 7.91 (8 H, one signal); $^{13}C\{^1H\}$ NMR (100 MHz, dmso-d_6): δ 133.4, 128.2, 127.9, 127.8 (the quaternary carbon atoms could not be assigned due to the weak signal intensity); HRMS (CI, CH_4): m/z calc. for $[M+H]^+$ 357.1395, found 357.1386 (100%); CHN analysis calc. for $C_{26}H_{16}N_2$: C, 87.62; H, 4.52; N, 7.86%; found C, 87.25; H, 4.54; N 7.85%. The NMR data are in accordance with literature.[127]

10.9 Synthesis of 3,7-dibromodibenzo[*b,d*]thiophene 5,5-dioxide[206]

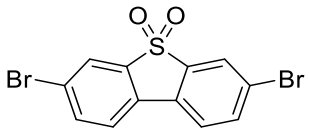

Dibenzothiophene sulfone (10 g, 46.24 mmol) was dissolved in H_2SO_4 (300 mL). *N*-bromosuccinimide (16.87 g, 94.79 mmol) was added portion wise and the resulting solution was stirred at 25°C in the dark for 2 days, before being poured into 1 L of water/ice. The solid was collected by filtration, and washed with water until neutral. The white powder was dried under vacuum, and recrystallised from chlorobenzene twice to get the product in 72% yield (12.4 g). ^{1}H NMR (400 MHz, $CDCl_3$): δ 7.94 (2H, d, *J* = 1.7 Hz), 7.78 (2H, dd, *J* = 8.2, 1.7 Hz), 7.64 (2H, d, *J* = 8.2 Hz); $^{13}C\{^1H\}$ NMR (100 MHz, $CDCl_3$): 139.0, 137.1, 129.6, 125.6, 124.6, 122.9; HRMS (CI, CH_4): m/z calc. for $[M+H]^+$ 267.0228, found 267.0223 (100%); CHN analysis calc. for $C_{12}H_6Br_2O_2S$: C, 38.53; H, 1.62%, found C, 38.67; H, 1.63%. The NMR data are in accordance with literature.[207]

10.10 Synthesis of CTF-1 to CTF-4

General procedure for the acid catalysed trimerisation polymerisation

Trifluoromethanesulfonic acid and $CHCl_3$ were added to a round-bottom flask under nitrogen, and a solution of the monomer dissolved in chloroform was added *via* a syringe pump at a rate of 2 ml min^{-1}. The reaction was stirred at room temperature for 48 hours before it was poured into an aqueous ammonia solution (28.0-30.0% NH_3 basis) to neutralise the trifluoromethanesulfonic acid. The suspension was left stirring for 1 hour after the addition of the ammonia solution. The resulting solid was filtered, collected by filtration, and washed successively with dichloromethane, ethanol, water, and methanol. The samples were dried under reduced pressure at 75 °C overnight to obtain the polymer.

CTF-1: Trifluoromethanesulfonic acid (2.83 mL, 32.0 mmol), $CHCl_3$ (5.00 mL) and 1,4-dicyanobenzene (513 mg, 4.00 mmol) in 40 mL $CHCl_3$ were used in the polymerisation. After the addition of the monomer, the solution was heated to 50 °C for 1 day, cooled to room temperature, and with the general procedure continued. After work-up, the product was obtained as a white powder (328 mg) in 63% yield. CHN analysis calc. for $(C_4H_2N)_n$: C, 74.99; H, 3.15; N, 21.86%, found: C, 57.71; H, 3.72; N, 15.88%.

CTF-2: Trifluoromethanesulfonic acid (2.83 mL, 32.0 mmol), $CHCl_3$ (5.00 mL) and 4,4'-biphenyldicarbonitrile (817 mg, 4.00 mmol) in 40 mL $CHCl_3$ were used in the polymerisation. After work-up, the product was obtained as a pale yellow powder (600 mg) in 73% yield. CHN analysis calc. for $(C_7H_4N)_n$: C, 82.33; H, 3.95; N, 13.72%, found: C, 75.88; H, 3.81; N, 12.21%, found for the ball milled sample: C, 75.62; H, 3.81; N, 12.17%.

CTF-3: Trifluoromethanesulfonic acid (0.40 mL, 4.48 mmol), $CHCl_3$ (0.10 mL) and [1,1':4',1''-terphenyl]-4,4''-dicarbonitrile (157 mg, 560 µmol) in 0.56 mL $CHCl_3$ were used in the polymerisation. After work-up, the product was obtained as a pale green powder (110 mg) in 70% yield. CHN analysis calc. for $(C_{10}H_6N)_n$: C, 85.69; H, 4.31; N, 9.99%, found: C, 81.54; H, 4.57; N, 8.90%.

CTF-4: Trifluoromethanesulfonic acid (0.40 mL, 4.48 mmol), $CHCl_3$ (0.10 mL) and [1,1':4',1'':4'',1'''-quarter-phenyl]-4,4'''-dicarbonitrile (200 mg, 560 µmol) in 0.56 mL $CHCl_3$ were used in the polymerisation. After work-up, the product was obtained as a pale green powder (164 mg) in 82% yield. CHN analysis calc. for $(C_{13}H_8N)_n$: C, 87.62; H, 4.52; N, 7.86%, found: C, 82.39; H, 4.47; N, 7.55%.

10.11 Synthesis of CTF-2 Suzuki to CTF-4 Suzuki

General procedure for the Pd(0)-catalysed Suzuki-Miyaura polycondensation:

The flask was charged with the monomers, *N,N*-dimethylformamide, and an aqueous solution of K_2CO_3 (2.0 M), and the solution degassed by bubbling with N_2 for 30 minutes. [$Pd(PPh_3)_4$] (1.2 mol %) was added and the solution was re-degassed by bubbling with N_2 for 10 minutes, before being heated to 150 °C for 48 hours. The mixture was cooled to room temperature and poured into water. The precipitate was collected by filtration and washed with water and methanol. Further purification of the polymer was carried out by Soxhlet extraction using cyclopentyl methyl ether for two days and the product was dried under reduced pressure at 75 °C.

CTF-2 Suzuki: 2,4,6-Tris[4-(4,4,5,5-tetramethyl-1,3,2-dioxaborolan-2-yl)phenyl]-1,3,5-triazine (500 mg, 728 µmol), 2,4,6-tris(4-bromophenyl)-1,3,5-triazine (397 mg, 728 µmol), *N,N*-dimethylformamide (10.9 mL), aqueous K_2CO_3 (2.0 M, 2.18 mL) and [$Pd(PPh_3)_4$] (10.1 mg, 1.2 mol %) were used in the polymerisation. After work-up, the product was obtained as a pale white powder (440 mg) in 98% yield. CHN analysis calc. for $(C_7H_4N)_n$: C, 82.33; H, 3.95; N, 13.72%, found: C, 69.26; H, 4.84; N 9.00%.

CTF-3 Suzuki: 1,4-Benzenediboronic acid (182 mg, 1.10 mmol), 2,4,6-tris(4-bromophenyl)-1,3,5-triazine (400 mg, 733 µmol) *N,N*-dimethylformamide (16.5 mL), aqueous K_2CO_3 (2.0 M, 3.3 mL) and [$Pd(PPh_3)_4$] (15 mg, 1.2 mol %) were used in the polymerisation. After work-up, the product was obtained as a pale green powder (225 mg) in 73% yield. CHN analysis calc. for $(C_{10}H_6N)_n$: C, 85.69; H, 4.31; N, 9.99%, found: C, 79.60; H, 4.49; N 8.97%.

CTF-4 Suzuki: 4,4'-Biphenyldiboronic acid bis(pinacol) ester (71.7 mg, 177 µmol), 2,4,6-tris(4-bromophenyl)-1,3,5-triazine (64.3 mg, 118 µmol) *N,N*-dimethylformamide (2.65 mL), aqueous K_2CO_3 (2.0 M, 0.53 mL) and [$Pd(PPh_3)_4$] (2.40 mg, 1.2 mol %) were used in the polymerisation. After work-up, the product was obtained as a pale green powder (45.0 mg) in 71% yield. CHN analysis calc. for $(C_{13}H_8N)_n$: C, 87.62; H, 4.52; N, 7.86%, found: C, 67.89; H, 3.89; N 6.12%.

10.12 Synthesis of CTF-5 to CTF-44

The general procedure for the Pd(0)-catalysed Suzuki-Miyaura polycondensation was used for all preparations – see subsection 10.11 for the method and Figure 25 for structures.

CTF-5: 2,4,6-Tris[4-(4,4,5,5-tetramethyl-1,3,2-dioxaborolan-2-yl)phenyl]-1,3,5-triazine (500 mg, 728 µmol), 1,3-dibromobenzene (257 mg, 1.09 mmol), *N,N*-dimethylformamide (10.9 mL), aqueous K_2CO_3 (2.0 M, 2.18 mL) and $[Pd(PPh_3)_4]$ (10.1 mg, 1.2 mol %) were used in the polymerisation. After work-up, the product was obtained as a grey powder (283 mg) in 92% yield. CHN analysis calc. for $(C_{20}H_{12}N_2)_n$: C, 85.69; H, 4.31; N, 9.99%, found: C, 78.75; H, 4.24; N 8.22%.

CTF-6: 2,4,6-Tris[4-(4,4,5,5-tetramethyl-1,3,2-dioxaborolan-2-yl)phenyl]-1,3,5-triazine (500 mg, 728 µmol), 2,4-dibromo-1,1'-biphenyl (340 mg, 1.09 mmol), *N,N*-dimethylformamide (10.9 mL), aqueous K_2CO_3 (2.0 M, 2.18 mL) and $[Pd(PPh_3)_4]$ (10.1 mg, 1.2 mol %) were used in the polymerisation. After work-up, the product was obtained as a brown (376 mg) in 96% yield. CHN analysis calc. for $(C_{26}H_{16}N_2)_n$: C, 87.62; H, 4.52; N, 7.86%, found: C, 78.37; H, 4.30; N 6.59%.

CTF-7: 2,4,6-Tris[4-(4,4,5,5-tetramethyl-1,3,2-dioxaborolan-2-yl)phenyl]-1,3,5-triazine (500 mg, 728 µmol), 3,5-dibromo-1,1'-biphenyl (340 mg, 1.09 mmol), *N,N*-dimethylformamide (10.9 mL), aqueous K_2CO_3 (2.0 M, 2.18 mL) and $[Pd(PPh_3)_4]$ (10.1 mg, 1.2 mol %) were used in the polymerisation. After work-up, the product was obtained as a grey powder (381 mg) in 97% yield. CHN analysis calc. for $(C_{26}H_{16}N_2)_n$: C, 87.62; H, 4.52; N, 7.86%, found: C, 74.53; H, 4.23; N 6.11%.

CTF-8: 2,4,6-Tris[4-(4,4,5,5-tetramethyl-1,3,2-dioxaborolan-2-yl)phenyl]-1,3,5-triazine (500 mg, 728 µmol), 2,7-dibromotriphenylene (421 mg, 1.09 mmol), *N,N*-dimethylformamide (10.9 mL), aqueous K_2CO_3 (2.0 M, 2.18 mL) and $[Pd(PPh_3)_4]$ (10.1 mg, 1.2 mol %) were used in the polymerisation. After work-up, the product was obtained as a pale green powder (468 mg) in 99% yield. CHN analysis calc. for $(C_{32}H_{18}N_2)_n$: C, 89.28; H, 4.21; N, 6.51%, found: C, 64.52; H, 3.40; N 4.43%.

CTF-9: 2,4,6-Tris[4-(4,4,5,5-tetramethyl-1,3,2-dioxaborolan-2-yl)phenyl]-1,3,5-triazine (500 mg, 728 µmol), 9,10-dibromoanthracene (367 mg, 1.09 mmol), *N,N*-dimethylformamide (10.9 mL), aqueous K_2CO_3 (2.0 M, 2.18 mL) and $[Pd(PPh_3)_4]$ (10.1 mg, 1.2 mol %) were used in the polymerisation. After work-up, the product was obtained as a bright yellow powder (356 mg) in 85% yield. CHN analysis calc. for $(C_{28}H_{16}N_2)_n$: C, 88.40; H, 4.24; N, 7.36%, found: C, 82.15; H, 4.16; N 6.74%.

CTF-10: 2,4,6-Tris[4-(4,4,5,5-tetramethyl-1,3,2-dioxaborolan-2-yl)phenyl]-1,3,5-triazine (500 mg, 728 µmol), 2,5-dibromofuran (246 mg, 1.09 mmol), *N,N*-dimethylformamide (10.9 mL), aqueous K_2CO_3 (2.0 M, 2.18 mL) and $[Pd(PPh_3)_4]$ (10.1 mg, 1.2 mol %) were used in the polymerisation. After

work-up, the product was obtained as a bright yellow powder (234 mg) in 79% yield. CHN analysis calc. for $(C_{18}H_{10}N_2O)_n$: C, 79.99; H, 3.73; N, 10.36%, found: C, 75.75; H, 3.79; N 9.48%.

CTF-11: 2,4,6-Tris[4-(4,4,5,5-tetramethyl-1,3,2-dioxaborolan-2-yl)phenyl]-1,3,5-triazine (500 mg, 728 µmol), 2,5-dibromothiophene (264 mg, 1.09 mmol), *N,N*-dimethylformamide (10.9 mL), aqueous K_2CO_3 (2.0 M, 2.18 mL) and $[Pd(PPh_3)_4]$ (10.1 mg, 1.2 mol %) were used in the polymerisation. After work-up, the product was obtained as an orange powder (297 mg) in 95% yield. CHN analysis calc. for $(C_{18}H_{10}N_2S)_n$: C, 75.50; H, 3.52; N, 9.87%, found: C, 68.07; H, 3.69; N 8.10%.

CTF-12: 2,4,6-Tris[4-(4,4,5,5-tetramethyl-1,3,2-dioxaborolan-2-yl)phenyl]-1,3,5-triazine (500 mg, 728 µmol), 2,5-dibromoselenophene (315 mg, 1.09 mmol), *N,N*-dimethylformamide (10.9 mL), aqueous K_2CO_3 (2.0 M, 2.18 mL) and $[Pd(PPh_3)_4]$ (10.1 mg, 1.2 mol %) were used in the polymerisation. After work-up, the product was obtained as a yellow powder (276 mg) in 75% yield. CHN analysis calc. for $(C_{18}H_{10}N_2Se)_n$: C, 64.88; H, 3.02; N, 8.41%, found: C, 62.72; H, 3.17; N 8.48%.

CTF-13: 2,4,6-Tris[4-(4,4,5,5-tetramethyl-1,3,2-dioxaborolan-2-yl)phenyl]-1,3,5-triazine (500 mg, 728 µmol), 2,5-dibromothiazole (265 mg, 1.09 mmol), *N,N*-dimethylformamide (10.9 mL), aqueous K_2CO_3 (2.0 M, 2.18 mL) and $[Pd(PPh_3)_4]$ (10.1 mg, 1.2 mol %) were used in the polymerisation. After work-up, the product was obtained as a grey powder (118 mg) in 37% yield. CHN analysis calc. for $(C_{17}H_9N_3S)_n$: C, 71.06; H, 3.16; N, 14.62%, found: C, 73.18; H, 4.20; N 12.10%.

CTF-14: 2,4,6-Tris[4-(4,4,5,5-tetramethyl-1,3,2-dioxaborolan-2-yl)phenyl]-1,3,5-triazine (500 mg, 728 µmol), 2,5-dibromothiophene dioxide (299 mg, 1.09 mmol), *N,N*-dimethylformamide (10.9 mL), aqueous K_2CO_3 (2.0 M, 2.18 mL) and $[Pd(PPh_3)_4]$ (10.1 mg, 1.2 mol %) were used in the polymerisation. After work-up, the product was obtained as a brown powder (177 mg) in 51% yield. CHN analysis calc. for $(C_{18}H_{10}N_2S)_n$: C, 75.50; H, 3.52; N, 9.78%, found: C, 67.91; H, 3.87; N 6.4%.

CTF-15: 2,4,6-Tris[4-(4,4,5,5-tetramethyl-1,3,2-dioxaborolan-2-yl)phenyl]-1,3,5-triazine (500 mg, 728 µmol), 2,5-dibromobenzonitrile (285 mg, 1.09 mmol), *N,N*-dimethylformamide (10.9 mL), aqueous K_2CO_3 (2.0 M, 2.18 mL) and $[Pd(PPh_3)_4]$ (10.1 mg, 1.2 mol %) were used in the polymerisation. After work-up, the product was obtained as a pale brown powder (309 mg) in 82% yield. CHN analysis calc. for $(C_{21}H_{11}N_3)_n$: C, 82.61; H, 3.63; N, 13.76%, found: C, 75.36; H, 3.58; N 12.23%.

CTF-16: 2,4,6-Tris[4-(4,4,5,5-tetramethyl-1,3,2-dioxaborolan-2-yl)phenyl]-1,3,5-triazine (500 mg, 728 µmol), 2,5-dibromo-1,4-benzenedicarbonitrile (312 mg, 1.09 mmol), *N,N*-dimethylformamide (10.9 mL), aqueous K_2CO_3 (2.0 M, 2.18 mL) and $[Pd(PPh_3)_4]$ (10.1 mg, 1.2 mol %) were used in the polymerisation. After work-up, the product was obtained as a dark yellow powder (355 mg) in 98% yield. CHN analysis calc. for $(C_{22}H_{10}N_4)_n$: C, 79.99; H, 3.05; N, 16.96%, found: C, 70.42; H, 3.79; N 14.14%.

CTF-17: 2,4,6-Tris[4-(4,4,5,5-tetramethyl-1,3,2-dioxaborolan-2-yl)phenyl]-1,3,5-triazine (500 mg, 728 µmol), 2,5-dibromoaniline (274 mg, 1.09 mmol), *N,N*-dimethylformamide (10.9 mL), aqueous K_2CO_3 (2.0 M, 2.18 mL) and $[Pd(PPh_3)_4]$ (10.1 mg, 1.2 mol %) were used in the polymerisation. After work-up, the product was obtained as a yellow powder (305 mg) in 94% yield. CHN analysis calc. for $(C_{20}H_{13}N_3)_n$: C, 81.34; H, 4.44; N, 14.23%, found: C, 72.90; H, 4.24; N 11.51%.

CTF-18: 2,4,6-Tris[4-(4,4,5,5-tetramethyl-1,3,2-dioxaborolan-2-yl)phenyl]-1,3,5-triazine (500 mg, 728 µmol), 1,4-dibromo-2-nitrobenzene (307 mg, 1.09 mmol), *N,N*-dimethylformamide (10.9 mL), aqueous K_2CO_3 (2.0 M, 2.18 mL) and $[Pd(PPh_3)_4]$ (10.1 mg, 1.2 mol %) were used in the polymerisation. After work-up, the product was obtained as a grey powder (270 mg) in 76% yield. CHN analysis calc. for $(C_{20}H_{15}N_3O_2)_n$: C, 73.84; H, 3.41; N, 12.92%, found: C, 42.49; H, 2.65; N 6.20%.

CTF-19: 2,4,6-Tris[4-(4,4,5,5-tetramethyl-1,3,2-dioxaborolan-2-yl)phenyl]-1,3,5-triazine (1.00 g, 1.46 mmol), 1,4-dibromotetrafluorobenzene (672 mg, 2.18 mmol), *N,N*-dimethylformamide (21.8 mL), aqueous K_2CO_3 (2.0 M, 4.36 mL) and $[Pd(PPh_3)_4]$ (20.2 mg, 1.2 mol %) were used in the polymerisation. After work-up, the product was obtained as a grey powder (521 mg) in 67% yield. CHN analysis calc. for $(C_{20}H_8F_4N_2)_n$: C, 68.19; H, 2.29; N, 7.95%, found: C, 45.79; H, 2.13; N 5.19%.

CTF-20: 2,4,6-Tris[4-(4,4,5,5-tetramethyl-1,3,2-dioxaborolan-2-yl)phenyl]-1,3,5-triazine (500 mg, 728 µmol), 1,4-dibromo-2,5-difluorobenzene (297 mg, 1.09 mmol), *N,N*-dimethylformamide (10.9 mL), aqueous K_2CO_3 (2.0 M, 2.18 mL) and $[Pd(PPh_3)_4]$ (10.1 mg, 1.2 mol %) were used in the polymerisation. After work-up, the product was obtained as a grey powder (325 mg) in 94% yield. CHN analysis calc. for $(C_{20}H_{10}F_2N_2)_n$: C, 75.94; H, 3.19; N, 12.01%, found: C, 66.32; H, 3.22; N 6.99%.

CTF-21: 2,4,6-Tris[4-(4,4,5,5-tetramethyl-1,3,2-dioxaborolan-2-yl)phenyl]-1,3,5-triazine (1.00 g, 1.46 mmol), 1,4-dibromo-2,3-difluorobenzene (593 mg, 2.18 mmol), *N,N*-dimethylformamide (21.8 mL), aqueous K_2CO_3 (2.0 M, 4.36 mL) and $[Pd(PPh_3)_4]$ (20.2 mg, 1.2 mol %) were used in the polymerisation. After work-up, the product was obtained as a grey powder (353 mg) in 70% yield. CHN analysis calc. for $(C_{20}H_{10}F_2N_2)_n$: C, 75.94; H, 3.19; N, 8.86%, found: C, 65.09; H, 2.96; N 6.78%.

CTF-22: 2,4,6-Tris[4-(4,4,5,5-tetramethyl-1,3,2-dioxaborolan-2-yl)phenyl]-1,3,5-triazine (500 mg, 728 µmol), 1,4-dibromo-2-fluorobenzene (277 mg, 1.09 mmol), *N,N*-dimethylformamide (10.9 mL), aqueous K_2CO_3 (2.0 M, 2.18 mL) and $[Pd(PPh_3)_4]$ (10.1 mg, 1.2 mol %) were used in the polymerisation. After work-up, the product was obtained as a grey powder (283 mg) in 86% yield. CHN analysis calc. for $(C_{20}H_{11}FN_2)_n$: C, 80.52; H, 3.72; N, 9.39%, found: C, 72.95; H, 3.63; N 7.96%.

CTF-23: 2,4,6-Tris[4-(4,4,5,5-tetramethyl-1,3,2-dioxaborolan-2-yl)phenyl]-1,3,5-triazine (1.00 g, 1.46 mmol), 2,5-dibromo-1,4-benzoquinone (580 mg, 2.18 mmol), *N,N*-dimethylformamide (21.8 mL),

aqueous K_2CO_3 (2.0 M, 4.36 mL) and $[Pd(PPh_3)_4]$ (20.2 mg, 1.2 mol %) were used in the polymerisation. After work-up, the product was obtained as a black powder (146 mg) in 21% yield. CHN analysis calc. for $(C_{20}H_{10}N_2O_2)_n$: C, 77.41; H, 3.25; N, 9.03%, found: C, 55.07; H, 3.04; N 5.33%.

CTF-24: 2,4,6-Tris[4-(4,4,5,5-tetramethyl-1,3,2-dioxaborolan-2-yl)phenyl]-1,3,5-triazine (1.00 g, 1.46 mmol), 2,5-dibromobenzene-1,4-diol (307 mg, 2.18 mmol), *N,N*-dimethylformamide (21.8 mL), aqueous K_2CO_3 (2.0 M, 4.36 mL) and $[Pd(PPh_3)_4]$ (20.2 mg, 1.2 mol %) were used in the polymerisation. After work-up, the product was obtained as a black powder (77 mg) in 11% yield. CHN analysis calc. for $(C_{20}H_{12}N_2O_2)_n$: C, 76.91; H, 3.87; N, 8.97%, found: C, 46.78; H, 2.86; N 4.82%.

CTF-25: 2,4,6-Tris[4-(4,4,5,5-tetramethyl-1,3,2-dioxaborolan-2-yl)phenyl]-1,3,5-triazine (500 mg, 728 µmol), 1,4-dibromo-2,5-dimethoxybenzene (323 mg, 1.09 mmol), *N,N*-dimethylformamide (10.9 mL), aqueous K_2CO_3 (2.0 M, 2.18 mL) and $[Pd(PPh_3)_4]$ (10.1 mg, 1.2 mol %) were used in the polymerisation. After work-up, the product was obtained as a pale yellow powder (364 mg) in 98% yield. CHN analysis calc. for $(C_{22}H_{16}N_2O_2)_n$: C, 77.63; H, 4.74; N, 8.23%, found: C, 73.95; H, 4.74; N 7.92%.

CTF-26: 2,4,6-Tris[4-(4,4,5,5-tetramethyl-1,3,2-dioxaborolan-2-yl)phenyl]-1,3,5-triazine (500 mg, 728 µmol), 6,6'-dibromo-2,2'-bipyridine (343 mg, 1.09 mmol), *N,N*-dimethylformamide (10.9 mL), aqueous K_2CO_3 (2.0 M, 2.18 mL) and $[Pd(PPh_3)_4]$ (10.1 mg, 1.2 mol %) were used in the polymerisation. After work-up, the product was obtained as a white powder (389 mg) in 99% yield. CHN analysis calc. for $(C_{24}H_{14}N_4)_n$: C, 80.43; H, 3.94; N, 15.63%, found: C, 75.02; H, 3.83; N 14.42%.

CTF-27: 2,4,6-Tris[4-(4,4,5,5-tetramethyl-1,3,2-dioxaborolan-2-yl)phenyl]-1,3,5-triazine (500 mg, 728 µmol), 5,5'-dibromo-2,2'-bipyridine (343 mg, 1.09 mmol), *N,N*-dimethylformamide (10.9 mL), aqueous K_2CO_3 (2.0 M, 2.18 mL) and $[Pd(PPh_3)_4]$ (10.1 mg, 1.2 mol %) were used in the polymerisation. After work-up, the product was obtained as a pale yellow powder (352 mg) in 90% yield. CHN analysis calc. for $(C_{24}H_{14}N_4)_n$: C, 80.43; H, 3.94; N, 15.63%, found: C, 69.48; H, 3.68; N 12.75%.

CTF-28: 2,4,6-Tris[4-(4,4,5,5-tetramethyl-1,3,2-dioxaborolan-2-yl)phenyl]-1,3,5-triazine (500 mg, 728 µmol), 4,4'-dibromo-2,2'-bipyridine (343 mg, 1.09 mmol), *N,N*-dimethylformamide (10.9 mL), aqueous K_2CO_3 (2.0 M, 2.18 mL) and $[Pd(PPh_3)_4]$ (10.1 mg, 1.2 mol %) were used in the polymerisation. After work-up, the product was obtained as a grey powder (276 mg) in 70% yield. CHN analysis calc. for $(C_{24}H_{14}N_4)_n$: C, 80.43; H, 3.94; N, 15.63%, found: C, 70.24; H, 4.17; N 12.68%.

CTF-29: 2,4,6-Tris[4-(4,4,5,5-tetramethyl-1,3,2-dioxaborolan-2-yl)phenyl]-1,3,5-triazine (500 mg, 728 µmol), 3,8-dibromo-1,10-phenanthroline (369 mg, 1.09 mmol), *N,N*-dimethylformamide (10.9 mL), aqueous K_2CO_3 (2.0 M, 2.18 mL) and $[Pd(PPh_3)_4]$ (10.1 mg, 1.2 mol %) were used in the

polymerisation. After work-up, the product was obtained as a brown powder (225 mg) in 53% yield. CHN analysis calc. for $(C_{26}H_{14}N_4)_n$: C, 81.66; H, 3.69; N, 14.65%, found: C, 73.83; H, 3.98; N 12.93%.

CTF-30: 2,4,6-Tris[4-(4,4,5,5-tetramethyl-1,3,2-dioxaborolan-2-yl)phenyl]-1,3,5-triazine (500 mg, 728 µmol), 2,5-dibromopyrazine (260 mg, 1.09 mmol), *N,N*-dimethylformamide (10.9 mL), aqueous K_2CO_3 (2.0 M, 2.18 mL) and $[Pd(PPh_3)_4]$ (10.1 mg, 1.2 mol %) were used in the polymerisation. After work-up, the product was obtained as a grey powder (188 mg) in 61% yield. CHN analysis calc. for $(C_{18}H_{10}N_4)_n$: C, 76.58; H, 3.57; N 19.85%, found: C, 65.12; H, 3.61; N 15.31%.

CTF-31: 2,4,6-Tris[4-(4,4,5,5-tetramethyl-1,3,2-dioxaborolan-2-yl)phenyl]-1,3,5-triazine (500 mg, 728 µmol), 2,5-dibromopyrimidine (260 mg, 1.09 mmol), *N,N*-dimethylformamide (10.9 mL), aqueous K_2CO_3 (2.0 M, 2.18 mL) and $[Pd(PPh_3)_4]$ (10.1 mg, 1.2 mol %) were used in the polymerisation. After work-up, the product was obtained as a pale brown powder (248 mg) in 80% yield. CHN analysis calc. for $(C_{18}H_{10}N_4)_n$: C, 76.58; H, 3.57; N 19.85%, found: C, 66.33; H, 3.51; N 17.09%.

CTF-32 2,4,6-Tris[4-(4,4,5,5-tetramethyl-1,3,2-dioxaborolan-2-yl)phenyl]-1,3,5-triazine (500 mg, 728 µmol), 2,5-dibromopyridine (259 mg, 1.09 mmol), *N,N*-dimethylformamide (10.9 mL), aqueous K_2CO_3 (2.0 M, 2.18 mL) and $[Pd(PPh_3)_4]$ (10.1 mg, 1.2 mol %) were used in the polymerisation. After work-up, the product was obtained as a yellow powder (305 mg) in 99% yield. CHN analysis calc. for $(C_{19}H_{11}N_3)_n$: C, 81.12; H, 3.94; N, 14.94%, found: C, 70.97; H, 3.74; N 12.63%.

CTF-33: 2,4,6-Tris[4-(4,4,5,5-tetramethyl-1,3,2-dioxaborolan-2-yl)phenyl]-1,3,5-triazine (500 mg, 728 µmol), 2,6-dibromopyridine (259 mg, 1.09 mmol), *N,N*-dimethylformamide (10.9 mL), aqueous K_2CO_3 (2.0 M, 2.18 mL) and $[Pd(PPh_3)_4]$ (10.1 mg, 1.2 mol %) were used in the polymerisation. After work-up, the product was obtained as a pale 305yellow powder (304 mg) in 99% yield. CHN analysis calc. for $(C_{19}H_{11}N_3)_n$: C, 81.12; H, 3.94; N, 14.94%, found: C, 63.19; H, 3.51; N 10.21%.

CTF-34: 2,4,6-Tris[4-(4,4,5,5-tetramethyl-1,3,2-dioxaborolan-2-yl)phenyl]-1,3,5-triazine (500 mg, 728 µmol), 3,7-dibromo-dibenzothiophene-*S,S*-dioxide (408 mg, 1.09 mmol), *N,N*-dimethylformamide (10.9 mL), aqueous K_2CO_3 (2.0 M, 2.18 mL) and $[Pd(PPh_3)_4]$ (10.1 mg, 1.2 mol %) were used in the polymerisation. After work-up, the product was obtained as a pale yellow powder (452 mg) in 98% yield. CHN analysis calc. for $(C_{26}H_{14}N_2O_2S)_n$: C, 74.63; H, 3.37; N, 6.69%, found: C, 66.00; H, 3.49; N 5.55%.

CTF-35: 2,4,6-Tris[4-(4,4,5,5-tetramethyl-1,3,2-dioxaborolan-2-yl)phenyl]-1,3,5-triazine (500 mg, 728 µmol), 3,7-dibromo-dibenzothiophene (373 mg, 1.09 mmol), *N,N*-dimethylformamide (10.9 mL), aqueous K_2CO_3 (2.0 M, 2.18 mL) and $[Pd(PPh_3)_4]$ (10.1 mg, 1.2 mol %) were used in the polymerisation.

After work-up, the product was obtained as a pale yellow powder (420 mg) in 99% yield. CHN analysis calc. for $(C_{26}H_{14}N_2S)_n$: C, 80.80; H, 3.65; N, 7.25%, found: C, 73.42; H, 3.64; N 6.29%.

CTF-36: 2,4,6-Tris[4-(4,4,5,5-tetramethyl-1,3,2-dioxaborolan-2-yl)phenyl]-1,3,5-triazine (500 mg, 728 µmol), 2,7-dibromofluorene (354 mg, 1.09 mmol), *N,N*-dimethylformamide (10.9 mL), aqueous K_2CO_3 (2.0 M, 2.18 mL) and $[Pd(PPh_3)_4]$ (10.1 mg, 1.2 mol %) were used in the polymerisation. After work-up, the product was obtained as an orange powder (399 mg) in 99% yield. CHN analysis calc. for $(C_{27}H_{16}N_2)_n$: C, 80.43; H, 3.94; N, 15.63%, found: C, 74.23; H, 3.75; N 6.13%.

CTF-37: 2,4,6-Tris[4-(4,4,5,5-tetramethyl-1,3,2-dioxaborolan-2-yl)phenyl]-1,3,5-triazine (500 mg, 728 µmol), 2,7-dibromo-9*H*-carbazole (354 mg, 1.09 mmol), *N,N*-dimethylformamide (10.9 mL), aqueous K_2CO_3 (2.0 M, 2.18 mL) and $[Pd(PPh_3)_4]$ (10.1 mg, 1.2 mol %) were used in the polymerisation. After work-up, the product was obtained as a yellow powder (402 mg) in 99% yield. CHN analysis calc. for $(C_{26}H_{15}N_3)_n$: C, 84.53; H, 4.09; N, 11.37%, found: C, 73.80; H, 4.01; N 9.32%.

CTF-38: 2,4,6-Tris[4-(4,4,5,5-tetramethyl-1,3,2-dioxaborolan-2-yl)phenyl]-1,3,5-triazine (500 mg, 728 µmol), 2,7-dibromo-9-fluorenone (369 mg, 1.09 mmol), *N,N*-dimethylformamide (10.9 mL), aqueous K_2CO_3 (2.0 M, 2.18 mL) and $[Pd(PPh_3)_4]$ (10.1 mg, 1.2 mol %) were used in the polymerisation. After work-up, the product was obtained as a grey powder (400 mg) in 95% yield. CHN analysis calc. for $(C_{27}H_{14}N_2O)_n$: C, 84.80; H, 3.69; N, 7.33%, found: C, 73.97; H, 3.66; N 5.61%.

CTF-39: 2,4,6-Tris[4-(4,4,5,5-tetramethyl-1,3,2-dioxaborolan-2-yl)phenyl]-1,3,5-triazine (500 mg, 728 µmol), 4,7-dibromo-2,1,3-benzothiadiazole (321 mg, 1.09 mmol), *N,N*-dimethylformamide (10.9 mL), aqueous K_2CO_3 (2.0 M, 2.18 mL) and $[Pd(PPh_3)_4]$ (10.1 mg, 1.2 mol %) were used in the polymerisation. After work-up, the product was obtained as a bright orange powder (333 mg) in 90% yield. CHN analysis calc. for $(C_{20}H_{10}N_4S)_n$: C, 70.99; H, 2.98; N, 16.56%, found: C, 65.81; H, 3.17; N 14.58%.

CTF-40: 2,4,6-Tris[4-(4,4,5,5-tetramethyl-1,3,2-dioxaborolan-2-yl)phenyl]-1,3,5-triazine (500 mg, 728 µmol), 4,7-dibromobenzo[*c*][1,2,5]oxadiazole (303 mg, 1.09 mmol), *N,N*-dimethylformamide (10.9 mL), aqueous K_2CO_3 (2.0 M, 2.18 mL) and $[Pd(PPh_3)_4]$ (10.1 mg, 1.2 mol %) were used in the polymerisation. After work-up, the product was obtained as a brown powder (318 mg) in 90% yield. CHN analysis calc. for $(C_{20}H_{10}N_4O)_n$: C, 74.53; H, 3.13; N, 17.38%, found: C, 68.02; H, 3.64; N 15.13%.

CTF-41: 2,4,6-Tris[4-(4,4,5,5-tetramethyl-1,3,2-dioxaborolan-2-yl)phenyl]-1,3,5-triazine (500 mg, 728 µmol), 4,7-dibromo-2,1,3-benzoselenadiazole (372 mg, 1.09 mmol), *N,N*-dimethylformamide (10.9 mL), aqueous K_2CO_3 (2.0 M, 2.18 mL) and $[Pd(PPh_3)_4]$ (10.1 mg, 1.2 mol %) were used in the

polymerisation. After work-up, the product was obtained as an orange powder (418 mg) in 99% yield. CHN analysis calc. for $(C_{20}H_{10}N_4Se)_n$: C, 62.35; H, 2.62; N, 14.54%, found: C, 55.40; H, 2.90; N 12.27%.

CTF-42: 2,4,6-Tris[4-(4,4,5,5-tetramethyl-1,3,2-dioxaborolan-2-yl)phenyl]-1,3,5-triazine (500 mg, 728 µmol), 4,7-dibromo-5,6-difluorobenzo[*c*][1,2,5]thiadiazole (360 mg, 1.09 mmol), *N,N*-dimethylformamide (10.9 mL), aqueous K_2CO_3 (2.0 M, 2.18 mL) and $[Pd(PPh_3)_4]$ (10.1 mg, 1.2 mol %) were used in the polymerisation. After work-up, the product was obtained as a brown powder (364 mg) in 70% yield. CHN analysis calc. for $(C_{20}H_8F_2N_2S)_n$: C, 64.17; H, 2.15; N, 14.97%, found: C, 49.90; H, 2.70; N 10.77%.

CTF-43: 2,4,6-Tris[4-(4,4,5,5-tetramethyl-1,3,2-dioxaborolan-2-yl)phenyl]-1,3,5-triazine (500 mg, 728 µmol), 4,7-dibromo-5-fluoro-2,1,3-benzothiadiazole (340 mg, 1.09 mmol), *N,N*-dimethylformamide (10.9 mL), aqueous K_2CO_3 (2.0 M, 2.18 mL) and $[Pd(PPh_3)_4]$ (10.1 mg, 1.2 mol %) were used in the polymerisation. After work-up, the product was obtained as a grey powder (340 mg) in 87% yield. CHN analysis calc. for $(C_{20}H_9FN_4S)_n$: C, 67.41; H, 2.55; N, 15.72%, found: C, 61.61; H, 2.83; N 13.33%.

CTF-44: 2,4,6-Tris[4-(4,4,5,5-tetramethyl-1,3,2-dioxaborolan-2-yl)phenyl]-1,3,5-triazine (500 mg, 728 µmol), 5,8-dibromoquinoxaline (314 mg, 1.09 mmol), *N,N*-dimethylformamide (10.9 mL), aqueous K_2CO_3 (2.0 M, 2.18 mL) and $[Pd(PPh_3)_4]$ (10.1 mg, 1.2 mol %) were used in the polymerisation. After work-up, the product was obtained as a grey powder (360 mg) in 99% yield. CHN analysis calc. for $(C_{22}H_{12}N_4)_n$: C, 79.50; H, 3.64; N, 16.86%, found: C, 68.12; H, 3.60; N 13.84%.

11 Appendix

This appendix gives a summary of data, while further information can be found for **6 Aryl based CTF** in the supporting information of reference[124] and **7 A library of 40 CTFs** in the data catalogue of the University of Liverpool **http://datacat.liverpool.ac.uk/id/eprint/639.**

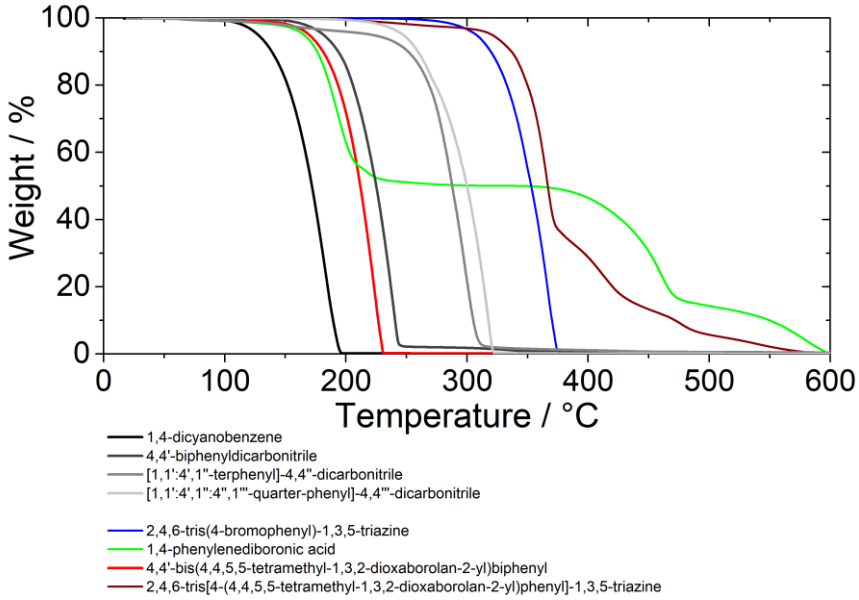

Figure 75: Thermogravimetric analysis curves for the monomers in air with a heating rate of 10 °C min^{-1}.

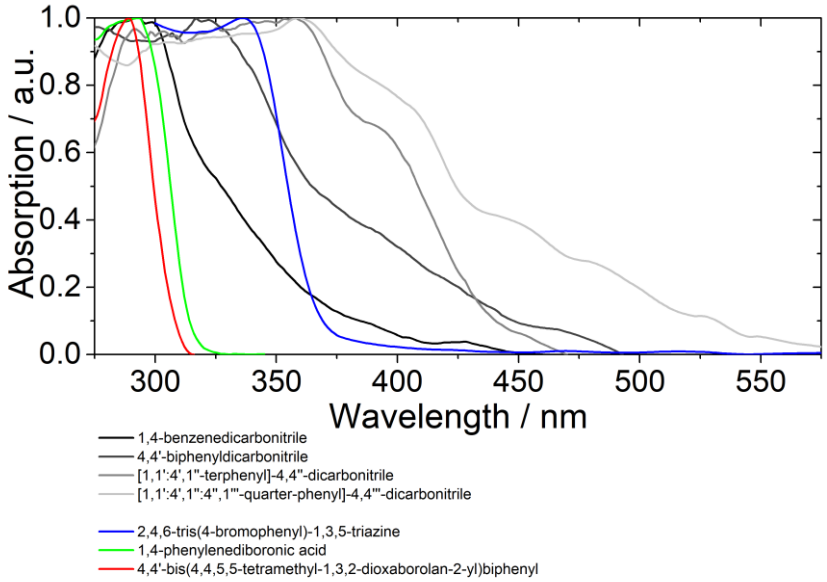

Figure 76: UV-Vis solid-state measurements of the monomers.

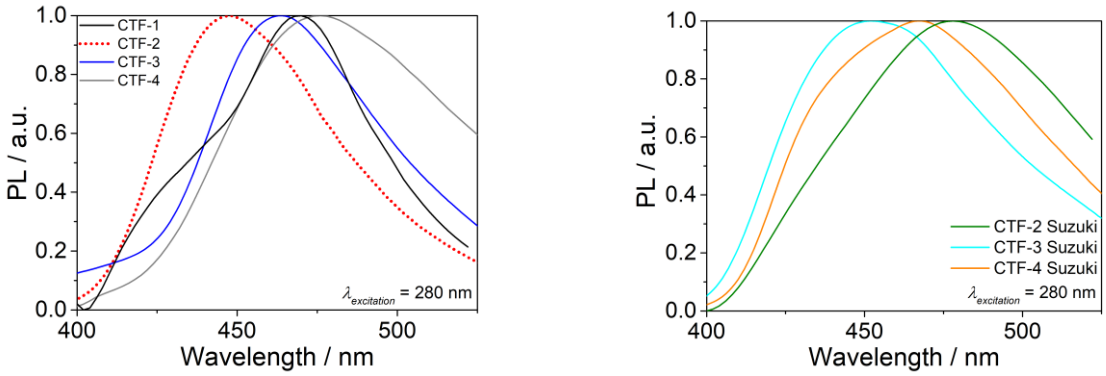

Figure 77: Photoluminescence spectra in the solid-state for CTF-1 to CTF-4 (left) and CTF-2 Suzuki to CTF-4 Suzuki (right). The excitation wavelength of λ_{ex} = 280 nm was used.

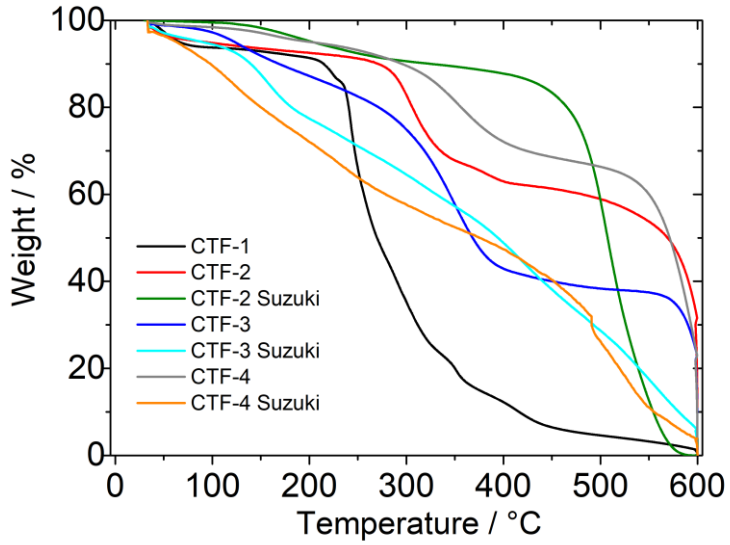

Figure 78: Thermogravimetric analysis curves for CTF-1 to CTF-4, and CTF-2 Suzuki to CTF-4 Suzuki, in air with a heating rate of 10 °C min^{-1}.

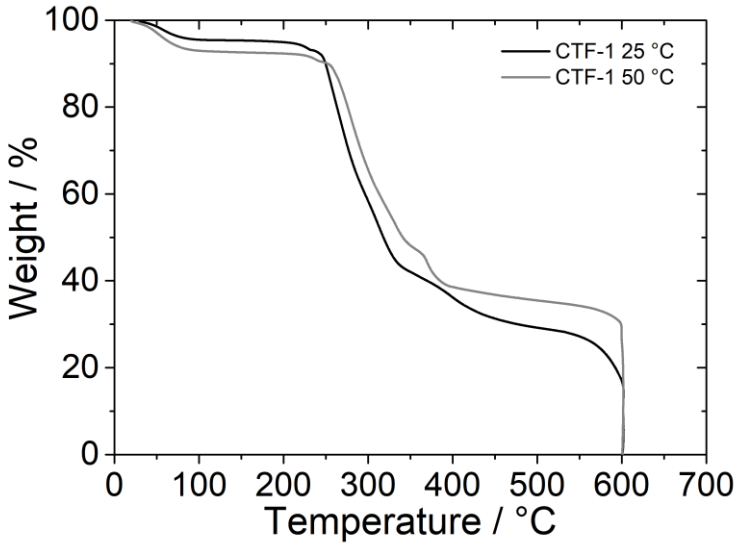

Figure 79: Thermogravimetric analysis curves for CTF-1 synthesised at 25 °C and 50 °C in air with a heating rate of 10 °C min^{-1}.

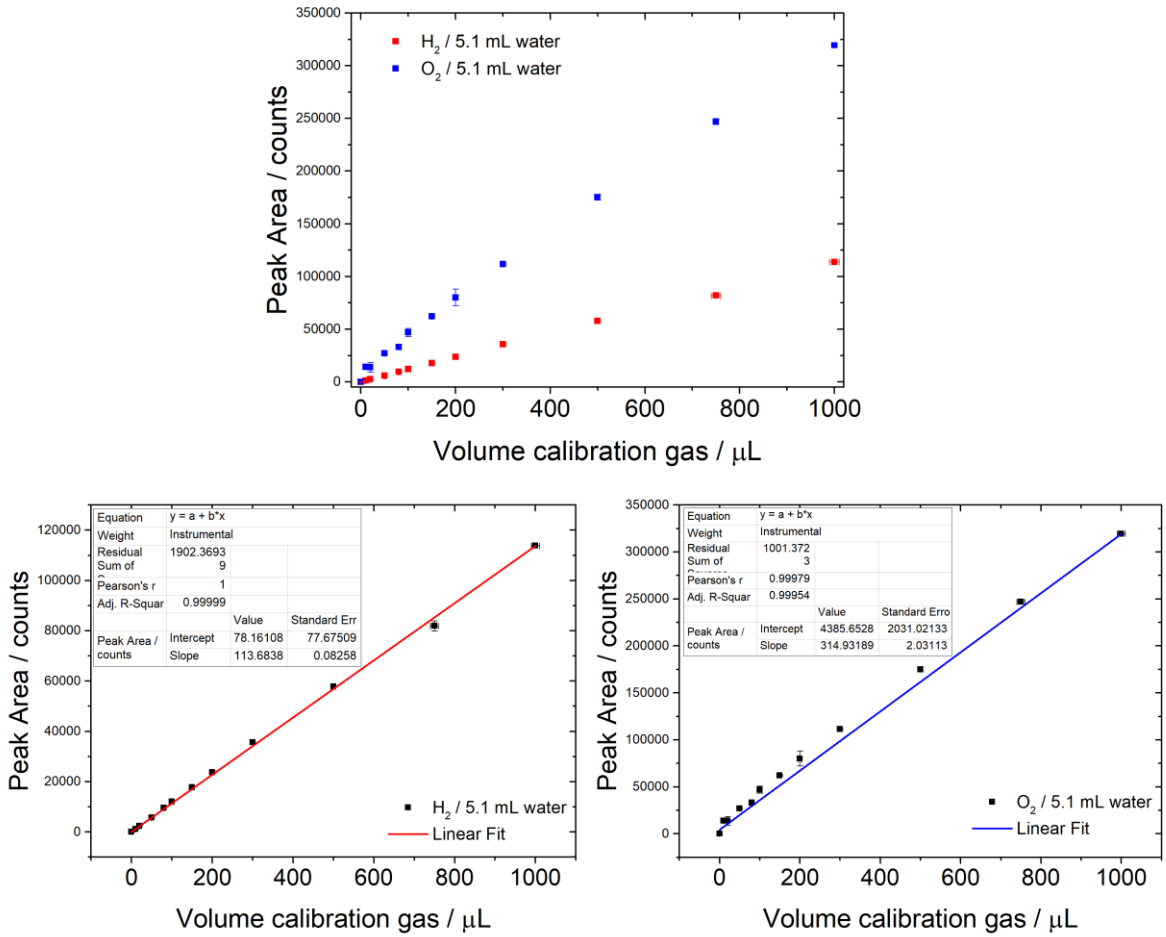

Figure 80: Calibration of the HT-setup with calibration gas (1.97% H_2, 2.96% O_2, 2.95% N_2, He balance).

Table 14: Output of xenon lamps tested with a calibrated Newport reference solar cell, model 91150V. 1.0 sun is equal to 1000 W/m² at 25 °C and AM 1.5G reference.

Filter	Output (5 cm) / sun[a]	Output (10 cm) / sun[a]
None (200-1050 nm)	2.95	1.91
λ > 295 nm	2.74	1.86
λ > 350 nm	2.70	1.68
λ > 420 nm	2.64	1.65

[a] the distance was measured from the black optics housing; a fluctuation of 0.02 sun was found in all measurements.

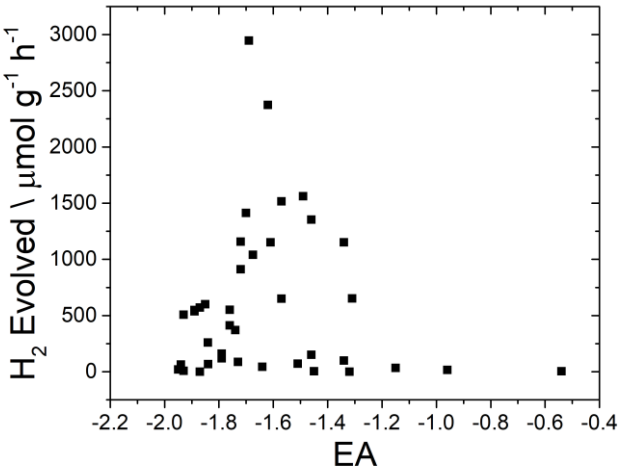

Figure 81: Correlation of the electron affinity and the hydrogen evolution rate from water/TEA/MeOH with 3 wt. % Pt under λ > 420 nm irradiation.

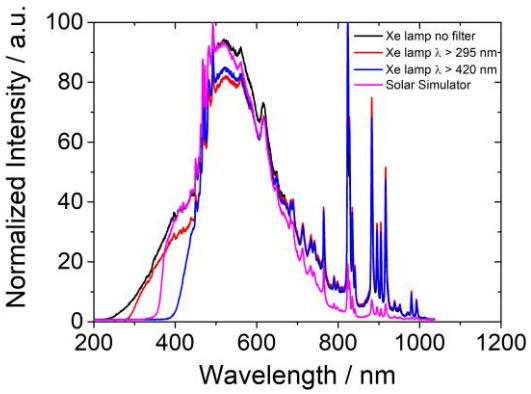

Figure 82: Output spectra of the xenon lamps equipped with no filter, a λ > 295 nm cut-off filter, and a λ > 420 nm cut-off filter. For comparison, the output of the solar simulator (AAA, HT-setup) is shown.

Table 15: Overview measurements library (first part).

Polymer	SN[a]	Yield[b] / %	TGA[c] on-set / °C	$H_2^{kin,d}$ / µmol g^{-1} h^{-1}	$H_2^{kin,e}$ error	H_2/CTF-3[f]	Peak Area[g] H_2^{rob} / a.u.	Peak Area[h] H_2^{rob} error	$H_2^{rob,i}$ / µmol g^{-1} h^{-1}	$H_2^{rob,j}$ error	SA_{BET} / m^2 g^{-1}	CA / °[k]	CA error	T^l / %	T^m / %
Nicanite	ref	-	600	59	3	0.37	678971	83700	524	65	23	0	0	16.8	11.4
CTF-2	ref	-	304	301	19	1.91	1325510	83700	1023	65	560	0	0	9.5	83.0
CTF-3 Suzuki	ref	-	423	158	56	1.00	1043881	83700	805	65	380	56	3	26.8	57.0
CTF-5	38	92	520	20	2	0.13	663066	83700	511	65	168	80	1	5.4	35.3
CTF-6	11	96	509	8	1	0.05	264636	83700	204	65	10	77	5	42.8	60.1
CTF-7	12	97	460	20	6	0.13	366196	83700	282	65	121	67	3	15.1	48.0
CTF-8	29	99	405	571	37	3.61	1701600	83700	1313	65	24	65	2	1.5	6.2
CTF-9	31	85	362	63	3	0.40	521594	83700	402	65	708	95	1	2.9	29.0
CTF-10	18	79	351	1412	63	8.94	1879770	37429	1450	29	597	90	4	4.9	23.4
CTF-11	3	95	365	1151	29	7.28	1203520	37429	928	29	184	68	2	31.3	33.8
CTF-12	19	75	424	1515	66	9.59	1307910	37429	1009	29	134	70	3	40.4	50.8
CTF-13	20	37	399	72	3	0.46	256851	83700	198	65	29	68	3	6.8	24.5
CTF-14	1	51	431	16	2	0.10	158550	83700	122	65	10	55	7	51.4	64.4
CTF-15	33	82	412	2946	381	18.65	2473980	19003	1909	15	383	[n]	-	0.8	85.2
CTF-16	40	98	364	1354	133	8.57	913453	37429	705	65	278	[n]	-	5.6	21.6
CTF-17	15	94	488	537	30	3.40	711724	83700	549	65	326	[n]	-	5.7	73.0
CTF-18	30	76	407	5	1	0.03	26453	83700	20	65	136	[n]	-	31.4	39.7
CTF-19	26	67	414	1158	78	7.33	1047180	37429	808	29	461	68	3	53.3	58.0
CTF-20	35	94	434	87	2	0.55	1278732	83700	986	65	244	87	5	6.2	35.3
CTF-21	27	70	423	550	28	3.48	1094090	83700	844	65	482	73	8	52.2	51.2
CTF-22	32	86	467	413	39	2.61	1233540	83700	952	65	338	81	3	3.7	54.7
CTF-23	36	21	241	5	1	0.03	211	83700	0	65	14	64	6	25.5	65.6
CTF-24	37	11	237	0	0	0.00	52	83700	0	65	7	66	4	59.4	77.6
CTF-25	39	98	378	548	97	3.47	1180854	37429	911	65	488	106	1	20.1	42.7
CTF-26	17	99	457	67	1	0.42	708920	83700	547	65	242	66	5	24.2	51.3
CTF-27	4	90	485	911	37	5.77	1846820	83700	1425	65	166	72	2	4.6	8.9
CTF-28	10	70	474	119	2	0.75	523284	83700	404	65	76	59	2	19.1	27.9
CTF-29	16	53	523	371	39	2.35	787848	83700	608	65	365	80	5	16.9	34.0
CTF-30	13	61	502	1561	150	9.88	1732470	83700	1336	65	25	[n]	-	4.5	3.9
CTF-31	14	80	490	650	45	4.11	932254	83700	719	65	33	[n]	-	5.0	3.9
CTF-32	7	99	496	1041	70	6.59	2106120	37429	1625	29	160	[n]	-	11.1	8.6
CTF-33	6	99	494	260	20	1.65	1174570	83700	906	65	99	56	3	21.7	28.8
CTF-34	2	98	400	2373	25	15.02	2102950	19003	1622	20	397	[n]	-	0.8	83.0
CTF-35	5	99	402	600	22	3.80	1623260	83700	1252	65	446	91	1	8.4	28.7
CTF-36	8	99	502	160	13	1.01	556118	83700	429	65	175	[n]	-	3.6	3.1
CTF-37	9	99	471	507	33	3.21	824017	83700	636	65	48	[n]	-	11.3	61.8
CTF-38	25	95	444	150	15	0.95	873549	83700	674	65	91	86	4	3.8	12.7
CTF-39	21	90	405	1151	75	7.28	1404440	37429	1083	29	536	78	4	2.2	20.0
CTF-40	22	90	420	33	3	0.21	138843	83700	107	65	412	[n]	-	41.9	13.3
CTF-41	23	99	474	0	0	0.00	397	83700	0	65	106	59	7	12.1	23.4
CTF-42	28	70	449	100	2	0.63	261811	83700	202	65	13	[n]	-	35.2	72.8
CTF-43	34	87	454	652	45	4.13	1526450	83700	1178	65	281	[n]	-	1.9	3.5
CTF-44	24	99	471	44	1	0.28	442557	83700	341	65	66	61	5	34.0	57.2

[a] synthesis number - [b] polymer yield after work-up - [c] TGA on-set temperature in air - [d] 25 mg polymer, 5 h, water/TEA/MeOH - [e] error determined from the slope - [f] ratio in comparison to CTF-3 Suzuki - [g] 5 mg polymer, 2 h, water/TEA/MeOH - [h] error determination in separate experiment - [i] converted from Peak Area H_2^{rob} - [j] converted from Peak Area $H_2^{rob}{}_{error}$ - [k] contact angle from water - [l] average transmission from water/TEA/MeOH - [m] average transmission from water - [n] polymer swelled in contact with water and no contact angle was determined

Table 16: Overview measurements library (second part).

Polymer	SN[a]	bg[b] / nm	bg[b] / eV	λ_{max}[c] / nm	λ_{max}[c] / eV	PL λ_{ex} / nm	PL_{max}[c] / nm	λ_{ex} TCSPC[d] / nm	λ_{em} TCSPC / nm	τ1 / ns	τ2 / ns	τ3 / ns	χ2	f(τ1) / %	f(τ2) / %	f(τ3) / %	average τ / ns
Nicanite	ref	455	2.73	383	3.24	280	522	375	477	0.38	1.14	4.79	1.11	75.72	21.02	3.26	0.68
CTF-2	ref	601	2.06	398	3.12	280	441	375	440	0.95	4.04	19.02	1.15	31.38	37.64	30.99	7.71
CTF-3 Suzuki	ref	430	2.88	377	3.29	280	440	375	442	0.44	1.51	7.67	1.13	75.61	21.98	2.41	0.85
CTF-5	38	422	2.93	318	3.90	280	464	375	560	1.14	2.87	15.49	1.05	61.86	33.88	4.26	2.34
CTF-6	11	481	2.58	356	3.48	280	468	375	494	0.76	2.67	10.25	1.15	40.82	45.38	13.80	2.93
CTF-7	12	428	2.90	355	3.49	280	465	375	466	0.49	1.43	4.66	1.19	40.81	48.09	11.10	1.40
CTF-8	29	495	2.51	376	3.30	280	481	375	437	0.19	0.91	4.69	1.19	77.38	18.89	3.73	0.49
CTF-9	31	498	2.49	407	3.05	360	563	375	583	1.01	3.21	10.31	1.03	41.28	53.32	5.40	2.68
CTF-10	18	506	2.25	409	3.03	360	537	375	440	0.23	1.20	5.13	1.15	49.96	38.23	11.82	1.18
CTF-11	3	576	2.15	426	2.91	360	576	475	577	0.20	0.83	6.48	1.13	65.88	31.05	3.07	0.59
CTF-12	19	515	2.41	451	2.75	280	435	475	545	0.08	1.16	6.29	1.15	90.53	6.96	2.51	0.31
CTF-13	20	482	2.57	374	3.32	280	435	375	445	0.13	0.73	3.98	1.14	81.11	16.19	2.70	0.34
CTF-14	1	800	1.55	479	2.59	280	463	375	463	0.31	2.09	7.26	1.20	59.41	29.23	11.36	1.62
CTF-15	33	480	2.58	374	3.32	280	461	375	483	0.59	2.37	9.48	1.21	82.09	13.29	4.62	1.23
CTF-16	40	477	2.60	359	3.45	280	462	375	550	0.67	2.85	10.19	1.20	47.67	36.28	16.06	2.99
CTF-17	15	512	2.42	397	3.12	360	530	445	535	0.17	0.96	4.73	1.03	74.30	22.16	3.54	0.50
CTF-18	30	457	2.71	386	3.21	280	468	375	480	0.09	1.22	8.03	1.14	84.44	10.44	5.12	0.61
CTF-19	26	426	2.91	349	3.55	280	433	475	580	0.31	1.19	4.68	1.10	80.05	16.78	3.17	0.60
CTF-20	35	457	2.71	362	3.43	280	434	375	454	0.43	1.68	5.76	1.14	54.38	35.59	10.03	1.41
CTF-21	27	420	2.95	355	3.49	280	435	375	452	0.20	1.06	4.58	1.03	78.26	18.45	3.29	0.51
CTF-22	32	434	2.86	379	3.27	280	437	375	458	0.51	1.46	5.45	1.16	75.20	19.81	4.99	0.95
CTF-23	36	340	2.25	433	3.00	280	433	375	452	0.76	2.99	7.85	1.11	30.18	55.91	13.91	2.99
CTF-24	37	795	1.56	626	1.98	280	400	375	436	0.12	1.20	6.12	1.08	92.70	4.84	2.45	0.32
CTF-25	39	461	2.69	381	3.25	280	485	375	506	0.82	2.36	8.58	1.04	57.46	38.87	3.67	1.70
CTF-26	17	402	3.08	345	3.59	280	420	375	471	0.38	1.59	5.80	1.13	46.56	43.92	9.52	1.43
CTF-27	4	460	2.70	378	3.28	280	519	445	550	0.55	1.82	8.82	1.17	58.24	34.21	7.55	1.61
CTF-28	10	420	2.96	355	3.49	280	427	375	450	0.32	1.39	5.20	1.11	63.92	27.24	8.85	1.05
CTF-29	16	463	2.68	374	3.32	280	470	375	501	0.52	1.72	8.20	1.13	57.54	36.43	6.03	1.42
CTF-30	13	473	2.62	375	3.31	280	473	375	475	0.53	1.15	7.22	1.18	37.36	55.26	7.38	1.37
CTF-31	14	560	2.21	406	3.05	360	560	475	570	0.21	1.00	4.89	1.16	63.86	29.03	7.11	0.77
CTF-32	7	460	2.69	375	3.31	280	460	375	480	0.11	0.76	3.77	1.14	83.95	13.94	2.10	0.28
CTF-33	6	434	2.86	355	3.49	280	468	375	500	0.93	3.43	12.74	1.05	37.45	42.44	20.12	4.37
CTF-34	2	460	2.69	392	3.16	280	474	375	474	0.19	0.95	4.62	1.06	68.39	27.27	4.34	0.59
CTF-35	5	460	2.70	398	3.12	280	471	375	472	0.25	0.89	3.69	1.19	62.15	31.63	6.23	0.67
CTF-36	8	544	2.28	374	3.32	360	579	445	580	0.39	1.42	3.92	1.13	26.29	56.65	17.06	1.57
CTF-37	9	496	2.50	418	2.97	280	501	445	524	0.05	0.94	7.66	1.15	98.25	1.44	0.30	0.08
CTF-38	25	543	2.28	374	3.32	360	581	375	515	1.02	2.38	15.79	1.04	46.55	51.54	1.92	2.00
CTF-39	21	561	2.21	403	3.08	360	567	375	440	0.27	0.74	3.76	1.21	52.78	40.40	6.83	0.70
CTF-40	22	600	2.07	409	3.03	280	435	375	580	0.81	2.30	15.85	1.15	85.44	12.38	2.18	1.33
CTF-41	23	554	2.24	455	2.72	360	564	375	455	0.17	0.78	7.35	1.21	86.57	12.44	0.99	0.32
CTF-42	28	649	1.91	455	2.72	280	401	437	375	0.15	1.34	5.65	1.17	74.74	15.56	9.70	0.87
CTF-43	34	539	2.30	406	3.05	360	548	445	600	0.19	1.13	4.88	1.15	67.31	26.73	5.96	0.72
CTF-44	24	476	2.60	399	3.10	280	493	475	590	0.31	1.39	5.69	1.10	49.69	32.69	17.62	1.61

[a] synthesis number - [b] band-gap - [c] measured in solid state - [d] the lifetime is calculated by a fit of the following equation:

$A + B1 \times \exp(-i/\tau1) + B2 \times \exp(-i/\tau2) + B3 \times \exp(i/\tau3)$.

Table 17: Overview of theoretical calculations library by Martijn A. Zwijnenburg, University College, London.

Polymer	SN[a]	dH_{solv} [b]	dH_{solv}/CTF-3	$opt_{calculated}$	$IP_{calculated}$ pH 7	$EA_{calculated}$ pH 7	Fundamental band-gap / eV
Nicanite	ref	n.d.	n.d.	n.d.	2.00	1.50	0.50
CTF-2	ref	-0.64	0.58	n.d.	1.69	-1.68	3.37
CTF-3 Suzuki	ref	-0.64	0.58	3.49	1.36	-1.80	3.16
CTF-5	38	-0.64	0.58	3.83	1.58	-1.95	3.53
CTF-6	11	-0.65	0.59	3.61	1.34	-1.93	3.27
CTF-7	12	-0.67	0.61	3.70	1.54	-1.94	3.48
CTF-8	29	-1.01	0.92	3.47	1.57	-1.74	3.31
CTF-9	31	-0.61	0.55	2.89	0.79	-1.94	2.73
CTF-10	18	-0.61	0.56	2.95	0.93	-1.70	2.63
CTF-11	3	-0.63	0.57	3.01	1.03	-1.61	2.64
CTF-12	19	-0.69	0.63	2.89	1.00	-1.57	2.57
CTF-13	20	-0.69	0.62	3.09	1.28	-1.51	2.79
CTF-14	1	-0.97	0.88	2.75	1.42	-0.96	2.38
CTF-15	33	-0.73	0.66	3.64	1.67	-1.69	3.36
CTF-16	40	-0.79	0.72	3.59	1.95	-1.46	3.41
CTF-17	15	-0.75	0.68	3.02	0.74	-1.89	2.63
CTF-18	30	-0.72	0.66	3.51	1.70	-1.45	3.15
CTF-19	26	-0.50	0.45	3.70	1.81	-1.72	3.53
CTF-20	35	-0.57	0.52	3.51	1.56	-1.73	3.29
CTF-21	27	-0.57	0.52	3.58	1.59	-1.76	3.35
CTF-22	32	-0.61	0.55	3.51	1.47	-1.76	3.23
CTF-23	36	-0.80	0.73	2.47	2.06	-0.54	2.60
CTF-24	37	-0.85	0.78	2.82	0.91	-1.87	2.78
CTF-25	39	-0.68	0.62	2.98	0.79	-1.89	2.68
CTF-26	17	-0.73	0.67	3.71	1.60	-1.84	3.44
CTF-27	4	-0.80	0.73	3.35	1.45	-1.72	3.17
CTF-28	10	-1.00	0.91	3.90	1.99	-1.79	3.78
CTF-29	29	-0.75	0.68	3.25	1.19	-1.87	3.06
CTF-30	13	-0.76	0.69	3.34	1.60	-1.49	3.09
CTF-31	14	-0.76	0.70	3.49	1.70	-1.57	3.27
CTF-32	7	-0.72	0.66	3.44	1.50	-1.67	3.17
CTF-33	6	-0.68	0.62	3.68	1.60	-1.84	3.44
CTF-34	2	-1.10	1.00	3.33	1.49	-1.62	3.11
CTF-35	5	-0.70	0.64	3.31	1.23	-1.85	3.08
CTF-36	8	-0.70	0.64	3.20	1.05	-1.79	2.84
CTF-37	9	-0.83	0.76	3.20	1.10	-1.93	3.03
CTF-38	25	-0.80	0.73	2.83	1.29	-1.46	2.75
CTF-39	21	-0.75	0.68	2.85	1.32	-1.34	2.66
CTF-40	22	-0.70	0.64	2.86	1.40	-1.15	2.55
CTF-41	23	-0.83	0.76	2.74	1.26	-1.32	2.58
CTF-42	28	-0.68	0.62	2.97	1.55	-1.34	2.89
CTF-43	34	-0.72	0.65	2.88	1.43	-1.31	2.74
CTF-44	24	-0.78	0.71	3.20	1.42	-1.64	3.06

[a] synthesis number - [b] calculated in water

Table 18: TGA determination of the monomer on-set temperatures in air and absorption on-set in the solid-state.

Monomer	T on-set / °C	Absorption on-set / nm	Monomer	T on-set / °C	Absorption on-set / nm
M5	71	301	**M25**	132	351
M6	158	359	**M26**	203	416
M7	163	326	**M27**	173	364
M8	295	378	**M28**	146	404
M9	192	380	**M29**	239	377
M10	-[a]	308	**M30**	89	536
M11	67	320	**M31**	75	342
M12	144	323	**M32**	88	313
M13	76	351	**M33**	98	312
M14	115	421	**M34**	249	402
M15	120	480	**M35**	200	362
M16	190	366	**M36**	194	353
M17	108	341	**M37**	217	392
M18	155	440	**M38**	199	524
M19	65	312	**M39**	165	327
M20	60	309	**M40**	119	439
M21	80	299	**M41**	214	523
M22	49	304	**M42**	121	418
M23	137	506	**M43**	146	432
M24	139	340	**M44**	171	417

[a] M10 was found to evaporate very quickly in the airflow of 5 mL/min and 25 mL/min due to a low boiling point of 54 °C, therefore a measurement was not possible.

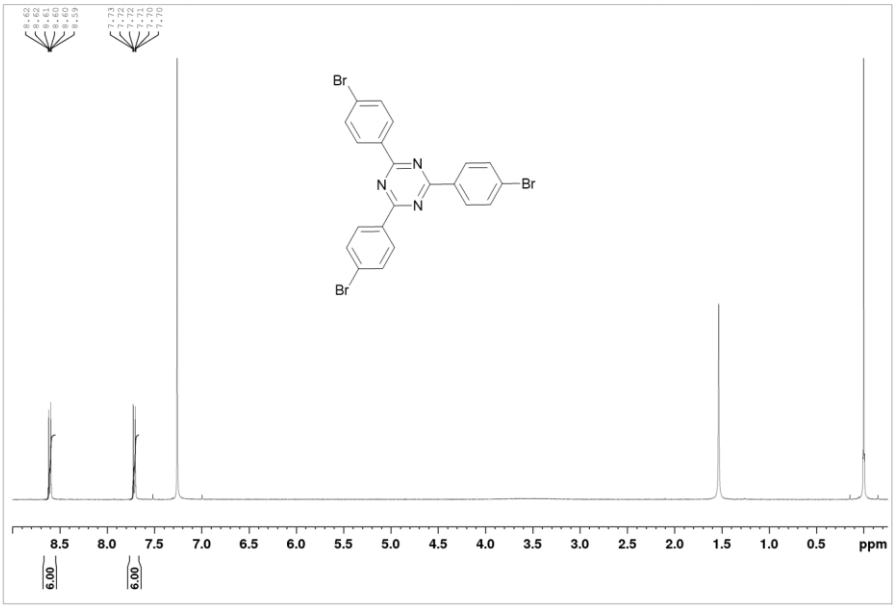

Figure 83: ^{1}H NMR spectrum of 2,4,6-tris(4-bromophenyl)-1,3,5-triazine in $CDCl_3$.

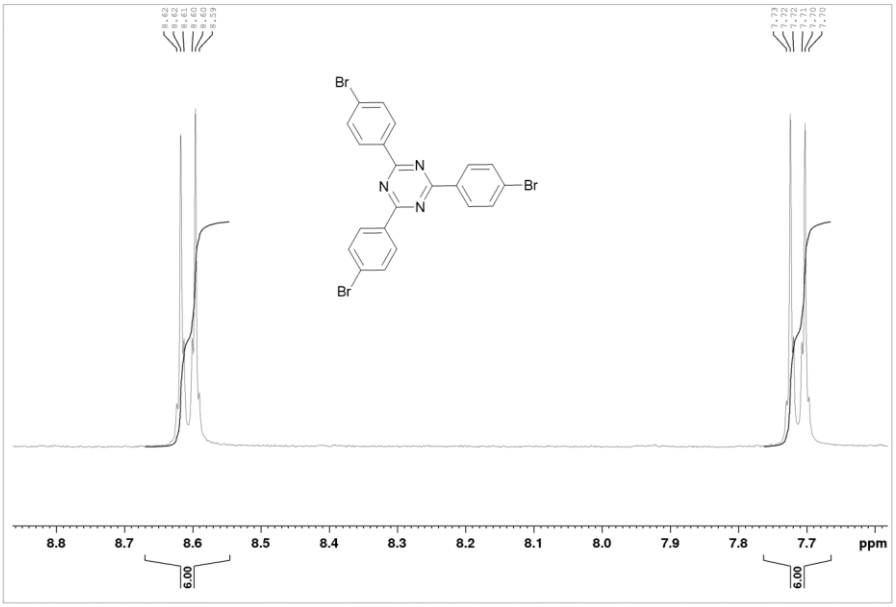

Figure 84: ^{1}H NMR spectrum of 2,4,6-tris(4-bromophenyl)-1,3,5-triazine magnified in the region from 8.9 to 7.6 ppm in $CDCl_3$.

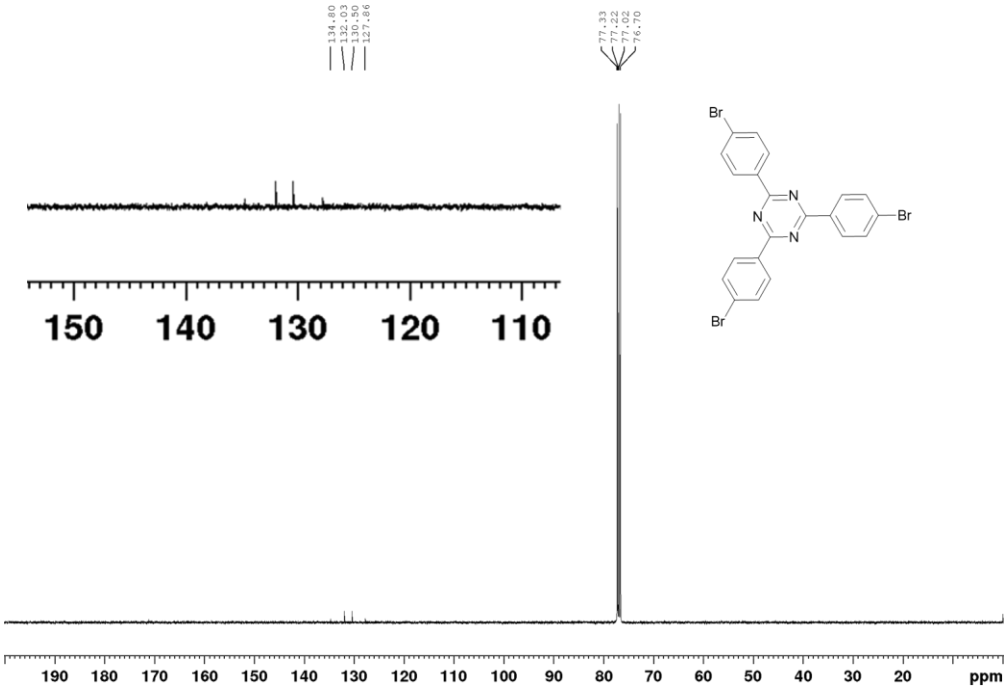

Figure 85: $^{13}C\{^{1}H\}$ NMR spectrum of 2,4,6-tris(4-bromophenyl)-1,3,5-triazine in $CDCl_3$.

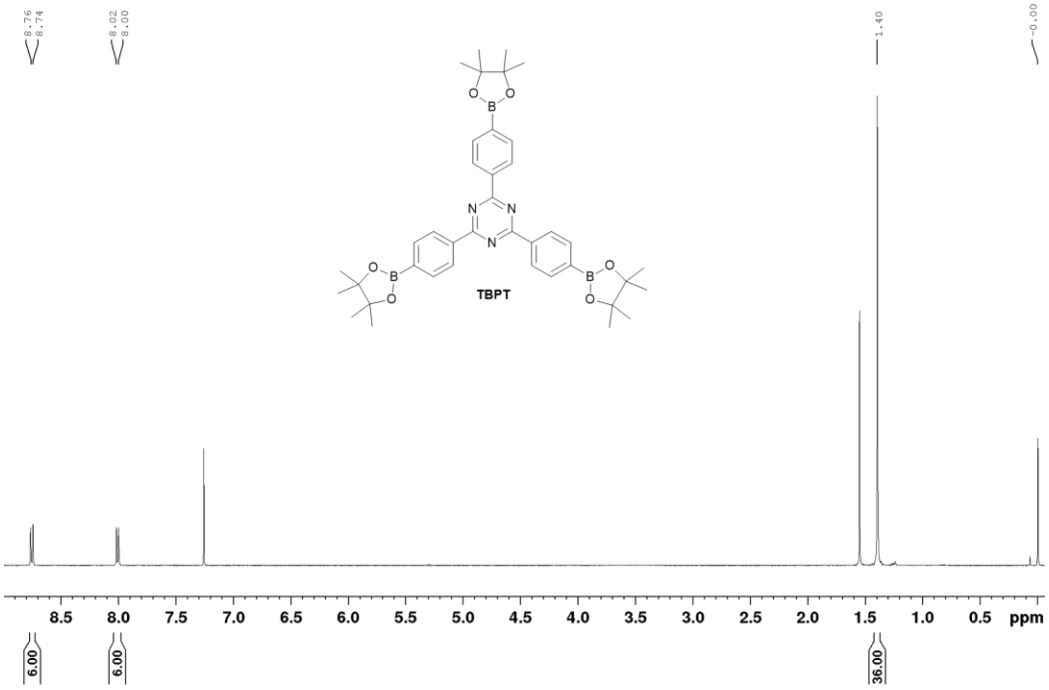

Figure 86: ^{1}H NMR spectrum of 2,4,6-tris[4-(4,4,5,5-tetramethyl-1,3,2-dioxaborolan-2-yl)phenyl]-1,3,5-triazine in $CDCl_3$.

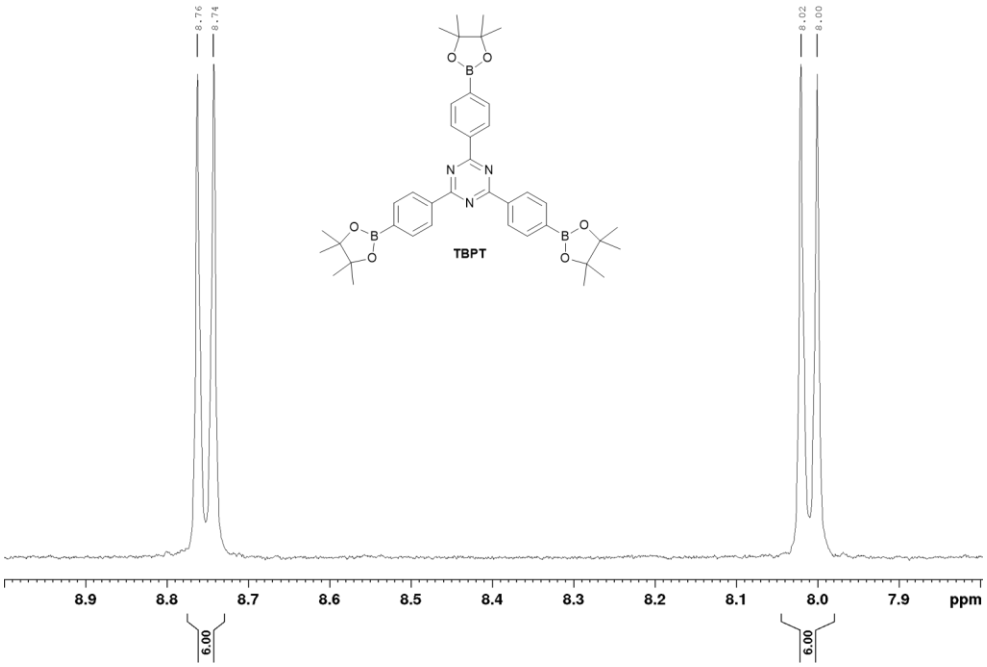

Figure 87: ^{1}H NMR spectrum of 2,4,6-tris[4-(4,4,5,5-tetramethyl-1,3,2-dioxaborolan-2-yl)phenyl]-1,3,5-triazine magnified in the region from 9.0 to 7.8 ppm in $CDCl_3$.

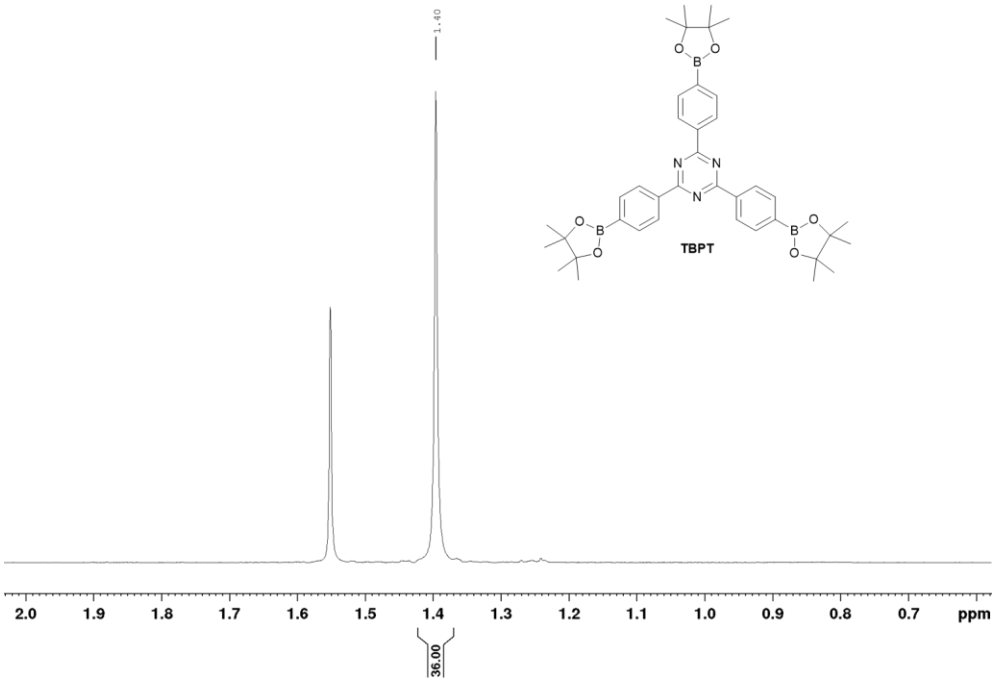

Figure 88: ^{1}H NMR spectrum of 2,4,6-tris[4-(4,4,5,5-tetramethyl-1,3,2-dioxaborolan-2-yl)phenyl]-1,3,5-triazine magnified in the region from 2.05 to 0.55 ppm in $CDCl_3$.

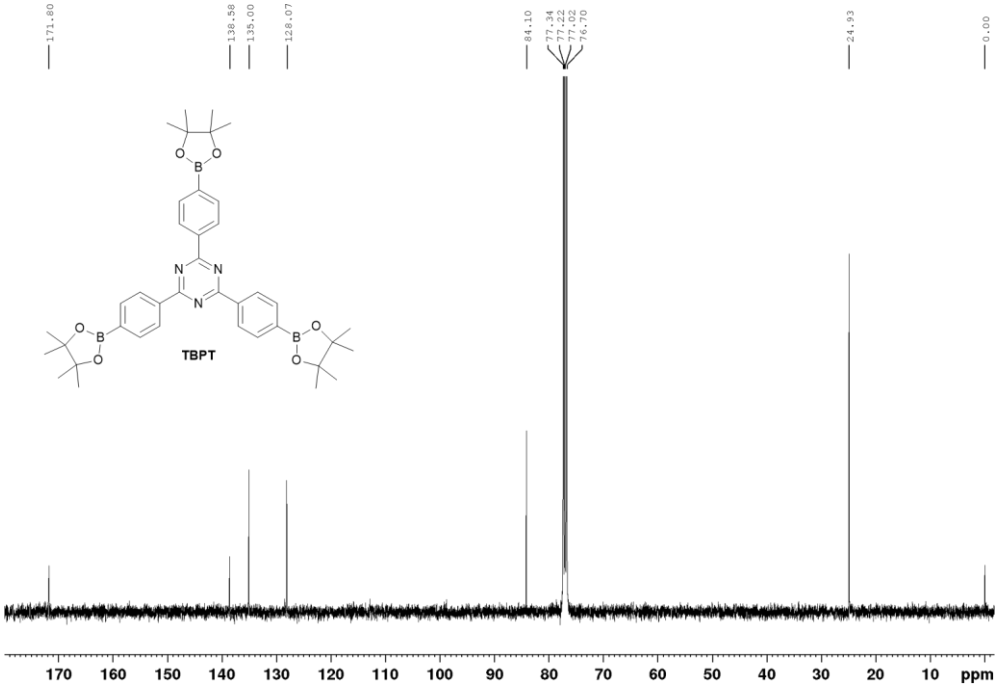

Figure 89: $^{13}C\{^{1}H\}$ NMR spectrum of 2,4,6-tris[4-(4,4,5,5-tetramethyl-1,3,2-dioxaborolan-2-yl)phenyl]-1,3,5-triazine in $CDCl_3$.

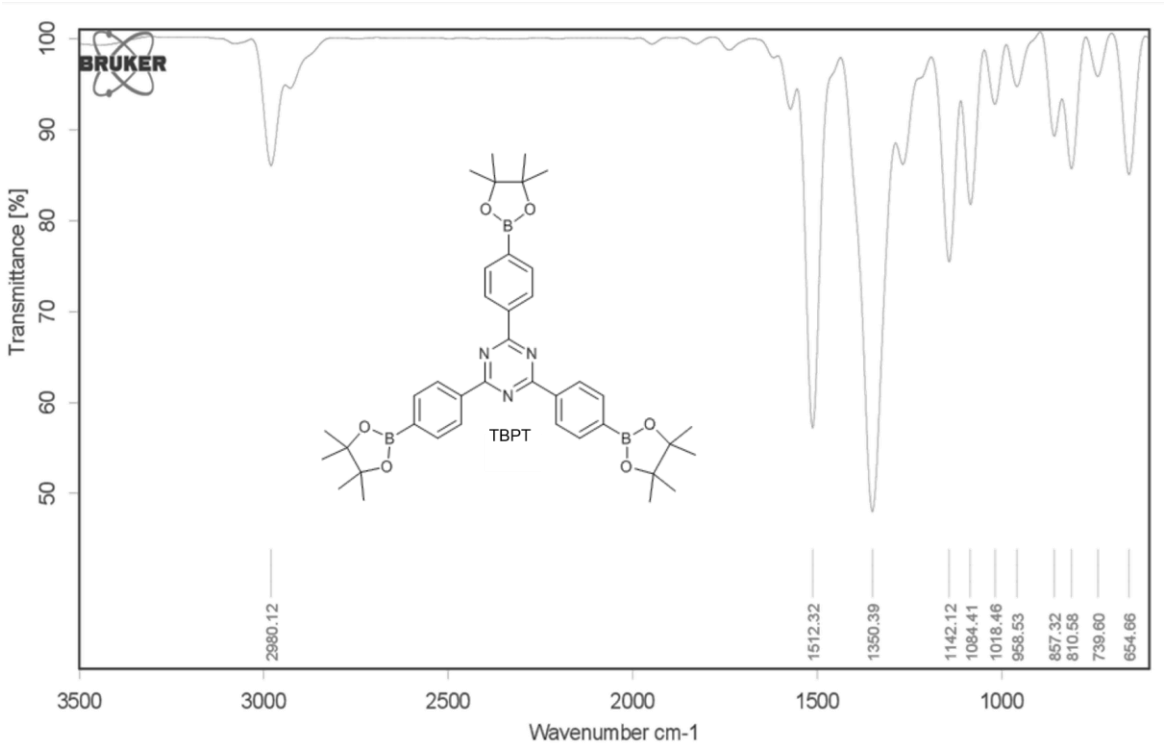

Figure 90: FT-IR spectrum of 2,4,6-tris[4-(4,4,5,5-tetramethyl-1,3,2-dioxaborolan-2-yl)phenyl]-1,3,5-triazine (KBr pellet).

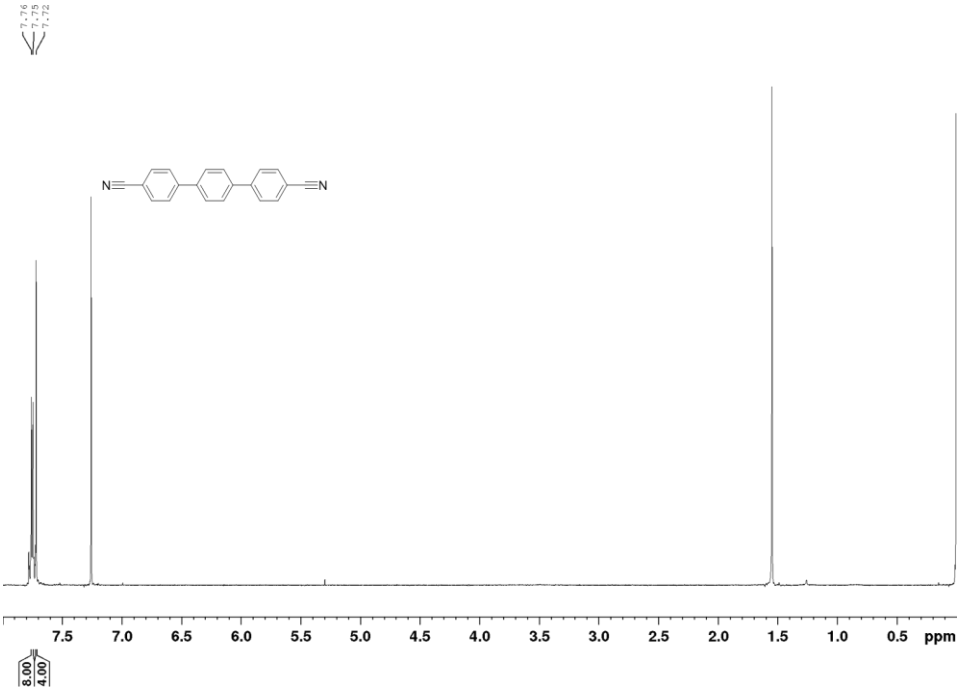

Figure 91: ^{1}H NMR spectrum of [1,1':4',1''-terphenyl]-4,4''-dicarbonitrile in $CDCl_3$.

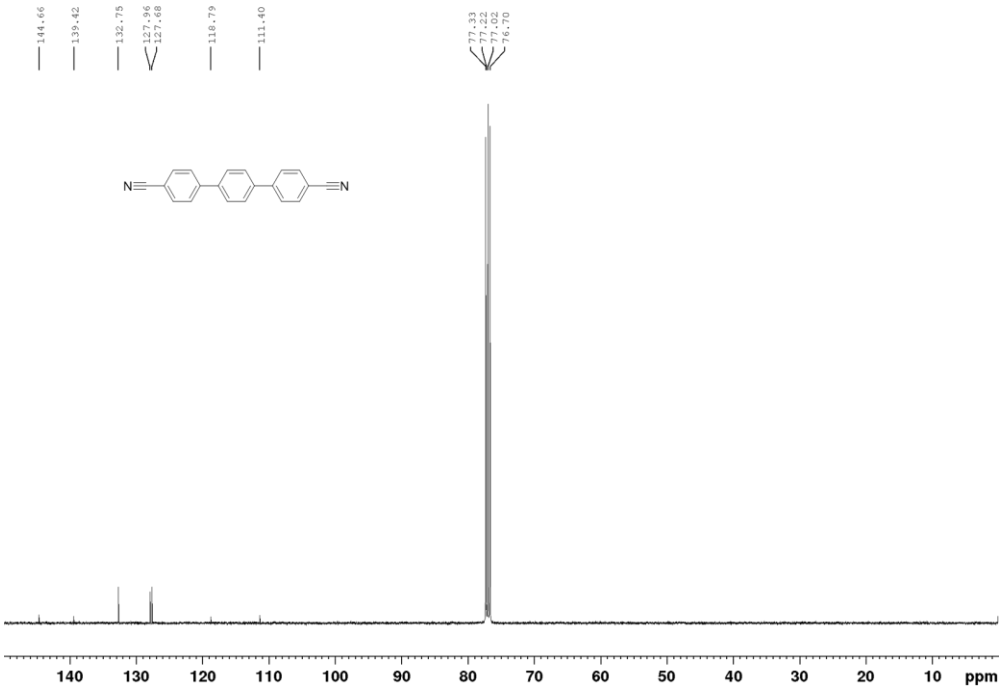

Figure 92: $^{13}C\{^{1}H\}$ NMR spectrum of [1,1':4',1''-terphenyl]-4,4''-dicarbonitrile in $CDCl_3$.

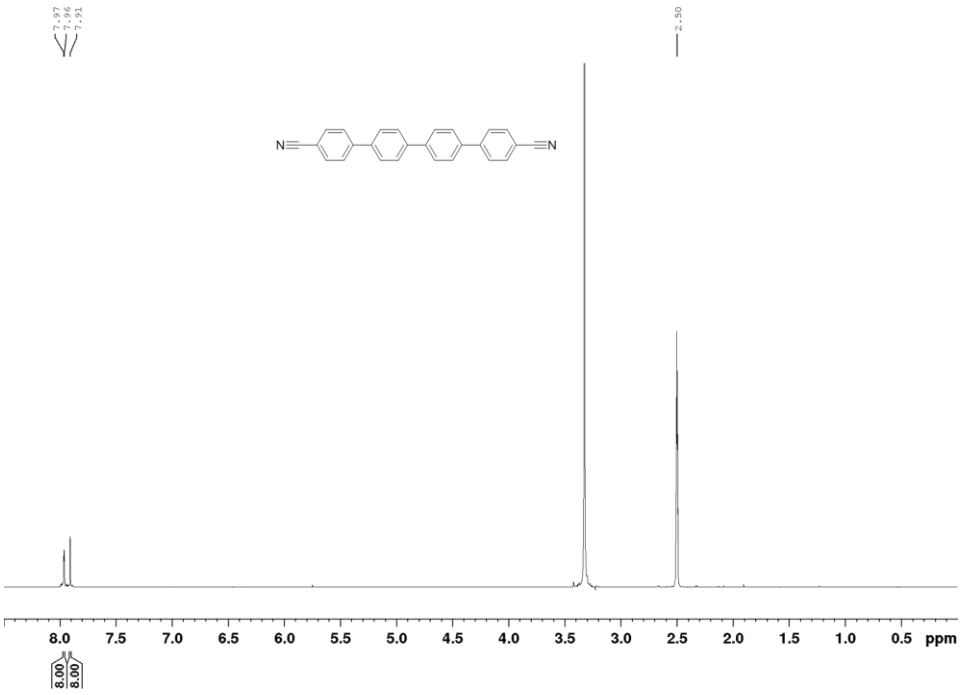

Figure 93: ^{1}H NMR spectrum of [1,1':4',1'':4'',1'''-quaterphenyl]-4,4'''-dicarbonitrile in dmso-d_6.

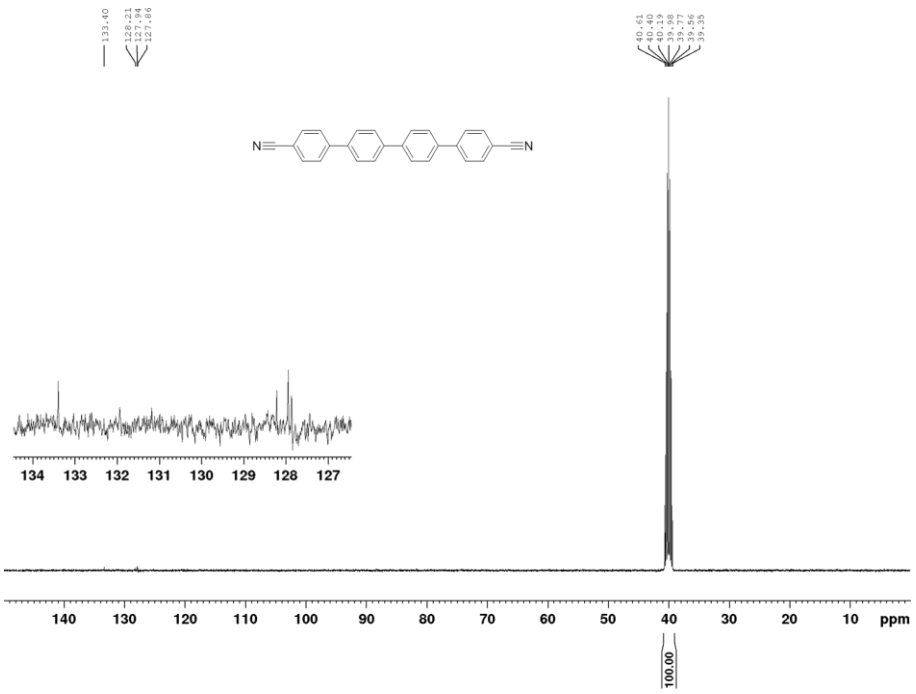

Figure 94: $^{13}C\{^{1}H\}$ NMR spectrum of [1,1':4',1'':4'',1'''-quaterphenyl]-4,4'''-dicarbonitrile in dmso-d_6.

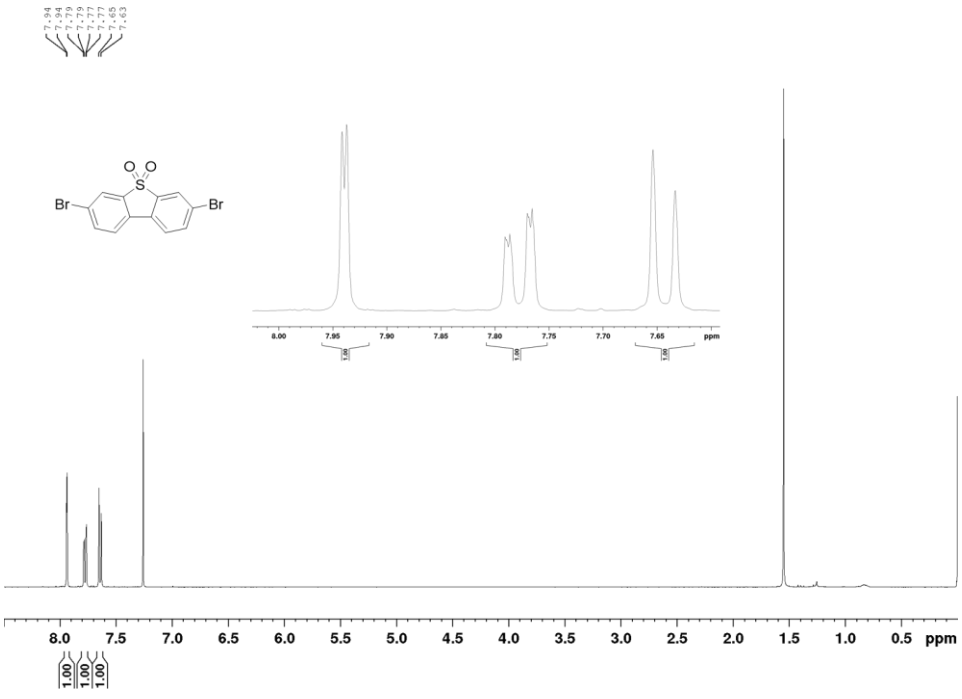

Figure 95: ^{1}H NMR spectrum of 3,7-dibromodibenzo[*b,d*]thiophene-5,5-dioxide in $CDCl_3$.

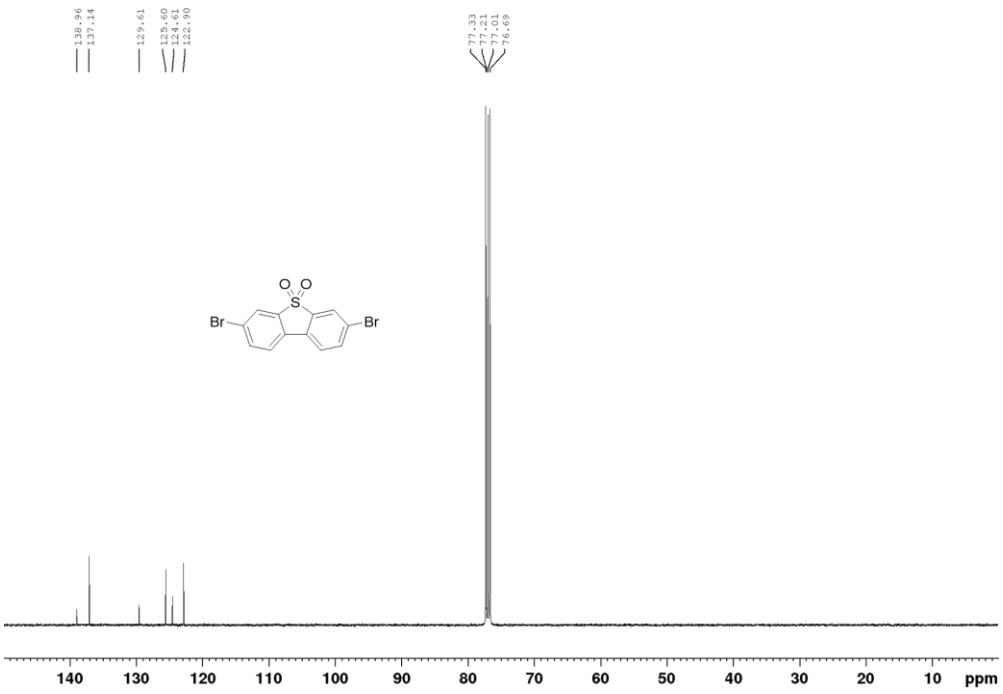

Figure 96: $^{13}C\{^{1}H\}$ NMR spectrum of 3,7-dibromodibenzo[*b,d*]thiophene-5,5-dioxide in $CDCl_3$.

12 References

1 V. A. Davankov, S. V Rogozhin and M. P. Tsyurupa, *US Pat.*, 1971, 3.729.457.

2 M. Thommes, K. Kaneko, A. V Neimark, J. P. Olivier, F. Rodriguez-Reinoso, J. Rouquerol and K. S. W. Sing, *Pure Appl. Chem.*, 2015, **87**, 1051–1069.

3 N. B. McKeown and P. M. Budd, in *Porous Polymers*, eds. M. S. Silverstein, N. R. Cameron and M. A. Hillmyer, Wiley, Hoboken, 1st edn., 2011, pp. 3–29.

4 O. W. Webster, F. P. Gentry, R. D. Farlee and B. E. Smart, *Makromol. Chem., Macromol. Symp.*, 1992, **54**–**55**, 477–482.

5 C. Urban, E. F. McCord, O. W. Webster, L. Abrams, H. W. Long, H. Gaede, P. Tang and A. Pines, *Chem. Mater.*, 1995, **7**, 1325–1332.

6 P. M. Budd, E. S. Elabas, B. S. Ghanem, S. Makhseed, N. B. McKeown, K. J. Msayib, C. E. Tattershall and D. Wang, *Adv. Mater.*, 2004, **16**, 456–459.

7 P. M. Budd, B. S. Ghanem, S. Makhseed, N. B. McKeown, K. J. Msayib and C. E. Tattershall, *Chem. Commun.*, 2004, **4**, 230–231.

8 N. B. McKeown, P. M. Budd, K. J. Msayib, B. S. Ghanem, H. J. Kingston, C. E. Tattershall, S. Makhseed, K. J. Reynolds and D. Fritsch, *Chemistry*, 2005, **11**, 2610–2620.

9 N. B. McKeown and P. M. Budd, *Chem. Soc. Rev.*, 2006, **35**, 675–683.

10 J. Germain, J. M. J. Fréchet and F. Svec, *J. Mater. Chem.*, 2007, **17**, 4989–4997.

11 R. Fricke, H. Kosslick, G. Lischke and M. Richter, *Chem. Rev.*, 2000, **100**, 2303–2406.

12 O. M. Yaghi, M. O'Keefe, N. W. Ockwig, H. K. Chae, M. Eddaoudi and J. Kim, *Nature*, 2003, **423**, 705–714.

13 N. W. Ockwig, A. P. Cote, M. O. Keeffe, A. J. Matzger and O. M. Yaghi, *Science*, 2005, **310**, 1166–1171.

14 J.-X. Jiang, F. Su, A. Trewin, C. D. Wood, N. L. Campbell, H. Niu, C. Dickinson, A. Y. Ganin, M. J. Rosseinsky, Y. Z. Khimyak and A. I. Cooper, *Angew. Chem., Int. Ed.*, 2007, **46**, 8574–8578.

15 N. Chaoui, M. Trunk, R. Dawson, J. Schmidt and A. Thomas, *Chem. Soc. Rev.*, 2017, **46**, 3302–

3321.

16 Y. Xu, S. Jin, H. Xu, A. Nagai and D. Jiang, *Chem. Soc. Rev.*, 2013, **42**, 8012–8031.

17 R. S. Sprick, J.-X. Jiang, B. Bonillo, S. Ren, T. Ratvijitvech, P. Guiglion, M. A. Zwijnenburg, D. J. Adams and A. I. Cooper, *J. Am. Chem. Soc.*, 2015, **137**, 3265–3270.

18 J. Langecker and M. Rehahn, *Macromol. Chem. Phys.*, 2008, **209**, 258–271.

19 J.-X. Jiang, F. Su, H. Niu, C. D. Wood, N. L. Campbell, Y. Z. Khimyak and A. I. Cooper, *Chem. Commun.*, 2008, **4**, 486–488.

20 Y. Jin, Y. Zhu and W. Zhang, *CrystEngComm*, 2013, **15**, 1484–1499.

21 S. Ren, R. Dawson, A. Laybourn, J.-X. Jiang, Y. Khimyak, D. J. Adams and A. I. Cooper, *Polym. Chem.*, 2012, **3**, 928–934.

22 R. S. Sprick, A. Thomas and U. Scherf, *Polym. Chem.*, 2010, **1**, 283–285.

23 J.-X. Jiang, F. Su, A. Trewin, C. D. Wood, H. Niu, J. T. A. Jones, Y. Z. Khimyak and A. I. Cooper, *J. Am. Chem. Soc.*, 2008, **130**, 7710–7720.

24 C. D. Wood, B. Tan, A. Trewin, F. Su, M. J. Rosseinsky, D. Bradshaw, Y. Sun, L. Zhou and A. I. Cooper, *Adv. Mater.*, 2008, **20**, 1916–1921.

25 G. Venkataramana and S. Sankararaman, *Eur. J. Org. Chem.*, 2005, 4162–4166.

26 L. Chen, Y. Yang and D. Jiang, *J. Am. Chem. Soc.*, 2010, **132**, 9138–9143.

27 J.-X. Jiang, A. Trewin, D. J. Adams and A. I. Cooper, *Chem. Sci.*, 2011, **2**, 1777–1781.

28 Y. Kou, Y. Xu, Z. Guo and D. Jiang, *Angew. Chem., Int. Ed.*, 2011, **50**, 8753–8757.

29 L. Chen, Y. Honsho, S. Seki and D. Jiang, *J. Am. Chem. Soc.*, 2010, **132**, 6742–6748.

30 X. Chen, S. Shen, L. Guo and S. S. Mao, *Chem. Rev.*, 2010, **110**, 6503–6570.

31 B. A. Pinaud, J. D. Benck, L. C. Seitz, A. J. Forman, Z. Chen, T. G. Deutsch, B. D. James, K. N. Baum, G. N. Baum, S. Ardo, H. Wang, E. Miller and T. F. Jaramillo, *Energy Environ. Sci.*, 2013, **6**, 1983–2002.

32 R. M. Navarro, M. A. Peña and J. L. G. Fierro, *Chem. Rev.*, 2007, **107**, 3952–3991.

33 R. Heap, *Potential Role of Hydrogen in the UK Energy System*, The Energy Research Partnership, London, 2017.

34 O. Ajayi-Oyakhire, *Hydrogen - Untapped Energy?*, Institution of Gas Engineers and Managers, Kegworth, 2012.

35 B. Pivovar, N. Rustagi and S. Satyapal, *Electrochem. Soc. Interface*, 2018, **27**, 47–52.

36 A. Fujishima, K. Honda and S. Kikuchi, *J. Chem. Soc. Japan (Kogyo Kagaku Zasshi)*, 1969, **72**, 108–113.

37 A. Fujishima and K. Honda, *Nature*, 1972, **238**, 37–38.

38 A. Kudo and Y. Miseki, *Chem. Soc. Rev.*, 2009, **38**, 253–278.

39 L. Yang, H. Zhou, T. Fan and D. Zhang, *Phys. Chem. Chem. Phys.*, 2014, **16**, 6810–6826.

40 K. Domen, S. Naito, M. Soma, T. Onishi and K. Tamaru, *J. Chem. Soc. Chem. Commun.*, 1980, **12**, 543–544.

41 K. Domen, S. Naito, T. Onishi and K. Tamaru, *Chem. Phys. Lett.*, 1982, **92**, 433–434.

42 S. Chen, T. Takata and K. Domen, *Nat. Rev. Mater.*, 2017, **2**, 17050–17067.

43 A. Kudo, H. Kato and I. Tsuji, *Chem. Lett.*, 2004, **33**, 1534–1539.

44 K. Maeda, T. Takata and K. Domen, in *Energy efficiency and renewable energy through nanotechnology*, ed. L. Zang, Springer London, London, 1st edn., 2011, pp. 487–529.

45 Y. Fan, D. Li, M. Deng, Y. Luo and Q. Meng, *Front. Chem. China*, 2009, **4**, 343–351.

46 M. G. Walter, E. L. Warren, J. R. McKone, S. W. Boettcher, Q. Mi, E. A. Santori and N. S. Lewis, *Chem. Rev.*, 2010, **110**, 6446–6473.

47 S. Y. Tee, K. Y. Win, W. S. Teo, L. Koh, S. Liu, C. P. Teng and M. Han, *Adv. Sci.*, , DOI:10.1002/advs.201600337.

48 T. Takata and K. Domen, *J. Phys. Chem. C*, 2009, **113**, 19386–19388.

49 J. Yang, D. Wang, H. Han and C. Li, *Acc. Chem. Res.*, 2013, **46**, 1900–1909.

50 J. Schneider, M. Matsuoka, M. Takeuchi, J. Zhang, Y. Horiuchi, M. Anpo and D. W. Bahnemann, *Chem. Rev.*, 2014, **114**, 9919–9986.

51 D. M. Fabian, S. Hu, N. Singh, F. A. Houle, T. Hisatomi, K. Domen, F. E. Osterloh and S. Ardo, *Energy Environ. Sci.*, 2015, **8**, 2825–2850.

52 D. G. Nocera, *Acc. Chem. Res.*, 2012, **45**, 767–776.

53 Q. Wang, T. Hisatomi, Q. Jia, H. Tokudome, M. Zhong, C. Wang, Z. Pan, T. Takata, M. Nakabayashi, N. Shibata, Y. Li, I. D. Sharp, A. Kudo, T. Yamada and K. Domen, *Nat. Mater.*, 2016, **15**, 611–617.

54 S. Yanagida, A. Kabumoto, K. Mizumoto, C. Pac and K. Yoshino, *J. Chem. Soc. Chem. Commun.*, 1985, **0**, 474–475.

55 T. Yamamoto, Y. Hayashi and A. Yamamoto, *Bull. Chem. Soc. Jpn.*, 1978, **51**, 2091–2097.

56 T. Shibata, A. Kabumoto, T. Shiragami, O. Ishitani, C. Pac and S. Yanagida, *J. Phys. Chem.*, 1990, **94**, 2068–2076.

57 S. Matsuoka, T. Kohzuki, Y. Kuwana, A. Nakamura and S. Yanagida, *J. Chem. Soc. Perkin Trans. 2*, 1992, 679–685.

58 S. Matsuoka, H. Fujii, T. Yamada, C. Pac, A. Ishida, S. Takamuku, M. Kusaba, N. Nakashima and S. Yanagida, *J. Phys. Chem.*, 1991, **95**, 5802–5808.

59 R. S. Sprick, B. Bonillo, R. Clowes, P. Guiglion, N. J. Brownbill, B. J. Slater, F. Blanc, M. A. Zwijnenburg, D. J. Adams and A. I. Cooper, *Angew. Chem., Int. Ed.*, 2016, **128**, 1824–1828.

60 K. Schwinghammer, B. Tuffy, M. B. Mesch, E. Wirnhier, C. Martineau, F. Taulelle, W. Schnick, J. Senker and B. V. Lotsch, *Angew. Chem., Int. Ed.*, 2013, **52**, 2435–2439.

61 K. Kailasam, J. Schmidt, H. Bildirir, G. Zhang, S. Blechert, X. Wang and A. Thomas, *Macromol. Rapid Commun.*, 2013, **34**, 1008–1013.

62 V. W.-H. Lau, M. B. Mesch, V. Duppel, V. Blum, J. Senker and B. V. Lotsch, *J. Am. Chem. Soc.*, 2015, **137**, 1064–1072.

63 J. Liebig, *Ann. der Pharm.*, 1834, **10**, 1–47.

64 F. Goettmann, A. Fischer, M. Antonietti and A. Thomas, *Angew. Chem., Int. Ed.*, 2006, **45**, 4467–4471.

65 F. Goettmann, A. Fischer, M. Antonietti and A. Thomas, *Chem. Commun.*, 2006, 4530–4532.

66 X. Wang, K. Maeda, A. Thomas, K. Takanabe, G. Xin, J. M. Carlsson, K. Domen and M. Antonietti, *Nat. Mater.*, 2009, **8**, 76–80.

67 S. Cao, J. Low, J. Yu and M. Jaroniec, *Adv. Mater.*, 2015, **27**, 2150–2176.

68 M. J. Bojdys, N. Severin, J. P. Rabe, A. I. Cooper, A. Thomas and M. Antonietti, *Macromol. Rapid*

Commun., 2013, **34**, 850–854.

69 S. Yang, Y. Gong, J. Zhang, L. Zhan, L. Ma, Z. Fang, R. Vajtai, X. Wang and P. M. Ajayan, *Adv. Mater.*, 2013, **25**, 2452–2456.

70 J. Xu, L. Zhang, R. Shi and Y. Zhu, *J. Mater. Chem. A*, 2013, **1**, 14766–14772.

71 T. Sano, S. Tsutsui, K. Koike, T. Hirakawa, Y. Teramoto, N. Negishi and K. Takeuchi, *J. Mater. Chem. A*, 2013, **1**, 6489–6496.

72 P. Niu, L. Zhang, G. Liu and H. M. Cheng, *Adv. Funct. Mater.*, 2012, **22**, 4763–4770.

73 Xinchen Wang, Kazuhiko Maeda, Xiufang Chen, Kazuhiro Takanabe, Kazunari Domen, Yidong Hou, Xianzhi Fu and M. Antonietti, *J. Am. Chem. Soc.*, 2009, **131**, 1680–1681.

74 J. Sun, J. Zhang, M. Zhang, M. Antonietti, X. Fu and X. Wang, *Nat Commun*, 2012, **3**, 1139–1145.

75 X. H. Li, J. Zhang, X. Chen, A. Fischer, A. Thomas, M. Antonietti and X. Wang, *Chem. Mater.*, 2011, **23**, 4344–4348.

76 X. Lu, Q. Wang and D. Cui, 2010, **26**, 925–930.

77 Y. Zang, L. Li, Y. Zuo, H. Lin, G. Li and X. Guan, *RSC Adv.*, 2013, **3**, 13646–13650.

78 M. Xu, L. Han and S. Dong, *ACS Appl. Mater. Interfaces*, 2013, **5**, 12533–12540.

79 Y. Lan, X. Qian, C. Zhao, Z. Zhang, X. Chen and Z. Li, *J. Colloid Interface Sci.*, 2013, **395**, 75–80.

80 L. Ge, F. Zuo, J. Liu, Q. Ma, C. Wang, D. Sun, L. Bartels and P. Feng, *J. Phys. Chem. C*, 2012, **116**, 13708–13714.

81 F. Yang, V. Kuznietsov, M. Lublow, C. Merschjann, A. Steigert, J. Klaer, A. Thomas and T. Schedel-Niedrig, *J. Mater. Chem. A*, 2013, **1**, 6407–6415.

82 Y. Sui, J. Liu, Y. Zhang, X. Tian and W. Chen, *Nanoscale*, 2013, **5**, 9150–9155.

83 S. Gawande and S. R. Thakare, *ChemCatChem*, 2012, **4**, 1759–1763.

84 G. Zhang, S. Zang and X. Wang, *ACS Catal.*, 2015, **5**, 941–947.

85 J. Liu, Y. Liu, N. Liu, Y. Han, X. Zhang, H. Huang, Y. Lifshitz, S.-T. Lee, J. Zhong and Z. Kang, *Science*, 2015, **347**, 970–974.

86 L. Lin, C. Wang, W. Ren, H. Ou, Y. Zhang and X. Wang, *Chem. Sci.*, 2017, **8**, 5506–5511.

87 M. G. Schwab, M. Hamburger, X. Feng, J. Shu, H. W. Spiess, X. Wang, M. Antonietti and K. Müllen, *Chem. Commun.*, 2010, **46**, 8932–8934.

88 R. S. Sprick, B. Bonillo, M. Sachs, R. Clowes, J. R. Durrant, D. J. Adams and A. I. Cooper, *Chem. Commun.*, 2016, **52**, 10008–10011.

89 L. Li, W.-Y. Lo, Z. Cai, N. Zhang and L. Yu, *Macromolecules*, 2016, **49**, 6903–6909.

90 L. Wang, Y. Wan, Y. Ding, Y. Niu, Y. Xiong, X. Wu and H. Xu, *Nanoscale*, 2017, **9**, 4090–4096.

91 C. Yang, B. C. Ma, L. Zhang, S. Lin, S. Ghasimi, K. Landfester, K. A. I. Zhang and X. Wang, *Angew. Chem., Int. Ed.*, 2016, **55**, 9348–9352.

92 D. J. Woods, R. S. Sprick, C. L. Smith, A. J. Cowan and A. I. Cooper, *Adv. Energy Mater.*, 2017, 1700479.

93 R. S. Sprick, C. Aitchison, E. Berardo, L. Turcani, L. Wilbraham, B. M. Alston, K. E. Jelfs, M. A. Zwijnenburg and A. I. Cooper, *J. Mater. Chem. A*, 2018, **6**, 11994–12003.

94 V. S. Vyas, F. Haase, L. Stegbauer, G. Savasci, F. Podjaski, C. Ochsenfeld and B. V Lotsch, *Nat. Commun.*, 2015, **6**, 8508–8516.

95 A. Haase, T. Banerjee, G. Savasci, C. Ochsenfeld, B. V. Lotsch, S. Takahashi, M. Addicoat, M. E. El-Khouly, T. Nakamura, S. Irle, S. Fukuzumi, A. Nagai and D. Jiang, *Faraday Discuss.*, 2017, **201**, 247–264.

96 L. Stegbauer, K. Schwinghammer and B. V. Lotsch, *Chem. Sci.*, 2014, **5**, 2789–2793.

97 J. Bi, W. Fang, L. Li, J. Wang, S. Liang, Y. He, M. Liu and L. Wu, *Macromol. Rapid Commun.*, 2015, **36**, 1799–1805.

98 J. Xie, S. A. Shevlin, Q. Ruan, S. J. A. Moniz, Y. Liu, X. Liu, Y. Li, C. C. Lau, Z. X. Guo and J. Tang, *Energy Environ. Sci.*, 2018, **11**, 1617–1624.

99 K. Schwinghammer, S. Hug, M. B. Mesch, J. Senker and B. V Lotsch, *Energy Environ. Sci.*, 2015, **8**, 3345–3353.

100 S. Kuecken, A. Acharjya, L. Zhi, M. Schwarze, R. Schomacker and A. Thomas, *Chem. Commun.*, 2017, **53**, 5854–5857.

101 Z. Zhang, J. Long, L. Yang, W. Chen, W. Dai, X. Fu and X. Wang, *Chem. Sci.*, 2011, **2**, 1826–1830.

102 S. Chu, Y. Wang, Y. Guo, P. Zhou, H. Yu, L. Luo, F. Kong and Z. Zou, *J. Mater. Chem.*, 2012, **22**,

15519–15521.

103 D. Schwarz, K. Y. S., A. Acharjya, A. Ichangi, O. M. V., J. Čejka, U. Lappan, A. Arki, J. He, J. Schmidt, P. Nachtigall, A. Thomas, J. Tarábek and M. J. Bojdys, *Chem. – A Eur. J.*, 2017, **23**, 13023–13027.

104 L. Li, W. Fang, P. Zhang, J. Bi, Y. He, J. Wang and W. Su, *J. Mater. Chem. A*, 2016, **4**, 12402–12406.

105 X. Li, J. Yu, J. Low, Y. Fang, J. Xiao and X. Chen, *J. Mater. Chem. A*, 2015, **3**, 2485–2534.

106 C. A. Caputo, M. A. Gross, V. W. Lau, C. Cavazza, B. V. Lotsch and E. Reisner, *Angew. Chem., Int. Ed.*, 2014, **53**, 11538–11542.

107 M. Qureshi and K. Takanabe, *Chem. Mater.*, 2017, **29**, 158–167.

108 J. R. Holst and E. G. Gillan, *J. Am. Chem. Soc.*, 2008, **130**, 7373–7379.

109 P. Guiglion, C. Butchosa and M. A. Zwijnenburg, *Macromol. Chem. Phys.*, 2016, **217**, 344–353.

110 Z.-A. Lan, Y. Fang, Y. Zhang and X. Wang, *Angew. Chem., Int. Ed.*, 2018, **57**, 470–474.

111 D. Schwarz, A. Acharja, A. Ichangi, P. Lyu, M. V Opanasenko, F. R. Goßler, T. A. F. König, J. Čejka, P. Nachtigall, A. Thomas and M. J. Bojdys, *Chem. Eur. J.*, 2018, **24**, 11916–11921.

112 P. Kuhn, M. Antonietti and A. Thomas, *Angew. Chem., Int. Ed.*, 2008, **47**, 3450–3453.

113 M. J. Bojdys, J. Jeromenok, A. Thomas and M. Antonietti, *Adv. Mater.*, 2010, **22**, 2202–2205.

114 S. Kuecken, J. Schmidt, L. Zhi and A. Thomas, *J. Mater. Chem. A*, 2015, **3**, 24422–24427.

115 W. Huang, Z. J. Wang, B. C. Ma, S. Ghasimi, D. Gehrig, F. Laquai, K. Landfester and K. A. I. Zhang, *J. Mater. Chem. A*, 2016, **4**, 7555–7559.

116 Q. Wang, T. Hisatomi, M. Katayama, T. Takata, T. Minegishi, A. Kudo, T. Yamada and K. Domen, *Faraday Discuss.*, 2017, **197**, 491–504.

117 A. Herrera, A. Riaño, R. Moreno, B. Caso, Z. D. Pardo, I. Fernández, E. Sáez, D. Molero, A. Sánchez-Vázquez and R. Martínez-Alvarez, *J. Org. Chem.*, 2014, **79**, 7012–7024.

118 G. Miller, *US Pat.*, 1971, 3.775.380A.

119 R. Berger, J. Hauser, G. Labat, E. Weber and J. Hulliger, *CrystEngComm*, 2012, **14**, 768–770.

120 S. Biswas and S. Batra, *Eur. J. Org. Chem.*, 2012, 3492–3499.

121 J. Artz, *ChemCatChem*, 2018, **10**, 1753–1771.

122 R. D. Howells and J. D. Mc Cown, *Chem. Rev.*, 1977, **77**, 69–92.

123 F. Blanc, S. Y. Chong, T. O. McDonald, D. J. Adams, S. Pawsey, M. A. Caporini and A. I. Cooper, *J. Am. Chem. Soc.*, 2013, 15290–15293.

124 C. B. Meier, R. S. Sprick, A. Monti, P. Guiglion, J.-S. M. Lee, M. A. Zwijnenburg and A. I. Cooper, *Polymer*, 2017, **126**, 283–290.

125 S. Ren, M. J. Bojdys, R. Dawson, A. Laybourn, Y. Z. Khimyak, D. J. Adams and A. I. Cooper, *Adv. Mater.*, 2012, **24**, 2357–2361.

126 M. A. Ismail, R. K. Arafa, R. Brun, T. Wenzler, Y. Miao, W. D. Wilson, C. Generaux, A. Bridges, J. E. Hall and D. W. Boykin, *J. Med. Chem.*, 2006, **49**, 5324–5332.

127 M. Schiek, K. Al-Shamery and A. Lützen, *Synthesis*, 2007, **4**, 0613–0621.

128 M. Iwasaki and Y. Nishihara, in *Applied Cross-Coupling Reactions*, ed. Y. Nishihara, Springer-Verlag Berlin Heidelberg, 1st edn., 2013, pp. 17–39.

129 V. K. Krieble and C. I. Noll, *J. Am. Chem. Soc.*, 1939, **61**, 560–563.

130 M. Hesse, H. Meier and B. Zeeh, *Spektroskopische Methoden in der organischen Chemie*, Thieme, 7th edn., 2012.

131 A.-D. Schlüter, *J. Polym. Sci. Part A Polym. Chem.*, 2001, **39**, 1533–1556.

132 M. Rehahn, A.-D. Schlüter, G. Wegner and W. J. Feast, *Polymer*, 1989, **30**, 1054–1059.

133 A.-D. Schlüter and G. Wegner, *Acta Polym.*, 1993, **44**, 59–69.

134 H. Furukawa, Y. B. Go, N. Ko, Y. K. Park, F. J. Uribe-Romo, J. Kim, M. O'Keeffe and O. M. Yaghi, *Inorg. Chem.*, 2011, **50**, 9147–9152.

135 T. Ishiyama, M. Murata and N. Miyaura, *J. Org. Chem.*, 1995, **60**, 7508–7510.

136 G. Cheng, B. Bonillo, R. S. Sprick, D. J. Adams, T. Hasell and A. I. Cooper, *Adv. Funct. Mater.*, 2014, **24**, 5219–5224.

137 L. Ching-Zong, G. Parthasarathy, J. Jayachandran, P. Kanniyappan, C. Yu-Wei and C. Chien-Hong, *Chem. Eur. J.*, 2013, **19**, 14181–14186.

138 S. S. Moleele, J. P. Michael and C. B. de Koning, *Tetrahedron*, 2006, **62**, 2831–2844.

139 F. Nemati, M. A. Bigdeli, G. H. Mahdavinia and H. Kiani, *Green Chem. Lett. Rev.*, 2010, **3**, 89–92.

140 M. Jayakannan, J. L. J. van Dongen and R. A. J. Janssen, *Macromolecules*, 2001, **34**, 5386–5393.

141 Y. Zeng, R. Zou, Z. Luo, H. Zhang, X. Yao, X. Ma, R. Zou and Y. Zhao, *J. Am. Chem. Soc.*, 2015, **137**, 1020–1023.

142 C. R. DeBlase and W. R. Dichtel, *Macromolecules*, 2016, **49**, 5297–5305.

143 D. Bartholomew, in *Reference Module in Chemistry, Molecular Sciences and Chemical Engineering Comprehensive Heterocyclic Chemistry II*, Pergamon, Oxford, 1st. edn., 1996, pp. 575–636.

144 J.-X. Jiang, F. Su, A. Trewin, C. D. Wood, H. Niu, J. T. A. Jones, Y. Z. Khimyak and A. I. Cooper, *J. Am. Chem. Soc.*, 2008, **130**, 7710–7720.

145 A. P. Côté, H. M. El-Kaderi, H. Furukawa, J. R. Hunt and O. M. Yaghi, *J. Am. Chem. Soc.*, 2007, **129**, 12914–12915.

146 D. Garrido-Diez and I. Baraia, in *2017 IEEE International Workshop of Electronics, Control, Measurement, Signals and their Application to Mechatronics (ECMSM)*, 2017, pp. 1–6.

147 A. Laybourn, R. Dawson, R. Clowes, T. Hasell, A. I. Cooper, Y. Z. Khimyak and D. J. Adams, *Polym. Chem.*, 2014, **5**, 6325–6333.

148 P. Guiglion, A. Monti and M. A. Zwijnenburg, *J. Phys. Chem. C*, 2017, **121**, 1498–1506.

149 P. Guiglion, C. Butchosa and M. A. Zwijnenburg, *J. Mater. Chem. A*, 2014, **2**, 11996.

150 T. Mitra, F. Moreau, A. Nevin, C. U. Perotto, A. Summerfield, E. S. Davies, E. A. Gibson, T. L. Easun and M. Schröder, *Chem. Sci.*, 2018, **9**, 6572–6579.

151 L. Li, Z. Cai, Q. Wu, W. Y. Lo, N. Zhang, L. X. Chen and L. Yu, *J. Am. Chem. Soc.*, 2016, **138**, 7681–7686.

152 M. Sachs, R. S. Sprick, D. Pearce, S. J. Hillman, A. Monti, A. A. Y. Guilbert, N. J. Brownbill, S. Dimitrov, F. Blanc, M. A. Zwijnenburg, J. Nelson, J. R. Durrant and A. I. Cooper, *Nat. Commun.*, 2018, **9**, 4968.

153 K. T. Nielsen, K. Bechgaard and F. C. Krebs, *Macromolecules*, 2005, **38**, 658–659.

154 F. C. Krebs, R. B. Nyberg and M. Jørgensen, *Chem. Mater.*, 2004, **16**, 1313–1318.

155 Z. Lin, M. D. Woodroof, L. Ji, Y. Liang, W. Krause and X. Zhang, *J. Appl. Polym. Sci.*, 2009, **116**,

895–901.

156 J. P. Erikson, *J. Chem. Educ.*, 2017, **94**, 75–78.

157 B. J. Hales, G. L. Bertrand and L. G. Hepler, *J. Phys. Chem.*, 1966, **70**, 3970–3975.

158 R. N. Goldberg, N. Kishore and R. M. Lennen, *J. Phys. Chem. Ref. Data*, 2002, **31**, 231–370.

159 V. W. Rosso, D. A. Lust, P. J. Bernot, J. A. Grosso, S. P. Modi, A. Rusowicz, T. C. Sedergran, J. H. Simpson, S. K. Srivastava, M. J. Humora and N. G. Anderson, *Org. Process Res. Dev.*, 1997, **1**, 311–314.

160 W. Zhang, J. Smith, R. Hamilton, M. Heeney, J. Kirkpatrick, K. Song, S. E. Watkins, T. Anthopoulos and I. McCulloch, *J. Am. Chem. Soc.*, 2009, **131**, 10814–10815.

161 K. Maeda, X. Wang, Y. Nishihara, D. Lu, M. Antonietti and K. Domen, *J. Phys. Chem. C*, 2009, **113**, 4940–4947.

162 J. Kosco and I. McCulloch, *ACS Energy Lett.*, 2018, 2846–2850.

163 J. Kosco, M. Sachs, R. Godin, M. Kirkus, L. Francas, M. Bidwell, M. Qureshi, D. Anjum, J. R. Durrant and I. McCulloch, *Adv. Energy Mater.*, 2018, **0**, 1802181.

164 K. Wenderich and G. Mul, *Chem. Rev.*, 2016, **116**, 14587–14619.

165 Chanjuan Xi, Zhengshi Chen, Qinglin Li and Zhensheng Jin, *J. Photochem. Photobiol. A Chem.*, 1995, **87**, 249–255.

166 T. Xue, Z. Lin, C.-Y. Chiu, Y. Li, L. Ruan, G. Wang, Z. Zhao, C. Lee, X. Duan and Y. Huang, *Sci. Adv.*, 2017, **3**, e1600615.

167 A. J. J. Lennox and G. C. Lloyd-Jones, *Chem. Soc. Rev.*, 2014, **43**, 412–443.

168 Y. Peng, W. K. Wong, Z. Hu, Y. Cheng, D. Yuan, S. A. Khan and D. Zhao, *Chem. Mater.*, 2016, **28**, 5095–5101.

169 I. Ullah, R. A. Khera, M. Hussain, A. Villinger and P. Langer, *Tetrahedron Lett.*, 2009, **50**, 4651–4653.

170 X. Wang, K. Maeda, X. Chen, K. Takanabe, K. Domen, Y. Hou, X. Fu and M. Antonietti, *J. Am. Chem. Soc.*, 2009, **131**, 1680–1681.

171 R. Zaleski, P. Krasucka, K. Skrzypiec and J. Goworek, *Macromolecules*, 2017, **50**, 5080–5089.

172 V. A. Davankov and A. V Pastukhov, *J. Phys. Chem. B*, 2011, **115**, 15188–15195.

173 Y. Pellegrin and F. Odobel, *Comptes Rendus Chim.*, 2017, **20**, 283–295.

174 C. G. Zoski, T. J. Smith and K. J. Stevenson, in *Handbook of Electrochemistry*, Elsevier, Amsterdam, Boston, 1st edn., 2007, pp. 73–110.

175 X. Zhang, Z. Jin, Y. Li, S. Li and G. Lu, *J. Phys. Chem. C*, 2009, **113**, 2630–2635.

176 G. Zhang, Z.-A. Lan and X. Wang, *Angew. Chem., Int. Ed.*, 2016, **55**, 15712–15727.

177 P.-K. Chuang, K.-H. Wu, T.-F. Yeh and H. Teng, *ACS Sustain. Chem. Eng.*, 2016, **4**, 5989–5997.

178 Z. Sun, H. Zheng, J. Li and P. Du, *Energy Environ. Sci.*, 2015, **8**, 2668–2676.

179 M. Katsuya, Y. Kazuyori, W. Yuji and Y. Shozo, *Bull. Chem. Soc. Jpn.*, 1993, **66**, 1053–1064.

180 R. S. Sprick, L. Wilbraham, Y. Bai, P. Guiglion, A. Monti, R. Clowes, A. I. Cooper and M. A. Zwijnenburg, *Chem. Mater.*, 2018, **30**, 5733–5742.

181 D. Chunhui, X. Shidang, L. Wei, G. Xuezhong, P.-F. Majid, L. Zitong, Z. Deqing, X. Can, L. K. Ping and L. Bin, *Small*, 2018, **14**, 1801839.

182 L. Wang, Y. Wan, Y. Ding, S. Wu, Y. Zhang, X. Zhang, G. Zhang, Y. Xiong, X. Wu, J. Yang and H. Xu, *Adv. Mater.*, 2017, **29**, 1702428.

183 L. Wang, X. Zheng, L. Chen, Y. Xiong and H. Xu, *Angew. Chem., Int. Ed.*, 2018, **57**, 3454–3458.

184 H. Rampf, *Allgemeine und anorganische Chemie: Grundlagen; mit ausführlichem Lösungsteil zum Heraustrennen; Extra: Lerntipps!*, mentor Verlag GmbH, München, 9th. edn., 2008.

185 H. Kominami, K. Yabutani, T. Yamamoto, Y. Kera and B. Ohtani, *J. Mater. Chem.*, 2001, **11**, 3222–3227.

186 W. Erbs, J. Desilvestro, E. Borgarello and M. Graetzel, *J. Phys. Chem.*, 1984, **88**, 4001–4006.

187 F. Peter, F. R. A., H. J. D. and M. M. A., *J. Am. Ceram. Soc.*, 2010, **93**, 1187–1194.

188 T. Takata, G. Hitoki, J. N. Kondo, M. Hara, H. Kobayashi and K. Domen, *Res. Chem. Intermed.*, 2007, **33**, 13–25.

189 S. Zhu, Y. Zhao, Y. He and D. Wang, *J. Chem. Phys.*, 2018, **150**, 41712.

190 K. Schwinghammer, M. B. Mesch, V. Duppel, C. Ziegler, J. Senker and B. V. Lotsch, *J. Am. Chem. Soc.*, 2014, **136**, 1730–1733.

191 E. R. Jette and F. Foote, *J. Chem. Phys.*, 1935, **3**, 605–616.

192 K. Sayama and H. Arakawa, *J. Phys. Chem.*, 1993, **97**, 531–533.

193 M. M. Najafpour, F. Rahimi, M. Amini, S. Nayeri and M. Bagherzadeh, *Dalt. Trans.*, 2012, **41**, 11026–11031.

194 M. M. Najafpour, *Dalt. Trans.*, 2011, **40**, 3805–3807.

195 M. Yoshida, K. Maeda, D. Lu, J. Kubota and K. Domen, *J. Phys. Chem. C*, 2013, **117**, 14000–14006.

196 A. Kudo, K. Domen, K. Maruya and T. Onishi, *Chem. Phys. Lett.*, 1987, **133**, 517–519.

197 E. Oakton, D. Lebedev, M. Povia, D. F. Abbott, E. Fabbri, A. Fedorov, M. Nachtegaal, C. Copéret and T. J. Schmidt, *ACS Catal.*, 2017, **7**, 2346–2352.

198 N. L. Campbell, R. Clowes, L. K. Ritchie and A. I. Cooper, *Chem. Mater.*, 2009, **21**, 204–206.

199 H. Sugiura, A. Wakamiya and O. Yoshikawa, *Jp. Pat.*, 2014, WO 2014157 A1.

200 J. Wudarczyk, G. Papamokos, T. Marszalek, T. Nevolianis, D. Schollmeyer, W. Pisula, G. Floudas, M. Baumgarten and K. Müllen, *ACS Appl. Mater. Interfaces*, 2017, **9**, 20527–20535.

201 P. Shen, H. Bin, Y. Zhang and Y. Li, *Polym. Chem.*, 2014, **5**, 567–577.

202 A. Casey, Y. Han, Z. Fei, A. J. P. White, T. D. Anthopoulos and M. Heeney, *J. Mater. Chem. C*, 2015, **3**, 265–275.

203 A. Creamer, C. S. Wood, P. D. Howes, A. Casey, S. Cong, A. V Marsh, R. Godin, J. Panidi, T. D. Anthopoulos, C. H. Burgess, T. Wu, Z. Fei, I. Hamilton, M. A. McLachlan, M. M. Stevens and M. Heeney, *Nat. Commun.*, 2018, **9**, 3237.

204 C. Yang, W. Huang, L. C. da Silva, K. A. I. Zhang and X. Wang, *Chem. Eur. J.*, , DOI:10.1002/chem.201804496.

205 Y.-L. Wong, J. M. Tobin, Z. Xu and F. Vilela, *J. Mater. Chem. A*, 2016, **4**, 18677–18686.

206 V. Dhananjayan, H. J. Niklas, S. Hayate, Y. Tomoyuki, Y. Hideki and O. Atsuhiro, *Asian J. Org. Chem.*, 2017, **6**, 1390–1393.

207 J. Liu, J. Zou, W. Yang, H. Wu, C. Li, B. Zhang, J. Peng and Y. Cao, *Chem. Mater.*, 2008, **20**, 4499–4506.